

University of Windsor

## Scholarship at UWindor

---

Electronic Theses and Dissertations

Theses, Dissertations, and Major Papers

---

2014

### Mechanical Analyses of Multi-piece Mining Vehicle Wheels to Enhance Safety

Zhanbiao Li  
*University of Windsor*

Follow this and additional works at: <https://scholar.uwindsor.ca/etd>

---

#### Recommended Citation

Li, Zhanbiao, "Mechanical Analyses of Multi-piece Mining Vehicle Wheels to Enhance Safety" (2014).  
*Electronic Theses and Dissertations*. 5197.  
<https://scholar.uwindsor.ca/etd/5197>

This online database contains the full-text of PhD dissertations and Masters' theses of University of Windsor students from 1954 forward. These documents are made available for personal study and research purposes only, in accordance with the Canadian Copyright Act and the Creative Commons license—CC BY-NC-ND (Attribution, Non-Commercial, No Derivative Works). Under this license, works must always be attributed to the copyright holder (original author), cannot be used for any commercial purposes, and may not be altered. Any other use would require the permission of the copyright holder. Students may inquire about withdrawing their dissertation and/or thesis from this database. For additional inquiries, please contact the repository administrator via email ([scholarship@uwindsor.ca](mailto:scholarship@uwindsor.ca)) or by telephone at 519-253-3000ext. 3208.

# **Mechanical Analyses of Multi-piece Mining Vehicle Wheels to Enhance Safety**

By

Zhanbiao Li

A Dissertation  
Submitted to the Faculty of Graduate Studies  
through Mechanical, Automotive, and Materials Engineering Department  
in Partial Fulfillment of the Requirements for  
the Degree of Doctor of Philosophy  
at the University of Windsor

Windsor, Ontario, Canada

2014

© 2014 Zhanbiao Li

# **Mechanical Analyses of Multi-piece Mining Vehicle Wheels to Enhance Safety**

By

Zhanbiao Li

APPROVED BY:

---

Dr. R. Hall, External Examiner  
University of British Columbia

---

Dr. S. Das  
Department of Civil and Environmental Engineering

---

Dr. N. Zamani  
Department of Mechanical, Automotive and Materials Engineering

---

Dr. D. Green  
Department of Mechanical, Automotive and Materials Engineering

---

Dr. W. Altenhof, Advisor  
Department of Mechanical, Automotive and Materials Engineering

September 4, 2014

## DECLARATION OF PREVIOUS PUBLICATION

This dissertation includes four (4) original papers that have been previously published in peer reviewed journals, as follows:

Dissertation Chapter	Publication title/full citation	Publication status*
<i>Chapter 4</i>	Tonkovich A., Li Z., DiCecco S., Altenhof W., Banting R., and Hu H. (2012) “Experimental Observations of tire Deformation Characteristics on Heavy Mining Vehicles under static and Quasi-Static Loading”. <i>Journal of Terramechanics</i> , Vol. 49, No. 3-4, pp. 215-231.	<i>Published</i>
<i>Chapter 5 and Chapter 6</i>	Li Z., Tonkovich A., DiCecco S., Altenhof W., Banting R., and Hu H. (2013) “Development and validation of a FE model of a mining vehicle tire”. <i>International Journal of Vehicle Design</i> , Vol.65, No.2/3, pp.176 – 201.	<i>Published</i>
<i>Chapter 8 and Chapter 9</i>	Li Z., DiCecco S., Tonkovich A., Altenhof W., Banting R., and Hu H. (2013) “A threaded-connection locking mechanism integrated into a multi-piece mining wheel for enhanced structural performance and safety”. <i>Journal of Terramechanics</i> , Vol. 50, No. 4, pp. 245-264.	<i>Published</i>
<i>Chapter 8 and Chapter 9</i>	Li Z., DiCecco S., Altenhof W., Thomas M., Banting R., and Hu H. (2014) “Stress and Fatigue Life Analyses of a Five-piece Rim and the Proposed Optimization with a Two-piece Rim”. <i>Journal of Terramechanics</i> , Vol. 52, pp. 31-45.	<i>Published</i>

I certify that I have obtained a written permission from the copyright owner(s) to include the above published material(s) in my dissertation. I certify that the above material describes work completed during my registration as graduate student at the University of Windsor.

I declare that, to the best of my knowledge, my dissertation does not infringe upon anyone’s copyright nor violate any proprietary rights and that any ideas, techniques, quotations, or any other material from the work of other people included in my dissertation, published or otherwise, are fully acknowledged in accordance with the standard referencing practices.

Furthermore, to the extent that I have included copyrighted material that surpasses the bounds of fair dealing within the meaning of the Canada Copyright Act, I certify that I have obtained a written permission from the copyright owner(s) to include such material(s) in my dissertation.

I declare that this is a true copy of my dissertation, including any final revisions, as approved by my dissertation committee and the Graduate Studies office, and that this dissertation has not been submitted for a higher degree to any other University or Institution.

## CLAIMS TO ORIGINALITY

Aspects of this work constitute, in the author's opinion, new and distinct contributions to the technical knowledge pertaining to enhancing the safety of multi-piece wheels. These include:

- (i) Analyses of fatality reports associated with multi-piece wheel failures. Through many fatality incident analyses, the root cause for the multi-piece wheel failures was identified to associate with the lock ring. This finding defined the focuses of this research and gave a clear direction for innovative designs. In the public domain, no literature was found to conduct systemic analysis of fatality incidents to identify the cause of multi-piece wheel failures, in the off-the-road (OTR) wheel design's point of view.
- (ii) Experimental testing of OTR tire/wheel assemblies. In-field tire deflection tests were conducted on heavy-duty underground mining vehicles. Linear relationships were found between the vertical wheel displacement and the maximum lateral tire deflection for linear static and quasi-static loading conditions. No literature was found in public domain to conduct in-field OTR tire deflection tests. The testing methods and findings are unique in this area. The in-field OTR tire testing led to the successful tire modeling and inclusion in the OTR tire/wheel assembly models, which were used for numerical predications of wheel performances and design improvements.
- (iii) Development of the finite element (FE) model of a five-piece OTR tire/wheel assemblies. A robust and high fidelity FE model of the assembly was developed using simplified yet efficient modeling approaches and validated using in-field experimental test data.
- (iv) Investigation of geometry and material degradation effect on fatigue life of a five-piece wheel. This research numerically investigated the effects of geometry degradation (material wear out in critical regions) and material property degradation (corrosion on wheels) on multi-piece wheel performances and fatigue lives.
- (v) BS (bead seat) band pull-out numerical testing method. This numerical testing is unique in determining the capability of the multi-piece wheel locking mechanism in holding the tire and wheel components in proper engaging positions under severe loading conditions.

- (vi) The threaded-connection mechanism design to replace the lock ring mechanism in the conventional five-piece wheel. This threaded-connection four-piece design reduced the possibility of failure due to the mismatched wheel components. The BS band pull-out simulation revealed that the threaded-connection design was twice as strong as the conventional five-piece design in holding wheel components and the tire together. The progressive failure mode of the threaded-connection had a much safer failure mode, compared to the instantaneous failure mode of the conventional five-piece lock ring design. The fatigue lives on the critical regions of the rim base were over two orders of magnitude higher than the fatigue lives of the rim base of the conventional five-piece wheel.
- (vii) The innovative two-piece wheel design. The two-piece wheel design completely removed the possibility of wheel failure due to mismatched wheel components that existed in other multi-piece wheels with a lock ring mechanism. It also reduced the numbers of pieces of the wheel. The fatigue lives at critical regions were increased by over two orders of magnitude, compared to the conventional five-piece wheel.

## ABSTRACT

In this research, experimental and numerical methods were used to analyse the performance of multi-piece wheel structures and two proposed innovative designs to enhance safety were validated by computer simulations. Fatality report analyses revealed that the majority (90%) of the multi-piece wheel failures were caused by use of lock rings.

Experimental tire and rim base tests were conducted to understand the deflection characteristics of off-the-road tires and to validate the finite element model of a five-piece wheel/tire (sized 29.5-29) assembly. A linear relationship was found between the vertical displacement of the wheel and the maximum lateral deflection of the tire for both static and quasi-static loading tests. A robust tire model was validated with an average accumulative error of 9.7% and an average validation metric of 0.96 for tire deflections, compared to the experimental tests. The rim base model was validated with an average error of 7.6% and an average validation metric of 0.93 for wheel deformations, and an average accumulative error of 12.7% and an average validation metric of 0.88 for strains, compared to experimental tests.

Based on validated FE model of the five-piece wheel/tire assembly, geometry degradation (material wear out at critical regions) and material degradation (fatigue and corrosion) were studied to estimate their effects on fatigue lives. Two design innovations were proposed to enhance safety and fatigue life of the five-piece wheel. The threaded-connection design reduced the possibility of failure due to the mismatched wheel components. The BS band pull-out simulation revealed that the threaded-connection design was twice as strong as the conventional five-piece design in holding wheel components and the tire together, and the wheel may fail in a safer mode. The fatigue lives of the rim base were two orders of magnitude higher than those of the conventional five-piece wheel. The two-piece wheel design completely removed the possibility of wheel failure due to mismatched wheel components; the fatigue lives were increased by over two orders of magnitude, compared to the conventional five-piece wheel.



## **DEDICATION**

This dissertation is dedicated to my wife, Helen Yu, for her patience and support, to my parents-in-law (Lanfang Liu and Xigang Yu) for their support by taking care of our children during these several years, and to my daughter Lena and my son Leeming for their sacrifice of their play time with me.

## **ACKNOWLEDGEMENTS**

The author would like to express his great appreciation to Dr. William Altenhof, his academic advisor, for his patience, understanding, encouragement, and guidance in the courses of this research and accomplishing the dissertation. There were ups and downs on the way, but they finally went through it and they both feel accomplished. The author would also like to thank Aleksander Tonkovich and Sante DiCecco, the other two members of Dr. Altenhof's research team, for their help and cooperation. The author would like to acknowledge the financial support from the Workplace Safety Insurance Board (WSIB) of Ontario, the Natural Sciences and Engineering Research Council of Canada (NSERC), and the Ministry of Training, Colleges and Universities (TCU) of Ontario. The author is obliged to the support and help from the industrial partners: North Shore Industry Wheel Mfg. (NSIW), Goldcorp Musselwhite Mine, Glencore Xstrata Nickel Sudbury Operations, Glencore Xstrata Copper Kidd Mine, Vale Inco., Goodyear Canada Inc., Royal Tire Sudbury, Fountain Tire Sudbury, and Workplace Safety North (WSN) of Ontario, with special thanks to the following individuals: Darrell Brown, Mark Thomas, Brent Tarini, Jude deCastro, and Rick Banking.

# TABLE OF CONTENTS

DECLARATION OF PREVIOUS PUBLICATION.....	iii
CLAIMS TO ORIGINALITY .....	v
ABSTRACT.....	vii
DEDICATION.....	viii
ACKNOWLEDGEMENTS.....	ix
LIST OF TABLES.....	xvii
LIST OF FIGURES .....	xviii
LIST OF APPENDICES.....	xxiv
LIST OF ABBREVIATIONS.....	xxv
LIST OF NOMENCLATURE.....	xxvii
Chapter 1. Introduction and Motivation .....	1
1.1. Mining Industry in Canada .....	1
1.2. The Differences between a Wheel and a Rim.....	2
1.3. On-the-road Wheels and Off-the-road (OTR) Wheels.....	3
1.3.1. The Size Difference .....	3
1.3.2. The Wheel Structure and Tire Mounting Differences.....	4
1.3.3. Manufacturing Materials and Maintenance Differences.....	5
1.4. Rationale for the Use of Multi-piece Wheels.....	6
1.5. Procedures and Regulations on Handling Multi-piece Wheel/Tire Assemblies .....	8
1.6. Motivation for Multi-piece Wheel Research .....	10
Chapter 2. Literature Review.....	12
2.1. Multi-piece Wheels and OTR Tires.....	12
2.1.1. On-the-road Single-piece Wheel and Tire Codes .....	12
2.1.2. Multi-piece Wheel Structures .....	13
2.1.2.1. Names and Size Specifications of Multi-piece Wheel Components.....	13
2.1.2.2. Other Multi-piece Wheel Structures .....	15
2.1.3. Off-the-road (OTR) Tires.....	17
2.1.3.1. OTR Tires Structures and Materials .....	17
2.1.3.2. Radial Tires and Bias Tires.....	18
2.1.3.3. The OTR Tire Deflections and Dimensions.....	20
2.1.3.4. Tire Load and Pressure Relationship .....	22

2.1.3.5.	OTR Tire Size and Code Designations .....	22
2.1.3.5.1.	Tire Size Designations.....	22
2.1.3.5.2.	Tire Industry Codes .....	23
2.2.	Fatalities Caused by Multi-piece Wheel/Tire Failures.....	24
2.2.1.	Fatalities in Canada since 1998.....	25
2.2.2.	Fatalities in the United States since 1998 .....	26
2.2.3.	Fatalities in Australia since 1998 .....	27
2.2.4.	Analysis and Summary of the Fatality Incidents .....	28
2.2.4.1.	Tire Explosions .....	28
2.2.4.2.	Tire Zipper Ruptures.....	29
2.2.4.3.	Tire Blow-outs .....	29
2.2.4.3.1.	Tire Blow-out Fatality Incident Analysis .....	30
2.2.4.3.2.	Lock Ring Improper Seating .....	31
2.2.4.3.3.	Wear, Corrosion, and Fatigue Cracks in the Gutter Region .....	32
2.2.4.4.	Tire Failures for on-the-road Tires.....	33
2.2.5.	Working with Multi-piece Wheel and OTR Tire .....	33
2.3.	Fatigue Life Analysis Theory .....	34
2.3.1.	Mechanism of Fatigue Failure .....	34
2.3.1.1.	Crack Initiation Stage.....	35
2.3.1.2.	Crack Propagation Stage.....	36
2.3.1.3.	Fracture .....	36
2.3.2.	The Stress-life ( <i>S-N</i> ) Approach.....	38
2.3.2.1.	Fatigue Loads.....	38
2.3.2.2.	Material Fatigue Test.....	39
2.3.2.3.	Factors Influencing Fatigue Life.....	40
2.3.2.4.	The Influence of Mean Stress .....	41
2.3.3.	Strain-life ( $\epsilon$ - <i>N</i> ) Approach .....	44
2.3.3.1.	Monotonic Stress-Strain Behaviour .....	44
2.3.3.2.	Cyclic Stress-Strain Behaviour .....	45
2.3.3.3.	The Strain-life ( $\epsilon$ - <i>N</i> ) Response .....	46
2.3.3.4.	Determination of Cyclic Fatigue Properties.....	47
2.3.3.5.	The Effect of Mean Stress.....	49
2.3.3.5.1.	The Morrow mean stress correction .....	49
2.3.3.5.2.	The Smith-Watson-Topper mean stress correction .....	50

2.3.3.6.	Factors Influencing Fatigue Strain Life .....	50
2.3.3.7.	Elastic-Plastic Corrections .....	50
2.3.4.	Multi-axial Loading in Fatigue .....	52
2.3.4.1.	Fatigue Life Prediction in Simple Multiaxial Stress/Strain Situations .....	52
2.3.4.2.	Fatigue Life Prediction in Complex Multiaxial Stress/Strain Conditions.....	54
2.3.4.3.	Critical Plane Approach .....	55
2.3.5.	Accumulated Fatigue Assessment .....	57
2.4.	Wheel Fatigue Testing Standards .....	58
2.4.1.	Dynamic Cornering Fatigue Testing.....	59
2.4.2.	Dynamic Radial Fatigue Testing.....	60
2.5.	FE-based Wheel Fatigue Testing .....	61
2.5.1.	FE-based Wheel Dynamic Cornering Fatigue Testing .....	62
2.5.2.	FE-based Wheel Dynamic Radial Fatigue Testing .....	63
2.5.3.	FE-Based Fatigue Testing on Other Vehicle Structures .....	64
Chapter 3.	Scope of Research.....	66
3.1.	Testing Methods Used in Multi-piece Wheel Fatigue Assessment .....	66
3.1.1.	Experimental Testing .....	66
3.1.2.	The Finite Element (FE) Method .....	67
3.1.3.	Fatigue Life Assessment Methods .....	67
3.2.	Innovative Designs.....	68
3.3.	Computer Software Used for This Research.....	68
Chapter 4.	Tire and Wheel Experimental Testing .....	70
4.1.	Experimental Testing of a Five-piece Wheel/Tire Assembly .....	70
4.1.1.	Experimental Procedure.....	71
4.1.1.1.	Testing Information .....	72
4.1.1.2.	Tire Physical and Engineering Data.....	72
4.1.1.3.	Testing Apparatus .....	73
4.1.1.4.	Static Deflection Scale Testing.....	76
4.1.2.	Results and Discussions .....	77
4.1.2.1.	Above Ground Quasi-Static Testing Observations .....	77
4.1.2.2.	Underground Static Testing Observations .....	83
4.2.	Rim Base Laboratory Tests.....	85
4.2.1.	Rim Base Testing Procedure.....	86
4.2.2.	Experimental Rim Base Testing Observations .....	89

Chapter 5.	Finite Element Model Development .....	91
5.1.	Tire Model Development .....	91
5.1.1.	On-the-road Tire Modeling in the Open Literature.....	91
5.1.2.	Tire Model Development for the Tire 29.5-29.....	92
5.1.2.1.	Tire Discretization .....	93
5.1.2.1.1.	The Bead.....	95
5.1.2.1.2.	The Chafer.....	95
5.1.2.1.3.	The Apex, Sidewall, Shoulder, Sidetread, Undertread, Tread, and Liner .....	95
5.1.2.1.4.	The Body Plies .....	97
5.1.2.2.	Tire Pressure Modelling.....	99
5.1.2.3.	Other Critical Modelling Features .....	100
5.1.2.4.	Static and Quasi-static Deflection Testing Simulations.....	101
5.1.2.4.1.	Static Loading Simulations.....	102
5.1.2.4.2.	Quasi-Static Loading Simulations .....	102
5.1.2.5.	The Computer Used for the Simulations and Simulation Time .....	104
5.2.	Numerical Rim Base Model Development .....	104
Chapter 6.	Stress and Fatigue Life Analyses .....	108
6.1.	FE Model Validation.....	108
6.1.1.	FE Model Validation for Tire 29.5-29 .....	108
6.1.1.1.	Validation Procedures .....	108
6.1.1.1.1.	Static Loading Behaviour Validation .....	108
6.1.1.1.2.	Quasi-Static Loading Behaviour Validation.....	109
6.1.1.2.	Results and Discussions .....	110
6.1.1.2.1.	Static Loading Behaviour .....	110
6.1.1.2.2.	Quasi-Static Loading Behaviour .....	112
6.1.2.	Rim Base FE Model Validation .....	118
6.2.	Geometry Degradation Modeling .....	120
6.2.1.	The OEM Wheel Information and Wear Conditions .....	120
6.2.2.	New and Worn Wheel Dimensions.....	122
6.2.3.	The Heave-duty HT2000 Rim Base.....	123
6.2.4.	FE Model Development.....	125
6.3.	Determination of Cyclic Fatigue Properties.....	127
6.3.1.	Mechanical Properties of the Rim Base from Monotonic Tensile Tests.....	127
6.3.1.1.	Tensile Test Results of Specimens Extracted from Rim Base .....	127

6.3.1.2.	Yield Criteria under Multiaxial Loading .....	129
6.3.1.2.1.	Maximum Shear Stress Yield Criterion (Tresca) .....	129
6.3.1.2.2.	Maximum Distortion-Energy or von Mises Criterion .....	129
6.3.1.2.3.	Determination of Yield Shear Stress under Multiaxial Loading .....	130
6.3.2.	Cyclic Fatigue Properties for Stress-life Approach .....	130
6.3.2.1.	Introduction of the Stress-Based Fatigue Tests.....	130
6.3.2.2.	Cyclic Fatigue Properties for Stress-Based Tests .....	131
6.3.3.	Cyclic Fatigue Properties for Strain-life Approach .....	134
Chapter 7.	Discussions on Simulation Results .....	138
7.1.	Geometry Degradation.....	138
7.1.1.	Maximum von Mises and Maximum Shear Stress Analyses.....	138
7.1.2.	Fatigue Life Analyses .....	139
7.2.	Material Degradation .....	140
Chapter 8.	Innovative Multi-piece Wheel Designs.....	142
8.1.	The Threaded-connection Design .....	142
8.1.1.	The Proposed Threaded-Connection Locking Mechanism.....	142
8.1.2.	Assessment Approaches for the Proposed Design .....	144
8.1.2.1.	BS Band Pull-out Simulations .....	145
8.1.2.2.	Wheel Stress and Fatigue Life Assessments.....	146
8.1.2.2.1.	Simulated Loading and Boundary Conditions for Stress and Fatigue Life Assessments.....	147
8.2.	The Two-piece Wheel Design.....	147
8.2.1.	The Proposed Two-piece Wheel Design.....	147
8.2.2.	The Tire and Wheel Model Development.....	149
8.2.2.1.	The Tire Model Development.....	149
8.2.2.1.1.	Tire Discretization .....	150
8.2.2.1.2.	Modelling of Steel Bead Coils and Body Pliers .....	152
8.2.2.1.3.	Other Critical Modelling Features .....	153
8.2.2.2.	Wheel Model Development .....	154
8.2.2.2.1.	Five-piece Wheel Model Development.....	154
8.2.2.2.2.	Two-piece Wheel Model Development.....	156
8.2.3.	Loading and Boundary Conditions for Tire Validation .....	156
8.2.4.	Tire Model Validation through Static Load Simulation .....	157
8.2.5.	Numerical Testing of the Multi-Piece Wheel Assemblies .....	159

8.2.5.1.	Loading and Bounding Conditions for FE Simulations.....	159
8.2.5.2.	Modelling Approaches for the Focused Regions.....	162
8.2.5.3.	Selection of Material Properties for Numerical Fatigue Assessment .....	163
Chapter 9.	Discussions on Innovative Designs.....	164
9.1.	Discussions on Threaded-connection Design .....	164
9.1.1.	BS Band Pull-out Simulation Results.....	164
9.1.2.	Wheel Stress and Fatigue Life Analyses.....	166
9.2.	Discussions on Two-piece Wheel Numerical Testing .....	167
9.2.1.	Stress Analysis.....	167
9.2.2.	Connecting Beam Element Forces.....	171
9.2.3.	Fatigue Life Simulation Results.....	173
Chapter 10.	Summaries and Conclusions .....	174
10.1.	Summary on the Analyses of the Fatality Reports.....	174
10.2.	Conclusions on Experimental Tire Testing and Rim Base Testing .....	174
10.2.1.	Experimental Tire Testing .....	174
10.2.2.	Laboratory Rim Base Testing .....	175
10.3.	Conclusions on the FE Model Developments.....	176
10.3.1.	Tire Model Development.....	176
10.3.2.	Rim Base Model Development.....	176
10.4.	Geometry Degradation Analysis of the Rim Base .....	176
10.5.	Material Degradation Analysis of the Rim Base .....	177
10.6.	Conclusions on Innovative Design Improvements to Enhance Safety .....	177
10.6.1.	Conclusions on the Threaded-connection wheel Design .....	177
10.6.2.	Conclusions on the Two-piece Wheel Design .....	178
Chapter 11.	Limitations of the Study and Future Work .....	180
11.1.	Limitations of the Study.....	180
11.2.	Future work.....	180
11.2.1.	Future Work on the Threaded-connection Design .....	180
11.2.2.	Future Work on the Two-piece Wheel Design .....	180
11.2.3.	Experimental Testing of Prototype Wheels for the New Designs .....	181
11.2.4.	Geometry Optimization of the Multi-piece Wheels.....	181
References.....		182
Appendix A: Fatigue Analysis within nCode DesignLife .....		194
Appendix B: Quasi-static Testing Observations for Event 2 and Event 3 .....		197



Appendix C: Experimental Observations from the Rim Base Testing .....	202
Appendix D: Tire Quasi-static Testing Results Comparisons between Experimental Tests and Computer Simulations for Test Event 2 and Event 3 Conditions .....	204
Appendix E: Partial Input Files Used for FE Simulations .....	210
E.1 Partial Input File Used of Tire Model Validation .....	210
E.2 Partial Input File Used for Tire Quasi-static Loading.....	216
E.3 Partial Input File Used for Rim Base Model Validation.....	225
E.4 Partial Input File Used for BS Band Pull-out Simulation.....	227
E.5 Partial Input File Used for Threaded-connection Design at Quasi-static Loading Condition .....	228
E.6 Partial Input File Used for Two-piece wheel Traveling and Steering Simulation .....	234
Appendix F: Copyright Permissions.....	245
VITA AUCTORIS .....	287

## LIST OF TABLES

Table 1.1	Lost-tie injuries and fatality in Canada and Ontario from 2009-2011. ....	2
Table 2.1	Standard tire industry code. ....	23
Table 2.2	Standard tread code, depth, and type. ....	24
Table 4.1	Test vehicle information. ....	72
Table 4.2	Tire physical data as given in Goodyear’s OTR Engineering Data Book [28]. ....	72
Table 4.3	Tire deflection characteristics based on Goodyear OTR data [28]. ....	73
Table 4.4	Tire wear based on mine site tire measurements. ....	73
Table 4.5	Tire stiffness comparison of experimental static loading and Goodyear OTR data. ....	84
Table 4.6	Tire deflection observations comparing experimental static loading to Goodyear OTR data. ....	85
Table 5.1	Liner elastic modulus change effects ....	96
Table 6.1	Vertical and Lateral Deflections for static loading condition. ....	110
Table 6.2	Slope comparisons for vertical and lateral deflections versus load. ....	111
Table 6.3	Errors and validation metrics between experimental test and simulation for event 1. ....	117
Table 6.4	Deflection (mm), strain (microstrain, $\mu\epsilon$ ), errors, and validation metrics for simulations and experimental tests under static load condition. ....	119
Table 6.5	Elastic moduli, engineering and true data for the three tests. ....	129
Table 6.6	<i>S-N</i> fatigue properties generated from fatigue tests. ....	133
Table 7.1	Maximum von Mises stresses/maximum shear stresses (MPa) on the shell elements at front gutter and back section regions. ....	139
Table 7.3	Fatigue life comparisons between new gutter and corroded gutter materials. ....	140
Table 8.1	Tire deflection comparisons. ....	158
Table 9.1	The maximum von Mises stress/maximum shear stress at the front regions of shell elements for the lock ring design and the threaded-connection design. ....	167
Table 9.2	Fatigue life predictions (cycles) and comparisons. ....	167
Table 9.3	Maximum effective/maximum shear stresses (MPa) at different focused regions. ....	170
Table 9.4	Minimum fatigue <i>S-N</i> / $\epsilon$ - <i>N</i> life (cycle) comparisons on focused regions. ....	173

## LIST OF FIGURES

Figure 1.1	A single-piece wheel (a) and a five- wheel (b) [5].....	3
Figure 1.2	The size difference between OTR tires and on-the-road tires [7]. (Reprinted Courtesy of Caterpillar Inc.) .....	4
Figure 1.3	A five-piece wheel wheel structure and tire mounting sequence [5]. .....	5
Figure 1.4	Severe cuts and wear on an OTR tire.....	7
Figure 1.5	Schematic view of the rationale for use of multi-piece wheel for OTR vehicles. ....	7
Figure 1.6	Multi-piece wheel failures kill people [9].....	8
Figure 1.7	Trajectory of multi-piece wheel parts in different scenarios [10].....	9
Figure 1.8	Place wheel and tire in a safety cage during tire inflation [11].....	9
Figure 2.1	The side view of a single piece wheel (a) [16] and tire codes for on-the-road tire (b) [17].....	13
Figure 2.2	Names and specifications of three-piece wheel components [18]. .....	14
Figure 2.3	Names and specifications of five-piece wheel components [18]. .....	14
Figure 2.4	Names of the components of a five-piece wheel involving an out board driver [18]. .....	15
Figure 2.5	A two-piece wheel with a split lock ring (a) [19, 20] and a two-piece wheel with connecting bolts. ....	15
Figure 2.6	Two different structures of four-piece wheels [21].....	16
Figure 2.7	The structure of a seven-piece wheel [22]. .....	16
Figure 2.8	Tire construction features of a radial tire (a) and a bias tire (b) [25]. .....	17
Figure 2.9	Radial structure tire and bias structure tire [26].....	19
Figure 2.10	Tire deflections and tire dimensions under static load [28]. .....	21
Figure 2.11	Tire size designations.....	23
Figure 2.12	Illustrations of sidewall markings of a Goodyear tire. ....	24
Figure 2.13	Detailed tire failure reasons specified in the incident reports in the failure mode of tire blow-out.....	30
Figure 2.14	A sprung lock ring (left) and a good lock ring (right) [18]. .....	31
Figure 2.15	Correct installation (left) and lock ring installed backward (right) [18]. .....	32
Figure 2.16	Wear and Fatigue cracks in the gutter region [5]. .....	32
Figure 2.17	Three common rotation loads.....	38
Figure 2.18	Fatigue strength versus the numbers of cycle to failure diagram.....	39

Figure 2.19	Estimated $S-N$ response for HCF regime (a) materials with an endurance limit (b) material without an endurance limit. ....	41
Figure 2.20	High cycle fatigue data showing the influence of mean stress. ....	42
Figure 2.21	Various failure lines for fluctuating stresses. ....	43
Figure 2.22	True stress versus true strain diagram. ....	45
Figure 2.23	Strain amplitude as a function of reversals to failure. ....	47
Figure 2.24	Log stress versus log plastic strain line. ....	48
Figure 2.25	Effect of mean stress on the strain-life curve. ....	49
Figure 2.26	The Neuber's method for estimating elastic-plastic strain and stress at a notch. ....	51
Figure 2.27	Dynamic cornering fatigue testing set-up [81]. (Reprinted with permission from SAE J328 Feb 2005 © 2005SAE International. Further use or distribution is not permitted without permission from SAE.) ....	59
Figure 2.28	Dynamic radial fatigue testing set-up. [81] (Reprinted with permission from SAE J328 Feb 2005 © 2005SAE International. Further use or distribution is not permitted without permission from SAE.) ....	60
Figure 4.1	Wheel assembly displacement measurement apparatus for R29.5-29 tire. Note: Positive vertical displacement is downwards in the $z$ -axis direction, positive lateral/sidewall displacement is inwards in the $x$ -axis direction, and positive longitudinal is towards the front of the vehicle in the $y$ -axis direction. ....	75
Figure 4.2	Excitation of the R2900G using the Caterpillar 990 front load scoop. ....	76
Figure 4.3	Quasi-static testing tire responses for test event 1, exhibiting maximum deflection in the (a) vertical and lateral directions as well as (b) lateral deflection versus vertical deflection. ....	78
Figure 4.4	Plot of validation metric, $V$ , given in Equation (4.2) as a function of relative error. .....	80
Figure 4.5	Vertical displacement comparisons for test event 1 between laser displacement transducer measurements and high-speed camera image tracking using ProAnalyst. .....	80
Figure 4.6	Location of points tracked on the physical tire 29.5-29. ....	81
Figure 4.7	Vertical deflection responses for tracked nodes for test event 1. ....	82
Figure 4.8	Horizontal deflection responses for tracked nodes for test event 1. ....	83
Figure 4.9	Static load-deflection data for the tire 29.5-29 showing a) vertical deflection versus load force and b) lateral deflection versus load force compared to the corresponding Goodyear engineering data point. ....	84
Figure 4.10	Testing apparatus and setup used during static rim base testing. ....	87
Figure 4.11	Locations of strain and displacement measurement on the rim base. ....	88

Figure 4.12	Experimental observations (a) lateral deflections at location ‘B’ and.....	90
	(b) circumferential strain at location ‘1’ .....	90
Figure 5.1	Five-piece wheel assembly model. ....	93
Figure 5.2	Tire region definitions and discretization. ....	94
Figure 5.3	Deformed tire (a) sidetread too soft, (b) shoulder too soft.....	96
Table 5.1	Liner elastic modulus change effects .....	96
Figure 5.4	(a) beam elements added and (b) deformation of the tire at the bottom contact patch. .....	98
Figure 5.5	Tire region definitions and the associated elastic moduli assigned (in MPa). ....	98
Figure 5.6	Set-up for simulating tire inflation.....	99
Figure 5.7	Load applications for static load simulation. ....	102
Figure 5.8	Load applications for quasi-static simulation. ....	103
Figure 5.9	Half rim base model illustrating mesh discretization.....	104
Figure 6.1	Location of points tracked on the physical test apparatus (a) and numerical model (b). .....	110
Figure 6.2	(a) Vertical deflection/load response and (b) lateral deflection/load response for tire 29.5-29. ....	111
Figure 6.3	(a) Lateral deflection versus time for event 1, (b) lateral versus vertical deflection for event 1, (c) lateral deflection versus time for event 2, (d) lateral versus vertical deflection for event 2, (e) lateral deflection versus time for event 3, (f) lateral versus vertical deflection for event 3. ....	113
Figure 6.4	Deflection comparisons at H points for event 1, (a) Vertical deflection versus time for H-in location, (b) horizontal deflection versus time for H-in location, (c) vertical deflection versus time for H-out location, (b) horizontal deflection versus time for H-out location. ....	114
Figure 6.5	Deflection comparisons at D points for event 1, (a) Vertical deflection versus time for D-in location, (b) horizontal deflection versus time for D-in location, (c) vertical deflection versus time for D-out location, (b) horizontal deflection versus time for D-out location. ....	115
Figure 6.6	Deflection comparisons at V points for event 1, (a) Vertical deflection versus time for V-in location, (b) horizontal deflection versus time for V-in location, (c) vertical deflection versus time for V-out location, (b) horizontal deflection versus time for V-out location. ....	116
Figure 6.7	Comparison of experimental and numerical (a) vertical displacements and (b) lateral displacements measured from locations ‘A’ and ‘B’, respectively.....	118

Figure 6.8	Comparison of experimental and numerical circumferential strains at (a) locations 1, 2 and 5 and (b) locations 3 and 4. ....	119
Figure 6.9	Gauges are used to check the back section. ....	121
Figure 6.10	Gauges is used to check front gutter region. ....	122
Figure 6.11	Profiles of back (a) and front (b) section of rim base – new (blue) and worn (red). .....	123
Figure 6.12	Cross section comparison between the OEM rim base and the HT2000 rim base. .....	123
Figure 6.13	Front gutter region comparisons between the OEM rim base and the HT2000 rim base. ....	124
Figure 6.14	The lock ring dislodged under “push out” simulation for the OEM rim.....	125
Figure 6.15	The FE model of the rim/tire assembly of the OEM new rim.....	126
Figure 6.16	Load application histories and illustrations of applied loads for fatigue life analysis – the OEM wheel assembly. ....	127
Figure 6.17	Engineering stress/strain behavior of the 29-25.00/3.5 rim base.....	128
Figure 6.18	R. R. Moore rotating beam fatigue testing machine. ....	131
Figure 6.19	High cycle fatigue (HCF) behaviors for specimens extracted from new gutter, back section, and corroded gutter regions. ....	132
Figure 6.20	Total strain-life curve and elastic strain-life curve deduced using universal slope approximations, and elastic strain- life curve transformed from stress-life testing. 135	
Figure 6.21	The curves of total strain life, elastic strain life and plastic strain life for the new gutter region. ....	136
Figure 6.22	The total strain life curves for the three conditions.....	137
Figure 7.1	Maximum von Mises stress contours for the three different rims, (a) the HT2000 new, (b) the OEM new, and (c) the OEM worn. ....	138
Figure 8.1	Schematic of a 29-25 five-piece wheel, illustrating rim width, flange height, and rim diameter.....	143
Figure 8.2	Illustrations of (a) O-ring placement and the BS band mating with the threaded rim base and (b) the threaded rim base and BS band, and the installation process. ....	143
Figure 8.3	(a) Feature lines of a conventional rim base and a threaded rim base and (b) critical dimension of the threaded BS band region. ....	144
Figure 8.4	Cross-section of the wheel/tire FE model illustrating the BS band pull-out simulation for the five-piece wheel/tire assembly. ....	145
Figure 8.5	(a) five-piece wheel structure and (b) Kalmar ContChamp 42-45 tonnes container handler [128]. ....	148
Figure 8.6	The proposed two-piece wheel design. ....	149

Figure 8.7	The FE model of the five-piece tire/rim assembly.....	150
Figure 8.8	Discretization of the tire showing elastic moduli (MPa) at different regions. ....	151
Figure 8.9	(a) Beam elements in the liner region and (b) beam elements in bead and chafer regions.....	153
Figure 8.10	Modelling of the five-piece wheel for tire validation purpose. ....	155
Figure 8.11	Modelling of bolt connection for two-piece wheel. ....	156
Figure 8.12	Load application histories for tire FE model validation. ....	157
Figure 8.13	Simulated tire deformation of the half model at 16,650 kg static load. ....	158
Figure 8.14	FE model set-ups for travelling (rotation) and steering (turning) simulation. ....	159
Figure 8.15	Load application histories for 24.14 km/h. ....	161
Figure 8.16	Analysis focused regions for the five-piece and two-piece wheels. ....	162
Figure 9.1	Simulation deformation predictions of the BS band disengagements of (a) the lock ring design and (b) the threaded-connection design.....	164
Figure 9.2	Predicted pull-out (a) force/displacement response and (b) energy/displacement response of the conventional and proposed wheel designs. ....	165
Figure 9.3	von Mises stress contours of the lock ring design (a) and the threaded-connection design (b) during quasi-static loading simulations.....	166
Figure 9.4	Initial and final positions of the tires, and moving traces of the axles with approximate dimensions (a) 8.05 km/h and (b) 24.14 km/h. ....	168
Figure 9.5	von Mises stress time histories for the shell elements on lock ring groove – 24.14 km/h. ....	169
Figure 9.6	Maximum shear stress contours at lock ring groove (FR1-1) (a) and at the FR2-1 and FR2-3 regions of the two-piece wheel (b) at $t = 1.65$ s under 24.14 km/h.....	170
Figure 9.7	Axial forces on the 4 beam elements – 8.05 km/h. ....	172
Figure A.1	The fatigue analysis “5-Boxes Trick” [105]. ....	194
Figure A.2	A simple example of DesignLife-based fatigue life analysis process.....	196
Figure B.1	Quasi-static testing tire responses for test event 2 (a) vertical and lateral directions as well as (b) lateral deflection versus vertical deflection. ....	197
Figure B.2	Quasi-static testing tire responses for test event 3 (a) vertical and lateral directions as well as (b) lateral deflection versus vertical deflection. ....	197
Figure B.3	Vertical displacement comparisons between laser displacement transducer measurements and high-speed camera image tracking using ProAnalyst (a) test event 2 and (b) test event 3. ....	198
Figure B.4	Vertical deflection responses for tracked nodes for test event 2.....	198
Figure B.5	Horizontal deflection responses for tracked nodes for test event 2.....	199

Figure B.6	Vertical deflection responses for tracked nodes for test event 3.....	200
Figure B.7	Horizontal deflection responses for tracked nodes for test event 3.....	201
Figure D.1	Deflection comparisons at H points for event 2, (a) Vertical deflection versus time for H-in location, (b) horizontal deflection versus time for H-in location, (c) vertical deflection versus time for H-out location, (b) horizontal deflection versus time for H-out location. ....	204
Figure D.2	Deflection comparisons at D points for event 2, (a) Vertical deflection versus time for D-in location, (b) horizontal deflection versus time for D-in location, (c) vertical deflection versus time for D-out location, (b) horizontal deflection versus time for D-out location. ....	205
Figure D.3	Deflection comparisons at D points for event 2, (a) Vertical deflection versus time for V-in location, (b) horizontal deflection versus time for V-in location, (c) vertical deflection versus time for V-out location, (b) horizontal deflection versus time for V-out location. ....	206
Figure D.4	Deflection comparisons at H points for event 3, (a) Vertical deflection versus time for H-in location, (b) horizontal deflection versus time for H-in location, (c) vertical deflection versus time for H-out location, (b) horizontal deflection versus time for H-out location. ....	207
Figure D.5	Deflection comparisons at D points for event 3, (a) Vertical deflection versus time for D-in location, (b) horizontal deflection versus time for D-in location, (c) vertical deflection versus time for D-out location, (b) horizontal deflection versus time for D-out location. ....	208
Figure D.6	Deflection comparisons at D points for event 3, (a) Vertical deflection versus time for V-in location, (b) horizontal deflection versus time for V-in location, (c) vertical deflection versus time for V-out location, (b) horizontal deflection versus time for V-out location. ....	209



## **LIST OF APPENDICES**

- Appendix A: Fatigue Analysis within nCode DesignLife
- Appendix B: Quasi-static Testing Observations for Event 2 and Event 3
- Appendix C: Experimental Observations from the Rim Base Testing
- Appendix D: Tire Quasi-static Testing Results Comparisons Between Experimental Tests and Computer Simulations for Test Event 2 and Event 3 Conditions
- Appendix E: Partial Input Files Used for FE Simulations
- Appendix F: Copyright Permissions

## LIST OF ABBREVIATIONS

<i>AR</i>	aspect ratio
<i>BS</i>	bead seat
<i>CAD</i>	computer aided design
<i>CAE</i>	computer aided engineering
<i>CPU</i>	center processing unit
<i>DIC</i>	digital image correlation
<i>GPD</i>	gross domestic product
<i>GUI</i>	graphical user interface
<i>FE</i>	finite element
<i>FEA</i>	finite element analysis
<i>FR</i>	free radius
<i>HCF</i>	high cycle fatigue
<i>HSLA</i>	high strength low alloy
<i>ICAM</i>	incident cause analysis method
<i>LCF</i>	low cycle fatigue
<i>LD</i>	lateral deflection
<i>LTI</i>	lost time injury
<i>LTA</i>	less than adequate
<i>LHD</i>	Load-haul-dump
<i>LSG</i>	loaded section growth
<i>LSTC</i>	Livermore Software Technology Corporation
<i>LSW</i>	loaded section width
<i>NDT</i>	non-destructive testing
<i>NSIW</i>	North Shore Industrial Wheel Mfg.
<i>OD</i>	overall diameter
<i>OEM</i>	original equipment manufacturer
<i>OTR</i>	off-the-road
<i>OW</i>	overall width
<i>PR</i>	ply rating
<i>SAE</i>	Society of Automotive Engineers
<i>SH</i>	section height
<i>SLR</i>	static load radius

<i>SW</i>	section width
<i>TRA</i>	Tire and Rim Association
<i>TSA</i>	tire standards associations
<i>TW</i>	tread width
<i>VD</i>	vertical deflection
<i>WSIB</i>	Workplace Safety and Insurance Board

## LIST OF NOMENCLATURE

$a$	fatigue strength factor
$A_0$	initial cross section area of the specimen
$b$	fatigue strength exponent
$b_1$	slope of the S-N response after $10^6$ cycles
$B$	stiffness proportional damping constants
$c$	fatigue ductility exponent
$C$	damping matrix
$C_{load}$	load factor
$C_m$	constant related to the specific material
$C_{reliab}$	reliability factor
$C_{size}$	size factor
$C_{surf}$	surface factor
$C_{temp}$	temperature factor
$d$	inset or outset of the wheel
$DC$	decay coefficient
$D^p_{ij}$	plastic component of the rate of deformation tensor
$e$	elongation of the specimen
$E$	modulus of elasticity
$Ev$	experimental measurement
$F_{damp}$	system damping force
$K$	strength coefficient
$K_f$	accelerated test factor
$K_s$	stiffness matrix
$K'$	cyclic strength coefficient
$l$	final length of the specimen
$L$	load rating of the wheel
$l_0$	initial length of the specimen
$m$	<i>nodal mass</i>
$M$	bending moment
$M_m$	mass matrix
$N$	fatigue life
$N_i$	life to crack initiation

$N_f$	cycles to failure
$N_p$	crack propagation life
$N_t$	total fatigue life
$N_v$	numerical variable
$n$	work hardening exponent
$n'$	cyclic work hardening exponent
$2N_f$	number of half cycles to failure
$O_{exp}$	single experimental data
$O_{FE}$	single FE prediction
$O_{Laser}$	laser transducer measurement
$O_{Tracked}$	tracked measurement using ProAnalyst
$P$	applied load
$R$	radial load of the tire
$Ra$	arithmetic average roughness
$Ry$	maximum peak height of roughness
$Rz$	maximum valley height of roughness
$Rq$	root mean squared roughness
$S$	stress
$S'$	equivalent fully reversed fatigue strength
$S_e$	corrected endurance limit
$S_E$	engineering stress
$S_e'$	endurance limit
$S_f$	corrected fatigue strength
$S_f$	fatigue strength
$S_{ij}$	deviatoric stress tensor
$slr$	static load radius of the tire
$S_m$	The material strength at 103 for low cycle fatigue
$S_{ut}$	ultimate tensile strength
$t$	time
$t_A$	fatigue shear strength for case A
$t_B$	fatigue shear strength for case B
$V$	validation metric
$v$	velocity
$v_{rel}$	relative velocity

$\beta$	stiffness proportional damping constant
$\gamma_{max}$	maximum shear strain
$\gamma_{max}^a$	maximum shear strain amplitude
$\gamma_e$	equivalent shear strain
$\varepsilon$	true strain
$\varepsilon_1$	first principal strain
$\varepsilon_2$	second principal strain
$\varepsilon_3$	third principal strain
$\varepsilon_a$	total strain amplitude
$\varepsilon_e$	true cyclic elastic strain amplitude
$\varepsilon_f$	fatigue ductility coefficient
$\varepsilon_n$	strain normal to the maximum shear
$\varepsilon_n^a$	strain amplitude normal to maximum shear
$\varepsilon_p$	plastic strain
$\overline{\varepsilon_p}$	effective plastic strain
$\mu$	coefficient of friction
$\mu_D$	dynamic coefficient of friction
$\mu_S$	static coefficient of friction
$\sigma$	true stress
$\sigma_1$	first principal normal stress
$\sigma_2$	second principal normal stress
$\sigma_3$	third principal normal stress
$\bar{\sigma}$	effective stress
$\sigma_a$	stress amplitude
$\sigma_{a,max}$	maximum stress normal to the plan of maximum shear
$\sigma_e$	stress amplitude
$\sigma_m$	mean stress
$\sigma_{max}$	maximum stress
$\sigma_{min}$	minimum stress
$\sigma_f'$	fatigue strength coefficient
$\sigma_o$	critical uniaxial tension stress (yield normal stress)
$\sigma_{n,max}$	maximum stress normal to the plan of maximum shear

$\sigma_{vm}$	von Mises stress (effective stress)
$\tau_1$	first principal shear stress
$\tau_2$	second principal shear stress
$\tau_3$	third principal shear stress
$\tau_a$	maximum allowable shear stress
$\tau_{eq}$	equivalent shear stress
$\tau_o$	critical shear stress (yield shear stress)
$\tau_t$	torsional stress amplitude
$\phi$	phase angle
$\omega$	natural frequency

# Chapter 1. Introduction and Motivation

## 1.1. Mining Industry in Canada

Mining impacts our everyday lives, not only from a broader economic and employment perspective, but in our day-to-day living. From mining come the highways, electrical and communications networks, clean-energy technologies, housing, automobiles, consumer electronics and other products and infrastructure essential to modern life.

Mining is one of Canada's most important economic sectors and is a major driver of our country's prosperity. According to Facts and Figures of The Canadian Mining Industry 2012 [1], in 2011, the industry contributed \$35.6 billion to the gross domestic product (GDP) and employed 320,000 workers in the sectors of mineral extraction, processing and manufacturing. It is an industry that stimulates and supports economic growth both in large urban centres and in remote rural communities, including numerous First Nations communities; mining is an important employer of Aboriginal Canadians.

Mining accounts for 22.8% of Canadian goods exports and \$9 billion in taxes and royalties paid to federal, provincial, and territorial governments [1]. The industry also generates considerable economic spin-off activity: there are more than 3,200 companies that provide the industry with services ranging from engineering consulting to drilling equipment. In addition, over half the freight revenues of Canada's railroads are generated by mining.

Globally, Canada remains the top destination for mining exploration, attracting 18% of the world's spending in this sector [1]. In the same vein, Canada is recognized internationally as a source of mining leadership and related finance expertise: there are approximately 1,000 Canadian exploration companies active in over 100 countries.

Ontario is the largest producer in Canada of gold, nickel, copper, platinum group metals, copper, salt, and structural materials [2]. The value of mineral production was \$6.3 billion in 2009, \$7.7 billion in 2010, and \$10.7 billion in 2011. This represented almost 25% of all Canadian nonfuel mineral production in 2011 and accounted directly for more than 1.6% of total Ontario GDP.

However, some factors hamper the development to mining industry. One of which is the injuries in the mining industry. Injuries have a tendency of decreasing due to technology advancement, stringent government safety regulations, and employee training. However, mining injuries and fatalities are still occurring around the world every year as regular occurrences.



According to the Association of Workers' Compensation Boards/Commissions of Canada [3], significant amounts of Lost Time Injury (LTI) and fatalities occur, as listed in Table 1.1 for recent years. A LTI occurs when a person is injured in the execution of his/her duties and as a result of this injury the person is unable to perform his/her regular duties for one full shift or more on the day following the injury.

Table 1.1 Lost-time injuries and fatality in Canada and Ontario from 2009-2011.

	Lost-time injuries		Fatalities	
	Canada	Ontario	Canada	Ontario
2009	1,896	222	69	23
2010	2,395	245	82	20
2011	2,814	322	75	21

Injuries not only claim human lives, it also increases the cost and reduces the efficiency of mining operation. The mining industry spent almost \$1,800 per employee in 2011 on training and health and safety initiatives [2].

The injuries and fatalities in the mining industry can be attributed to the following situations, [3] (i) slips and falls, (ii) power haulage/transportation off site, (iii) unconsciousness, (iv) falls of ground/rock burst, (v) falling, rolling, sliding of rock, or material of any kind, and (vi) machinery. Among the last situation, a significant number of injuries were caused by the failures of wheel/tire assemblies of mining vehicles.

To better understand the failure mechanisms of the wheel/tire assemblies of mining vehicles, some concepts, definitions, and working conditions related to mining wheels need to be first explained.

## 1.2. The Differences between a Wheel and a Rim

A rim and a wheel are two different entities. The rim is the "outer edge of a wheel, holding the tire." [4] In a wheel/tire assembly, the metal components directly contacting the tire are called a rim. Some rims are made of one piece of metal, such as bicycle wheels and car wheels (Figure 1.1 (a)); some rims are made of multiple pieces, such as wheels used in mining vehicles, which may be composed of a rim base, a bead seat (BS) band, flanges, and a lock ring (Figure 1.1 (b) [5] shows a five-piece rim). In order to install a rim to a vehicle, a mounting ring (wheel disc) or mounting spokes are needed to mount the rim to an axle or hub. The mounting ring or spokes may be welded, bolted, riveted, or clamped to the rim base. When the mounting devices are integrated together with the rim, the assembly is called a wheel. So the wheel includes the rim

and the mounting structures. A wheel is a rotating load-carrying member between the tire and the axle.

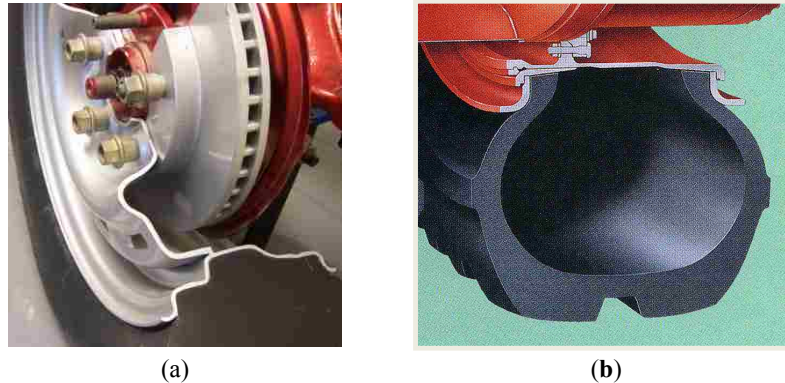


Figure 1.1 A single-piece wheel (a) and a five-piece wheel (b) [5].

### 1.3. On-the-road Wheels and Off-the-road (OTR) Wheels

The wheels used on vehicles running on the road are called on-the-road wheels, such as passenger vehicle and haulage truck wheels. The wheels used on vehicles running off the road are called off-the-road (OTR) wheels, such as wheels used in vehicles for mining, agriculture, logging, construction, in ports and garbage dumping sites. The differences between on-the-road wheels and OTR wheels can be attributed to vehicle applications and working environments. They are different in the aspects of size, manufacturing material, structures, and service life.

Wherever possible, the International System of units (abbreviated SI from French: *Système international d'unités*) were used throughout this dissertation. However, units of tires and wheel components are commonly measured using imperial units in North America. The tires and wheels are often referred by their dimensions. If SI units were used, the names of the tires and wheel components will be changed and cannot be recognized. In these cases, the imperial unit “inch” is used. In some cases, both SI units and imperial units (tire pressure and tire/wheel size) are used for clarity.

#### 1.3.1. The Size Difference

On-the-road wheels run on smooth ground, where shallow potholes and small obstacles can be easily negotiated by wheels and tires. Therefore the wheel diameters are usually not significant, usually 0.45 meters to 0.6 meters [6] and they travel at high speeds. For OTR wheels, due to the deep potholes and big obstacles on the ground, wheels have to be made big for continuous traveling and they travel at low speeds. The high tire pressure required to support the high payload also dictates that large thickness of sidewall and large tire structures are necessary

for OTR tires (to have enough volume of air inside the tire to increase load support capability and tire stability). Therefore the diameters of OTR wheels are usually much bigger than those of road wheels. Figure 1.2 [7] shows that the tires used on Cat® 797 Mining Truck, which is approximately 2.5 m in diameter. The tire size difference between the passenger vehicle and the mining truck can be clearly observed from the figure.



Figure 1.2 The size difference between OTR tires and on-the-road tires [7]. (Reprinted Courtesy of Caterpillar Inc.)

### 1.3.2. The Wheel Structure and Tire Mounting Differences

Road wheel tires are usually small and the tire beads are not significantly thick and the tire can be easily mounted/dismounted on a single piece wheel. Therefore road wheels are usually made of one single piece. On the other hand, OTR tires are usually very large and tire beads are very thick and stiff. OTR wheels are usually made of multiple pieces for tire mounting/dismounting purpose. The rationale for use of multi-piece wheels will be detailed in the following section.

Due to the structure difference between the rims of road wheels and OTR wheels, the tire mounting/dismounting methods are different. The road tire can be easily mounted on or dismantled off a single piece wheel by prying the tire bead onto or off the rim lip using a prying bar or some other mounting device, due to the thin and flexible tire beads. For OTR wheels, tire mounting/dismounting has to follow a specific sequence. Figure 1.3 [5] illustrates the structure of a five-piece wheel, in which the numbers behind the component names indicate tire mounting sequence. The five-piece wheel is composed of a rim base, a split lock ring, a bead seat (BS) band, and front/back flanges. Mounting of the tire begins with placing the rear flange onto the rim base. The tire is subsequently installed on the rim base, followed by the front flange being placed against the tire. A rubber O-ring is inserted into the O-ring groove located on the rim base

to ensure tire pressure is maintained. Next, the BS band is inserted in place and the final step is the installation of the split lock ring, which engages the BS band and fits firmly in the lock ring groove located on the rim base. Inflating the tire to its recommended pressure and tight engagement among tire and wheel components is ensured. The tire demounting procedure is the reverse of the mounting process. The number of components used with multi-piece wheels varies according to different applications; however the split lock ring is an indispensable and essential component for tire mounting/demounting and to ensure safe operation as it ensures proper engagement of all wheel components.

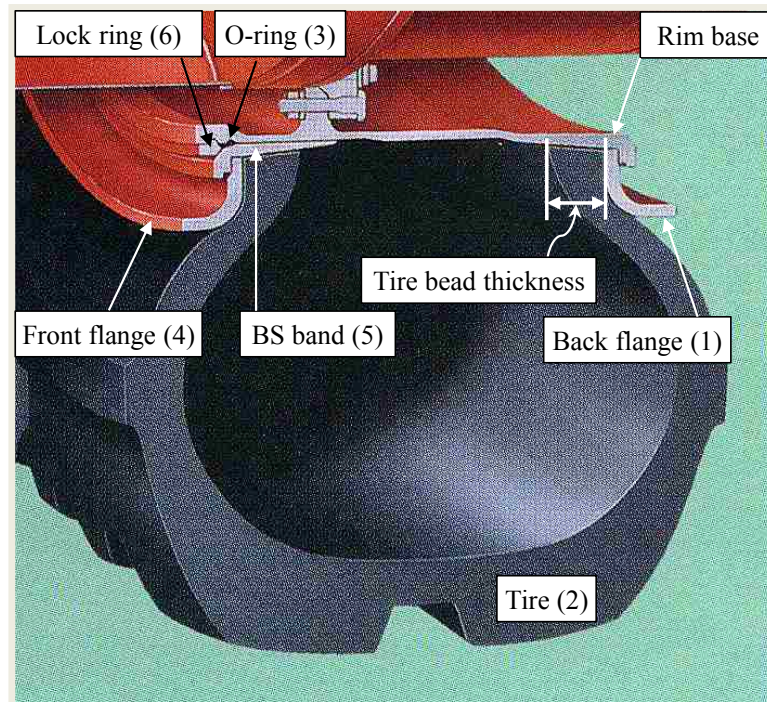


Figure 1.3 A five-piece wheel structure and tire mounting sequence [5].

For two-piece bolted wheels, the tire mounting/demounting process is simpler; first the tire is placed onto the first piece of the wheel and followed by the placement of an O-ring in the O-ring groove, then the second piece of the wheel is appropriately positioned and the two pieces are bolted together. Finally the tire is inflated to make tight engagement between the tire and the wheel.

### 1.3.3. Manufacturing Materials and Maintenance Differences

Road wheels are often made of cast iron, light-weight aluminum, or magnesium alloys to increase fuel efficiency. Road wheels usually outlive the vehicles they are attached to and generally are maintenance free. OTR vehicles are usually designed to carry high payloads to

increase productivity and wheels are often subjected to loads and pressures at their maximum capabilities, therefore rims must be strong and durable, and like other components they have a shorter service life. In mine sites, various terrains and high payloads result in higher than normal stresses on a wheel. Therefore OTR wheels are required to travel at low speed (usually lower than 40 km/h) in order to reduce impact load and cornering load on wheels. The effects of corrosion and fretting between wheel components in mining environments can produce surface irregularities and expedite the initiation of fatigue cracks and ultimately component fractures. Therefore, OTR wheels are usually made with high strength low alloy (HSLA) steel to improve load-carrying capability and fatigue life.

OTR wheels are consumable items and are not maintenance free. A significant number of multi-piece wheel failures occurred in the 1990s since the wheels were considered “maintenance free”. For wheels mounted on vehicles used in underground mines, scheduled maintenance on wheels will be conducted usually in a period of once a year and once every 2-3 years for wheels used above ground.

#### **1.4. Rationale for the Use of Multi-piece Wheels**

For OTR vehicles, due to the requirement for high payload and high productivity, high tire pressure (within the range of 344.7 kPa (50 psi) to 1034.2 kPa (150 psi)) is needed to support the payload. This requires large tire thickness to hold the high pressure and therefore thick tire beads (within the range of 50.8 mm (2 inches) and 203.2 mm (8 inches) as shown in Figure 1.3) are required to support the thick sidewall. Thick and stiff beads are also needed to support the high load and increase tire stability. Thick beads increase the contacting area between the tire and rim and therefore are helpful to reduce impact force on the wheel from the tire and reduce wear on both tire beads and rims. Harsh and corrosive ground conditions also require thick tread and sidewall to increase wear and cut resistance of the tires, which leads to thick tire beads. Figure 1.4 shows the cuts and wears on a tire of smooth structure (no tread) having an overall diameter of 1,684 mm and mounted on a Sandvik/Tamrock EJC-210 Load-haul-dump (LHD) truck. Even under the severe wear and cut conditions (200 mm long and 50 mm deep), the tire was still safe for use due to the thick sidewall. Mounting a tire with such large and stiff beads onto a single piece wheel is impossible without damaging the tire or the rim. Thus, a single piece design is not feasible for OTR wheels. Instead, a multi-piece wheel design is conventionally employed for use with OTR tires. The rationale for use of thick and stiff tire beads can be illustrated in Figure 1.5.

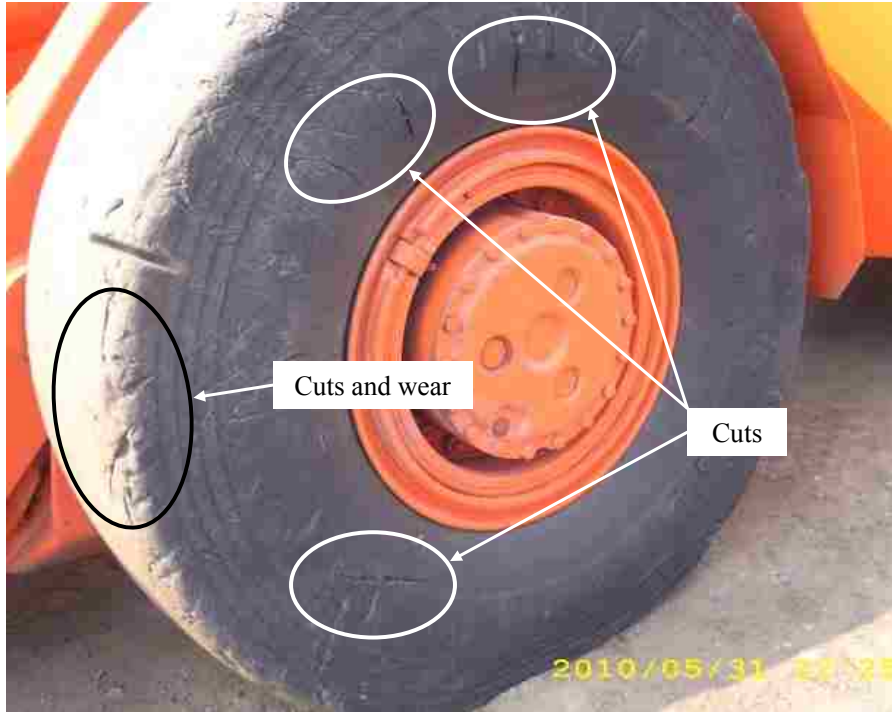


Figure 1.4 Severe cuts and wear on an OTR tire.

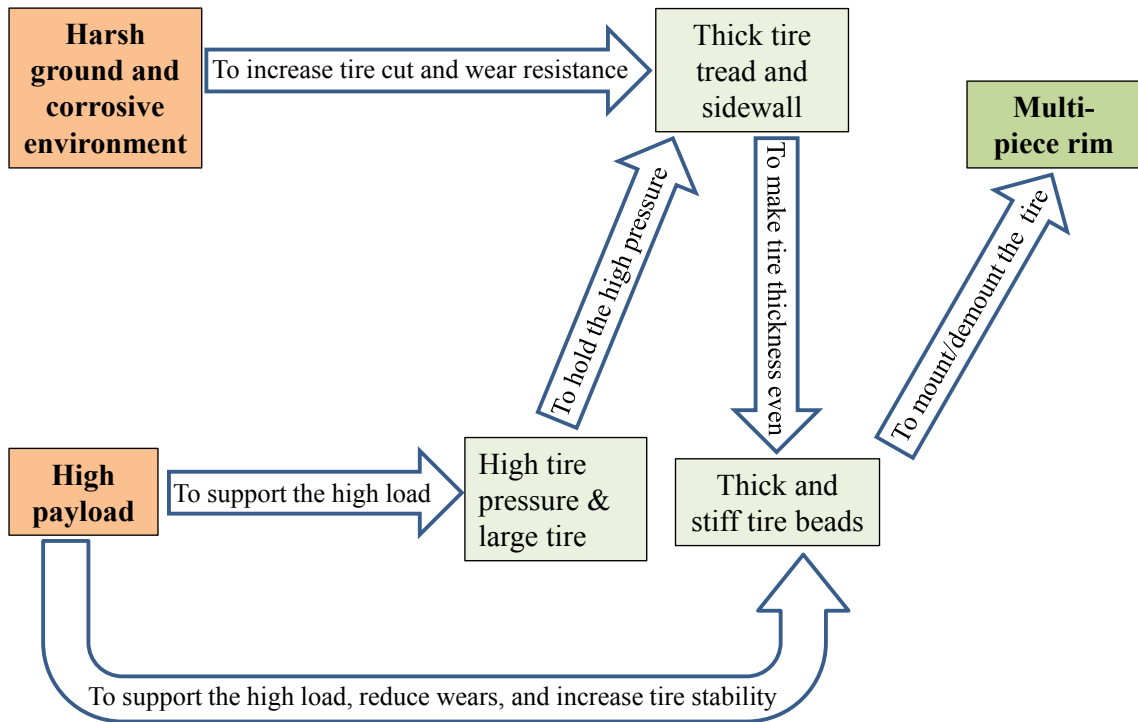


Figure 1.5 Schematic view of the rationale for use of multi-piece wheel for OTR vehicles.



## 1.5. Procedures and Regulations on Handling Multi-piece Wheel/Tire Assemblies

OTR tires are inflated with very high tire pressure in order to support large payloads. Thus tires contain a large amount of highly-compressed gas. A 0.50 m-diameter tire inflated to 690 kPa (100 psi) can contain up to approximately 180 kN (40,000 lbs) of explosive force [8]. If the energy of the gas is released suddenly under an uncontrolled manner, due to tire or wheel failures, the flying objects from the wheel and blast air can injure or kill persons within the vicinity of the projectiles as illustrated in Figure 1.6.

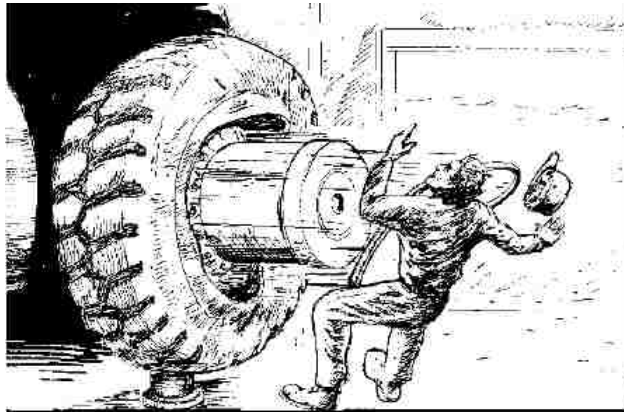


Figure 1.6 Multi-piece wheel failures kill people [9].

Due to the potential dangers working with multi-piece wheels, government regulations and safety operation procedures have been laid out through many countries and companies. The most relevant and important regulations are from the Department of Labor of the United States of America [9], which are listed below:

- Only trained personnel are allowed to service multi-piece wheels, using the correct tools and following specific procedures.
- Always remove the valve core and exhaust all air from a single tire and from both tires of a dual assembly prior to demounting a tire.
- Stay out of the trajectory paths of the wheel components (Figure 1.7) and use a safety cage (Figure 1.8) or other restraining device when inflate a tire. Use an air hose that has an in-line air gauge and sufficient hose length between the clip-on chuck and the in-line gauge.
- Never re-inflate a tire of multi-piece wheel when the pressure is below 80% of recommended pressure while the wheel is on the vehicle. Demount the tire and

disassemble the wheel assembly, repair any damage and reinstall the assembly prior to inflation.

- Enforce scheduled preventive inspection and maintenance. Multi-piece wheels are consumable items and are not maintenance-free.

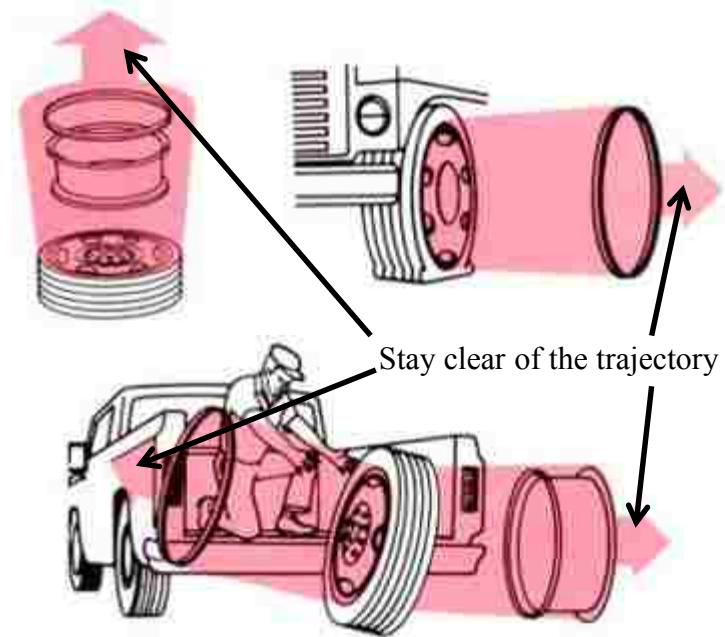


Figure 1.7 Trajectory of multi-piece rim parts in different scenarios [10].



Figure 1.8 Wheel and tire in a safety cage during tire inflation [11].



## 1.6. Motivation for Multi-piece Wheel Research

The majority of OTR wheels are made of multiple piece wheels. This design has great potential for wheel failure under very high tire pressure (275.8 kPa to 1034.2 kPa or 40 psi to 150 psi) due to corrosion, wear, metal fatigue, impact damage, over inflation, under inflation, and incorrect assembly. The multi-piece wheel design has not significantly improved for 30 to 40 years. With improved workplace safety conditions and personnel training, the incidents associated with multi-piece wheel failures have been reduced significantly in recent years. Yet the multi-piece wheel-related incidents still occur worldwide regularly and continue to claim human lives.

In Ontario, the failure of a multi-piece wheel assembly resulted in one fatality and one serious injury during vehicle maintenance at Detour Lake mine in 2000 [12]. In the same year, another mechanical failure of a multi-piece wheel assembly resulted in one fatality and one serious injury at Musselwhite mine (Ontario), during scheduled maintenance of a 30 ton underground haulage truck [13]. The inquest into the death of Mr. J. Burns [13] at Musselwhite mine in 2000 made a number of recommendations, two of which were associated with multi-piece wheels listed as following:

- (i) The Ministry of Labour and all industries using multi-piece wheel assemblies should require further research to be conducted by engineers to construct a tire cage or a holding device to contain these large multi-split wheels and tires during inflation.
- (ii) The Ministry of Labour and all industries using multi-piece wheel assemblies should require further research to be conducted by engineers to manufacture a better quality, (eg. thicker and stronger) safer wheel for heavy equipment.

Item (i) has already been considered by the mining industry and a safety procedure to inflate multi-piece wheel/tire assemblies in a cage or container has been developed. To the best of the author's knowledge, based upon documentation available in the open literature, the only research which has attempted to consider item ii) was conducted by Vijayan et al. [6, 14]. In their research, the finite element (FE) method was used to create the model of a three-piece wheel and the FE model was validated through static load testing. To assess the fatigue lives of the wheel components, the Society of Automotive Engineers' standard SAE J1992 testing protocol [15] was simulated, in which a rotary load was applied to the wheel axle. The stresses from the FE simulation results were used to assess the fatigue lives of wheel components and an infinite fatigue life was estimated.

However, literature and documented incident reports indicate that multi-piece wheels have limited fatigue lives. In the research conducted by Vijayan et al. [6,14], geometry degradation due to wear and impact damage and material degradation due to corrosive environmental conditions were not considered, which led to the conclusion of infinite fatigue life prediction. Another limitation in [6] and [14] was the exclusion of OTR tires in the structural analysis. All these factors affect the accuracy of the analysis results.

Supported by Workplace Safety and Insurance Board (WSIB) of Ontario, further research was conducted by the University of Windsor research team, led by Dr. Altenhof, to consider the aforementioned factors affecting fatigue life of multi-piece wheels. In this research, innovative designs were also proposed to make multi-piece wheels safer.

## Chapter 2. Literature Review

The literature review introduces topics relevant to this study. Section 2.1 introduces some general concepts of multi-piece wheels and OTR tires. Fatality reports associated with multi-piece wheel failures and analysis of multi-piece wheel failure mechanisms are included in section 2.2. Fatigue life analysis theory is discussed in section 2.3. On-the-road wheel testing standards are dealt with in section 2.4. Finally, relevant works on FE-based fatigue analysis are summarized in section 2.5.

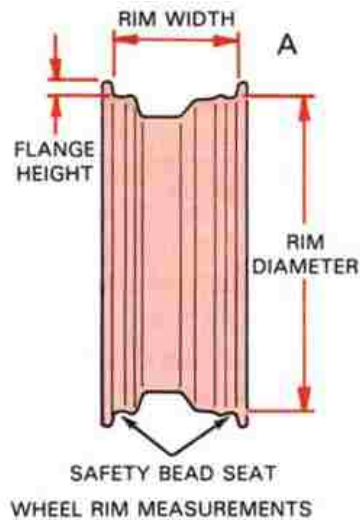
### 2.1. Multi-piece Wheels and OTR Tires

Wheels are always assembled together with tires in order to perform required functions. In order to understand wheel failure mechanisms, it is necessary and helpful to understand different multi-piece wheel structures, basic OTR tire structures and materials, and how a wheel and tire work together. For comparison, on the road single piece wheel structure and tire are briefly introduced first.

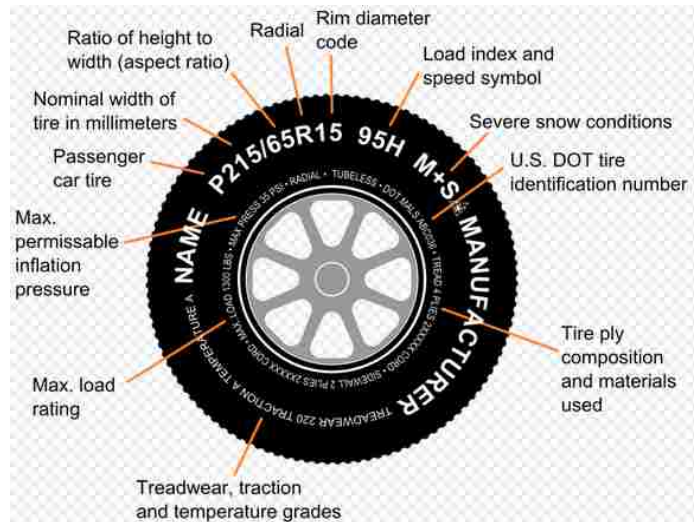
#### 2.1.1. On-the-road Single-piece Wheel and Tire Codes

Figure 2.1 (a) [16] is the side view of a typical single piece wheel with annotations to indicate the wheel width, wheel diameter, and flange height. At the outer edge is the flange, which holds the tire bead in place and acts as a good attaching point for wheel weights. Inside that area is the tire bead area, a flat portion on which the tire's inner bead rests. The wheel size is usually expressed by Diameter – Width/Flange Height (unit: inch). For example, a wheel sized 15-8/1.0 means the wheel's diameter is 15 inches (381 mm), having a width of 8 inches (203.2 mm), and a flange height of 1.0 inch (25.0 mm).

The codes and their meanings are clearly illustrated for a typical on-the-road passenger vehicle tire in Figure 2.1 (b) [17], in which tire size is expressed as P215/65R15 (wheel diameter is 15 inches (38 mm)). Almost all on-the-road tires are fabricated using radial structure and the rationale for this will be detailed in section 2.1.3.1. Wheels and tires must be appropriately assembled in terms of size and weight-carrying capabilities in order to function properly.



(a)



(b)

Figure 2.1 The side view of a single piece rim (a) [16] and tire codes for on-the-road tire (b) [17].

## 2.1.2. Multi-piece Wheel Structures

### 2.1.2.1. Names and Size Specifications of Multi-piece Wheel Components

Figure 2.2 and 2.3 illustrate the names and specifications of three-piece wheel components and five-piece wheel components by cross section views [18]. For multi-piece wheels, the sizes are expressed in the same way as one-piece wheel: Diameter – Width/Flange Height (unit: inch). Figure 2.4 illustrates the names of the components of a five-piece wheel in a three-dimensional view [18].

A multi-piece wheel is usually the assembly of a rim base, flanges, a lock ring, and a bead seat (BS) band. A rim base is the part of the rim on which flanges, BS band, and lock ring are supported. The rim base may consist of a number of separate components, which are welded together, e.g. back section, center section, and gutter section (the front section of rim base, where lock ring is seated on). The flanges help hold the tire on the rim. The knurling on the rim base at the bead seat areas helps prevent circumferential relative slippage between the tire and the rim base or the BS band. It is usually used in heavy duty, five-piece wheels. The BS band is used to create a seal to contain internal pressure. The outboard driver key is used to prevent relative rotation between the rim base and the BS band. The gutter region refers to the front section of rim base, where the lock ring groove is located.

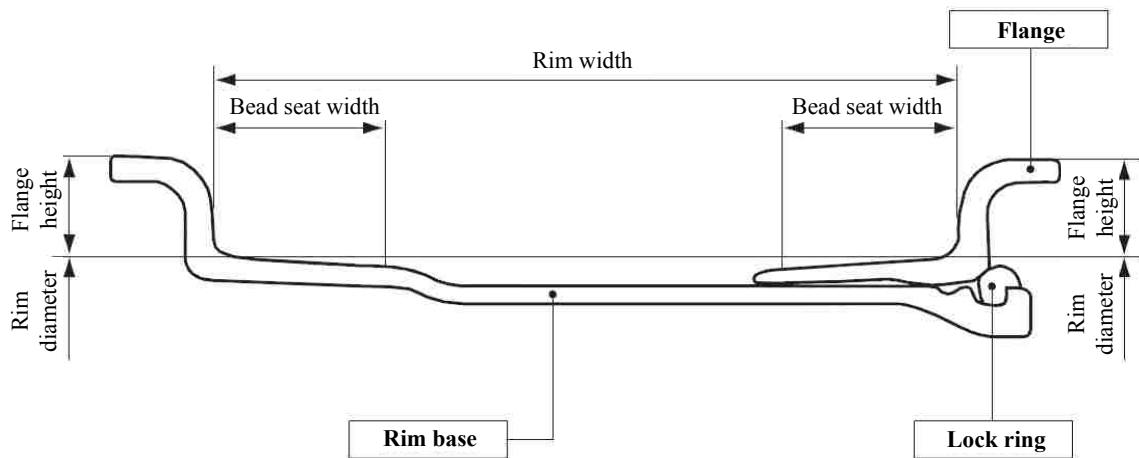


Figure 2.2 Names and specifications of three-piece wheel components [18].

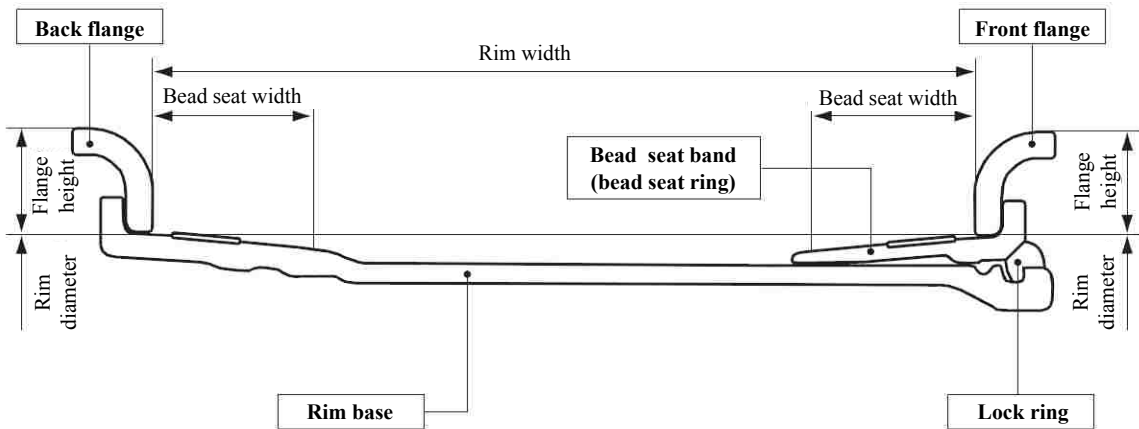


Figure 2.3 Names and specifications of five-piece wheel components [18].

A fixed back flange is used and the bead seat (BS) band and the front flange are combined to one entity for three-piece wheel. Due to wear between the flange and the tire and between the flange and the rim base or the BS band, flanges are consumable items. Five-piece wheels are more convenient for tire replacement since it is easy to break the connection between tire and wheel when dismantling the tire from the wheel, especially for heavy duty underground mining vehicles. Since flanges are consumable items, a loose flange (separate from the wheel) is more economical and convenient for wheel maintenance (repairing and change). For a three-piece wheel, when the back flange (one body with the rim base) is worn out, the worn flange has to be cut out and a new one will be welded to the rim base, which increases maintenance procedures and introduces unsafe factors, such as defective welding and excessive heat in the welding process. For normal usage, the flange will be replaced in approximately 8 to 12 months. During accidents and abusive conditions, flanges will be replaced in a shorter period. Usually

five-piece wheels are used on heavy-duty vehicles since severe wear on the flanges require more frequent flange replacement.

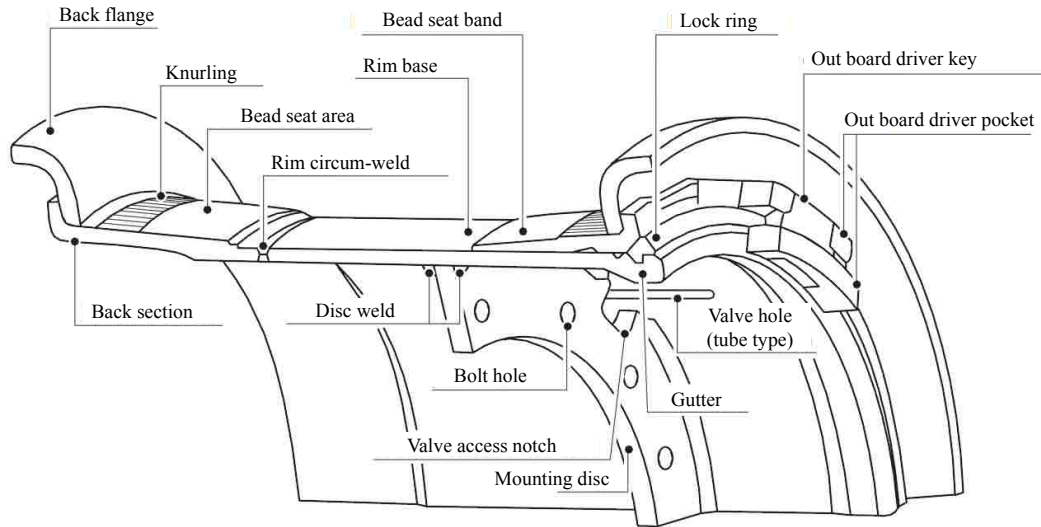


Figure 2.4 Names of the components of a five-piece wheel involving an out board driver [18].

### 2.1.2.2. Other Multi-piece Wheel Structures

Except the three-piece and five-piece wheels shown above, there are other different structures of multi-piece wheels according to the number of pieces composed of the wheel, such as two-piece wheels, four-piece wheels, and seven-piece wheels.

There are two different kinds of two-piece wheels. Figure 2.5 (a) [19, 20] illustrates the two-piece wheel with a split lock ring (side flange) and Figure 2.5 (b) illustrates the two-piece wheel with bolts connecting the separate pieces together.

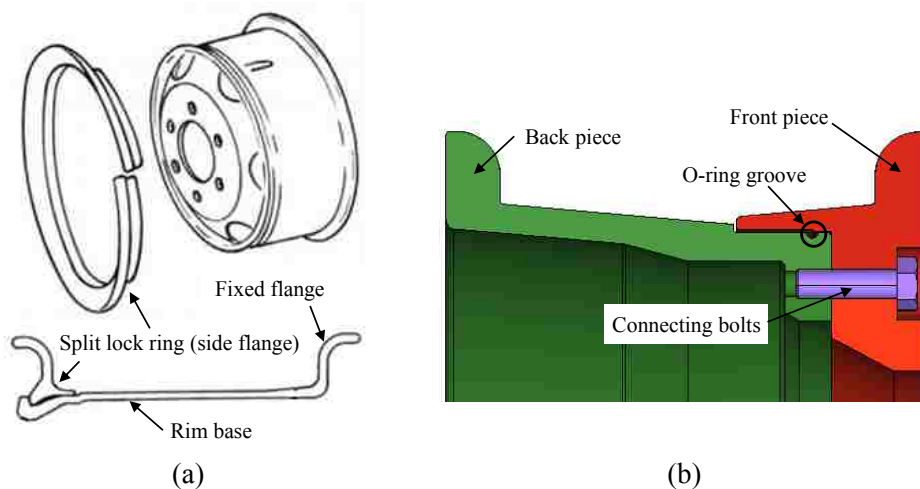


Figure 2.5 A two-piece wheel with a split lock ring (a) [19, 20] and a two-piece wheel with connecting bolts.

Figure 2.6 illustrates the structures of two different four-piece wheels [21]. Figure 2.6 (a) shows a four-piece wheel without a BS band and Figure 2.6 (b) with a fixed flange and a BS band. Figure 2.7 shows the structure of a seven-piece wheel [22]. The seven-piece wheel is designed for use on the outside rear wheel position for a dual wheel assembly. Once installed, there is no need to remove nuts or clamps to rotate tires off and on. The two lock rings make tire assembly and disassembly easier, increasing tire change efficiency. As the outer dual wheel is not removed from the truck when the inner tire needs to be removed, the seven-piece wheel keeps the vehicle in operation longer, and no torqueing and re-torqueing of bolting nuts during tire change or rotation will reduce the risk of the wheel running loose.

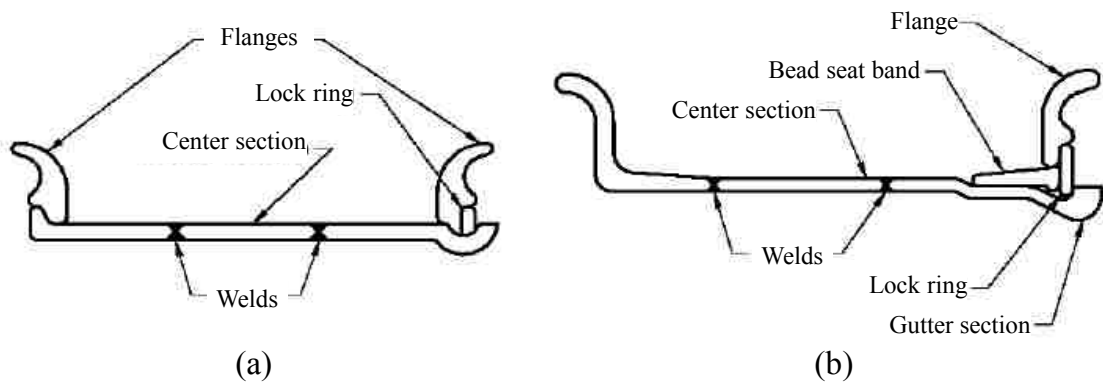


Figure 2.6 Two different structures of four-piece wheels [21].



Figure 2.7 The structure of a seven-piece wheel [22].

Except for two-piece bolted wheels, all multi-piece wheels have a split lock ring. For bolted two-piece wheels, strong bolt connections and preventions to wrongly remove the connecting bolts are important aspects to ensure safety.

Multi-part wheels are made in many different styles, sizes, and configurations. Parts are marked with identifying numbers which must be matched according to the manufacturer's directions. These parts are not interchangeable. A wheel assembled from unmatched components is lethally dangerous [23].

### 2.1.3. Off-the-road (OTR) Tires

#### 2.1.3.1. OTR Tires Structures and Materials

For multi-piece wheels, two kinds of tires are widely used: radial construction tire and bias construction tire. Both share a common nomenclature [24]. Figure 2.8 [25] illustrates the construction features of a radial tire and a bias tire. The majority of on-the-road tires are radial ply construction and their structure and material are similar to OTR radial tires.

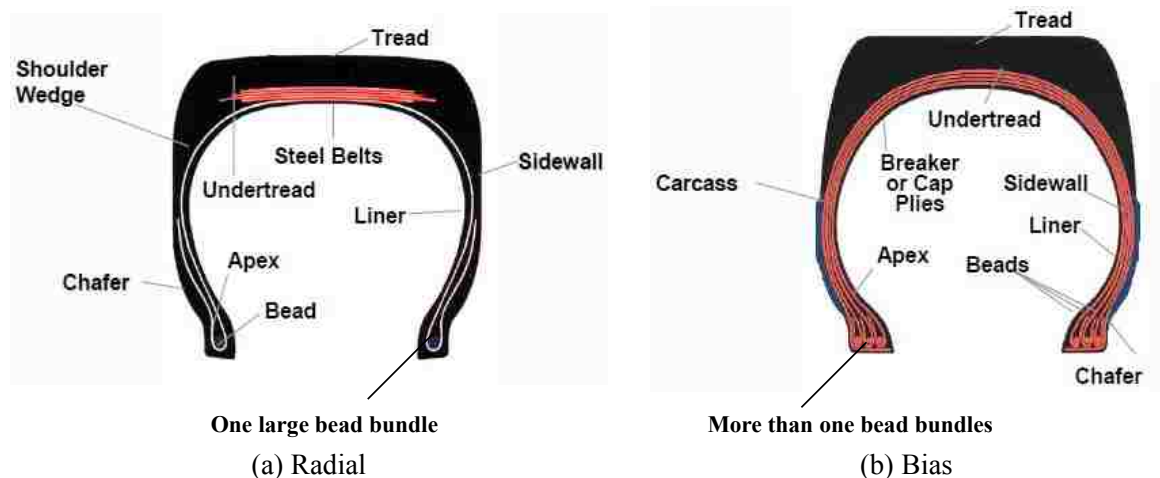


Figure 2.8 Tire construction features of a radial tire (a) and a bias tire (b) [25].

**The tread** is the part of the tire in contact with the ground. It must provide traction, durable wear and cut resistance. The tread is a thick rubber, or rubber/composite compound formulated to provide an appropriate level of traction that does not wear too quickly. The tread depth and design vary based on site and application. Various tread patterns are designed to meet different applications. Some specialized tires do not have any tread pattern and they are termed as “smooth tread” design to provide the maximum rock type damage resistance, which are widely used in heavy duty vehicles in rough environments, such as underground mines.

**The carcass** is made of plies and contains the inflation medium. A series of plies of cord reinforces a tire. Without this, a tire would be flexible and weak. The network of cords that gives the tire strength and shape is called the carcass. The greater its strength, the greater the pressure it can hold. The plies are layers of inextensible fabric cord extending from bead to bead to reinforce the tire. Plies are embedded in the rubber to hold its shape by preventing the rubber from stretching in response to the internal pressure. The plies must transmit all loads, associated with driving, braking, and steering forces between the wheel and the tire tread. The orientation of the plies plays a large role in the performance of the tire and is one of the main ways that tires are



categorized. Bias tire carcasses use many angled plies of fabric to achieve strength. Radial tires have one ply of steel wire or multiple body plies of other materials running directly from bead to bead.

**Belts** are placed between the tread and carcass. They help to join these parts and distribute road shock to protect the carcass. They control the diameter of the tire and impart superior tread impact and penetration resistance.

**The bead** is that part of the tire that contacts the rim. Beads anchor the tire to the rim. The beads seat tightly against the rim on the wheel to ensure that a tubeless tire holds the inflation medium without leakage and to ensure the tire does not shift circumferentially as the wheel rotates. The bead is typically reinforced with high tensile-strength steel wire and compounded of high strength, low flexibility rubber. Bias tires may have several bundles of steel wires. Radial tires have one large bundle of wires. This indicates that the bias tires usually have thicker beads, compared to radial tires.

**The sidewall** is that part of the tire that bridges between the tread and bead. Sidewalls are the protective rubber covered on the side of a tire and are reinforced with fabric or steel cords that provide for tensile strength and flexibility. The rubber is compounded to flex without cracking. It also resists cuts and forms a barrier to protect the carcass from the weather.

**The Inner Liner** is a specially formulated rubber compound inside the tire that minimizes permeation. It works with the rim, beads, and O-ring to contain the inflation medium in tubeless tire designs.

**The apex** is a triangular extruded profile that mates against the bead. The apex provides a cushion between the rigid bead and the flexible inner liner and body ply assembly.

**The chafer** is a layer of hard rubber that resists rim chafing. It consists of narrow strips of material around the outside of the bead that protect the cord against wear and cutting by the rim, distributes flex above the rim, and prevents dirt and moisture from getting into the tire.

**The shoulder** is that part of the tire at the edge of the tread as it makes transition to the sidewall. **The undertread** is high adhesive compound forming a full-width base for the tread. It improves a tire's capability and guards against bruise break.

### **2.1.3.2. Radial Tires and Bias Tires**

Prior to the 1970's, most tires (on-the-road and off-the-road) were designed and manufactured using bias ply structure. Radial ply tire construction is a relative new technology

and it has now become the standard design for essentially all automotive tires due to its advantages. Figure 2.8 and 2.9 illustrate the structures of these two different tires.

Radial ply tires are made with the cord material running in a radial or direct line from bead (at 90 degrees to the centerline of the tire), and are typically made with one steel body ply or multiple body plies of other materials [26]. Under the tread area, the radial tire usually has three or four crossed plies or belts made of steel cord to stabilize the crown area and offer better puncture resistance. A radial tire allows the sidewall and the tread to function as two independent features of the tire. Because of the construction of a radial tire, the tire has more flex and will allow for more ground contact. That will improve traction and better tread wear. It also gives the radial tire better stability and accounts for the slightly “low on air” (bulging) look that radial tire sidewalls have, especially when compared to bias tires.

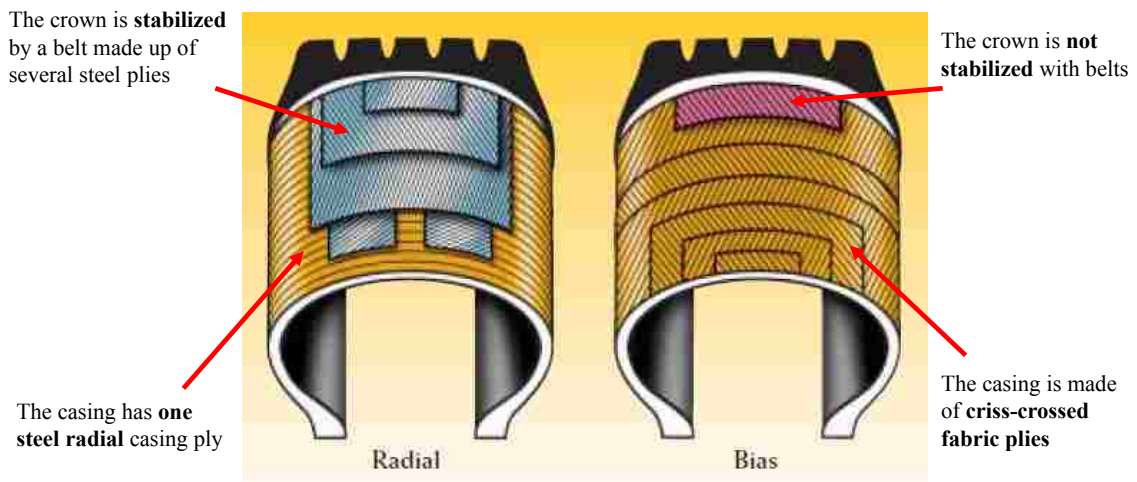


Figure 2.9 Radial structure tire and bias structure tire [26].

Bias ply tires are constructed of overlapping crossed layers of cord material and are typically made with nylon, polyester, or other materials. The crossed plies run on a diagonal from tire bead to tire bead and comprise a generally stiff sidewall area. Sometimes extra crossed plies or breakers are used under the tread area to further stiffen the crown area and provide better wear resistance or other performance parameters (such as puncture resistance, etc.) to withstand severe service conditions and high loads. The overlapping structure of the plies result in the plies rubbing against each other as the tire flexes, reducing tire rolling efficiency. It also increases the wear of plies and heat can easily build up in the tire.

Radial tires have the following advantages [27]: long tire life, exceptional traction on all types of surfaces, low fuel consumption due to lower rolling resistance, improved comfort, increased resistance to punctures and flats. Bias tires have the following advantages: stiffer

sidewalls give better driver handling/feel; lower susceptibility to sidewall snags/rusting; and lower initial tire purchase price. With the advent of the radial tire and some of its inherent advantages, the bias tire is now used much less frequently in long haul on-the-road application.

In the OTR applications, bias tires are still widely used mainly due to the following two extra advantages, especially in underground mines with heavy duty vehicles. Firstly, due to the thick beads of the bias tires, less wear and stress will be generated on wheel components and tire beads and a more stable tire response is observed. Secondly, due to the specialized nature of OTR vehicle usage, loads in excess of those specified in the appropriate load tables in the TRA year book [27] are often encountered. These excessive loads result from items such as actual vehicle weight exceeding the design weight, varying density of materials, field modifications to the equipment, load transfer, and overloading for productivity, to name a few. Under these conditions, the actual tire load in service may exceed the TRA load ratings for the tire [28]. When excessive loads are encountered, cold inflation pressures must be increased to compensate for higher loads. For each 1% increase in load, the inflation pressure must be increased by 2% [28]. The bias structure tires can withstand load increase by 15% for daily average overload, whereas the radial tire can withstand only 7%. The bias tire can withstand tire pressure increase by 30% and the radial tire can withstand tire pressure increase by 14%, compared to the TRA recommended tire pressures.

### **2.1.3.3. The OTR Tire Deflections and Dimensions**

The tire deflects under inner pressure and external loads. The bulge of the tire at the bottom occurs as a result of tire deflection under external load. Figure 2.10 shows the tire dimensions under unloaded and loaded conditions with the recommended tire pressure [28]. The tire dimensions are defined as follows:

**Overall Diameter (OD)** is the diameter of the new tire when mounted on the recommended wheel and inflated to the suitable reference tire pressure. The tire is supported so the tread touches the ground. However, no load is applied, not even the weight of the tire and wheel. The **Free Radius (FR)** is the half of the Overall Diameter.

**Overall Width (OW)** is the inflated width of a new tire under reference tire pressure – including elevations due to lettering, decorations, and protective ribs. **Section Width (SW)** is the inflated width of the tire under reference tire pressure – excluding elevations due to lettering, decorations and protective ribs. **Tread Width (TW)** is the distance between the extreme edges of the tread, as measured at the surface of the tread. **Section Height (SH)** is the distance from the

bead seat to the outer tread contour of the inflated tire at its central line. **SH** is half of the difference between the tire overall diameter and rim diameter.

**Static Loaded Radius (SLR)** is the distance from centre of wheel to the ground on a vehicle under reference load and pressure at static loading condition. **Vertical Deflection (VD)** is the difference between the Free Radius and Static Loaded Radius. **Static Loaded Width (LSW)** is the maximum width of the tire under reference load and pressure at static condition. The difference between Static Loaded Width and Overall Width is the **Loaded Section Growth (LSG)**. In this research, Loaded Section Growth is also referred as tire **Lateral Deflection (LD)**. Another important tire size parameter is **Aspect Ratio (AR)**, which is defined as the ratio of the tire Section Height (SH) to its Section Width (SW) expressed as a percentage.

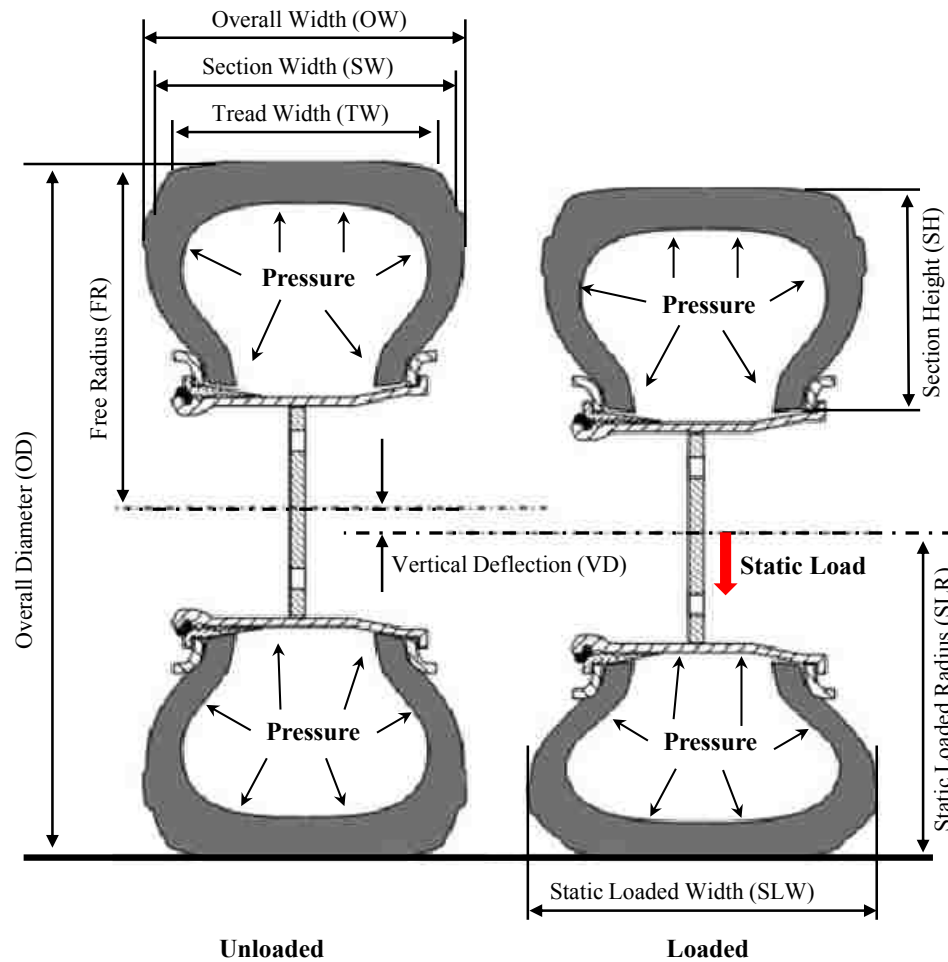


Figure 2.10 Tire deflections and tire dimensions under static load [28].

#### **2.1.3.4. Tire Load and Pressure Relationship**

Each tire is designed to carry a specific load at a specific inflation pressure. In tire manufacturers' engineering data books, load/inflation tables are listed [28] for each tire. When the tire is inflated to the correct pressure for the load, deflection will be within design limits. Loading a tire above the specified limit will result in over-deflection. Inflating a tire above the specified limit will result in over-inflation. Over-inflation and/or over-loading can reduce tire performance and reduce tire life, which leads directly to a higher cost per ton mile (or kilometer).

Overloading may lead to premature tire failure. If the inflation pressure is not adjusted for heavier loads, tires will become unserviceable due to tread and ply separation, disintegration of the carcass and inner liner, radial sidewall cracking, and excessive bead chafing. Overloads with the inflation adjusted accordingly may exceed the carcass strength, which will result in impact breaks and cuts, rapid wear, and fabric fatigue. Under extreme conditions, this can lead to a tire rupture, which can cause property damage, serious injury, or even death.

For a given tire size, inflation pressure determines how much load can be carried (the inflation medium can be air or nitrogen). There are factors other than inflation pressure which affect tire load capacity [24]. Larger tires (with larger internal air volumes) can carry higher loads at the same pressure. Load capacity also varies with speed. The Tire Standards Associations (TSA) and tire manufacturers publish tables of maximum loads at specified speeds in order to reduce heat buildup inside the tires.

The tire's pressure capacity is determined by its carcass strength. Carcass strength is indicated by a ply rating (PR) for bias tires. Symbols or star ratings are used to indicate radial tire strength. Some OTR tires are marked with Load Indexes and Speed Symbols.

#### **2.1.3.5. OTR Tire Size and Code Designations**

##### **2.1.3.5.1. Tire Size Designations**

Categorized by the aspect ratio, there are three different kinds of tires: conventional (narrow base), wide base, and "65 series" tires. The tire size designations have minor differences between different tire manufacturers. Figure 2.11 illustrates the tire size designations for the three different kinds of tires. Based on the Goodyear OTR Engineering Data Book [28], the definitions of the three different tires are as follows:

**Conventional (narrow base tire):** the aspect ratio is approximately 95. In the tire size marking, the section width, given in inches, is a whole number, followed by “.00”, which means the aspect ratio is in the range of 95.

**Wide base:** the aspect ratio is approximately 83. The section width, given in inch, is a whole number followed by a fraction.

**65 series:** The section width is given in inches or in millimeters followed by the number 65.

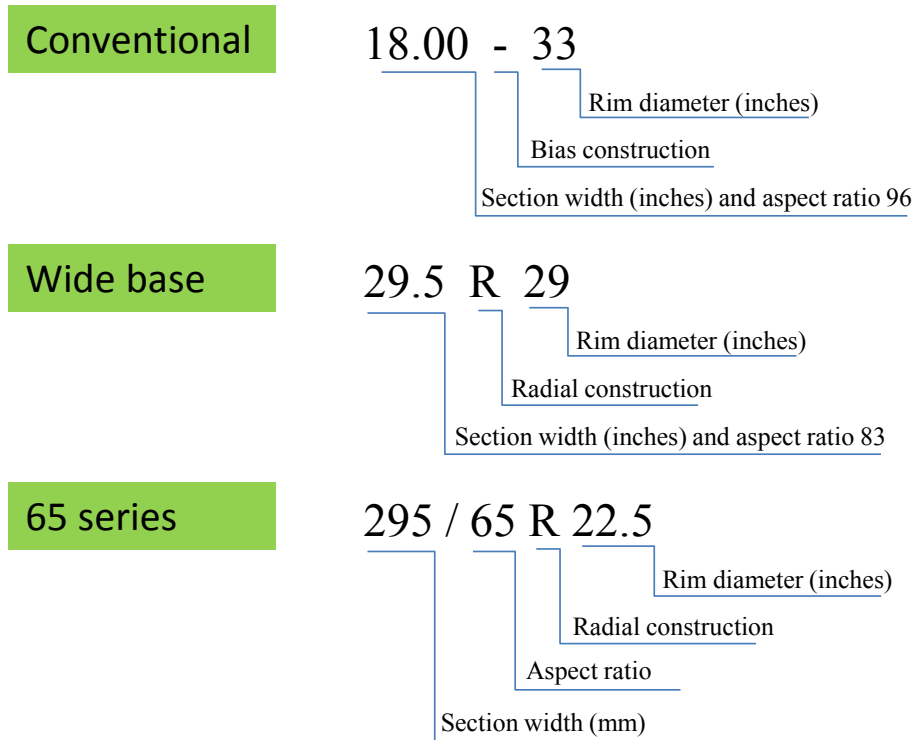


Figure 2.11 Tire size designations.

### 2.1.3.5.2. Tire Industry Codes

According to service applications, there are standard TRA industry codes for different tires [27]. Table 2.1 illustrates the code corresponding to the service condition. The standard tread depth codes are illustrated in Table 2.2.

Table 2.1 Standard tire industry code.

Code	C	E	G	L
Service condition	Compactor	Earthmover	Grader	Loader & Dozer

Table 2.2 Standard tread code, depth, and type.




Tread depth illustration			
Tread depth	Standard tread depth	Extra tread depth	Super extra tread depth
Code	C-1/C-2, E-1/E-2/E-3, G-1/G-2/G-3, L-2/L-3/L-3S	E-4, G-4, L-4, L-4S	L-5, L-5S
Tread type	Rib, Rock, Traction, Smooth	Rock deep tread, smooth deep tread	Rock extra deep tread, Smooth extra deep tread

Figure 2.12 illustrates the meanings of the sidewall markings of a tire installed on a five-piece wheel of Sandvik/Tamrock EJC-210 Load-haul-dump (LHD) truck.

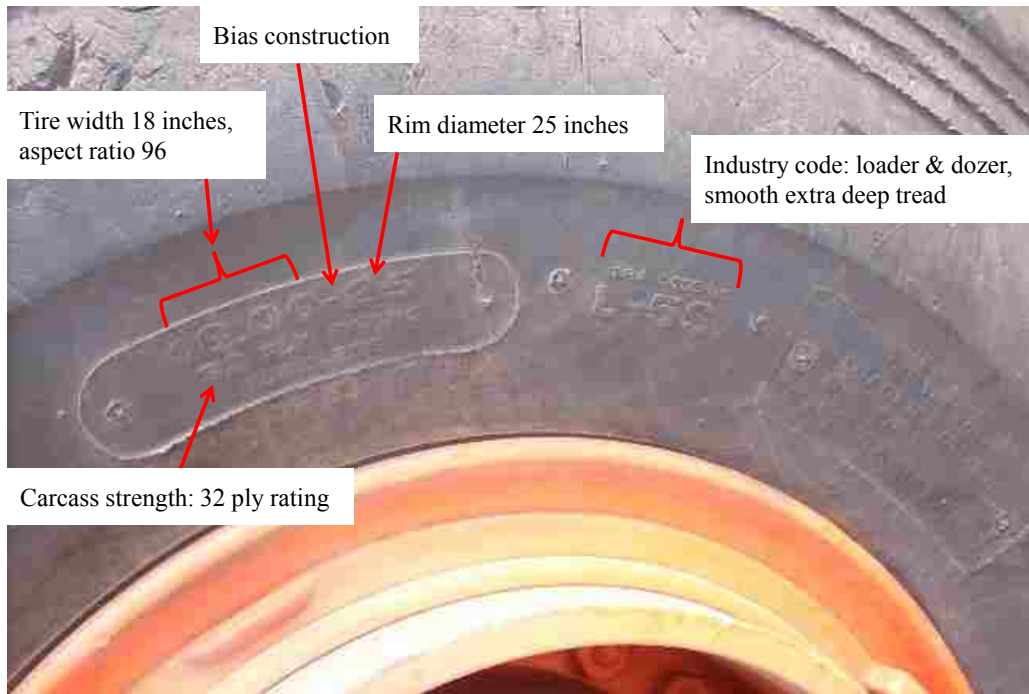


Figure 2.12 Illustrations of sidewall markings of a Goodyear tire.

## 2.2. Fatalities Caused by Multi-piece Wheel/Tire Failures

The purpose of a search for incidents are two folds, namely, (1) to demonstrate the motivation to this research through fatalities relevant to multi-piece wheel failures, (2) to determine the mechanisms of multi-piece wheel failures by analyses of incidents to reveal potential design aspects to improve the safety of multi-piece wheels.

Incidents reports related to multi-piece wheel failures were searched mainly through government organizations' (such as Workplace Safety North of Ontario, Occupational Safety & Health Administration of U.S. Department of Labor, etc.) websites. The following incident reports are mainly focused on the publicly available fatality reports since 1998 in Canada, The United States, and Australia. It is believed that fatalities associated with multi-piece wheels occurred more frequently before 1998 as after this year stringent safety procedures were implemented in the aforementioned three regions. It is also believed that a great number of incidents must have taken place in developing countries with prevalent mining industries, given their lack of safety standards, official governing safety bodies and organizations, and under-developed reporting systems. All the incident reports compiled here are associated with fatalities and multi-piece wheels. It is important to note that 20% of all tire or wheel accidents are fatal [23].

### **2.2.1. Fatalities in Canada since 1998**

In Edmonton, Alberta, (February 26, 2012) [29], two workers were welding a wheel to repair a flat tire of a dump truck, and the tire exploded, fatally injured one worker and seriously injured the other one at a repair shop. In Fort McMurray, Alberta (August 28, 2009) [30], a worker was fatally injured when he was inflating the tire of a five-piece wheel. He was having difficulty to get the lock ring in place before the air could be filled. In British Columbia (March 2006) [31], when a worker was removing the connecting bolts to uninstall a two-piece bolted wheel with inflated tire on it, the outer rim and tire were blown off the hub and struck the worker lethally. On Vancouver Island, British Columbia (March 2005) [32], a leaking tire was deflated and then the multi-piece wheel was welded to stop the leak. Approximately 50 minutes later, while the tire was inflating, the tire exploded at the top, inflicting a fatal injury. In Saskatchewan (2004) [33], when an inflated three-piece wheel/tire assembly was being installed onto the truck axle, the tire blew out, killing the worker. An investigation found that the flange had been distorted, not allowing itself and the lock ring to engage properly in the gutter region. At Placer Dome (CLA) Ltd.'s Detour Lake Mine, Timmins (July 24, 2000) [12], one worker was fatally injured and another worker was critically injured when the tire blew out during inflation. The wheel was a three-piece type with a lock ring. At Musselwhite Mine, Timmins (November 22, 2000) [13], two mechanics were working to remove an inflated wheel assembly from a 30D Tamrock underground haulage truck. As a result of the failure of the multi-piece wheel components, the tire was propelled off the axle and struck the two workers. One employee was fatally injured and the second was seriously injured. At Fairview, Albert (September 15,



2000) [34], two tire service technicians were mounting a 60-centimetre-wheel tire onto a grader. When they started to inflate the tire, the tire blew out and struck both workers. One worker received minor injuries, and the other 23-year-old worker received head injuries and died the next day. In Saskatchewan (February 14, 1998) [35], a mechanic was killed while removing the left rear wheel from a Toro 35D underground haul truck. As the mechanic removed the last nut holding the wheel assembly onto the axle, the wheel failed and the out bolting flange was projected away by air pressure, which struck the mechanic in the chest.

### **2.2.2. Fatalities in the United States since 1998**

In Newport News, Virginia (January 17, 2011) [36], when a worker inflated a Modin Nylon Tube Type N500 tire on a 24-inch multi-piece wheel, the wheel failed and killed the worker. The tire/wheel assembly was mounted on a 1975 Chevrolet C60 Dump Truck. In Clyde, Ohio (October 14, 2010) [37], when a 58-year-old male contract auto detailer was cleaning the wheel assembly of a commercial truck in preparation for the vehicle's eventual sale, the assembly (known as a multi-piece wheel) exploded, sending sharp metal fragments and other material deep into the employee's forehead and left arm. The resulting injuries killed him. In Norco, California (January 18, 2010) [38], a worker was killed when he was inflating a split wheel tire of a Mitsubishi fork lift. In Hazard, Kentucky (January 23, 2009) [39], a worker was killed when he was inflating a three-piece wheel tire and the wheel explosively separated and struck him in the head. In Elk Grove Village, Illinois (August 28, 2009) [40], a truck tire technician was killed when he was installing a wheel with inflated tire. The wheel exploded and struck him in the head. In Woodruff, Wisconsin (December 9, 2008) [41], a mechanic was fatally struck when he was inflating a tire and the tire blew out.

In New York (December 2007) [42], a male equipment operator was fatally injured by a metal lock ring propelled from a three-piece wheel tire assembly he was inflating. The victim operated a front-end loader that was a 1985 model with tire size of 17.5-25. After the victim started his loader, he noticed that the left front tire on his loader was “soft” or under-inflated. When the worker was inflating the tire, the tire blew out and the lock ring was propelled out and struck his head and he was fatally injured. The investigation found that the possible reason for the incident was the dislodged lock ring. The investigation suggested that if the pressure in a multi-piece wheel tire is reduced to 80% of the recommended operating pressure, the tire assembly shall be completely deflated, removed from the vehicle, disassembled, inspected and reassembled prior to inflation. If a tire mounted on multi-piece wheel loses a significant amount of air, the wheel components that are secured in the rim base under the normal tire air pressure

may be offset or dislodged. When the flat tire is inflated, due to the rapid increase of the air pressure and volume, the dislodged wheel components can be propelled at great distances with great forces and can cause serious injury or death to anyone in the trajectory area.

In Massachusetts (December 31, 2007) [10], a 59-year-old male mechanic was fatally injured while changing a container handler's dual front inner tire that was mounted on a five-piece wheel. The investigation found there had been a crack in the lock ring groove and severe wear, rust, and pitting were found on the rim base. The tire should have been completely deflated prior to demounting and a routine inspection of wheel would have detected the crack. In Marietta, Georgia (April 19, 2007) [43], a mechanic at a lumber company was performing two tire changes on a forklift truck that incorporated two-piece wheel assemblies. The wheel blew apart under pressure and the top portion of the wheel was blown toward the mechanic, fatally striking him in the face. In Cullman, Alabama (December 13, 2007) [44], a worker was reinstalling a split wheel tire on a lowboy trailer. He initially placed the tire/wheel assembly onto the lowboy. As he took the tire/rim assembly off and laid it down, there was an explosion. The failed wheel fatally struck the worker.

The above mentioned ten fatality incidents occurred from 2007 to 2011. There are another twenty-eight fatality incidents that occurred from 1998 to 2006, in which one incident [19] occurred in Alaska in 2006 and the other twenty-seven [45-71] occurred in continental USA. Totally, there are 38 fatalities involved with multi-piece wheels in the United States during this period, based on available reports.

### **2.2.3. Fatalities in Australia since 1998**

In Queensland (2005) [72], while removing a tire and wheel assembly from a drive axle bogey of an off-highway coal transport prime mover, the operator suffered fatal injuries when the five-piece wheel failed and blew parts of the wheel assembly toward the worker. In Queensland (February 2004) [73], two workers were changing wheels on a 170-tonne truck when the split lock ring became dislodged and caused the tire to move uncontrollably, projecting the tire assembly about 15 meters away. It struck one person who sustained a broken jaw. The second person, who was pinned under the tire assembly, suffered fatal injuries. The other two incidents [74, 75] that occurred during this period did not cause death. An incident [74] occurred in 2002 due to tire zipper rupture and another incident [75] was caused by installing the lock ring backward.

#### **2.2.4. Analysis and Summary of the Fatality Incidents**

Totally there were forty-nine fatality incidents cited in the previous sections which occurred from 1998 to 2012; 9 in Canada, 38 in the USA, and 2 in Australia. The majority of the fatalities were caused by the failure to follow correct procedures of handling multi-piece wheel/tire assemblies. Multi-piece wheels are high-risk assemblies and need to be treated accordingly. Many serious and fatal accidents can be attributed to poor removal and fitting practices, inadequate inspection regimes, and a lack of training for personnel involved in tire and wheel maintenance tasks.

In 2006, Rasche et al. [76] compiled and analyzed 82 OTR wheel/tire assembly failure incident reports of earthmover vehicles which occurred in the United States, Canada, and Australia from 1987 to 2006. It was found that 33% of the cases resulted in the death of the tire serviceman or personnel involved in the work. A further 50% of all other incidents were classified as potential fatalities based on their similarity to other fatality cases. The actual and potential fatalities accounted for 83% of the cases. Using the Incident Cause Analysis Method (ICAM), the analyses show that the leading cause of the incidents is the LTA (less than adequate) material testing and fatigue NDT (non-destructive testing). Multi-piece wheels are consumable items and rigorous, systematic, and reliable wheel component testing and maintenance are required in order to ensure safe operation. The other main causes of failure include heating of wheel assembly, LTA matching of assembly components, LTA wheel integrity, and LTA deflation practice.

Analyses of the forty-nine fatality incidents referenced in the previous sections reveal the similar causes as Rasche et al. [76] did. Multi-piece wheel/tire assembly failures can be classified in three failure modes: tire explosion, tire rupture, and tire blow-out [77]. This classification is helpful to find the direct causes of the multi-piece wheel/tire assembly failures to provide directions for design improvement of multi-piece wheels.

##### **2.2.4.1. Tire Explosions**

Tire explosion is caused by the rapid buildup of tire pressure due to fire inside the tire. The heat and the flame of the fire weaken the tire's integrity, resulting in the tire bursting through the affected sidewall or tread area. Before the tire explodes, the internal pressure is much higher than the recommended working pressure. A tire explosion is a chemical reaction involving energy many orders of magnitude greater than that of a tire blow-out or zipper rupture. A shock wave will create pressures typically in excess of 6894.8 kPa (1,000 psi) during tire explosion [78].

Therefore tire explosion is more violent than other two tire failure modes. The explosion can propel the tire, the wheel components, and the axle components as far as 500 m (1500 feet) or more from the machine [78]. Both the force of the explosion and the flying objects can cause property damage, personal injury, or death. A tire explosion may occur when the truck is in motion or stationary [78]. In the 49 fatality incidents, two incidents [29, 32] were caused by tire explosion.

In some cases, the buildup of flammable gases results from pyrolysis, the decomposition of a chemical (the tire rubber) by extreme heat. Pyrolysis can occur if the vehicle's wheel/tire components have been heated. This can occur after the vehicle comes near or touches a high voltage power line [79], after a brake has been heated, after the wheel has been heated with a torch, after a stud has been cut off a wheel or by welding on the wheel [29, 32], and when the truck is struck by lightning [80]. Under-inflation (pressure is 20% lower than the recommended pressure) or overload can also cause pyrolysis since tire extreme deformation and wear between wheel components may cause heat buildup and accelerate the decomposing of the tire rubber under this condition.

#### **2.2.4.2. Tire Zipper Ruptures**

Another hazard is the failure of the tire sidewall, either because of weakening during service under fatigue loading and corrosive environments or from an overpressure [77]. This type of tire failure is called a "zipper rupture" in steel cord radial tires. The steel wires in the sidewall of a radial tire may be weakened by corrosion, under inflation, over inflation, overloading, an operational damage or a result of a manufacturing defect. The blast of air can cause direct injuries or blow pieces of the tire and wheel assembly towards the worker during inflation of the tire. A tire zipper rupture usually occurs when a truck is in motion.

In the 49 fatalities, two incidents [52, 53] were caused by tire zipper rupture due to over inflation by using a faulty pressure gauge or not using a pressure regulator. The tire rupture in incident [74] was caused by a previous tire tear.

#### **2.2.4.3. Tire Blow-outs**

When the tire is not strong enough to hold the high internal pressure, tire failure will occur in the mode of explosion or zipper rupture. When the metal multi-piece wheel is not strong enough to hold the internal pressure, or the wheel's integrity is weakened, the failure is referred to as tire blow-out. Incorrect assembly, metal fatigue, corrosion, wear, impact damage, over

inflation, and under inflation can result in separation of the engaged wheel components whilst the tire is being inflated, hit, transported, removed, replaced, or in service [77]. The sudden and violent release of high pressure can propel wheel components or parts of tire away at great speed. Any person in the trajectory path may be injured or killed. These issues can also result in violent bursting of tires from other types of multi-piece wheels not fitted with locking rings, such as two-piece bolted wheels. Blow-outs usually happen when tires have just been mounted on their wheels and are being inflated.

#### 2.2.4.3.1. Tire Blow-out Fatality Incident Analysis

In the above cited 49 fatalities, 4 incidents [39, 32, 52, and 53] were identified to be caused in the failure modes of tire explosion and tire zipper rupture. The other 45 fatalities are classified as failures in the mode of tire blow-out. The detailed causes for failure are illustrated by in Figure 2.13.

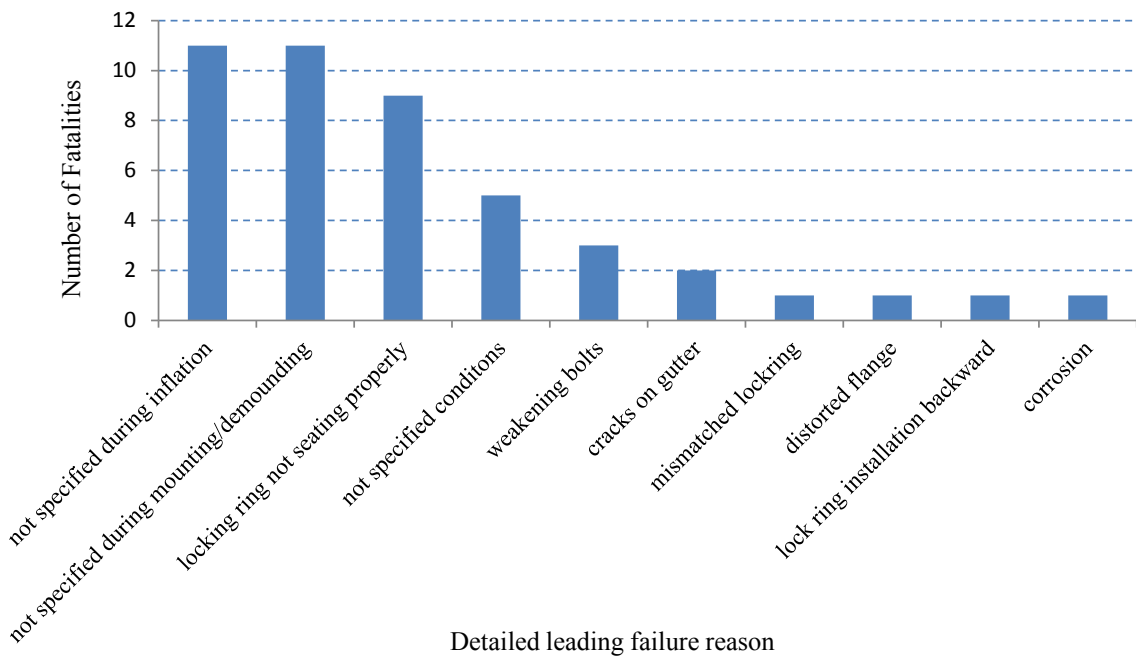


Figure 2.13 Detailed tire failure reasons specified in the incident reports in the failure mode of tire blow-out.

In the above graph, there are 11 incidents [12, 34, 36, 39, 41, 51, 54, 55, 60, 61, 64] that detailed reasons to cause the fatalities during tire inflation were not specified in the incident reports. In these reports, the tire pressures were not mentioned going beyond the recommended limit and the tires were not weakened, therefore failure modes of tire explosion and zipper rupture can be ruled out. Their failure modes can be referred to as tire blow-out. Another 11 incidents [13, 40, 43, 44, 47, 49, 56, 57, 58, 72, and 73] with unspecified reasons in the reports during

wheel mounting/dismounting process exhibited the failure mode of tire blow-out since the sources did not mention any heat factor or over inflation or weakened tires. Another 9 incidents [30, 42, 45, 50, 62, 66, 68, 69, and 71] were caused due to the lock ring not seating properly in the lock ring groove. The lock ring did not seat properly in incident [42] due to a sprung lock ring, which resulted in loss of the retracting force. The lock ring did not seat properly in incident [69] due to dirt within the lock ring groove. The incident reports did not provide clear conditions for the 5 incidents reported in [37, 38, 48, 63, and 70]. There are 3 incidents [31, 46, 59] involved two-piece bolted wheels due to weakened bolts. Two incidents were caused by cracks on the gutter region [10 and 35]. Mismatched lock ring [65], distorted flange [33], lock ring installed backward [67], and corroded lock ring [19] are further reasons for worker fatalities. In each accident the referenced issue was responsible for the life of one worker.

Multi-piece wheels without a split lock ring (mostly two pieces bolted together) usually fail due to fatigue, corrosion, weakened connecting bolts, and accidental removal of connecting bolts. For multi-piece wheels with a split lock ring, failures result mainly due to (1) improper seating of the lock ring and (2) wear, corrosion and fatigue cracks in the gutter region.

#### 2.2.4.3.2. Lock Ring Improper Seating

In the majority of tire blow-out incidents, lock ring disengagement is the result of incorrect seating of the lock ring. Damaged/corroded lock ring, sprung lock ring, using a mismatched lock ring with the rim base, unclean and un-lubricated lock ring or dirt inside lock ring groove, and backward installation of lock ring can all cause improper seating of the lock ring. Figure 2.14 [18] shows the difference between a good lock ring and a sprung lock ring. For a sprung lock ring, the open ends do not touch. A sprung lock ring has lost the needed retracting force and cannot seat properly within the lock ring groove. Figure 2.15 [18] illustrates a correctly installed lock ring and a lock ring installed backward. Correct installation of the lock ring can only be achieved if the markings on the locking ring can be seen before, during, and after installation [18]. If the locking ring is installed back to front it will not interface properly with the gutter band and there is a risk of the locking ring dislodging under pressure.



Figure 2.14 A sprung lock ring (left) and a good lock ring (right) [18].

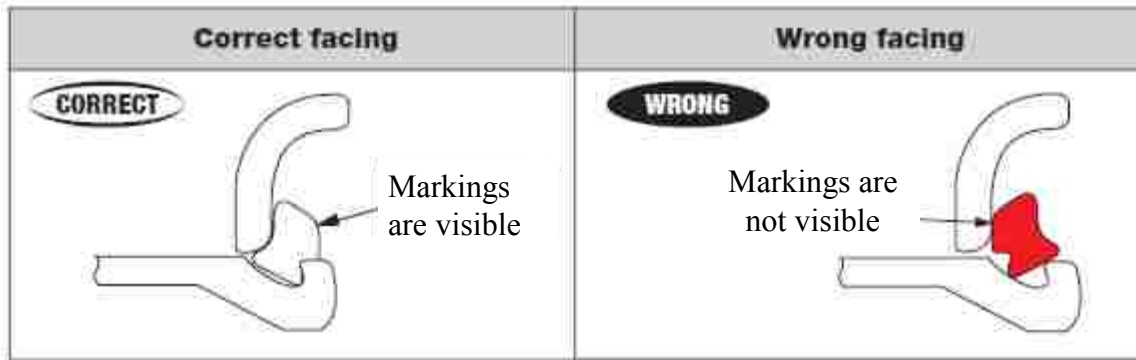


Figure 2.15 Correct installation (left) and lock ring installed backward (right) [18].

### 2.2.4.3.3. Wear, Corrosion, and Fatigue Cracks in the Gutter Region

Corrosion, wear, and fatigue are other factors responsible for the deteriorating of the integrity of wheel components, especially the gutter region, where the lock ring groove is located, as shown in Figure 2.16 [5]. Under high internal pressure and high load, stress concentration can be easily generated in the small region of lock ring groove on the rim, inducing fatigue cracks in the gutter region. When fatigue crack propagation occurs, the engagement of the wheel components can suddenly break down, resulting in separation of wheel components under great speed. Additionally, the sliding and galling of the lock ring can wear away material in the lock ring groove. Loss of material in the groove can impair the engagement of wheel components and accelerate the initiation and propagation of cracks. Harsh working conditions in the mine sites with corrosive environments have synergistic effects on accelerating material wear and crack related failures.

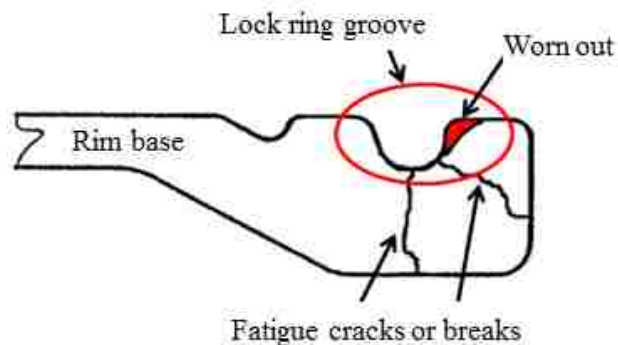


Figure 2.16 Wear and Fatigue cracks in the gutter region [5].

#### **2.2.4.4. Tire Failures for on-the-road Tires**

Tire explosion and zipper rupture occur for on-the-road tires used on passenger vehicles and haulage trucks too. Due to the lower tire pressure, smaller tire size, and favorable service conditions, the energy released by on-the-road tires when explosion or rupture happens is much lower, compared to the OTR tires. Tire blow-out is very common for OTR tires and very rare for on-the-road tires since a single-piece wheel is used.

Tire explosion and zipper rupture are initiated from the tires. Tire blow-out starts with multi-piece wheel components. The above incident report analysis shows that over 90% of the fatalities occurred in the mode of tire blow-out. Tire blow-outs are actually caused due to the multi-piece wheel design. This research is focused on improving the design of multi-piece wheels to minimize or completely remove the occurrence of tire blow-out.

#### **2.2.5. Working with Multi-piece Wheel and OTR Tire**

Wheel dimensions are standardized by the Tire and Rim Association [27] for size and contour only, and particular tire and wheel combinations are designated to ensure proper mounting and fit of the tire. The load and cold inflation pressure imposed on the wheel must not exceed the wheel manufacturers' recommendations even though the tire may be approved for a higher load or inflation.

Wheels and tires represent one of the major direct expenses in OTR equipment operations [24]. They are consumable items and regular maintenance will not only help them last longer, but will also reduce the incident rates. For underground mines, the rule of thumb for wheel life before recertification/intensive inspection is 1 year or 3,000 service hours; and 8,000 service hours for wheels used above ground. Tires used above ground last typically for one year, and tires used underground last for 3 to 8 months.

Over-inflation can reduce tire's service time. Under-inflation is more detrimental. Under-inflation can lead to irregular or uneven tread wear, sidewall radial cracks, ply separation, loose or broken cords inside the tire, fabric carcass fatigue, and belt edge separation. Low pressure can accelerate the wear of the wheel component and reduce service time. Most severely, tires with less than optimum air pressure are very dangerous. Under-inflation may damage the engagement among wheel components, causing tire blow-outs. Tires with less than 80% working pressure should be safely deflated and serviced [23]. Checking tire pressure regularly is an



important precaution for safety operations. In some mine sites, tire pressure is checked every shift.

Since the 1950's, the OTR wheel assemblies (rim and tire, geometry and structure) has not changed, but the payloads and travel speeds of the OTR vehicles have increased tremendously. For example, the 26.5×25 tire was previously in LHD trucks with a capacity of 7 yard<sup>3</sup> (5.35 m<sup>3</sup>), however such a tire is now used in 9 yard<sup>3</sup> (6.88 m<sup>3</sup>) truck at higher travel speeds and rougher conditions. The mass density of the ore also has a great effect on load (with nickel and gold ores being heavier). In order to catch up with the load increase, the tire pressure has increased from 344.7 to 689.5 kPa (50 psi to 100 psi). The increased pressure accelerates the failure of multi-piece wheel/tire assembly and is dangerous to human life.

Given the criticality of correct fitment, severe loading and working environment, and the much higher inflation pressures, working with OTR wheel assemblies carries much higher risks than working with on-the-road tires where risks have largely been mitigated due to lower individual wheel loads and smooth road conditions. The hazardous characteristics and incident preventions require strict controls at the management and operational level, and by the individuals carrying out the task.

## **2.3. Fatigue Life Analysis Theory**

Most failures in machinery are due to time-varying loads [84]. These failures typically occur at stress levels significantly lower than the yield strengths of the materials. This kind of failure is termed “fatigue failure”. Fatigue is defined as the progressive and localized structural damage that occurs when a material is subjected to cyclic loading [84]. The fatigue failure phenomenon was first noticed in the 1800s when railroad-car axles began failing after only limited service in Europe. The axles were made of ductile steel but exhibited sudden, brittle-like failures due to fatigue. Research within the area of fatigue failure is less than two hundred years old and research efforts continue.

### **2.3.1. Mechanism of Fatigue Failure**

Fatigue failures always begin at a crack [85]. Fischer and Yen [86] have shown that virtually all structural members contain discontinuities, ranging from microscopic (<0.25 mm) to macroscopic, introduced in the manufacturing or fabricating process. There are three stages of fatigue failure, namely, crack initiation, crack propagation, and sudden fracture due to unstable

crack growth. The first stage can be of short duration, the second stage involves most of the life of the part, and the third stage is instantaneous.

#### **2.3.1.1. Crack Initiation Stage**

At a microscopic scale, all metals are heterogeneous and anisotropic [86]. Metals are composed of groups of small crystal grains. For each grain, its behavior is anisotropic due to the crystal planes and if a grain boundary is crossed, the orientation of these planes changes. Inhomogeneities also exist due to the presence of tiny voids or particles of a different chemical composition than the bulk of the material, such as hard silicate or alumina inclusions in steel [86]. Stress concentrations may cause local yielding, even though the nominal stress in the section is well below the yield strength of the material. The localized yielding causes distortion and creates slip bands (regions of intense deformation due to shear deformation) along the crystal boundaries. When more slip bands occur due to cyclic loading, the slip bands coalesce into microscopic cracks. Pre-existing voids or inclusions will serve as stress raisers to initiate the crack.

It is almost universally agreed that fatigue failures start at the surface of a specimen or component [87]. This is true whether the test is carried out in a rotating-beam machine where the maximum stress is always at the surface, or in a push-pull machine which gives a simple tensile-compressive stress cycle. The mechanism of surface crack initiation can be accounted for in the following three aspects.

Firstly, all structures experience some degree of bending under cyclic loading, even in uniaxial loading conditions, due to imperfect geometries of the structures and inexact uniaxial loading. This creates uneven stress distributions in the structures, with the maximum at the surface of the structures. Secondly, all structure surfaces have, to some extent, defects, including dents, pitting, scratches, wear, corrosion, and surface roughness caused in the machining processes. These defects act as stress-raisers to cause local yielding under maximum tensile stresses at the surface. Finally, compared to the material inside the structure, the material at the surface only has half side of materials to resist deformation under loading, allowing for deformation to happen at the surface with more ease at lower stress levels.

It is very important to understand the surface crack initiation mechanism in FE modeling of fatigue structures. To accurately predict the surface stresses, shell elements have to be used on the surfaces of structures since solid elements cannot accurately capture the stress levels on the surfaces.

### **2.3.1.2. Crack Propagation Stage**

In the beginning of micro-crack propagation, micro-cracks move along shear planes thus having a tendency to form an angle of 45 degree to the surfaces [86]. During this stage, the micro-cracks can enlarge freely until micro-structural barriers stop them. The micro-structural barriers include grain boundaries and other hard material faces. If the micro-cracks do not have enough energy (at low stress levels) to overcome the barriers, the micro-cracks will stop propagation. Knowledge of micro-cracks propagation can be used to prolong this stage by introducing compressive residual stresses through several types of treatments of structures, namely, thermal treatments, surface treatments (shot peening and cold forming), and mechanical prestressing.

Once a micro-crack is established, the prolonged crack creates stress concentrations at the front tip. The crack begins to propagate in the direction perpendicular to the applied stress. Each time a tensile stress opens the crack, the crack grows a small amount. When the stress cycles to a compressive-stress regime, or to zero, or to a sufficiently lower tensile stress, the crack closes. Crack growth is due to tensile stress and the crack grows along planes normal to the maximum tensile stress. Therefore, fatigue failure is considered to be due to the tensile stress, even though shear stress initializes the crack in ductile materials. Cyclic stresses that are always compressive will not cause crack growth, as they tend to close the crack. The crack propagation growth rate is very small, but this adds up over a large number of cycles.

If a part containing a crack is in a corrosive environment, the crack will grow under static stress. The combination of stress and corrosive environment has a synergistic effect and the material corrodes more rapidly than if unstressed. If the part is cyclically stressed in a corrosive environment, the crack will grow more rapidly than from either factor alone. This is called corrosion fatigue. While the frequency of stress cycling appears to have no detrimental effect on crack growth in a noncorrosive environment, it does in corrosive environments. Lower cyclic frequencies allow the environment more time to act on the stressed crack tip while it is held open under tensile stress, and this substantially increases the rate of the crack growth per cycle.

### **2.3.1.3. Fracture**

The crack will continue to grow as long as the cyclical tensile stress and/or corrosion factors of sufficient severity are present. At some point, the crack size becomes large enough that the amount of undamaged material is insufficient to carry the maximum load, and an abrupt, brittle failure occurs.

Generally, the fatigue process can be viewed in terms of the following expression [87]:

$$N_t = N_i + N_p \quad (2.1)$$

In the Equation,  $N_t$  is total fatigue life,  $N_i$  is life to crack initiation, and  $N_p$  is crack propagation life. Crack propagation is strongly dependent on the applied stress and the material strength. If the stress is high enough, there will be enough energy for crack propagation in a short period of time and the structure will experience low-cycle fatigue (LCF) before failure. Otherwise, the structure will experience high-cycle fatigue (HCF) before failure. Under identical loading and structural conditions, a material with higher fatigue strength may experience HCF; on the other hand, a material with lower fatigue strength may experience LCF.

There are three common practices associated with the fatigue process to estimate material fatigue life, [85] namely, (1) stress-life ( $S-N$ ), (2) strain-life ( $\varepsilon-N$ ), and (3) Linear Elastic Fracture Mechanics ( $LEFM$ ). Each approach has its place and purpose.

The stress-life ( $S-N$ ) approach is commonly used in situations where the stress is below the material yield strength and the structure experiences HCF where the total number of cycles is greater than  $10^3$ . This approach is fairly easy to implement, and large amounts of relevant strength data are available due to its long-time use. However, it is the most empirical and least accurate of the three approaches in terms of defining the true local stress/strain states in the part, especially for LCF finite-life situations where the total number of cycles is expected to be less than  $10^3$  and the stresses will be high enough to cause local yielding.

The strain-based approach gives a reasonably accurate description of the crack initiation stage. It can also account for cumulative damage due to variations in the cyclic load over the life of the part. This method can be used for both LCF and HCF problems. It is the most complicated of the three approaches and requires a computer solution due to significant amount of computations required.

The linear elastic fracture mechanics method is applied to LCF, finite-life problems where the cyclic stresses are known to be high enough to cause the formation of cracks and is most useful in predicting the remaining life of cracked parts in service. It is often used in conjunction with non-destructive testing (NDT) in a periodic service-inspection program, especially in the aerospace industry.

In the following section, only stress-life ( $S-N$ ) and strain-life ( $\varepsilon-N$ ) approaches will be briefly introduced here since only these two approaches are relevant to this research.

## 2.3.2. The Stress-life (*S-N*) Approach

### 2.3.2.1. Fatigue Loads

Any loads that vary with time can potentially cause fatigue failure. In rotating machinery, the loads tend to be consistent in amplitude over time and repeat with some frequency. In service equipment, the loads tend to be quite variable in amplitude and frequency over time and may even be random in nature. The shape of the waveform of the load-time function seems not to have any significant effect on fatigue failure in the absence of corrosion, so the functions are usually depicted as a sinusoidal or saw-tooth wave. Also, the presence or absence of periods of quiescence in the load history is not significant as long as the environment is noncorrosive. The significant factors that affect the fatigue life are the amplitude and the average value of the stress-time (or strain-time) waveform and the total number of the stress/strain cycles that the part has seen.

The typical stress-time functions experienced by rotating machinery can be modeled as shown in Figure 2.17 as periodic responses. Figure 2.17 (a) illustrates the fully reversed case for which the mean value is zero. Figure 2.17 (b) shows a repeated stress case in which the waveform ranges from zero to a maximum with a mean value equal to the alternating component, and Figure 2.17 (c) shows a fluctuating stress case with all component values nonzero.

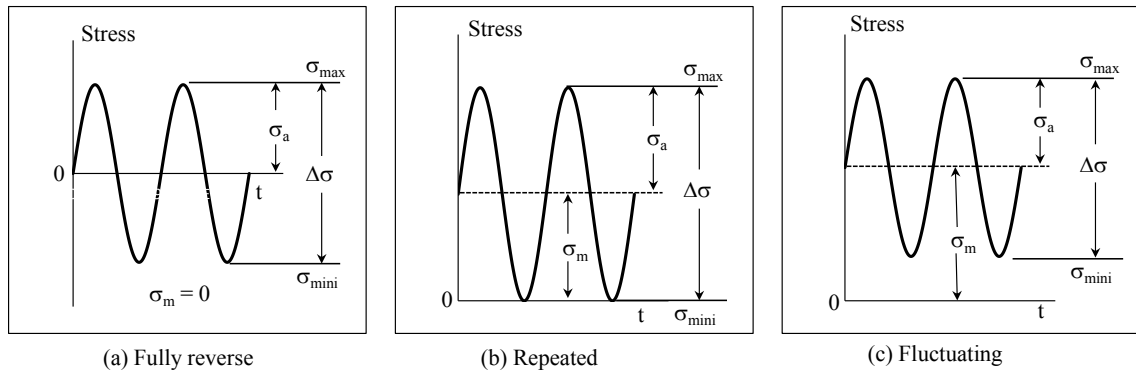


Figure 2.17 Three common rotation loads.

The alternating component  $\sigma_a$  and the mean component  $\sigma_m$  are defined using Equation (2.2) and (2.3) separately.

$$\sigma_a = \frac{\sigma_{max} - \sigma_{min}}{2} \quad (2.2)$$

$$\sigma_m = \frac{\sigma_{max} + \sigma_{min}}{2} \quad (2.3)$$

### 2.3.2.2. Material Fatigue Test

The most common fatigue test is the rotating-beam test, in which a highly polished specimen of about 7.6 mm (0.3 inch) diameter is mounted in a fixture which allows a constant-magnitude, pure-bending moment to be applied while the specimen is rotated. This creates a fully reversed bending stress at any point on the circumference of the specimen. The test is run at one particular stress level until it fails, and the number of cycles to failure and the applied stress level is recorded. This test is repeated with multiple specimens of the same material loaded at different stress levels. The collected data are then plotted as normalized failure strength,  $S_f/S_{ut}$  against number of cycles,  $N$ , (typically on log coordinates) to obtain an  $S-N$  diagram.  $S_f$  and  $S_{ut}$  represent fatigue strength and ultimate tensile strength separately. At the same stress level, the fatigue life for different samples may be different due to variation of the defects contained in the samples, although all the samples are polished to a fine finish to minimize the possibility of surface defects starting a crack. After the collected data are averaged, the stress-life ( $S-N$ ) curve can be plotted as shown in Figure 2.18.

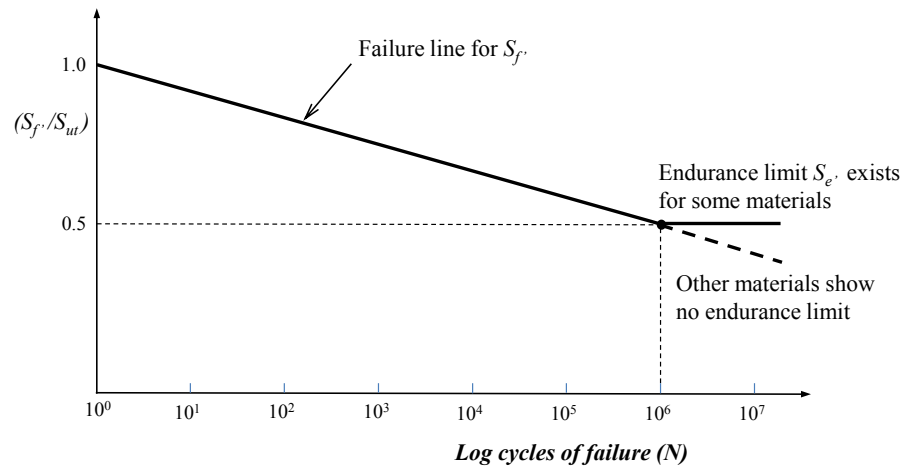


Figure 2.18 Fatigue strength versus the numbers of cycle to failure diagram.

In the diagram there is a discontinuity commonly known as the “knee” of  $S-N$  response, defining an endurance limit  $S_e$  for steel material at  $N=10^6$ , which is a stress level below which it can be cycled infinitely without failure. An approximate endurance limit can be defined for steels:

for steel	$S_e \cong 0.5 S_{ut}$	$S_{ut} < 1379 \text{ MPa}$
	$S_e \cong 100 \text{ ksi}$	$S_{ut} \geq 1379 \text{ MPa}$

Not all materials exhibit this endurance limit. Other materials, such as aluminum, magnesium, and copper, show that the fatigue strengths continue to fall with increasing  $N$ . For

the material lack of a distinct discontinuity, their fatigue strength  $S_f$  is usually taken as the average failure stress at  $N = 5 \times 10^8$  cycles or some other value of  $N$ .

$$\begin{aligned} \text{for aluminum: } S_{f@5 \times 10^8} &\cong 0.4 S_{ut} & S_{ut} < 331 \text{ MPa} \\ S_{f@5 \times 10^8} &\cong 19 \text{ ksi} & S_{ut} \geq 331 \text{ MPa} \end{aligned}$$

### 2.3.2.3. Factors Influencing Fatigue Life

The aforementioned fatigue strength or endurance limit is obtained through a bending test on a polished 7.6-mm diameter specimen at room temperature with non-corrosive environment. Any other testing conditions will affect the fatigue strength. Strength-reduction factors have to be introduced to obtain a corrected fatigue strength or endurance limit for the particular application as shown in the following equation.

$$S_e = C_{load} \cdot C_{size} \cdot C_{surf} \cdot C_{temp} \cdot C_{reliab} \cdot S_e' \quad \text{and} \quad S_f = C_{load} \cdot C_{size} \cdot C_{surf} \cdot C_{temp} \cdot C_{reliab} \cdot S_f' \quad (2.4)$$

Where  $S_e$  represents a corrected endurance limit for a material that exhibits a “knee” in its  $S$ - $N$  curve and  $S_f$  a corrected fatigue strength at a particular number of cycles  $N$  for a material that does not exhibit a “knee”. The strength reduction factors  $C_{load}$ ,  $C_{size}$ ,  $C_{surf}$ ,  $C_{temp}$ , and  $C_{reliab}$  are load factor, size factor, surface factor, temperature factor, and reliability factor respectively, with all values between 0 and 1. When a corrosive environment exists, a drastic reduction of fatigue strength will be observed and the endurance-limit “knee” may be eliminated.

The reliability factor  $C_{reliab}$  has to be further detailed since fatigue is a statistical, not deterministic, phenomenon. Many of the reported fatigue strength data are mean values from test data. There is considerable scatter in multiple tests of the same material under the same test conditions. A 50% reliability has a factor of 1 (representing the mean value) and the factor reduces as a higher reliability is chosen. For example, if one wishes to have 99.99% probability that samples meet or exceed the assumed strength, multiply the mean strength value by 0.702 ( $C_{reliab}$ ).

Equation (2.4) provides information about the material’s fatigue strength in the high-cycle region of the  $S$ - $N$  diagram. With similar information for the low-cycle region, an  $S$ - $N$  diagram for the particular material can be constructed. The material strength at  $10^3$  cycles can be termed as  $S_m$ . Test data indicate the following estimates of  $S_m$ :

$$\text{Bending: } S_m = 0.9 \cdot S_{ut}$$

$$\text{Axial loading: } S_m = 0.75 \cdot S_{ut}$$

The estimated  $S$ - $N$  curves can be constructed from high-cycle region ( $N > 10^3$ ) as shown in Figure 2.19, in which figure (a) shows materials with an endurance limit and (b) materials without an endurance limit.

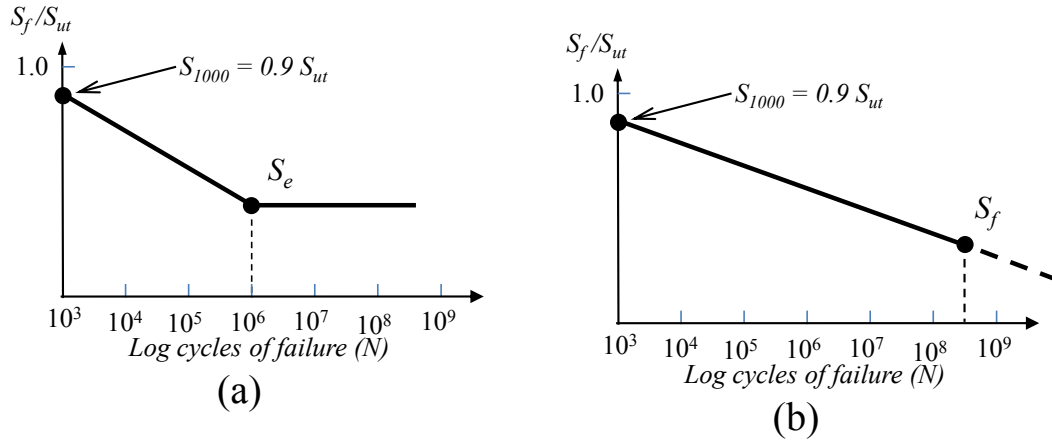


Figure 2.19 Estimated  $S$ - $N$  response for HCF regime (a) materials with an endurance limit (b) material without an endurance limit.

The equation of the line from  $S_m$  to  $S_e$  or  $S_f$  can be written as

$$S(N) = a \cdot N^b \quad (2.5)$$

In which  $b = -\frac{1}{3} \log\left(\frac{S_m}{S_e}\right)$  for material with a knee and  $b = -\frac{1}{5.699} \log\left(\frac{S_m}{S_f}\right)$  for material without a knee and  $S_f$  at  $5 \times 10^8$ ;  $\log(a) = \log(S_m) - 3 \cdot b$ .

Methods of representing the  $S$ - $N$  curve in the range 1 to  $10^3$  cycles have been developed but they must be treated with extreme caution. In the low cycle regime, high levels of loading result in large plastic strain. The  $S$ - $N$  method cannot accurately predict the fatigue life in this region. Low cycle fatigue analysis is best treated by a strain based procedure which accounts for, rather than ignore, the effects of plasticity.

#### 2.3.2.4. The Influence of Mean Stress

The majority of basic fatigue data are collected in the laboratory by means of testing procedures which employ fully reversed loading as shown in Figure 2.17 (a). However, most realistic service situations involve non-zero mean stress as shown in Figure 2.17 (b) and (c). Therefore, it is very important to know the influence that mean stress has on the fatigue process so that the fully reversed laboratory data can be usefully employed in the assessment of practical situations.



Fatigue data collected from a series of tests designated to investigate different combinations of stress amplitude and mean stress are characterized in Figure 2.20 for a given number of cycles to failure. The majority of steel and aluminum materials show this kind of relationship between stress amplitude and mean stress for a given number of cycles to failure. The diagram plots the mean stress, both tensile and compressive, along the  $x$ -axis and the alternating stress amplitude along the  $y$ -axis. The stress amplitude at zero mean stress corresponds to the stress amplitude at  $N$  cycles to failure as measured by the fully reversed fatigue test. The failure data points tend to follow a curve which if extrapolated would pass through the ultimate tensile strength  $S_{ut}$  on the mean stress axis. The influence of mean stress is different for compressive and tensile mean stresses. Failure appears to be more sensitive to tensile mean stress, than compressive mean stress.

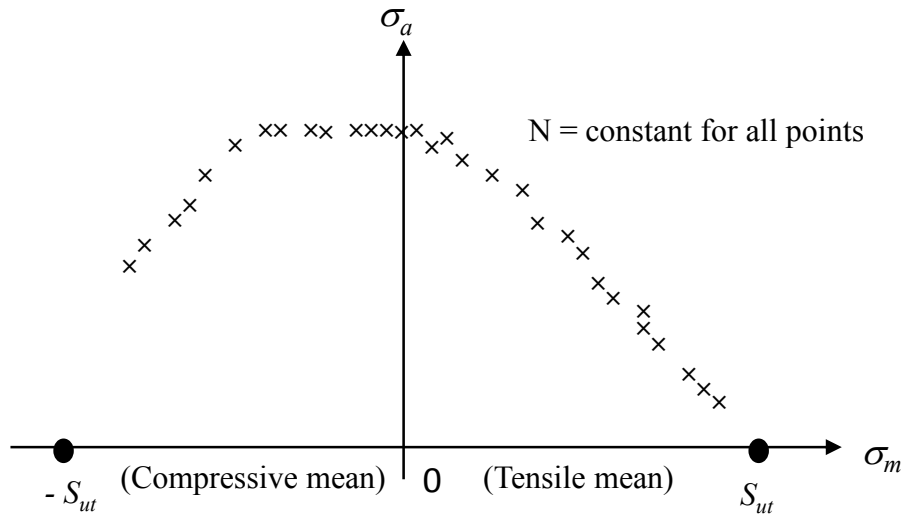


Figure 2.20 High cycle fatigue data showing the influence of mean stress for the majority of steel and aluminum materials.

Several empirical relationships which relate alternating stress amplitude to mean stress have been developed. For infinite life design strategies, the methods use various curves to connect the corrected endurance limit  $S_e$ , or fatigue strength  $S_f$  on the alternating stress axis to either the yield stress  $S_y$ , or ultimate strength  $S_{ut}$ , on the mean stress axis. Figure 2.21 shows the modified-Goodman line, Gerber parabola, Soderberg line and the yield line plotted on  $\sigma_m - \sigma_a$  axes.

Of all the proposed relationships, the modified-Goodman and Gerber relationships have been most widely accepted [84]. Experience has shown that actual test data tend to fail between the Goodman and Gerber curves. The corrected-Goodman line and Gerber parabola are usually drawn for the infinite-life of steel or very high-cycles ( $N > 10^6$ ). However it can be drawn for any

cycle of fatigue life. Whichever lines are chosen to represent failure, safe combinations of  $\sigma_m$  and  $\sigma_a$  lie to the left and below the lines. These failure lines are defined by

$$\text{Modified-Goodman line: } \left(\frac{\sigma_a}{S_e}\right) + \left(\frac{\sigma_m}{S_{ut}}\right) = 1 \quad (2.6)$$

$$\text{Gerber parabola: } \left(\frac{\sigma_a}{S_e}\right) + \left(\frac{\sigma_m^2}{S_{ut}^2}\right) = 1 \quad (2.7)$$

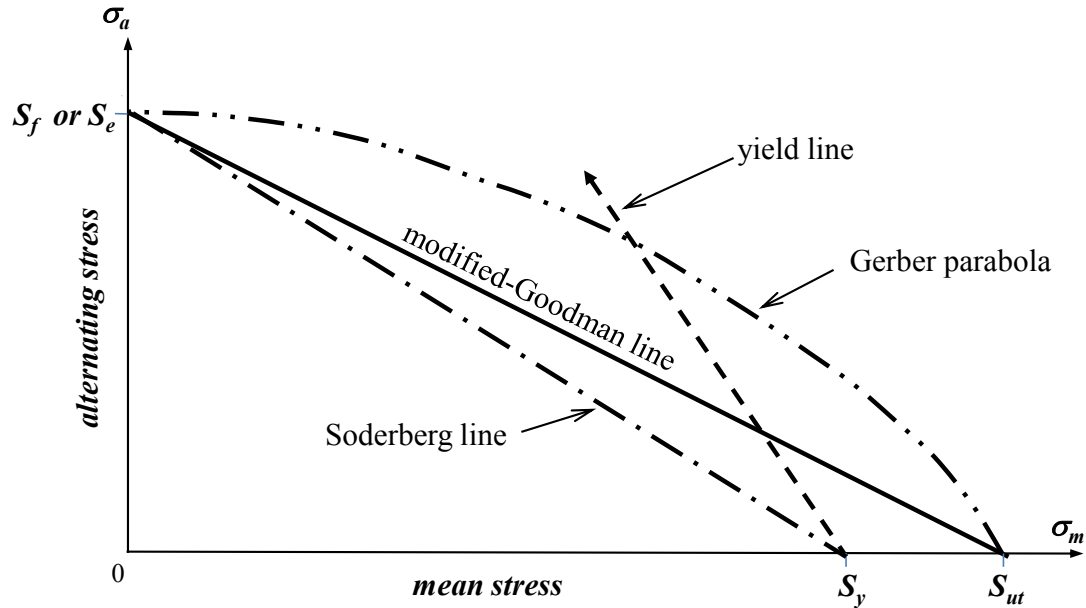


Figure 2.21 Various failure lines for fluctuating stresses.

In fatigue life prediction, replacing  $S_e$  with the equivalent fully reversed fatigue strength  $S'$ , the above Equations (2.6) and (2.7) can be used to calculate the equivalent fully reversed fatigue strength  $S'$ , knowing  $\sigma_a$ ,  $\sigma_m$ , and  $S_{ut}$ . If calculated  $S'$  is less than the material endurance limit  $S_e$ , an unlimited fatigue life will be predicted; otherwise, the fatigue life can be calculated using Equation (2.5) for high cycle fatigue life (greater than 1000 cycles).

In actual product design, a factor of safety  $n$  is taken into consideration. In Equation (2.6),  $\sigma_a$  and  $\sigma_m$  are replaced with  $n \cdot \sigma_a$  and  $n \cdot \sigma_m$  respectively, and then the modified Goodman relation takes the form in Equation (2.8).

$$\left(\frac{\sigma_a}{S_e}\right) + \left(\frac{\sigma_m}{S_{ut}}\right) = \frac{1}{n} \quad (2.8)$$

### 2.3.3. Strain-life ( $\epsilon$ - $N$ ) Approach

As in-service cycles have become more severe and components more complicated, another pattern of fatigue behaviour has emerged. In this regime, the cyclic loads are relatively large and have significant amounts of plastic deformation associated with them together with relatively short lives. The analytical procedure evolved to deal with strain-controlled fatigue is termed the strain-life, local stress-strain, or critical location approach.

#### 2.3.3.1. Monotonic Stress-Strain Behaviour

The engineering tension test is widely used to provide basic information on the strength of materials. In this test, a cylindrical specimen is subjected to a continually rising, monotonic, uniaxial load while simultaneously its elongation is measured. The engineering stress ( $S_E$ ) and engineering strain ( $e$ ) can be defined as follows:

$$S_E = P/A \quad (2.9)$$

$$e = (l-l_0)/l_0 \quad (2.10)$$

Where:  $P$  is the applied load,  $A_0$  is the initial cross-sectional area of the specimen,  $l$  is the final length of the specimen and  $l_0$  is the initial length of the specimen.

The true stress ( $\sigma$ ) and true strain ( $\epsilon$ ) up to necking can be determined as:

$$\sigma = S_E \cdot (1 + e) \quad (2.11)$$

$$\epsilon = \ln (1 + e) \quad (2.12)$$

The true stress versus true strain relation can be expressed in the following equation:

$$\epsilon(\sigma) = \sigma/E + (\sigma/K)^{1/n} \quad (2.13)$$

Where  $K$  is the strength coefficient and  $n$  is the work hardening exponent.

Figure 2.22 illustrates the true stress versus true strain response and engineering stress versus engineering strain curves.

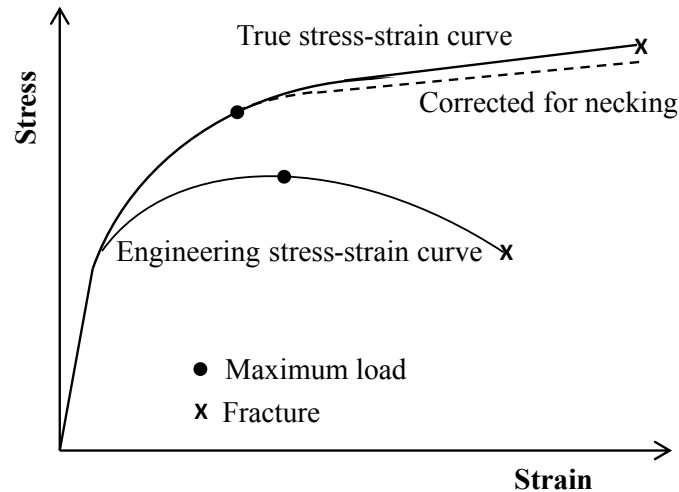


Figure 2.22 True stress versus true strain diagram.

### 2.3.3.2. Cyclic Stress-Strain Behaviour

If a material is repeatedly cycled between fixed strain limits, one of several things may happen depending on the material alloys and initial conditions of heat treatment. It could cyclically harden, soften, or remain stable. It is clear that in the case of hardening, the maximum stress reached in each successive strain cycle increases with the number of cycles and in the case of softening, the maximum stress decreases with number of imposed cycles. This process does not continue indefinitely. In both cases the stress will find a constant level and remain stable at that level until the first emergence of a fatigue crack. After a relatively small number of cycles, typically no more than about 10% of total life, the stress amplitude tends to remain reasonably constant over the remaining portion of fatigue life. If the stabilized stresses and strains of differing strain amplitudes are plotted in stress-strain space, then the locus of these points defines the cyclic stress versus strain curve.

Similar to the monotonic loading condition, the stress – strain relation for cyclic loading can be expressed in the following Equation [87]:

$$\varepsilon = \sigma/E + (\sigma/K')^{1/n'} \quad (2.14)$$

Where:

$K'$  is the cyclic strength coefficient and  $n'$  is the cyclic strain hardening exponent.

Typically,  $K'$  takes values in the range 1000 to 3000 MPa and  $n'$  varies between about 0.1 to 0.2. In general, metals with a high monotonic strain hardening exponent,  $n$ , will harden whilst those with a low monotonic strain hardening exponent will cyclically soften [87].

### 2.3.3.3. The Strain-life ( $\varepsilon$ - $N$ ) Response

The  $\varepsilon$ - $N$  method is used to model the fatigue life up to crack initiation. This method is widely used in ground vehicle industries to model the fatigue performance of 'safety critical' systems such as the suspension, steering, and chassis components [88-90]. In these structures fatigue cracks must be avoided at practically all cost. For the multi-piece wheel under investigation, it is critical to identify an initial fatigue crack on wheel components before catastrophic failures occur.

Basquin [91, 92] observed that the stress-life data may be represented by a straight line relationship under elastic deformation, when plotted using log scales. The relationship could be expressed in terms of true stress as presented in Equation (2.15):

$$\sigma_e = \sigma'_f (2N_f)^b \quad (2.15)$$

In the equation,  $\sigma_e$  is the true cyclic elastic stress amplitude,  $\sigma'_f$  is the regression intercept called fatigue strength coefficient,  $2N_f$  is the number of half cycles, or reversals, to failure, and finally  $b$  is the regression slope called the fatigue strength exponent.

This equation may be re-written in terms of elastic strain amplitude ( $\varepsilon_e$ ) as presented in Equation (2.16).

$$\varepsilon_e = \sigma_e / E = \frac{\sigma'_f (2N_f)^b}{E} \quad (2.16)$$

in which  $E$  is the elastic modulus of the material. The Basquin equation may be rearranged so that:  $\sigma_e = \sigma'_f 2^b (N_f)^b$ . Since  $b$  is approximately equal to -0.1, then  $2^b$  is approximately equal to 1. It is clear that Equation (2.5) and Equation (2.16) are the same. It can be noted that the classical  $S$ - $N$  curve is actually a subset of the  $\varepsilon$ - $N$  life curve.

Coffin and Manson [91-94] independently proposed that the plastic strain component ( $\varepsilon_p$ ) of a fatigue cycle may also be related to  $N_f$  by a simple power law:

$$\varepsilon_p = \varepsilon'_f (2N_f)^c \quad (2.17)$$

in which,  $\varepsilon'_f$  is the regression intercept called fatigue ductility coefficient,  $c$  is the regression slope called the fatigue ductility exponent.

Morrow [95] indicated that the total strain amplitude ( $\varepsilon_a$ ), that is the sum of the elastic and plastic components, may be better correlated to  $N_f$  as expressed in Equation (2.18).

$$\varepsilon_a = \frac{\sigma'_f(2N_f)^b}{E} + \varepsilon'_f(2N_f)^c \quad (2.18)$$

$\sigma'_f$  and  $b$  are considered to be material properties with the fatigue strength coefficient being approximately equal to the monotonic fracture stress,  $\sigma_f$ , and  $b$  varies between -0.05 and -0.12. The terms  $\varepsilon'_f$  and  $c$  are considered to be material properties with the fatigue ductility coefficient being approximately equal to the monotonic fracture strain,  $\varepsilon_f$ , and  $c$  varies between -0.5 and -0.8. Figure 2.23 illustrates schematically the nature of the total strain-life curve.

Typical values for steel are:  $E=207,000$  MPa,  $\sigma'_f = 1,300$  MPa,  $b = -0.1$ ,  $\varepsilon'_f = 0.5$  and  $c = -0.5$ . In Figure 2.23, the point where the plastic and elastic life lines intersect is called the transition life. At lives less than the transition, plastic events dominate and at lives longer than the transition elastic events dominate.

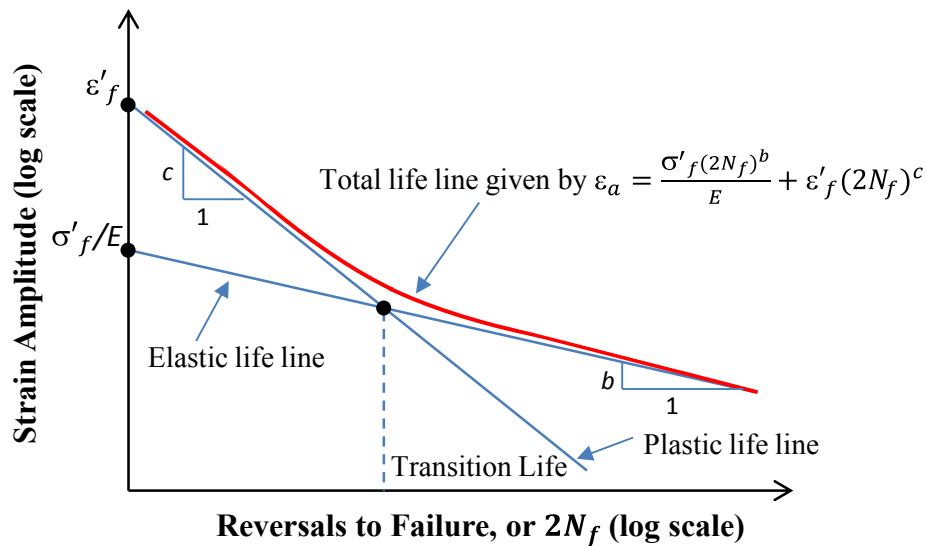


Figure 2.23 Strain amplitude as a function of reversals to failure.

#### 2.3.3.4. Determination of Cyclic Fatigue Properties

The cyclic material properties required to define the cyclic stress strain curve and the strain life curve are usually determined by carrying out tests, under strain control, on a series of smooth highly polished hourglass shaped specimens. Typically, about 15 tests need to be performed at differing strain amplitudes. The properties can then be calculated by regression analysis on the following curves:

$\sigma'_f$  and  $b$ : from a log elastic strain versus  $\log(2N_f)$  regression as shown in Figure 2.23.

The slope is  $b$  and the intersection with the vertical axis is  $\frac{\sigma'_f}{E}$ .

$\epsilon'_f$  and  $c$ : from a log plastic strain versus  $\log(2N_f)$  regression as shown in Figure 2.23.

The slope is  $c$  and the intersection with the vertical axis is  $\epsilon'_f$ .

$K'$  and  $n'$ : from a log stress versus log plastic strain regression as shown in Figure 2.24.

For cyclic loading, the stress  $\sigma$  equals to  $(K' \epsilon_p^{n'})$ . When  $\epsilon_p = 1$ ,  $\sigma = K'$ . So  $K'$  and  $n'$  can be determined from a log stress versus log plastic strain regression as shown in Figure 2.24.

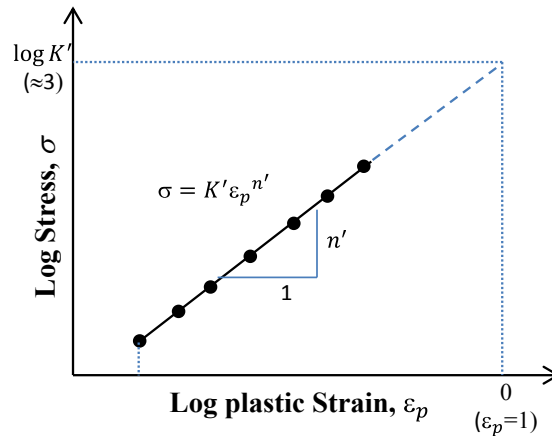


Figure 2.24 Log stress versus log plastic strain line.

It is often difficult to gain access to material parameters under cyclic loading. For this reason, considerable effort has been put into finding ways of relating monotonic properties, of which there is an abundant supply, to cyclic properties. The approaches have all been empirical but have provided some useful approximations. The first method of approximating the strain life relationship from monotonic properties was proposed by Manson [93] and later modified by Muralidharan [96] as shown in Table 2.3. The procedure is usually referred to as the method of universal slopes and it has been suggested that this method can be applied to any metal [87].

Table 2.3 Estimation of material cyclic properties

Parameters	Universal Slopes (Manson)	Modified Universal Slopes (Muralidharan)
$\sigma'_f$	$1.9 \cdot S_{ut}$	$0.623 \cdot S_{ut} \cdot 0.823 \cdot E^{0.168}$
$b$	$-0.12$	$-0.09$
$\epsilon'_f$	$0.76 \cdot \epsilon_f^{0.6}$	$0.0196 \cdot \epsilon_f^{0.115} \cdot (S_{ut}/E)^{-0.53}$
$c$	$-0.6$	$-0.56$
$K'$	$\sigma'_f / (\epsilon'_f)^{0.2}$	$\sigma'_f / (\epsilon'_f)^{0.2}$
$n'$	$0.2$	$0.2$

In Table 2.3,  $S_{ut}$  is the ultimate tensile strength,  $\epsilon_f$  is the true fracture strain calculated from  $\ln(1 / (1 - RA))$ , and RA is the reduction in area.

### 2.3.3.5. The Effect of Mean Stress

Most basic fatigue data are collected in the laboratory by means of testing procedures which employ fully reversed loading. However, most realistic service situations involve non-zero mean stresses. It is, therefore, very important to know the influence that mean stress has on the fatigue process so that the fully reversed laboratory data can be usefully employed in the assessment of real situations.

Figure 2.25 illustrates schematically the effect mean stress has on the strain-life response [87]. Typically, the effects are greater at the greater value of  $N_f$ , with compressive mean stress extending life and tensile mean stress reducing life. At high strain amplitudes, mean stress relaxation occurs and the effect of mean stress tends towards zero.

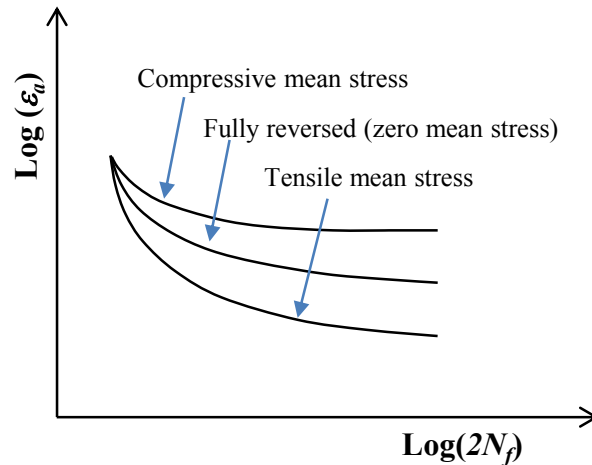


Figure 2.25 Effect of mean stress on the strain-life curve.

#### 2.3.3.5.1. The Morrow mean stress correction

Morrow [95] was the first to propose a modification to the baseline strain-life curve which can account for the effect of mean stress. He suggested that mean stress could be taken into account by modifying the elastic part of the strain-life curve by the mean stress,  $\sigma_m$ , the entire strain life curve becoming:

$$\epsilon_a = \frac{(\sigma'_f - \sigma_m)(2N_f)^b}{E} + \epsilon'_f(2N_f)^c \quad (2.19)$$



The Morrow equation is consistent with observation that mean stress effects are significant at low values of plastic strain and little effect at high plastic strains.

#### 2.3.3.5.2. The Smith-Watson-Topper mean stress correction

Smith, Watson and Topper [97] have proposed a slightly different approach to account for mean stress through consideration of the maximum stress present in any given cycle. In this case the damage parameter is taken to be the product of the maximum stress,  $\sigma_{max}$ , and the strain amplitude,  $\epsilon_a$ , of a cycle.

For fully reversed loading the maximum stress is given by  $\sigma_{max} = \sigma_f'(2N_f)^b$  and multiplying the strain-life Equation (2.18) yields the following equation

$$\sigma_{max}\epsilon_a = \frac{\sigma_f'^2(2N_f)^{2b}}{E} + \sigma_f'\epsilon_f'(2N_f)^{(b+c)} \quad (2.20)$$

The Smith-Watson-Topper equation predicts that no fatigue damage can accrue when the maximum stress becomes zero or negative, which is not strictly true.

It is difficult to categorically select one procedure in preference to the other to determine the effect of mean stress. However, for loading sequences which are predominantly *tensile* in nature the Smith-Watson-Topper approach is more conservative and is, therefore, recommended. In the case where the loading is predominantly compressive, particularly for wholly compressive cycles, the Morrow correction can be used to provide more realistic life estimates.

#### 2.3.3.6. Factors Influencing Fatigue Strain Life

A standardized, fully reversed, strain controlled, fatigue test is used to determine the baseline strain-life relationship for a polished specimen of approximately 6 mm diameter. As with the *S-N* method, similar fatigue strength reduction factors can be used to modify the fatigue strength to account for variations of component size, the type of loading, the effect of surface finish, and the effect of surface treatment [87].

#### 2.3.3.7. Elastic-Plastic Corrections

The local strain approach requires total (elastic-plastic) strain as well as stress, yet for efficiency reasons, calculations often have to be based on linear elastic FE calculations. Notch corrections allow elastic-plastic strains and stresses to be estimated based on elastic FE results.

The Neuber method [98] provides a simple way of estimating the total elastic-plastic strain and stress at an “average” stress concentration, based on the local elastic stress/strain.

Consider a simple notched specimen subjected to a uniaxial loading as shown in Figure 2.26. As long as the yield stress is not exceeded, linear FE analysis gives (assuming a good model) a reasonably accurate estimate of the strain and stress at the root of the notch. However, once the yield stress is exceeded, the elastic solution becomes increasingly unrealistic. In practice, as yielding occurs, there will be a redistribution of stress and strain around the notch, so that the real strain will be greater than the elastic value and the real stress less than the value from elastic analysis. The true solution must lie somewhere on the material stress-strain response. To get a reasonably accurate estimate of the way this stress and strain is redistributed, an elastic-plastic FE solution, taking into account the geometry of the specimen, could be carried out, but this could be rather time consuming, especially if many loading cycles have to be considered.

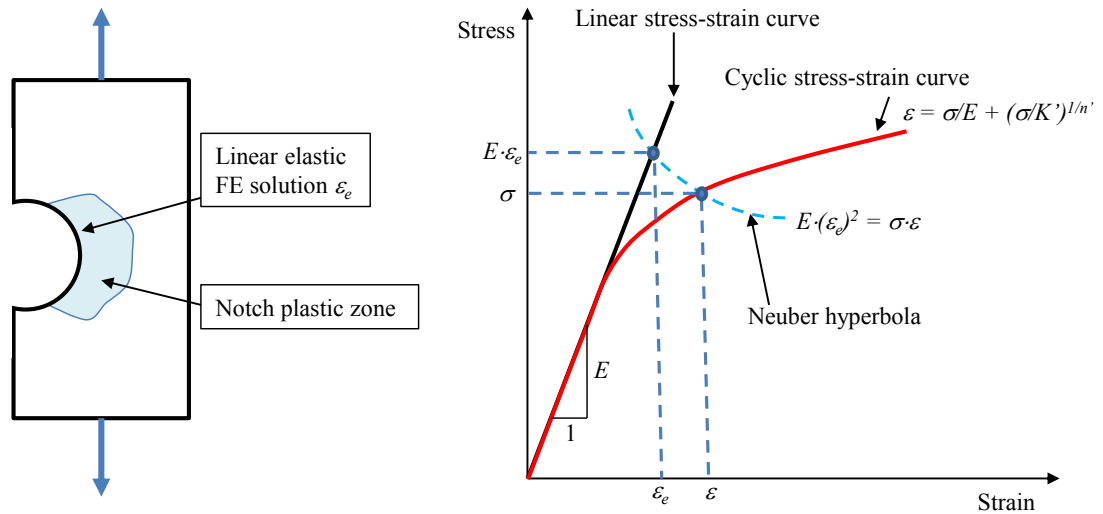


Figure 2.26 The Neuber's method for estimating elastic-plastic strain and stress at a notch.

The Neuber method provides a simple alternative that provides a rough estimate for how the stress and strain might redistribute, without reference to the real geometry. The Neuber method assumes that the product of stress and strain before and after redistribution is constant. This is represented by the Neuber hyperbola, where the product of stress and strain is constant and equal to the product of elastic stress and elastic strain. From the FE results of elastic stress/strain, the corrected total elastic-plastic stress/strain can be calculated using Equation (2.21) and cyclic stress-strain Equation (2.13).

$$E \cdot (\varepsilon_e)^2 = \sigma \cdot \varepsilon \quad (2.21)$$

The Neuber method can be only applied to uniaxial loading. In reality, the stress state is very often not uniaxial, and the Hoffmann-Seeger method [87] may give more realistic results. The Hoffmann-Seeger method is a modified version of the Neuber method that takes into account

the state of stress, allowing it to be extended to proportional multiaxial loadings (the orientation of the principal axes remain fixed). When multi-axial loading is not proportional, the Hoffmann-Seeger method is not applicable. If the input from the FE analysis is elastic-plastic strain and stress, the notch corrections will not be used. A suitable plasticity model will have to be implemented in the FE calculation so that there is no need to use a notch/plasticity correction in the fatigue calculation to estimate the redistribution of stress and strain.

#### **2.3.4. Multi-axial Loading in Fatigue**

The previous discussions were limited to cases in which the loading produced uniaxial stresses in the part. However, most practical situations, including rotating shafts, connecting links, automotive and aircraft components and many mechanical components involve a multiaxial state of cyclic stress. This often means that, at any point, both the directions and the magnitudes of the principal stresses can vary during the loading cycle and, therefore, as a function of time. The multiple time-varying loads may be periodic, random, or some combination of the two. If periodic, they can be mutually synchronous, or asynchronous. If synchronous, they may have phase relationships from in-phase to 180° out-of-phase or anything in between. The possible combinations are quite varied, and only a few simple combinations have been studied to determine their effects on fatigue failure. Collins [99] suggests that the assumption that loads are synchronous and in-phase is usually accurate for machine design and usually, but not always, conservative.

The most-studied cases are those of periodic, synchronous, in-phase loads that cause combined stresses/strains whose principal directions do not change with time. This is referred to as simple multiaxial stress/strain. Other situations, in which the directions of the principal stresses/strains vary with time, or stresses/strains are asynchronous or out-of-phase, are called complex multiaxial stress/strain and are still being studied.

##### **2.3.4.1. Fatigue Life Prediction in Simple Multiaxial Stress/Strain Situations**

Traditionally, the approach to the design of components subjected to multiaxial loading is to make the fundamental assertion by using an equivalent modulus. The assertion states that failure under multiaxial loading is predicted to occur if and when the cyclically induced magnitude of that modulus is sufficiently large that failure would occur in the uniaxial state for an identical magnitude of the same modulus. The modulus is a measurable quantity such as principal stress, principal shear stress, or distortion energy. This philosophy has led to what is usually referred to as the equivalent stress-strain approach, where an equivalent stress or strain

modulus is calculated under multiaxial loading and then applied to uniaxial data. A problem with all these methods is that they do not take into account the fact that fatigue is essentially a directional process, with damage and cracking taking place on particular planes. These methods are not suitable for application in complex multiaxial loading conditions.

These methods are based on extensions to static yield theories. They are assumed that fatigue life, under multiaxial loading, can be predicted by substituting combined stress or strain parameters in the uniaxial stress-life or strain-life equations. The main stress and strain parameters used are the maximum principal, the maximum shear, and the von Mises stress and strain. The big advantage of this kind of approach is that it enables the large amount of available uniaxial fatigue test data to be applied to multiaxial situations. The stress-based theories ( $S-N$ ) are usually confined to the HCF regime and strain-based ones ( $\varepsilon-N$ ) to the LCF where plasticity becomes increasingly important.

The maximum principal stress or strain models are analogous to the use of applied amplitudes in the uniaxial case. The amplitudes of the maximum principal, on maximum principal plane, are considered to be the appropriate moduli to describe fatigue damage. The maximum principal stresses and strains are taken to be the maximum principal stress or strain ( $\sigma_e = \sigma_1$  and  $\varepsilon_e = \varepsilon_1$ ). The main benefit of this approach is its simplicity; however, its main difficulty is that no account of the other two principals, namely,  $\sigma_2$ ,  $\sigma_3$  and  $\varepsilon_2$ ,  $\varepsilon_3$ , is taken into consideration. The direction of the maximum principal is also assumed to be fixed.

It has been shown over the past 20 years that principal stresses/strains should only be used for fatigue analysis of 'brittle' metals, for example cast irons and some very high strength steels. A fatigue analysis using principal stresses/strains tends to give very unsafe fatigue life predictions for more ductile metals including most commonly-used steels and aluminum alloys [100].

In the maximum shear stress and strain approach, equivalent stresses or strains are taken to be the maximum shear components, respectively. This is an extension to the Tresca yield theory and assumes that multiaxial shear stress or strain amplitude will correlate with the shear stress or strain amplitudes under uniaxial tension. The required moduli for the Tresca formulation are given in Equations (2.22) and (2.23)

$$\tau_e = \frac{|\sigma_1 - \sigma_2|}{2} \quad (2.22)$$

$$\frac{\gamma_e}{2} = \frac{|\varepsilon_1 - \varepsilon_2|}{2} \quad (2.23)$$

This model is a little more complicated to apply than the maximum principal stress approach. However, it does take into account the magnitude of the minimum principal stress or strain and also accumulates damage on the plane of maximum shear.

The von Mises' effective strain (or stress) may be thought of as the root-mean square of the maximum principal strain (or stress) normalised to uniaxial loading conditions.

$$\sigma_e = \sqrt{[(\sigma_1 - \sigma_2)^2 + (\sigma_2 - \sigma_3)^2 + (\sigma_3 - \sigma_1)^2]}/\sqrt{2} \quad (2.24)$$

$$\varepsilon_e = C_m \cdot \sqrt{[(\varepsilon_1 - \varepsilon_2)^2 + (\varepsilon_2 - \varepsilon_3)^2 + (\varepsilon_3 - \varepsilon_1)^2]} \quad (2.25)$$

In the Equation (2.25),  $C_m$  is a constant related to the specific material.

As opposed to the maximum principal and shear models, the von Mises' model does take into account the influence of the median principal. The effective von Mises' stresses and strains are scalar quantities and offer no information on the physical damage observed during the fatigue process.

A major problem with the practical application of the von Mises criteria is that the von Mises stress or strain is always positive, even for negative values of stress or strain, and so rain-flow cycle counting cannot be applied directly. Some approximations have been proposed, such as to assign the sign of the largest stress or strain to the von Mises stress or strain, or alternatively to assign the sign of the hydrostatic stress or strain to the von Mises stress or strain. These are termed 'signed von Mises' criteria. The different methods of determining the sign can give significantly different life estimates. The von Mises criteria correlate poorly with test data, particularly for biaxial stresses when the two in-plane principal stresses change their orientation during the fatigue loading [99].

#### **2.3.4.2. Fatigue Life Prediction in Complex Multiaxial Stress/Strain Conditions**

This topic is still under investigation by numerous researchers. Many specific cases of complex multiaxial stresses have been analyzed but no overall design approach applicable to all situations has yet been developed [101].

Nishihara and Kawamoto [102] found that the fatigue strengths of two steels, a cast iron, and an aluminum alloy tested under complex multiaxial stress were not less than their in-phase fatigue strengths at any phase angle. For the common biaxial stress case of combined bending and torsion, such as occurs in shafts, several approaches have been proposed [101]. One of these, called SEQA, will be introduced. SEQA is an equivalent or effective stress, which combines the effects of normal and shear stresses and the phase relationship between them into an effective

stress value which can be compared to a ductile material's fatigue and static strength on a modified-Goodman diagram. It is calculated from

$$SEQA = \frac{\sigma_b}{\sqrt{2}} \cdot \sqrt{1 + \frac{3}{4} \cdot Q^2 + \sqrt{1 + \frac{3}{2} \cdot Q^2 \cdot \cos(2 \cdot \phi) + \frac{9}{16} \cdot Q^4}} \quad (2.26)$$

In which,  $\sigma_b$  is bending stress amplitude including any stress concentration effects,  $Q$  equals to  $(2 \cdot (\tau_i/\sigma))$ ,  $\tau_i$  is torsional stress amplitude including any stress concentration effects, and  $\phi$  is phase angle between bending and torsion. The SEQA stress can be computed for both mean and alternating components of stress.

Obviously, the fatigue strength predicted using the SEQA approach is conservative and is not accurate if the sources of the multiple loads are decoupled and have a random or unknown time-phase relationship.

#### 2.3.4.3. Critical Plane Approach

Fatigue cracks normally initiate on planes of maximum shear and grow initially in a shear-dominated mode. Subsequently, crack growth is perpendicular to the direction of the maximum principal stress/strain. In the critical plane approach, in addition to the importance of the maximum shear, the stress and strain normal to this plane also have been recognized to strongly influence the development of fatigue cracks.

The normal stress/strain is calculated on multiple planes. The critical plane is the plane with the most predicted fatigue damage. The planes on which the normal stress/strain is determined have normals that lie in the plane of the physical surface, i.e., in the x-y plane of the 2-D stress/strain results coordinate system. The orientation of each plane is defined by the angle  $\varphi$  made with the local x-axis.

The normal stress/strain on each plane is calculated from

$$\sigma_\varphi = \frac{\sigma_{xx} + \sigma_{yy}}{2} + \frac{\sigma_{xx} - \sigma_{yy}}{2} \cdot \cos 2\varphi + \sigma_{xy} \cdot \sin 2\varphi \quad (2.27)$$

$$\varepsilon_\varphi = \frac{\varepsilon_{xx} + \varepsilon_{yy}}{2} + \frac{\varepsilon_{xx} - \varepsilon_{yy}}{2} \cdot \cos 2\varphi + \varepsilon_{xy} \cdot \sin 2\varphi \quad (2.28)$$

$\varphi$  can take the values 0, 10, 20, 30, ... 170 degrees.

Within stress-life approach, the maximum allowable shear stress amplitude ( $\tau_a$ ) was formulated by McDiarmid [103] in the following equation.

$$\frac{\tau_a}{t_{A,B}} + \frac{\sigma_{n,max}}{2 \cdot S_{ut}} = 1 \quad (2.29)$$

The reversed shear fatigue strength,  $t_A$  or  $t_B$ , is used depending on whether case A or case B crack exists. In case A, cracks grow along the surface; in case B, cracks grow into the surface. The variable  $\sigma_{n,max}$  is the maximum normal stress on the critical plane of maximum shear stress amplitude ( $\tau_a$ ).  $S_{ut}$  is the tensile strength of the material. If  $\varepsilon_{n,max} = 0$ , then  $\tau_a = t_{A,B}$ , the maximum allowable shear stress amplitude is equal to the reversed shear fatigue strength.

In the stage of product design, the above equation can be used to calculate the fatigue factor of safety by multiplying the left side of the equation with the safety factor  $n_{cp}$ , the above equation can be transformed to:

$$n_{cp} = \frac{2S_{ut} \cdot t_{A,B}}{\tau_a \cdot 2S_{ut} + \sigma_{n,max} \cdot t_{A,B}} \quad (2.30)$$

In fatigue life prediction, the McDiarmid equation can be used to calculate the equivalent shear stress  $t_{eq}$  using critical plane approach and then the uniaxial shear stress fatigue life data can be used.

$$\frac{\tau_a}{t_{eq}} + \frac{\sigma_{n,max}}{2 \cdot S_{ut}} = 1 \quad (2.31)$$

Within strain-life approach, Brown and Miller [104] presented a two parameter formulation as:

$$\gamma_{max} = f(\varepsilon_n) \quad (2.32)$$

Where  $\gamma_{max}$  is the maximum shear strain and  $\varepsilon_n$  is the strain normal to  $\gamma_{max}$ .

The maximum shear strain is the primary force in crack initiation and the strain normal to the plane of the maximum shear is a modifying factor. This approach is similar to the maximum shear stress and strain approach (Tresca), but with normal strain component added. With these ideas, the strain-life equation becomes:

$$\gamma_{max}^a + \varepsilon_n^a = 1.65 \frac{\sigma'_f(2N_f)^b}{E} + 1.75 \varepsilon'_f(2N_f)^c \quad (2.33)$$

In which,  $\gamma_{max}^a$  is the maximum shear strain amplitude and  $\varepsilon_n^a$  is the strain amplitude normal to the plane of maximum shear.

In situations of non-proportional loading, the direction of the principal stresses or strains can vary with time. The plane of maximum shear has a fixed relationship, to the plane on which the maximum principals are located and so the plane of maximum shear itself will rotate. Under

these circumstances, even the Miller Brown damage parameter will fail to account for this effect. The net result of this is an averaging or smoothing out of the damage estimate and almost certainly an underestimate of the actual damage.

A strategy for accounting for these effects is to calculate fatigue damage across a range of orientations of the shear plane in an effort to identify the most damaging [87]. The effect of the applied loading on a particular plane is determined by a tensor rotation of the stresses and strains to that plane and estimating the damage that accumulates on it. This process is continued until a number of planes have been analyzed, and the most damaging plane identified. Typically, under conditions of plane stress, possibly 18 calculations, in increments of 10 degrees, would need to be made. For tri-axial stress states, which occur on surfaces under pressure (e.g. bearings) or inside of components, many more planes have to be considered. The normal vectors of all the planes form a hemisphere (e.g. about 200 planes with about 10 degree angular separation). With the advancement of computer technology, this method is becoming more effective in computer simulation.

### 2.3.5. Accumulated Fatigue Assessment

In practice, a mechanical part is often exposed to a complex, random, sequence of loads, large and small. When the cyclic load level varies during the fatigue process, a cumulative damage model is often hypothesized. According to Miner's rule [87], a linear damage concept can be used to assess the fatigue life of the part. Miner's rule states that cycles act together linearly to cause "damage" and consume the fatigue life. Failure occurs when damage sums to 1 (load sequence effects are not accounted for). Mathematically, it can be expressed as follows: Fatigue failure occurs when

$$\sum_{i=1}^m \frac{n_i}{N_{fi}} \geq 1 \quad (2.34)$$

Where "m" represents the number of different stress/strain levels in the complex load,  $n_i$  represents the cycles at stress  $\sigma_i$  or strain  $\varepsilon_i$ , and  $N_{fi}$  represents the number of cycles to failure under stress  $\sigma_i$  or strain  $\varepsilon_i$  only. The term  $\frac{n_i}{N_{fi}}$  can be assumed as the fractional damage at stress  $\sigma_i$  or strain  $\varepsilon_i$ .

In a practical situation, the sequence of the different levels of load is random. In order to count the cycles in different stress/strain levels for assessing fatigue life using Miner's rule, the rain-flow counting method is used to find the fatigue cycles in the stress/strain history.



## 2.4. Wheel Fatigue Testing Standards

Great efforts were taken to find testing standards associated with multi-piece wheel design and durability analyses in the open literature. Unfortunately only one manuscript by Vijayan et al. [14] was found which deals with the fatigue analysis of a three-piece wheel, whose structure is similar to that as shown in Figure 2.2. In the three-piece wheel analysis, the testing method used (SAE J1992) is for military bolted two-piece wheels, not for three-piece wheels with a lock ring. As stated in Section 1.6, this analysis has some limitations without including a tire in the model and the consideration of geometry and material degradation. To the best of the author's knowledge, no other testing standards or manuscripts relevant to this topic have been published.

There are a limited number of fatigue testing standards and abundant manuscripts available in the open literature about passenger car and truck wheels (single-piece). As stated in Section 2.1, OTR tires and on-the-road tires have similar structures and materials and multi-piece and single-piece wheels have a common fundamental structure. Therefore, the methods used to assess the fatigue life of single piece wheel can be useful for the fatigue life estimate of multi-piece wheels.

In automotive engineering, wheels are one of the most critical components and their function is of vital importance in human safety. In the fatigue evaluation of a wheel design, the commonly accepted procedure for wheel manufacturers is to pass two durability tests, namely the cornering fatigue test and the radial fatigue test [80]. There are several Society of Automotive Engineers (SAE) testing standards for different kinds of on-the-road wheels. SAE J328 [81] provides minimum performance requirements and procedures for fatigue testing of wheels intended for normal highway use and temporary use on passenger cars, light trucks, and multi-purpose vehicles. SAE 267 [82] provides procedures and minimum performances required for fatigue testing of wheels and demountable wheels intended for normal highway use on heavy trucks, buses, truck-trailers and multipurpose vehicles. SAE J1992 [83] provides laboratory procedures for fatigue testing certain production disc wheels, demountable rims, and bolt-together divided wheels intended for normal highway use on military trucks, buses, truck-trailers and multi-purposed passenger vehicles. Each standard provides two fatigue testing procedures, namely, cornering and radial fatigue testing. These three testing standards provide almost identical cornering and radial testing procedures.

### 2.4.1. Dynamic Cornering Fatigue Testing

The purpose of the dynamic cornering fatigue test is to simulate the loading of the wheel during cornering on the road. The relevant forces acting on the wheel are a combination of the vertical load and lateral force developed between the tire and the ground. The two components of loading result in a rotating bending moment on the hub of the wheel. In the dynamic cornering fatigue test, the test wheel is clamped securely on the test table as shown in Figure 2.27 [81]. The wheel rotates with the test table. A rigid shaft is mounted at the centre of the wheel and a constant static load parallel to the plane of the wheel is applied at the tip of the shaft. Wheel nuts are torqued to  $115 \text{ N}\cdot\text{m} \pm 7 \text{ N}\cdot\text{m}$  ( $85 \text{ ft}\cdot\text{lb} \pm 5 \text{ ft}\cdot\text{lb}$ ) or as specified by the vehicle or wheel manufacturer. The rotation of the table imparts a constant rotating bending moment to the wheel. The test loads are calculated based upon Equation (2.35).

$$\text{Testload} = \frac{M}{\text{Moment arm}} = \frac{L \cdot K_f \cdot (\mu \cdot slr + d)}{\text{Moment arm}} \quad (2.35)$$

In the equation,  $M \text{ (N}\cdot\text{m)}$  is the bending moment generated during cornering,  $\text{Moment arm}$  is greater than 762 mm,  $L \text{ (N)}$  is load rating of the wheel as specified by the wheel manufacturer,  $K_f$  is accelerated test factor, which ranges from 1.1 ~ 1.75,  $\mu$  (assumed to be 0.7) is the coefficient of friction developed between tire and road,  $slr \text{ (mm)}$  is the largest static loaded radius of the tires to be used on the wheel as specified by the current Tire and Rim Association Yearbook or the vehicle/wheel manufacturer,  $d \text{ (mm)}$  is inset or outset (positive for inset, negative for outset) of the wheel.

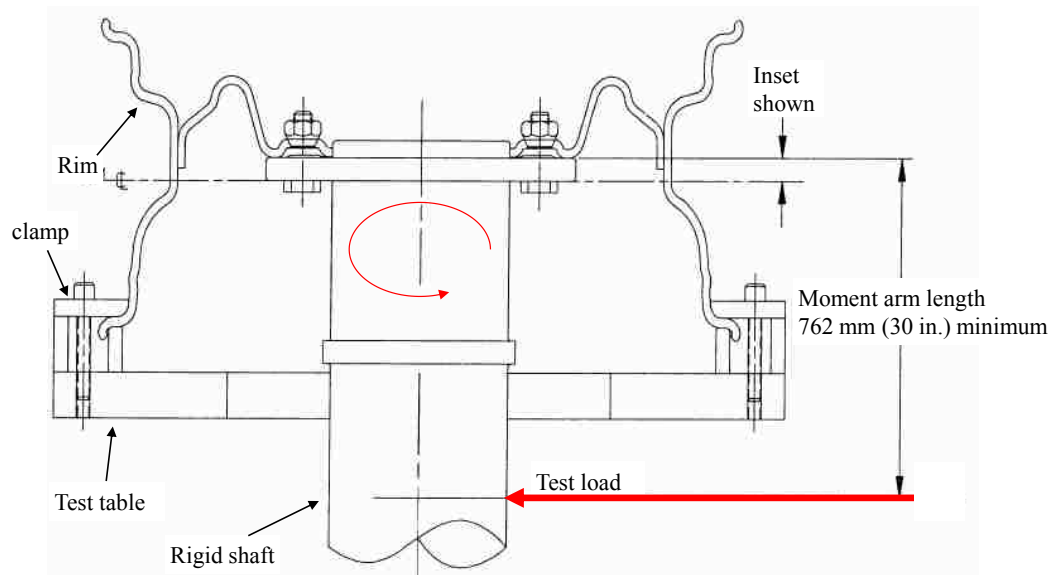


Figure 2.27 Dynamic cornering fatigue testing set-up [81]. (Reprinted with permission from SAE J328 Feb 2005 © 2005SAE International. Further use or distribution is not permitted without permission from SAE.)

The wheel must complete the minimum number of test cycles prior to test termination. The test shall be terminated by any one or more of the following, (1) the inability of the wheel to sustain load, (2) a visually detected fatigue crack penetrating through a section, and (3) a broken wheel clamp bolt separated from the wheel assembly. Broken studs or other parts of the test fixture do not justify test termination but may result in damage to the wheel and test invalidation.

For passenger car and light weight truck wheels, the minimum number of cycles is 18,000 for ferrous wheels and 50,000 for aluminum wheels. For heavy truck wheels, and bus and military bolt together wheels, the minimum number of cycles are dependent on the materials of the wheels (ferrous or aluminum), wheel diameters and inset (outset) dimensions, with minimum number of cycles in the range of 18,000 and 250,000.

#### 2.4.2. Dynamic Radial Fatigue Testing

Dynamic radial fatigue testing is meant to simulate the straight driving condition and evaluate the overall wheel performance. Figure 2.28 [81] illustrates the dynamic radial fatigue testing apparatus. The test machine has a driven rotating drum which presents a smooth surface wider than the loaded test tire section width. A constant load is imparted to the test wheel and tire, normal to the surface of the drum, and in line radially with the centre of the test wheel and drum. The rotational axis of the test wheel and drum are parallel. The testing procedures are similar to the dynamic cornering fatigue testing.

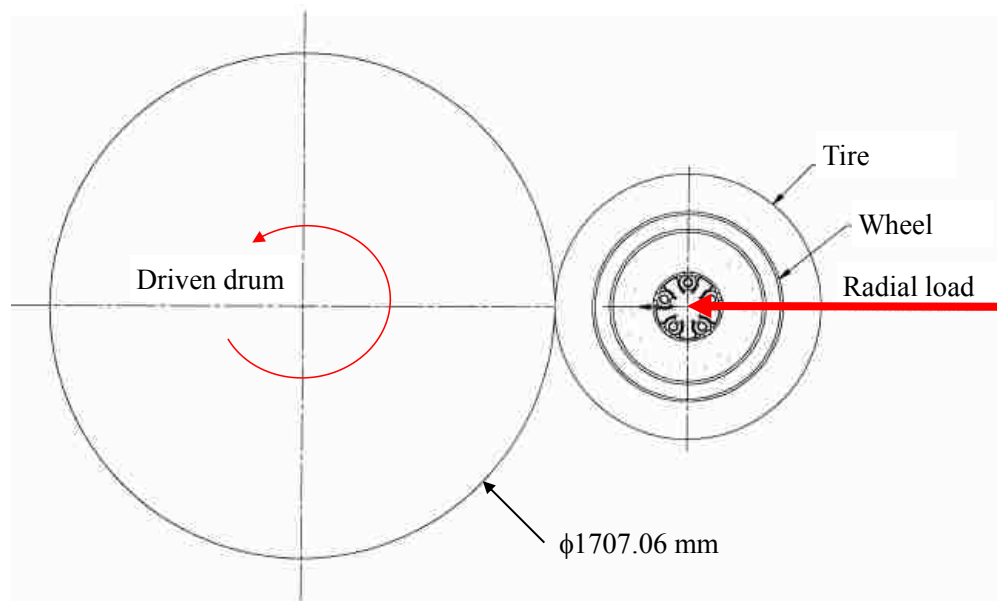


Figure 2.28 Dynamic radial fatigue testing set-up. [81] (Reprinted with permission from SAE J328 Feb 2005 © 2005SAE International. Further use or distribution is not permitted without permission from SAE.)

The radial load ( $R$ ) to be applied to the wheel is determined using Equation (2.36)

$$R = K_f \cdot L \quad (2.36)$$

The parameters in the equation have the same meanings as in Equation (2.35).

## 2.5. FE-based Wheel Fatigue Testing

Fatigue analysis can be determined using field testing, laboratory testing and/or analytical methods. Traditional methods for fatigue analysis are based on field testing and/or laboratory testing, while analytical approaches have been increasingly integrated over the last decade due to the advancement of computer technology. On-the-road wheel fatigue life can be assessed using the aforementioned SAE testing standards within the laboratory. Traditionally, in the new wheel development stage, experimental testing can only be conducted when prototype wheels are available. If the performance does not meet the cycle of life requirements, the wheel design will be modified and new prototype wheels be fabricated and the fatigue testing repeated. This repetitive process continues until the wheel meets the fatigue life requirements before mass production. This process is very costly and time-consuming. Analytical fatigue life analysis is limited to simply structure under simply loading conditions due to the massive, prohibitive calculations required.

With the advancement of computer technology, computer-aided engineering (CAE) is widely used in the early stage of product development, testing, and manufacturing. The use of calculations and simulations is a key feature of the modern design process. Several properties such as strength, stiffness, durability, handling, ride comfort and crash resistance can today be numerically analyzed with varying levels of accuracy. Development time can be shortened by ensuring that some, or all, of these properties fulfill established requirements even before the first prototype is built.

To reduce the cost and time of product development, iterations must be reduced at the physical prototype stage and a reliable methodology to predict the durability parameters, such as fatigue life and fatigue factors of safety, is critical in the early virtual prototype stage. The most appropriate product development process is to test as few prototypes as possible, preferably only one of any finalized model. The FE-based fatigue analyses, feeding stress/strain data from FE analysis to fatigue prediction software to estimate fatigue parameters, are widely used in the automotive industry. Calculations based on fatigue theory and accurate loading histories permit structures and components to be optimized for durability without the need for expensive and time-consuming testing of series of prototypes. Thus, designs can be obtained that are less

conservative (i.e. better optimized) than those based on traditional criteria, such as maximum load or stress for a series of standard load cases.

### **2.5.1. FE-based Wheel Dynamic Cornering Fatigue Testing**

Wang et al. [106] simulated the dynamic cornering fatigue test of a steel passenger car disc wheel, according to SAE J328. A linear transient dynamic FE analysis was conducted to obtain the stress/strain data and the local strain approach was used to predict fatigue life of the wheel. HyperMesh was used to create the FE model and the linear solver OptiStruct was used to solve the FE model. In the FE model, the wheel was mounted to a rotating table by clamping its rim and a shaft was attached to the center of the wheel, and a constant normal force was applied to the tip of the shaft in order to create a rotatory moment. FE results showed that the critical (high stress) areas were located around the cooling (ventilation) holes and the centre of the disc. The FE model was validated with experimental measurements of strains at five locations using five 45° strain rosettes. The strain history of the element was applied to predict the fatigue life of the critical element with local strain approach, which was quite close to the test results.

Following SAE J328 protocol, Shang et al. [107] assessed the safety factors for a newly designed forged magnesium wheel with ten spokes, using FE analysis. The wheel model was developed using the commercial software HyperMesh and was solved using the explicit FE code LS-DYNA. In their study, a fatigue analysis post-processor, developed in the programming language Java was used to calculate the safety factors of each element. Experimental tests found that the location of the crack initiation on the spoke was identical to the location of the element with the minimum safety factor calculated numerically. A design modification, namely, increasing the thickness of the spokes, was incorporated and both the experiment tests and numerical simulations on the modified wheel passed the SAE J328 fatigue test requirements.

Based on SAE J1992, Vijayan et al. [5] investigated the fatigue factors of safety of a three-piece mining wheel. A FE model of the three-piece wheel was developed and validated under static bending loading conditions by comparing strain values between experiment testing and FE simulation at various locations on the rim. The model predicted strains, for the majority of locations, within 15% error in comparison to experimental results. Numerical tests of the SAE J1992 fatigue loading condition using LS-DYNA were performed on the validated model by applying a rotatory bending force of 22 kN. Stresses predicted from these simulations were used to calculate the element-based fatigue factor of safety utilizing four different methods, namely von Mises (Goodman), Sines (Goodman), damage mechanics, and critical plane approaches. The

least fatigue factors of safety estimated were 1.9140, 1.9345, 1.1570 and 1.8770, respectively. These fatigue factors of safety imply that an infinite life of the mining wheel existed. The experimental and numerical tests both showed that the maximum stresses/strains were located at the lock ring groove region, correspondingly, the least fatigue factors of safety were also located in the same region. The infinite fatigue life prediction deviated from the in-field observation of the limited fatigue life of the three-piece wheel. The difference was attributed to the difference in loading conditions between SAE J1922 testing protocol and in-field use of the three-piece wheel, specifically, the loading condition specified in SAE J1992 underestimates the severity of the loading condition experienced by the three-piece wheel in normal service. The lack of wear, material degradation due to corrosion, and localized damage of the three-piece wheel in numerical simulation efforts were hypothesized to contribute towards the limited fatigue life observed in service condition.

### **2.5.2. FE-based Wheel Dynamic Radial Fatigue Testing**

Topac et al. [108] investigated the fatigue failure on the cooling holes of a newly designed heavy commercial vehicle steel wheel under dynamic radial fatigue according to SAE J267 standards. The stress/strain analysis was performed through the commercial FE software code ANSYS. In the FE model, the tire was not included and the radial forces were applied statically at the tire bead-rim contact region. Tire pressure was uniformly applied along the outer circumference of the wheel flange. Any effect of centrifugal force was ignored. The material properties of the wheel were determined through coupon tensile tests and hardness tests. To predict the minimum number of wheel turns before fatigue crack initiation, the stress life approach was utilized. The estimated *S-N* diagram was constructed using the ultimate tensile strength of the processed wheel material which was determined through hardness tests. The effects of factors such as surface roughness, size and stress concentration were also taken into account using endurance-limit modifying factors. The Gerber approach was used to predict the fatigue life of the wheel. The results obtained correspond to the results of radial fatigue tests. To obtain an extended fatigue life, a design enhancement solution, including both increasing the local thickness and the cross-sectional radius at the critical regions was applied. Stress analyses showed that by using this solution, it was possible to decrease the equivalent von Mises stress at these regions.

Firat et al. [109] simulated dynamic radial fatigue testing according to SAE J328 on a disc-type truck wheel. In their analysis, a linear elastic wheel FE model was created and analyzed using ANSYS. In the model, the tire was not included and spring elements were used to simulate

vertical and horizontal loads from the tire. Centrifugal forces acting on the wheel were modeled with distributed body forces at a constant rotational speed. The experimental fatigue test cycles and failure locations were predicted using effective strain, Smith–Watson–Topper and Fatemi–Socie parameters using computed stress–strain histories. Nodal points on the cooling hole and the rim-well welding were identified as the fatigue critical locations. Favorable correlations were obtained with the critical plane parameters involving mean stress correction terms when compared with strain gauges. Fatigue test cycles predicted using Fatemi–Socie damage parameter was observed to be conservative and considerably close to actual test cycles for all camber angles.

### **2.5.3. FE-Based Fatigue Testing on Other Vehicle Structures**

Many other investigations in the open literature have considered structural fatigue testing, which are very useful for this multi-piece wheel fatigue life analyses.

In Llano-Vizcaya et al.'s [110] work, multiaxial fatigue and failure of helical compression springs were investigated. A linear stress analysis was carried out in the FE code ANSYS and the stresses on the spring surface were transferred to the nCode module DesignLife. A local strain life approach was used to assess the fatigue life. The strain life material properties were estimated using monotonic uniaxial tensile strength as shown in Table 2.3 of Section 2.3.3.4. To deal with multiaxial loading fatigue, the critical plane approach was used to conduct fatigue life analysis. Experimental fatigue findings were compared with multiaxial fatigue criteria predictions using the approaches of Fatemi–Socie, Wang–Brown, and the Coffin–Manson method based on shear deformation. The Fatemi–Socie critical plane approach predicted a good estimate of the fatigue life. The Wang–Brown criterion overestimated spring fatigue life, the Coffin–Manson model provided conservative results. It was noted that the universal slopes method to estimate strain-life properties from the monotonic uniaxial tension test, gave better predictions of the spring fatigue life than the modified universal slopes method.

Conle and Chu [111] introduced the development of fatigue analysis and the local stress–strain approach in complex vehicular structures in the last 20 years. The strain-life fatigue analysis has achieved the status of industry standard in automotive, truck and earth moving industries. Although the fundamental concepts of the method are quite simple, the recent advancement of massive computerization technology has made it viable by creating fatigue simulation software. Linear elastic FE models are widely used to obtain stress/strain data for fatigue life estimates. The multiaxial Neuber type of plasticity correction method must be used to translate the elastic local stress estimates into approximations that are corrected for elastic/plastic

stress–strain behaviour. Conle and Chu found that the traditional uniaxial parameters and the equivalent stress/strain type parameters do not work well under multiaxial conditions for which an all-encompassing damage algorithm must search for the most damaging plane at the critical location (termed “the critical plane approach”) and utilize both normal stress/strain and shear stress/strain on the critical plane.



## Chapter 3. Scope of Research

The prime goal of this study is to improve the integrity of multi-piece wheel for safety. The fatigue failure of wheel components is a major cause of the breakdown of wheel integrity. To extend fatigue life, numerical computer simulations, assisted with experimental testing, were used to improve multi-piece wheel design.

The literature in the aforementioned wheel fatigue tests show that the road wheels fail mostly in the spoke region and bolt connection region [106-109]. The critical stress regions on a disc type wheel are disc-rim weld, cooling hole, and lug bolt contact area [112]. Based on the incident report analyses, the fatigue failure region on the multi-piece wheel with a lock ring is mainly focused on the gutter (lock ring groove). Due to the differences between on-the-road wheels (single-piece) and multi-piece OTR wheels in terms of structures, applications, and loading conditions, the SAE testing protocols used to assess the fatigue parameters of on-the-road wheels are not applicable to assess the fatigue behavior of multi-piece wheels.

### 3.1. Testing Methods Used in Multi-piece Wheel Fatigue Assessment

Due to the large structure and high tire pressure of multi-piece wheel assemblies, experimental fatigue testing of OTR wheels is costly and safety prohibitive. Computer simulations are used to assess stresses and fatigue parameters of wheel components. For the simulated loading conditions to be realistic and representative to service conditions, in-field experimental tests are needed. The experiment testing serves two purposes, namely, providing loading data for numerical simulations and FE model validations.

#### 3.1.1. Experimental Testing

In the early stage of this research, the research team made trips to several mine sites, a mine equipment provider, two OTR wheel and tire manufacturers and suppliers in Northern Ontario to educate the author on multi-piece wheels. In June 2011, static and quasi-static tire tests were conducted at MusselWhite underground mine and above ground mechanic shops. The static loading tests were conducted on a R2900 LHD vehicle through weighing the vehicle and measuring tire deflections (Section 4.1.1) in a variety of loading conditions. The quasi-static tests were conducted on the same vehicle to obtain tire deflection characteristics under severe loading conditions. The tested severe loading conditions were used to validate tire models and to assess OTR wheels' strength and fatigue performance.

To validate the wheel model, laboratory rim base tests were conducted under static loading conditions. Laser displacement measuring devices, force measuring devices, and strain gauges were used to obtain the deformation information of the rim base. Detailed descriptions of the tire and rim base experimental tests are in the following chapter.

### **3.1.2. The Finite Element (FE) Method**

In the previous cited works conducting fatigue assessment, FE modeling was used for all cases. As pointed out by Conle and Chu [111], plastic modeling gives poor quality of stress/strain assessment when faced with reversals in loading direction. In this research, a linear elastic model was created to simulate the static and quasi-static tests for fatigue life analysis. Using linear elastic FEA to obtain stress/strain data is a common acceptable practice for durability study. During fatigue life analyses, stresses/strains were corrected to elastic-plastic stresses/strains using the Hoffmann-Seeger method. To simulate BS bank pull-out tests, an elastic-plastic material model was used to model large deformation, non-cyclic loading condition, which was detailed in Section 8.1.2.1.

In this study, a unique OTR tire was modelled and validated through experimental testing. The methodology used for the tire modelling was published in an international journal. This OTR tire modelling is the first to be found in open literature.

### **3.1.3. Fatigue Life Assessment Methods**

The *S-N* approach is a traditional and well developed and accepted method to conduct fatigue estimates. The *S-N* fatigue material properties can be easily obtained by conducting fatigue testing. Strain life is more suitable to simulate crack initiation and has become greatly incorporated in practice. It accounts for material plasticity and usually gives more appropriate (less conservative) results. The multi-piece wheels are safety critical components and it is important to detect fatigue cracks before failures. Therefore in this study, both methods were used to estimate fatigue lives of multi-piece wheel components. The *S-N* responses were generated by experimental fatigue testing of the extracted samples from multi-piece wheel components. Due to the high investment to perform tests to get the strain-life material parameters, the strain life material properties were estimated using monotonic ultimate tensile stress according to Table 2.3 [96] of Section 2.3.3.4.

In both fatigue assessment approaches, the critical plane fatigue failure theory was used to account for multiaxial loading conditions. Given the past practical implementation of

durability analyses, this is the most accurate approach to simulate fatigue life, although it demands more computational efforts.

### **3.2. Innovative Designs**

Based on the stress/strain and fatigue life assessments, innovative designs were proposed and tested numerically. The primary criterion to assess the efficiency of the new designs is fatigue performance. By comparing the fatigue lives between the new and original designs, the durability enhancement of proposed new designs were investigated. In the new designs, installation convenience and fail-safe mechanisms were considered to ensure the viability of the new designs.

In the open literature, no information relevant to OTR wheel modifications was found. In this research, two innovative OTR wheel design modifications were proposed and their durability performances were investigated using numerical methods. The proposed threaded-connection four-piece wheel and two-piece wheel show significant durability improvement.

### **3.3. Computer Software Used for This Research**

The software used for this FE-based fatigue assessment was HyperMesh [113], LS-DYNA [114], LS-PrePost [115], and nCode DesignLife [87].

HyperMesh is one module inside HyperWorks, created by Altair Incorporated. HyperMesh is a high-performance FE pre-processor to generate FE models, starting from import of CAD geometry to exporting a FE input file. HyperMesh enables engineers to generate high quality meshes with maximum accuracy in the shortest time possible. A complete set of geometry editing tools helps to efficiently prepare CAD models for the meshing process. Additionally, meshing algorithms for shell and solid elements provide full discretization control.

LS-DYNA is an advanced general-purpose multi-physics simulation software package developed by the Livermore Software Technology Corporation (LSTC). While the package continues to contain more and more possibilities for the calculation of many complex real world problems, its origins and core-competency lie in highly nonlinear transient FE analysis using explicit time integration. The code can model contacts among structures with great accuracy and simulate large deformation in transient states. LS-DYNA possesses many analysis capabilities, including nonlinear dynamics, quasi-static simulations, linear statics, and many more. LS-DYNA is widely used by the automotive industry to analyze vehicle designs.

LS-PrePost is an advanced pre- and post-processor designed specifically for LS-DYNA. Here it is mainly used for post-processing simulation results from LS-DYNA. It was used to create simulation animation files, contours of various parameters (displacement, stress, and strain), curve plotting, and to output simulation data.

nCode DesignLife provides fatigue life prediction from FE results even before a prototype product is available. It directly supports many FEA result data including LS-DYNA. It has a wide range of fatigue analysis capabilities including stress-life, strain-life, multiaxial, weld analysis, and more. nCode DesignLife was used to assess the fatigue lives of the multi-piece wheels in this research. A brief introduction to the nCode DesignLife is explained in Appendix A.

Other software was used for data acquisition and analysis. During experimental testing, LabVIEW was used for data acquisition and synchronization of transducer data to high speed images. Sigmaplot was used to generate high quality plots. ProAnalyst was used to track the motion of the tires and wheels in the video footage recorded using high speed camera during the experimental tests. Using ProAnalyst, translational and angular displacements and velocities at specific points were tracked and quantified.

## Chapter 4. Tire and Wheel Experimental Testing

The purposes of the experimental tests are to understand the characteristics of the deflection versus loading of the multi-piece wheel/tire assemblies, to provide realistic loading/boundary data for the FE models of the tire/wheel assemblies for fatigue life assessments, and to validate the FE models. The scale tests and quasi-static tests were conducted at a mine site. The laboratory rim base tests were performed at the University of Windsor.

### 4.1. Experimental Testing of a Five-piece Wheel/Tire Assembly

Given the complex nature and physical dimensions of OTR tire structures, great challenges arise in accurately modelling and predicting their dynamic performance under load and in-use, when applying computer-aided engineering (CAE) methods. One significant challenge in OTR tire modelling is the lack of experimental data pertinent for model validation. A literature review on the topic of OTR tires reveals that there is no extensive information available regarding the load-deflection behaviour of OTR tires. Fortunately, the tire manufacturer Goodyear OTR does provide limited load-deflection tire data, however, the data is specified for only a single loading condition. Therefore, OTR tire testing is required to obtain high fidelity in-field data, encompassing the general and localized vertical and side-wall deformation of the OTR tire as a function of load, for FE model validation purposes.

OTR tire modelling and experimentation has been primarily restricted to tire manufacturers and this kind of information is not available in the public domain. The methodologies used to study on-the-road tires are equally applicable to study OTR tires since the structures and basic materials are similar between OTR tires and on-the-road tires.

In the study of Burke et al. [116], a model of a 195/65R15 car tire was created using Nastran to investigate the static tire/road interaction. To validate the predictive capabilities of the model, a downward force was applied to the wheel hub using an electro/hydraulic actuator and displacement as a function of load was recorded using the actuator controller and an externally mounted dial test indicator. Testing was carried out over a range of loads and inflation pressures for comprehensive validation of the numerical tire model.

Neves et al. [117] created a model of a 175/65R 14 82T tire used on passenger vehicles. The purpose of their model was to investigate tire performance under sudden impact loadings. Model validation was completed by performing full wheel/tire impact tests. The velocity of the indenter was measured using a laser Doppler Polytec OFV-323, which was subsequently time

differentiated to obtain acceleration and impact force data. Other instrumentation included the OFV-3020 laser capturing system and a high-speed camera which recorded the impact events at a rate of 10,000 frames per second. Indenter mass and tire inflation pressure were varied throughout experimentation for a greater range of testing conditions.

In the study of Nguyen et al. [118], the behaviour of aircraft tires undergoing indentation due to runway debris was recorded using digital image correlation (DIC) techniques. In the study, the load-indentation behaviour of the tires was obtained for a C-130 Hercules nose wheel and a Goodyear flight custom 6.50-10 tire. The wheel-tire assembly was mounted in an Instron TT-DM testing machine fitted with a 5 kN load cell, to track indentation loads. In parallel, an Aramis DIC system was setup using two 1.3 megapixel cameras for acquiring strain measurements. Each tire was coloured with a stochastic pattern of white dots for DIC calibration and tracking. Cameras were maintained at a safe operating distance away from the testing apparatus, which prevented data acquisition within the immediate proximity of the indenter, in the tire grooves and close to the tire shoulders. Testing was performed for a series of tire pressures with results demonstrating a good correlation between tire inflation pressure and released indentation energy.

In the aforementioned literatures, experimental tests were conducted to help build and validate numerical FE models. Once the FE models were validated, they were further used to investigate tire performance under other scenarios. In this multi-piece wheel research, similar procedures were utilized.

#### **4.1.1. Experimental Procedure**

Detailed mechanical characteristics of off-the-road tires used on heavy mining vehicles are unavailable in open literature, with little information available from manufacturers. Since the tire of interest in this study is of the Goodyear brand, the Goodyear Off-The-Road Tire Engineering Data Book [28] is referenced for comparison and validation purposes and discussed in future sections. To gain a better understanding of tire behaviour and characteristics, a variety of measurements were taken using different approaches to excite the test vehicles. Testing on underground heavy vehicle scale was done to acquire the static load-deflection behaviour of the tire, while above-ground testing consisted of severe vehicle excitation for the purpose of obtaining the quasi-static relationship between vertical and lateral sidewall tire deflection behaviour.

#### 4.1.1.1. Testing Information

Over the course of several days, testing was conducted at a remote Canadian underground mine site where several vehicles were instrumented and tested in the summer of 2011. All test vehicles were Caterpillar brand equipment and were either load-haul-dump (LHD) scoop vehicles or an underground articulated truck. Only one wheel assembly was measured during the course of each vehicle test, with the specific machine, tire, and wheel information of interest summarized in Table 4.1. All tests on the three vehicles yielded similar tire deflection data. In this dissertation, discussion is limited to the tire/wheel assembly with the tire sized 29.5-29 since this tire/wheel assembly will be the focus for mechanical analysis for enhanced safety.

Table 4.1 Test vehicle information.

Machine	Tire Specification	Tire	Rim Specification
Caterpillar AD45B Truck (equipped with push box)	Goodyear 29.5R29 RL-5K; L-5 Type 6SCold Tire Pressure: 660 kPa	Radial	5-piece wheel NSIW Model HT2000
Caterpillar R2900G LHD Scoop	Goodyear 29.5-29 SMO; D/L-5D Type 6SCold Tire Pressure: 591 kPa	Bias	5-piece wheel; Unknown manufacturer
Caterpillar R1700G LHD Scoop	Goodyear 26.5-25 SMO; D/L-5D Type 6SCold Tire Pressure: 646 kPa	Bias	5-piece wheel; Unknown Manufacturer

#### 4.1.1.2. Tire Physical and Engineering Data

The tire under study is of bias-ply construction. Table 4.2 lists the engineering data for this tire according to the Goodyear Engineering Data Book [28]. Where applicable, the U.S. Imperial system of measurements was used as it is the base standard for tire and wheel, however, where possible, data is based on the SI system of units or presented in both. All observations are based on SI unit measurements.

Table 4.2 Tire physical data as given in Goodyear's OTR Engineering Data Book [28].

Tire Model	Inflated Overall Diameter (inch/mm)	Inflated Overall Width (inch/mm)	Static Loaded Width (inch/mm)	Static Loaded Radius (inch/mm)	Mass (kg)	Static load (kN)	Inflated Pressure		Rim Width - Flange height (inch)
							PSI	kPa	
29.5-29	78.9/2004	30.1/765	33.0/838	36.3/922	1304	230kN	91	627	25.00 - 3.5

Using the Goodyear OTR data, it is possible to calculate basic deflection characteristics. Given the above information, it is known that the unloaded Overall Diameter (OD) is 2024 mm or an approximate radius of 1012 mm, and the Static Loaded Radius (SLR) is given as 890 mm at a rated tire pressure of 648 kPa (94 psi) and 231 kN load, meaning a loaded tire should decrease in radius by 122 mm. Furthermore, change in section width can be calculated as the difference between the Loaded Section Width (LSW) and the unloaded, inflated Overall Width (OW) which yields an increase of approximately 73 mm, or a one side “bulge” of 36.5 mm. The tire deflection data are summarized in Table 4.3 below. The highlighted columns are tire vertical and lateral deflections, which will be used for comparisons with experimental tests and tire model validation.

Table 4.3 Tire deflection characteristics based on Goodyear OTR data [28].

Tire Model	Inflated, Unloaded Radius (mm)	Static Loaded Radius (mm)	Decrease of Radius (mm)	Unloaded Overall Width (mm)	Loaded Section and Growth (mm)	Increase in Section Width	Approximate Load/Vertical Deflection (kN/mm)	Approximate Load/Lateral Deflection (kN/mm)
29.5-29	1002	922	80	765	838	73	2.89	6.3

It is important to note that the tire under investigation had some levels of use and wear, as highlighted in Table 4.4. While it is possible that wear may affect tire performance to some degree, it was beyond the scope of this study to quantify such effects, and not physically possible given the limited available testing time. Furthermore, it was assumed that the wear did not significantly affect tire deformation behaviour, given the very large tire sizes.

Table 4.4 Tire wear based on mine site tire measurements.

Tire	Approx. Service Hours on Vehicle	Tread Level (Current / Original in mm)	Percent Remaining	Tire Condition
29.5-29	312	95 / 102	93%	Good

#### 4.1.1.3. Testing Apparatus

A testing methodology was developed and replicated for each vehicle to minimize measurement error. The three test vehicles represent a wide range of vehicle and wheel assembly styles, with significantly different payloads. The wheel of interest was selected based on suggestions from technical professionals and the researcher’s capacity to best capture maximum excitation, such as the rear wheels of the AD45B truck, since load input could be more easily and safely be completed through the bucket of the truck versus anywhere on the front of the vehicle. In the case of the LHD vehicles, the vehicles’ own scoops were used to create a controlled simulated loading condition with maximum excitation exerted on the front wheel assemblies.



Additionally, the testing methodology implemented accurately reflected how load would be input during vehicle operation.

All vehicles were initially prepared by setting up the required instrumentation. To prepare for aboveground quasi-static excitation testing, a National Instrumentation NI-9188 Compact DAQ (cDAQ) 8-slot ethernet chassis data acquisition system was utilized to obtain transducer data connected wirelessly to a control laptop using a D-Link DIR-655 XTREME N Gigabit router. Due to the large tire size, desire to use non-invasive measurement techniques, and limited testing time available at the mine site, observations were acquired using optical methods. Acuity AR700 series laser displacement transducers with measurement ranges of 300 mm and 100mm were used to take vertical deflection and sidewall lateral deflection measurements, respectively. The vertical measurements were obtained through use of a magnetically mounted horizontal plate, which acted as a reference point for the vertical displacement measurement. The horizontally mounted plate was attached to the hub of the wheel assembly. The sidewall lateral deflection measurements were taken as close to the centreline of the tire as possible, on the lower “bulge” of the tire sidewall, where maximum deflection was anticipated, and measured directly on the surface of the tire. These transducers were connected to the NI-9188 cDAQ chassis with a NI-9215 module. Acquisition of the displacement transducer measurements occurred at 5 kHz. Additionally, high-speed camera images were recorded to capture greater aspects of the tire deformation field. A Fastec Imaging Troubleshooter HR camera was utilized and time synchronized with the NI-9188 cDAQ data using a NI-9401 digital I/O module. Digital images, having a resolution of 640 by 480 pixels, were acquired at 125 Hz and with a shutter speed of the camera specified as 8 milliseconds. The use of industrial-grade Arri 1000W spot lights was necessary at times to ensure optimal lighting for video capture. To track tire displacements with the high speed images, careful marking of the tire with white dots, was necessary to provide reference points during image post-processing. Due to the complexity and time constraint, strain gauges were not used to measure the strains on the wheels. The tire preparation, as well as equipment setup, is shown in Figure 4.1 for the tire 29.5-29.

For each test, it took several hours for vehicle cleaning, marking the tire, and apparatus set-up. Once the preparation work was finished, it took approximately one hour to finish the test. There was no significant environmental change during the tests (such as temperature and wind conditions). The temperature of the testing environment was approximately 20 °C to 25°C.

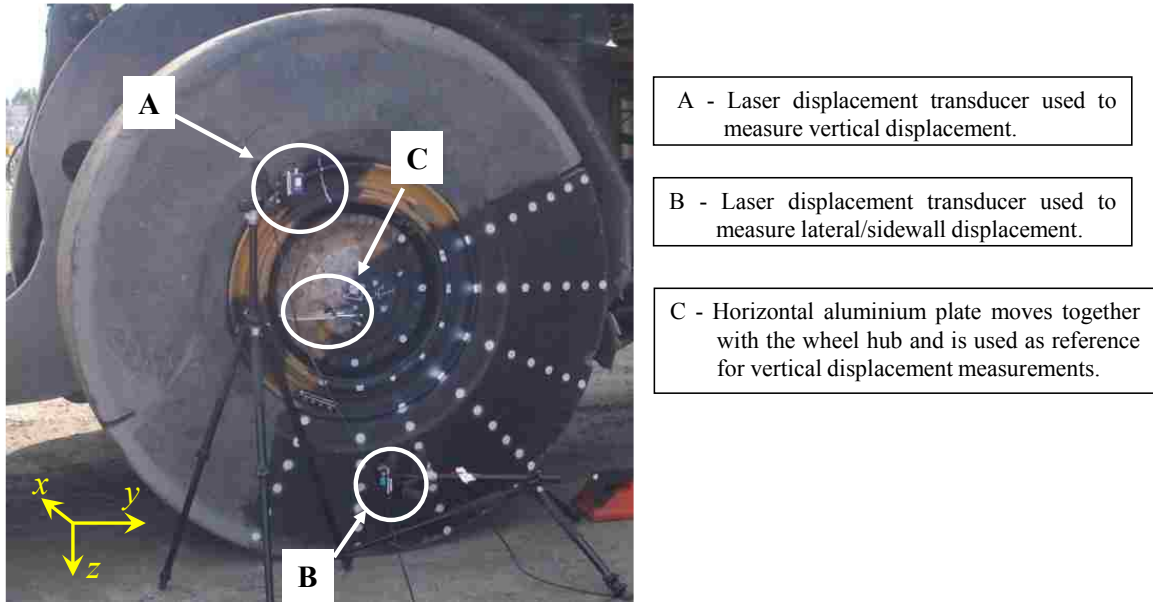


Figure 4.1 Wheel assembly displacement measurement apparatus for R29.5-29 tire. Note: Positive vertical displacement is downwards in the  $z$ -axis direction, positive lateral/sidewall displacement is inwards in the  $x$ -axis direction, and positive longitudinal is towards the front of the vehicle in the  $y$ -axis direction.

Quasi-static testing was performed above ground, near the mine site’s maintenance building, where initial instrumentation took place. To induce the desired severe loading conditions in a safe, controlled manner, a significantly higher capacity front load aboveground scoop, a Caterpillar 990, was employed. The test vehicle’s scoop was actuated by the operator against the rear structural protective metal of the Caterpillar 990 front load scoop. The relative size and weight differences between the vehicles allowed the Caterpillar 990 to act as an anchor of sorts for the test vehicle and when the scoop was activated, significant tire deformation was observed. Load input during the test events where maximum excitation occurred, was similar to a singular step function where load was applied, held for approximately 3 seconds and then completely removed. The experimental setup for the test vehicle is shown in Figure 4.2.

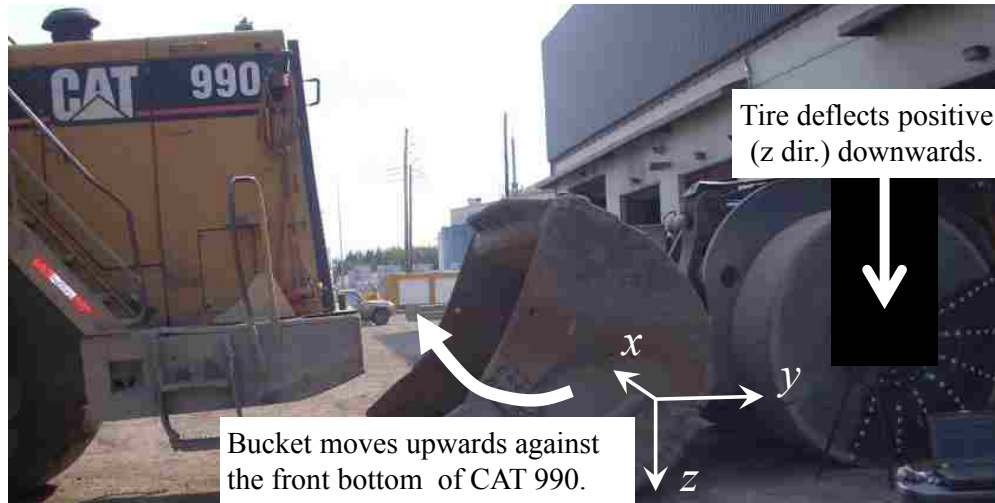


Figure 4.2 Excitation of the R2900G using the Caterpillar 990 front load scoop.

#### 4.1.1.4. Static Deflection Scale Testing

Static deflection testing occurred underground, within the mine site, using the site's Mettler Toledo Model 7566 Extreme Duty heavy vehicle weigh scale for measuring load. Testing entailed loading the test vehicle to varying payloads of ore and obtaining the static load-deflection behaviour of the tire.

Ideally, optical measurement methods such as those used above ground would be implemented during the underground testing, however, given the harsh surroundings, low lighting, and limited space around the scale and limited time available with the vehicle at the scale, these measurement techniques proved impractical. Instead, vertical deflection measurements were taken by manually measuring vertical tire deflection as a function of load using the vehicle's axle centre point to the ground as a reference measurement. To record loads, the visual output of the Mettler Toledo scale was taken, due to issues with the scale's ability to output data using an analog signal. This, of course, resulted in the inability to record effects of hysteresis during vehicle unloading. Maximum lateral tire sidewall position, or "tire bulge", was also recorded by measuring along the centreline position of the wheel assembly from the vertical face of the hub to the maximum lateral point on the tire. During this measurement process, only the axle with the wheel assembly under study was placed on the scale. Given that payloads were consistently loaded as evenly as possible, it was assumed that the recorded weight was evenly split between both wheels of the axle, on the scale.

## **4.1.2. Results and Discussions**

### **4.1.2.1. Above Ground Quasi-Static Testing Observations**

Aboveground testing constituted all quasi-static excitation testing that was performed. Given that tire deformation behaviour was acquired using laser displacement transducers as well as a high-speed camera, a comparison between both observations techniques was completed to ensure correct and consistent measurements. Laser displacement measurements considering only the planar motion of the wheel (i.e. the vertical displacement of the wheel hub) could be compared with the high speed images as only in plane observations from the post-processing of the images could be completed.

Post-test examination of the observations revealed that the time-deformation history of all six tests were unique, for a given vehicle. This behaviour is attributable to the fact that the vehicles did not experience consistent excitation (as applied by the vehicle operator), and is by no means, to the best of the researcher's knowledge, a reflection of any variation in testing apparatus. This becomes apparent when eliminating the time domain from the analysis, and instead examining the relationship between vertical wheel displacement and sidewall tire bulge. In doing so, identical relationships were observed between the vertical displacement of the wheel and the lateral sidewall deflection of the tire amongst all tests. Thus, it is evident that consistent tire deformation characteristics were observed amongst all tests completed, despite the discrepancies observed in the time-deformation profiles. For clarity and brevity, results from only the most significant loading/excitation condition, which resulted in the greatest degree of tire deformation and wheel displacement, are presented within this dissertation.

Three data sets were recorded corresponding to the three different excitations of the vehicle, which are referred to as test events. For the tire 29.5-29, Figure 4.3 (a) presents the vertical wheel displacement and tire lateral deflection as functions of time for test event 1. Cross-plotting such information results in Figure 4.3 (b) which illustrates the lateral tire displacement as a function of wheel vertical displacement. As can be observed in these figures, maximum values of vertical deflection and sidewall lateral deflection were observed to be approximately 80 mm and 35 mm, respectively. This is the most severe loading condition among all the test events. The vertical and lateral deflection graphs and the cross-plotting of data from the other two events (event 2 and event 3) are listed in Appendix B.

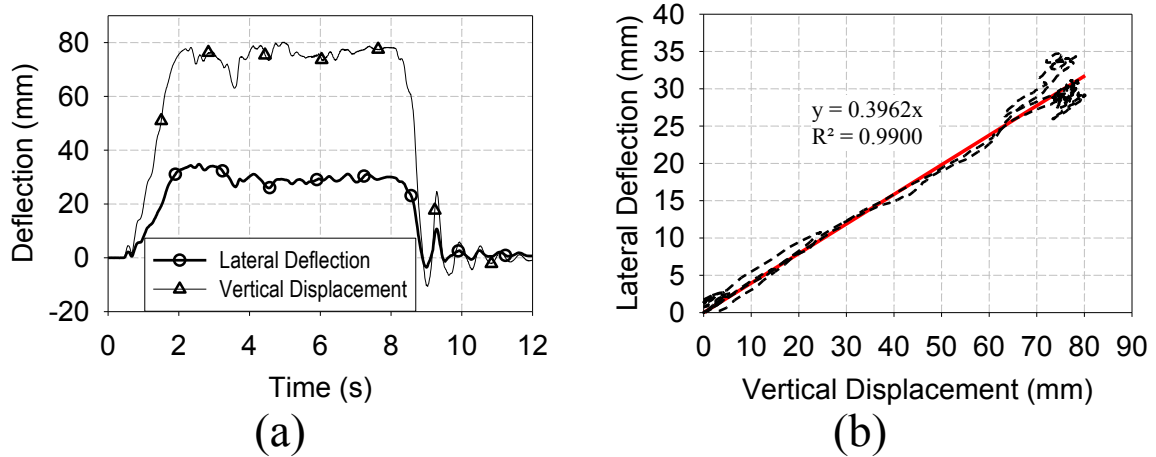


Figure 4.3 Quasi-static testing tire responses for test event 1, exhibiting maximum deflection in the (a) vertical and lateral directions as well as (b) lateral deflection versus vertical deflection.

A minor degree of hysteresis was observed in the lateral tire displacement presented as a function of vertical wheel displacement. This observation may be attributed to the dissipative nature of the tire materials and construction, a result of measurement error, or slipping occurring between any contacting interfaces. The last two reasons presented are believed to have only a very minor contribution to the observed hysteresis. In general, direct relationships between lateral tire deflections and vertical wheel displacements were observed for all tests. Linear regression of the two measurements was performed for each test and proportionality constants of 0.3962, 0.3585, and 0.3486 were determined for event 1, event 2, and event 3, respectively, with an average constant of 0.3678 was determined for the tire 29.5-29. Coefficient of determination ( $R^2$ ) for the proportionality constant was determined to be 0.99.

An important characteristic of the measurement apparatus should be noted regarding sidewall lateral displacement measurements. During testing, the sidewall lateral displacement transducer was supported by a fixed height tripod, leveled on solid ground and isolated from the test vehicle. Given that the wheel deflection was essentially vertical during testing, this meant that the sidewall transducer would not record the lateral deflection of a single point on the tire, but instead the lateral deflection of the varying points on the tire passing through the laser path of the transducer during vertical deformation. To compensate for this situation, the transducer was placed such that it recorded lateral deflection within the vicinity of the expected maximum sidewall tire deflection.

To investigate local tire deformation behaviour, post-processing of the digital images acquired with the high speed camera was completed using the digital image analysis software,

ProAnalyst. In the ProAnalyst, the marked dots on the tire and wheel were tracked and the displacements versus time data were output and plotted, using the shutter speed and calibration information. To ensure suitable calibration within the digital image analysis as well as consistent measurements between both the laser displacement transducer and the image analysis an examination of the error between the two measurement techniques was completed, for the vertical displacement of the wheel hub only. A rigorous error analysis was completed which involved comparisons between the two measurement techniques within the complete time domain of data acquisition. Additionally, a validation metric ‘V’, as proposed by Oberkampf and Trucano [119] was computed. The error between the two measurement techniques was quantified using Equation (4.1) and the validation metric was determined using Equation (4.2). In these equations,  $t_2$  and  $t_1$  are the time boundaries between which integration of the error function is performed. In this study, they represent a period of time of interest for which tire deformation was occurring.  $O_{Tracked}$  represents the deformation of the tire, as tracked using digital image techniques, while  $O_{Laser}$  represents deformation of the tire, as tracked using the previously discussed laser transducers.

$$Error = \frac{1}{t_2 - t_1} \cdot \int_{t_1}^{t_2} \left| \frac{O_{Tracked}(t) - O_{Laser}(t)}{O_{Laser}(t)} \right| dt \quad (4.1)$$

$$V = 1 - \frac{1}{t_2 - t_1} \cdot \int_{t_1}^{t_2} \tanh \left( \left| \frac{O_{Tracked}(t) - O_{Laser}(t)}{O_{Laser}(t)} \right| \right) dt \quad (4.2)$$

The above validation metric has the following four characteristics. First, it normalizes the difference between the transducer (laser) results and the tracked (ProAnalyst) data by computing a relative error norm. Second, the absolute value of the relative error only permits the difference between the transducer results and the tracked data to accumulate. Third, when the difference between the transducer results and the tracked data is zero at all measurement times, then the validation metric is unity. And fourth, when the summation of the relative error becomes large, the validation metric approaches zero. Figure 4.4 shows how the validation metric given in Equation (4.2) varies as a function of constant values of the relative error throughout the specified domain from 0 to 3 seconds. If the summation of the relative error is 100% of the experimental measurement, the validation metric would yield a value of 23.9%. Numerical error occurs when attempting to evaluate the relative error if the laser transducer measurement is near or equal to zero.

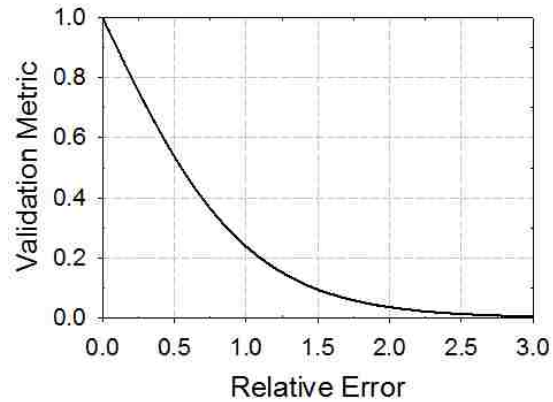


Figure 4.4 Plot of validation metric,  $V$ , given in Equation (4.2) as a function of relative error.

Figure 4.5 illustrates the vertical displacement comparison for test event 1 between laser displacement transducer measurements and digital image analysis tracking. The error and validation metric were determined to be 2.31% and 0.979 respectively. The plot comparisons for test event 2 and 3 are listed in Appendix B with errors and validation metrics of 1.25% and 0.985, 1.12% and 0.989, respectively. This analysis ensured confidence with regards to the optical measurement techniques applied within this research.

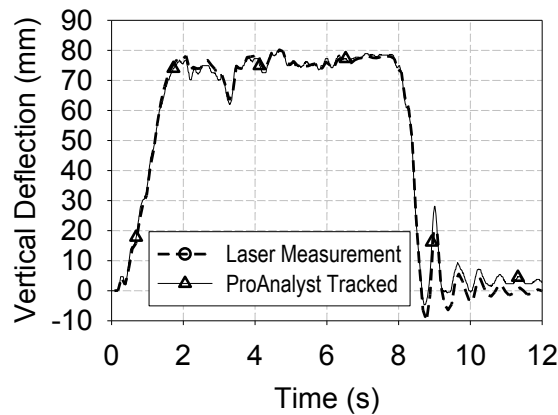


Figure 4.5 Vertical displacement comparisons for test event 1 between laser displacement transducer measurements and high-speed camera image tracking using ProAnalyst.

Determination of local tire deformation behaviour occurred after the error analysis was completed. Six locations amongst all markings applied to the tire were considered for tracking. Figure 4.6 illustrates the locations of these points for the 29.5-29 tire. The selection of these points was based upon the desire to eliminate any excessive analyses, yet provide a thorough understanding of the local tire deformation. As a result points H-in and H-out, which pass through the wheel center horizontally, D-in and D-out, which pass through wheel center

diagonally ( $45^\circ$ ), V-in and V-out, which pass through wheel center vertically at the bottom of the tire, as illustrated in Figure 4.6, were selected for planar tracking ( $y/z$  plane of motion).

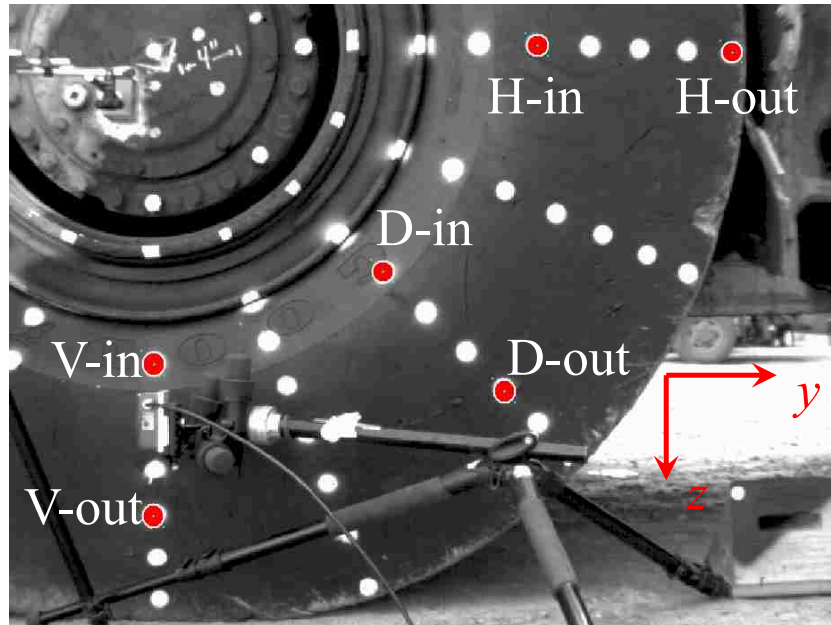
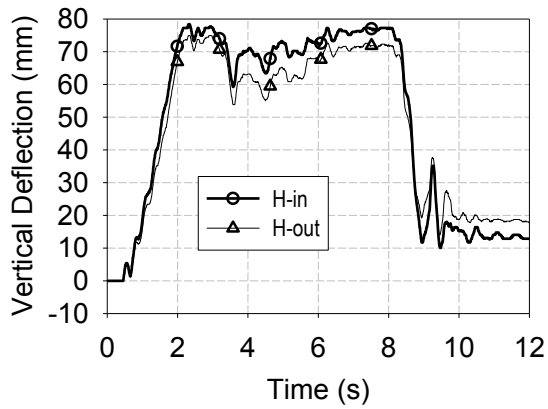


Figure 4.6 Location of points tracked on the physical tire 29.5-29.

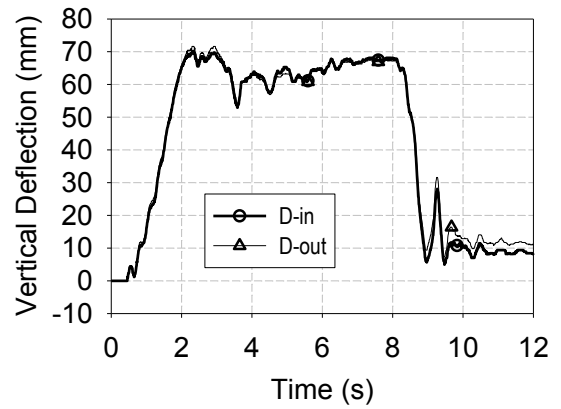
Figures 4.7 (a)-(c) and 4.8 (a)-(c) illustrate the vertical ( $z$ -axis) and horizontal ( $y$ -axis) deflections associated with the tracked locations for event 1. It can be seen in Figure 4.7 that the V-out point experiences approximately 50% of the vertical displacement of the V-in point, while the displacements of the D-in and D-out points and H-in and H-out points are, respectively, similar. This intuitively makes sense and demonstrates that the measurement apparatus is functioning as anticipated, given that the V-out point is located on an area of the tire within the vicinity of the contact patch, and is thus already under increased compression relative to other tire points. Furthermore, this point is stiffer in the radial direction of deformation due to the tire's internal structure.

It is important to note that the vertical deflection of all points, more notably H-in, H-out, D-in, D-out and V-in do not return to a value of zero after excitation is removed. This is a result of the minor degree of angular rotation which the tire/wheel assembly experienced during testing. The plots for test event 2 and event 3 are listed in Appendix B.

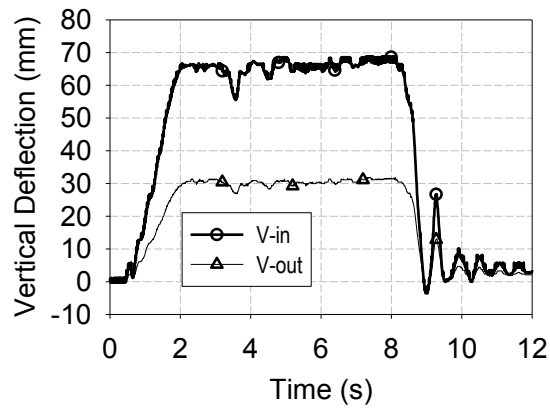




(a)



(b)



(c)

Figure 4.7 Vertical deflection responses for tracked nodes for test event 1.

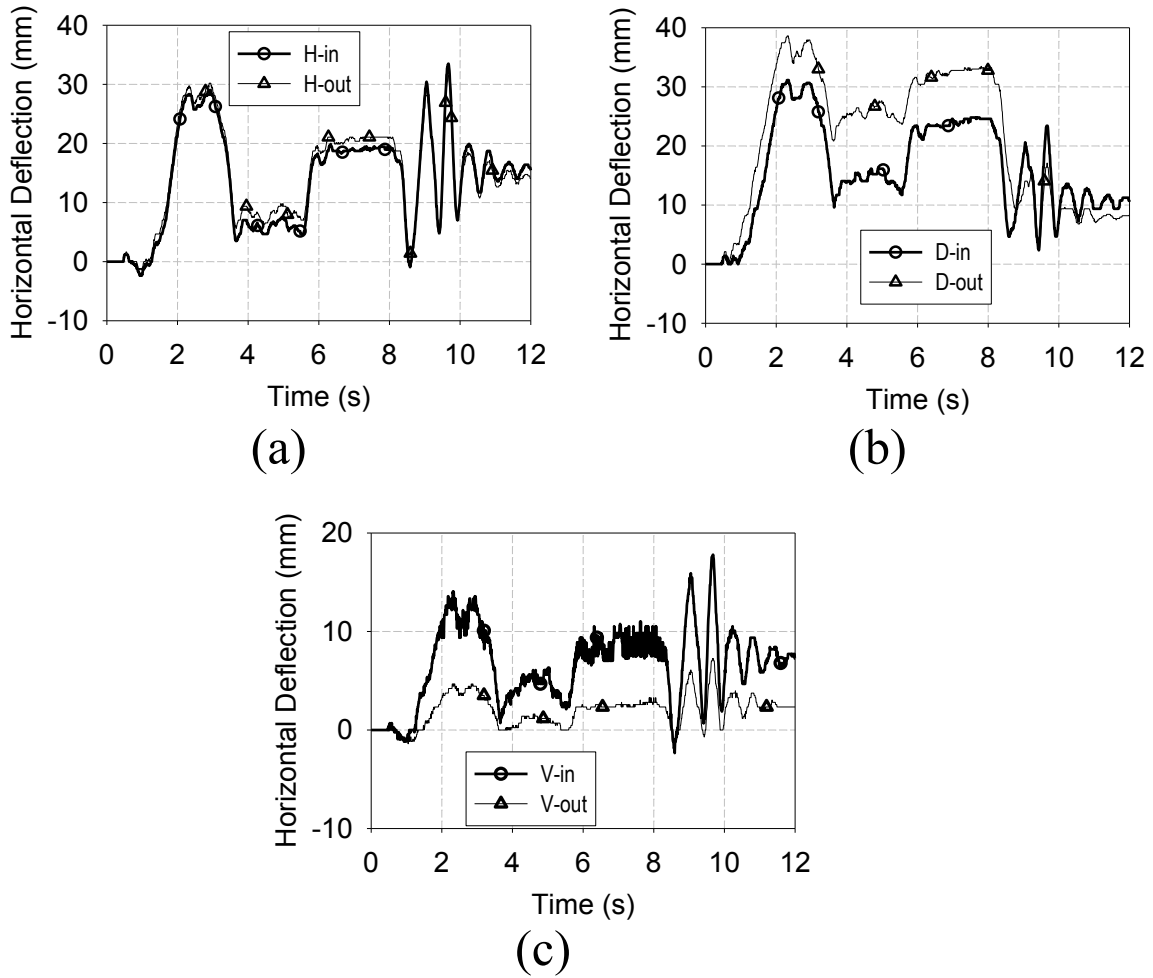


Figure 4.8 Horizontal deflection responses for tracked nodes for test event 1.

#### 4.1.2.2. Underground Static Testing Observations

The underground testing consisted of vertical and sidewall lateral deflection measurements at corresponding payloads on the mine site's heavy vehicle weighing scale. Measurements were taken manually and weight readings were based on the scale's visual output, with the purpose being to correlate load-deflection characteristics of the tire. As validation of the testing methodology, observations are summarized in Figure 4.9 and Table 4.5, where experimental measurements are compared to manufacturer's engineering data for the tire 29.5-29. The observed loads are based on recorded weight measurements and divided in half under the assumption that both wheels are equally loaded. Furthermore, the observations are corrected to remove approximate static wheel and tire weights to equally compare to the engineering data points.

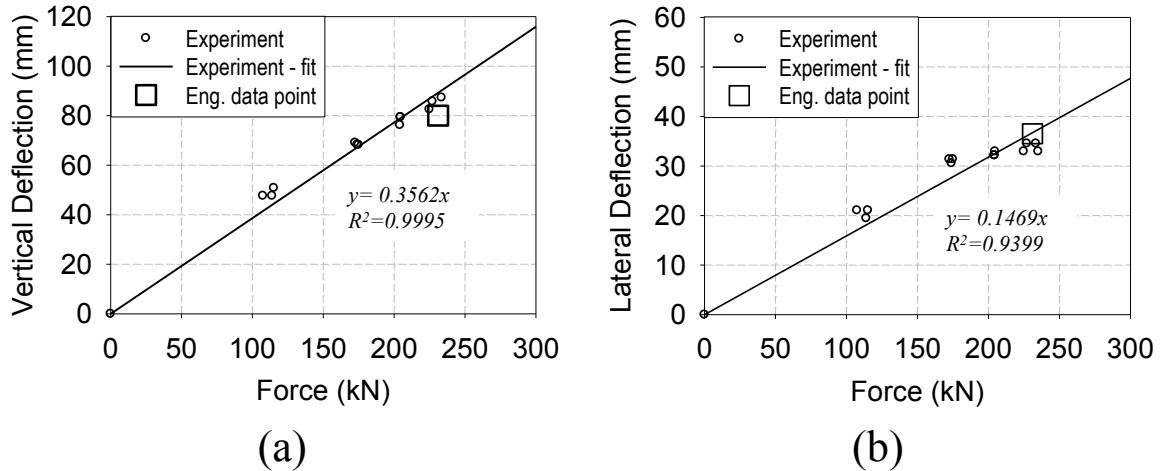


Figure 4.9 Static load-deflection data for the tire 29.5-29 showing a) vertical deflection versus load force and b) lateral deflection versus load force compared to the corresponding Goodyear engineering data point.

Regression analysis, to determine a linear relationship between force/displacement (stiffness), was completed for each vertical and lateral set of deflection observations. Based on the equations of these lines, approximations of the load/deflection (stiffness) behaviour were quantified as shown in Figure 4.9. Furthermore, these relationships were used as an additional method to validate the experimental methodology through comparison with manufacturer data. First, load versus vertical and lateral deflection values were determined and compared to manufacturer values, as given in Table 4.5, based on underground static loading. This was achieved by using the values of linear regression, for example 0.3562 mm/kN and 0.1469 mm/kN for the 29.5-29 tire, and solving the inverse to determine kN/mm values. These are summarized in Table 4.5 and referenced manufacturer data are included for comparison. The relative errors of the stiffness were calculated using Equation (4.3). The maximum relative errors were -2.7% and 8.1% respectively, for vertical stiffness and lateral stiffness of the tire 29.5-29.

$$Relative\ Error = \left| 1 - \frac{(Experimental\ Deflection\ Value)}{(Engineering\ Deflection\ Value)} \right| \quad (4.3)$$

Table 4.5 Tire stiffness comparison of experimental static loading and Goodyear OTR data.

Tire Model	Load/Vertical Deflection (kN/mm)			Load/Lateral Deflection (kN/mm)		
	Experimental Observations	Goodyear OTR Eng. Data	Relative difference	Experimental Observations	Goodyear OTR Eng. Data	Relative difference
29.5-29	2.81	2.89	-2.7%	6.81	6.30	8.1%

Subsequently, an additional critical comparison was made by evaluating the ability of the experimentally observed load-deflection behaviour in predicting deflection relative to the Goodyear engineering data values. This is achieved by determining the deflections corresponding to the reference loads provided in the Goodyear OTR Engineering Data Book (listed in Table 4.3) using the linear regress equations illustrated in Figure 4.9 and comparing the calculated deflections to the Engineering deflection values at the identical loads. The corresponding magnitude of errors were determined to be 2.4% and 7.4% respectively, for vertical and lateral deflections. These findings are summarized in Table 4.6 below.

Table 4.6 Tire deflection observations comparing experimental static loading to Goodyear OTR data.

Tire Model	Vertical Deflection (mm)			Lateral Deflection (mm)		
	Experimental Observations	Goodyear OTR Eng. Data	Relative difference	Experimental Observations	Goodyear OTR Eng. Data	Relative difference
29.5-29	81.9	80	2.4%	33.8	36.5	-7.4%

It is important to note that error is introduced in this comparison due to varying tire pressures, since Goodyear engineering data is provided as deflection for a given load at a specified tire pressure shown in Table 4.2 and is different from the test vehicles' tire pressures in Table 4.1. Furthermore, all tires under investigation showed some degree of wear and general deterioration, as summarized in Table 4.4. The degree of deterioration is impossible to quantify. This is another source of error as manufacturer specifications are based on a new tire, and tread wear, sidewall damage and deterioration, and overall manufacturing variances affect tire performance and deflection characteristics. Additionally, no information is provided by the manufacturer that states multi-piece wheel information or the general testing apparatus used to determine deflection data, which concludes it is appropriate to assume testing methodologies varied to a minor extent between the manufacturer and experimental observations.

## 4.2. Rim Base Laboratory Tests

In the previous section, the deformation behaviour of the 29.5-29 sized OTR tire was experimentally investigated under extreme loading conditions. The results from this testing were subsequently used to validate the predictive accuracy of the corresponding numerical tire model. To understand the failure mechanisms of the multi-piece wheel, it is essential that a high fidelity

wheel model be developed with the capacity to accurately predict load/deformation behaviour of the entire wheel/tire assembly and the stress/strain levels of the wheel components.

In this section, the mechanical performance of the rim, sized 29-25.00/3.5 (Diameter-width/flange height, units: inch), for use with the tire 29.5-29 was experimentally investigated. This data was useful in validating the methodologies used in developing numerical wheel models. In the multi-piece wheel, the rim base has the most complicated geometry and is the supporting structure for other components. Therefore only the rim base structure was selected for testing. This evaluation is believed to be sufficient since all other parts of the multi-piece wheel under investigation follow similar model development methodologies and geometries.

#### **4.2.1. Rim Base Testing Procedure**

Static testing of the rim base was facilitated by making use of a custom built hydraulic load frame, as shown in Figure 4.10. The rim base was stabilized on the supporting beam of the testing apparatus by placing the rim on two 50.8 mm thick steel support blocks. These blocks were machined, using a numeric control machining centre, to conform to the contour of the rim base at designated locations. During testing, a static load was applied to the top of the rim base using a hydraulic actuator with a load cell mounted to the tip of the rod of the actuator. To ensure stability of the rim base due to possible non-symmetric loading conditions and to reduce stress concentration levels, an aluminum block with a contact area of 80 mm by 103 mm was placed onto the rim base and under the piston head. The bottom of the block was machined to match the curved profile of the outer surface of the rim base. Additionally, a 50.8 mm diameter aluminum pad with a height of 38.1 mm was placed between the aluminum block and the load cell to allow suitable clearance between the tested rim base and the laser displacement transducer located in the vicinity of the load cell.

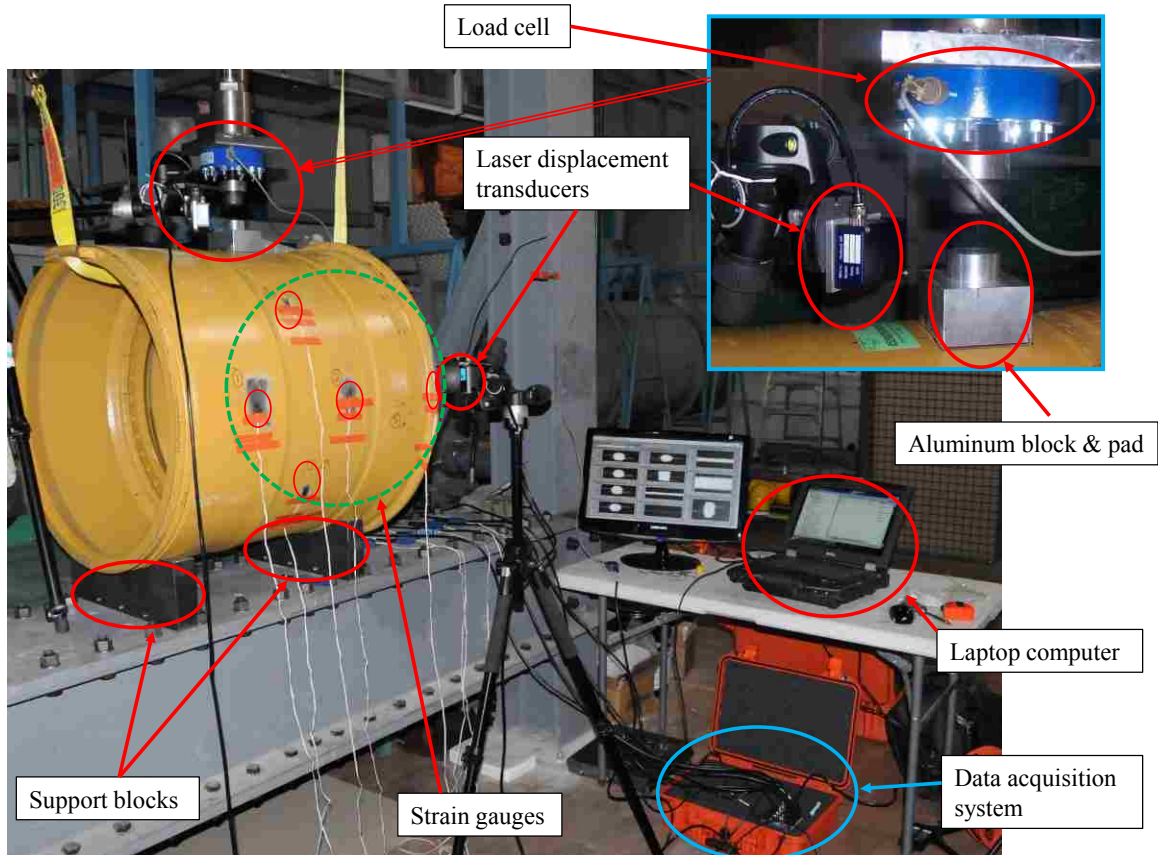


Figure 4.10 Testing apparatus and setup used during static rim base testing.

Five strain gauges, one load cell, and two non-contact laser displacement transducers were used to measure strains, static load, as well as vertical and lateral deflections, respectively. The locations of strain and displacement measurement are indicated in Figure 4.11. Note the coordinate axis defined in Figure 4.11 as it is used to describe the displacement measurement directions.

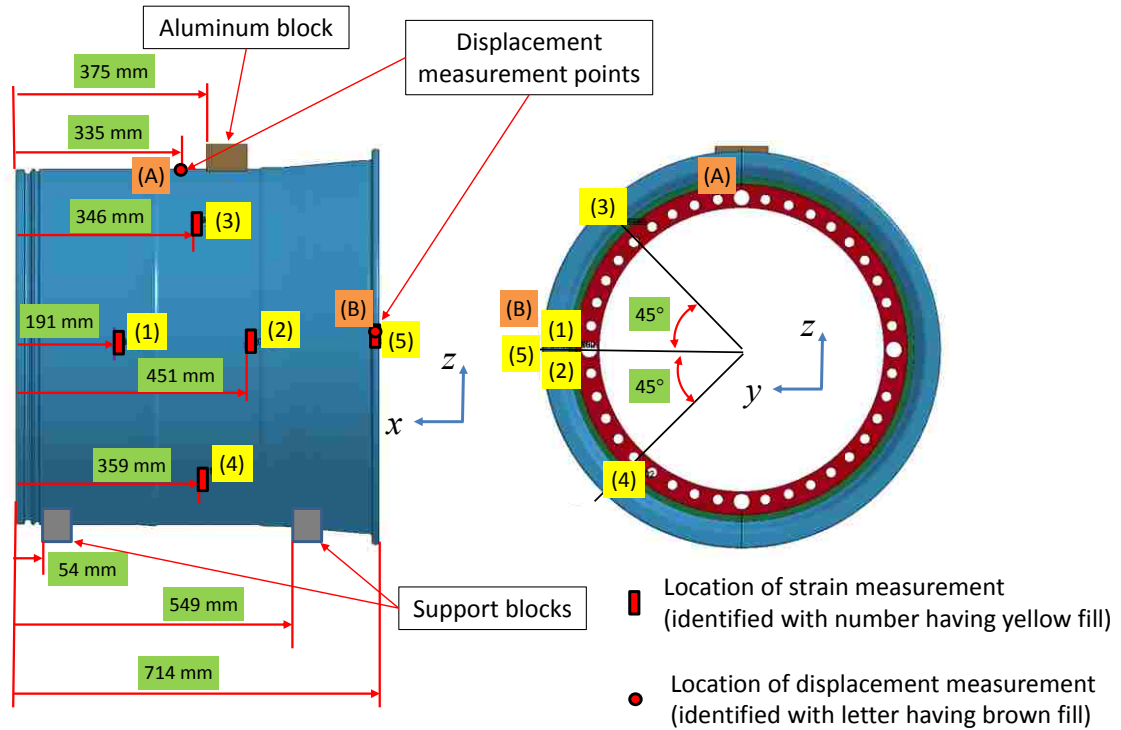


Figure 4.11 Locations of strain and displacement measurement on the rim base.

The displacement measurement device used to measure vertical,  $z$ -axis, deflection (location (A) in Figure 4.11), was an AR700-1 laser displacement transducer (model #AP7010010) with a measurement range of 25 mm. The displacement transducer used to measure lateral,  $y$ -axis, rim base deflection (location (B) in Figure 4.11) was an AR700-0500 laser displacement transducer (model AP7010005) with a measurement range of 13 mm. The load cell was a 220 kN PCB strain gauge based load cell (serial number SN628) with a maximum load capacity of 220 kN. The strain gauges used were pre-wired KFG series (KFG-5-350-C1-11L3M3R) strain gauges with a nominal resistance of 350 ohms, and were manufactured by OMEGA Engineering, Inc. Data acquisition was controlled by a laptop computer using a National Instruments Compact DAQ USB data acquisition system (model cDAQ-9174) and a custom developed LabVIEW program. All test data was collected at a sampling rate of 2 kHz.

Prior to adhesion of the strain gauges to the outer surface of the rim base, each location was cleaned of any paint or debris, using fine sandpapers, with final cleansing with acetone. After drying of each surface, the strain gauges were adhered to the rim base using the adhesive provided by the strain gauge manufacturer. Each strain gauge was oriented to measure strains in the circumferential direction at its respective location. Strain gauges (1), (2), and (5) were all placed on the horizontal plane ( $x/y$  plane) passing through the centre of the rim base as shown in

Figure 4.11. In those locations, maximum strains were anticipated under static loading at the top of the rim base. Gauges (1) and (2) were located on either side of the  $y/z$  plane of the applied load and gauge (5) was placed at the ridge of the back section of the rim base. Strain gauges (3) and (4) were placed on planes approximately 45 degrees above and below the horizontal plane, respectively, near the centre region of the rim base. The five strain locations were carefully selected in order to capture representative strains on the rim base.

Prior to conducting any testing, a preliminary numerical simulation was conducted under conditions similar to the anticipated physical tests. This simulation was performed to obtain information regarding the approximate load/deflection behaviour of the rim base, as well as strains and deflections corresponding to strain gauge and displacement transducer placements. This information was used for selection of appropriate transducers. Additionally, the information was used to ensure that the maximum applied experimental load was within the elastic deformation range of the rim base; thus ensuring no permanent deformation of the rim. The primary purpose of load control was meant to ensure repeatable testing could be done without changes in the rim base mechanical properties due to strain hardening and plastic deformation.

Load application was manually controlled through a hydraulic fluid flow control valve and operator review of the feedback from the LabVIEW program. Loads were gradually and continuously applied to minimize any effects associated with dynamic loading. Throughout the loading process, the strain gauge voltages, load cell output and rim base deflections were viewed in real-time using the data acquisition system to ensure that the loading of the rim base remained within its elastic range. The duration of load application, followed by unloading, was approximately 45 seconds for each test. Seven tests were conducted in total to assess the reliability and repeatability of the experimental data.

#### **4.2.2. Experimental Rim Base Testing Observations**

Experimental observations included circumferential strain and displacement measurements (vertical for location 'A' and lateral for location 'B') from a number of locations previously indicated in Figure 4.11. Excellent consistency in the experimental observations over the seven tests was found. Additionally, all responses were noted to behave in a linear fashion as was expected from the trial numerical simulations. Test #1 has a maximum external load slightly larger than 160 kN applied to the rim base. All subsequent tests had maximum external loads approximately equal to 130 kN. Observations of the lateral displacement at location 'B' and the circumferential strain measured at location '1' are presented in Figure 4.12. All other experimental observations are provided in Appendix C.



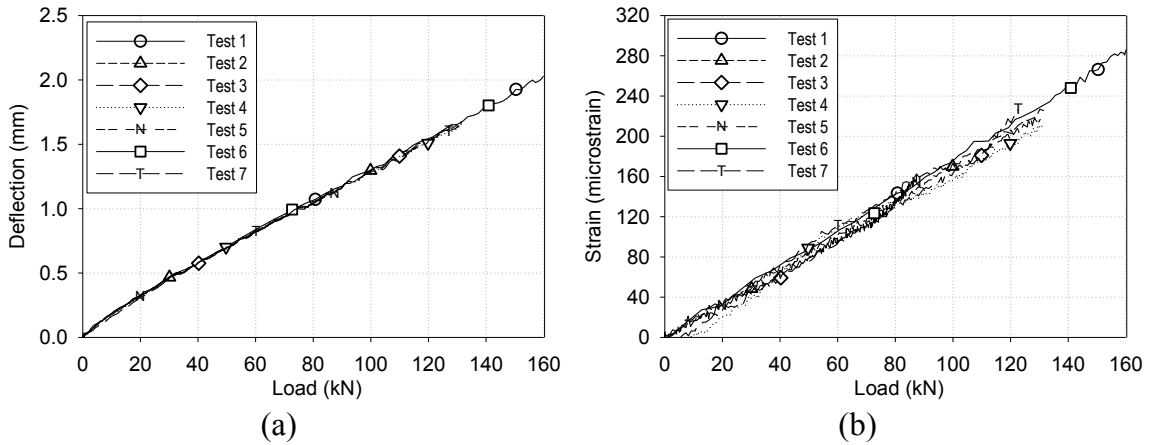


Figure 4.12 Experimental observations (a) lateral deflections at location ‘B’ and (b) circumferential strain at location ‘1’.

Displacement data was noted to be less than 3 mm for both measurement locations. Additionally, circumferential strain measurements were typically less than 300  $\mu\epsilon$  with the exception of location ‘5’, which should be expected as this location is radially further from the centreline of the wheel and the amount of material in this region is reduced compared to other locations.

It is evident that similar observations were noted for each location of measurement over the seven tests completed. Since Test #1 experienced the largest applied load, and is an excellent representation of the data over of all other tests, the information obtained from this test was further used for the comparison and validation of the numerical model to experimental findings.

## Chapter 5. Finite Element Model Development

### 5.1. Tire Model Development

#### 5.1.1. On-the-road Tire Modeling in the Open Literature

Tire modeling and experimentation has been primarily restricted to tire manufacturers, with no studies known to be available regarding the simulation of mining wheel tires in the open literature. Regardless, studies of on-the-road tires are applicable to a reasonable degree, since the structures and materials of the two different types of tires are similar, despite significant differences in bead and sidewall thickness when compared proportionally.

To create a detailed tire model for crash applications, Reid et al. [120] conducted two types of tire tests, namely, single-sided compression and double-sided compression. The first test was achieved by placing a flat rigid ground type surface below the tire and subsequently prescribing a displacement to the centre of the wheel. The second test follows similar methodology to the first, except the prescribed motion was made in reference to a solid plate placed on top of the tire; thus resulting in double-sided compression. In both tests load-deflection curves were obtained and were used to improve the accuracy of the tire model. The researchers took a unique approach to the model development, which avoided the discretization of all structures of the tire and wheel; however, the majority of the components which influenced the response of the tire and wheel assembly were carefully modelled such that good predictive capabilities of the model existed under a number of testing conditions.

In the work of Orengo et al., [121] tire blow-out of a passenger vehicle in roadside hardware simulations was modelled using the commercial software LS-DYNA. In their numerical tire model, the modelling of different tire components was simplified to shell, beam and solid elements. The model was subsequently verified against experimental observations and found to correlate well; thus validating the model simplifications.

Neves et al. [117] created a model of a 175/65R 14 82T tire used on passenger vehicles, to investigate the tire performance under sudden impact loadings. The researchers used the FE software Abaqus for their investigations. To validate their model, impact tests were conducted on the tire and deformation was tracked using laser displacement transducers and a high speed camera.

In the study of Burke and Olatunbosun [116], a model of a 195/65R15 tire was created using Nastran to investigate the static tire/road interaction. In their research, a gap formulation

was implemented to model the interaction so that the contact patch area, shape and deflection were automatically accounted for under a given load and inflation pressure. To validate their model, a downward force was applied to the wheel centre and tire displacement as a function of load was recorded and compared against model behaviour. This simplistic approach was used to assess the predictive capabilities of the numerical model.

### **5.1.2. Tire Model Development for the Tire 29.5-29**

The OTR tire modeled was the tire sized 29.5-29, used on the mining vehicle Caterpillar R2900G LHD Scoop, which was experimentally tested. Detailed tire physical and deflection information were listed in Table 4.2 and 4.3 in Chapter 4. This tire has a bias structure and smooth tread pattern.

Great efforts were taken to obtain more detailed information about the tire structure and material properties than information presented in previous sections, however, only geometric dimensions, such as bead and sidewall thickness by manually measuring a physical tire, could be obtained due to the proprietary and confidential nature of the tire design. A lack of specific material properties also arose for Reid et al. [120] while modelling a Chevrolet C2500 pickup truck tire. In their study, a C2500 pickup truck tire was cut in half and the detailed tire geometry was obtained. Similar methodologies were sought to be used in this investigation, however, it was found unfeasible to obtain relevant tire cross-sections, primarily due to the size and the weight of the tire and the availability of cutting equipment, without causing significant degradation to the tire near the potentially cut regions. Instead, acknowledgement is made that the model of this study seeks to simulate overall tire performance rather than the detailed, highly localized structural performance of the tire components. As such, a simplified tire model meeting the overall performance of the tire was chosen as the basis of model development.

Since the tire and wheel always work together, the tire and wheel assembly was tested and modeled together. Prior to tire model development, a basic wheel model was established. The wheel structure was composed of seven pieces, namely, the rim base, bead seat (BS) band, locking ring, front and back flanges, support disc and mounting disc as shown in Figure 5.1. In real-world operation the mounting disc's deformation is minimal and is not of primary interest to this study. Correspondingly, a rigid material property was assigned to this part of the model. The remaining wheel components were modelled using the elastic material properties of steel.

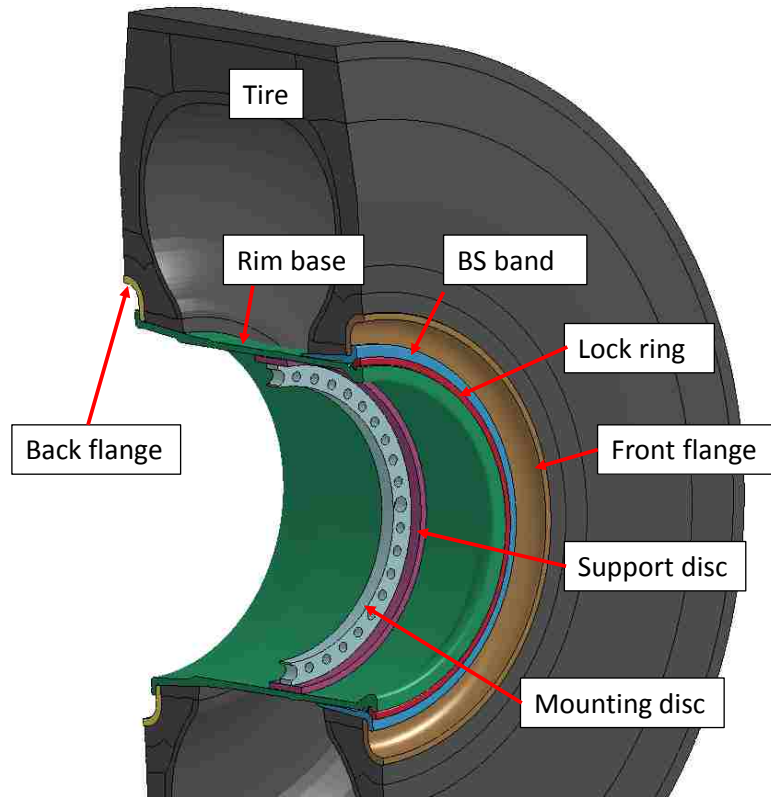


Figure 5.1 Five-piece wheel assembly model.

In the work of Orengo et al. [121] and Shiraishi et al. [122] development of a tire model for passenger vehicles was attempted with shell elements; however, it was found that shell elements do not have a sufficiently high bending stiffness. This issue caused abnormal deformation in the sidewall and tread regions of the modelled tires and was only corrected when solid elements were used in place of the original shell elements.

In the development of the 29.5–29 tire model, it was observed that the thickness of the physical tire was highly non-uniform. The non-uniformity of the tire resulted in geometrical characteristics that are not suitable for shell element implementation and would create problems similar to those encountered by Orengo et al. [121] and Shiraishiet et al. [122]. Consequently, the tire was meshed with solid elements.

#### 5.1.2.1. Tire Discretization

The majority of the material comprising the tire structure is rubber, especially on the outer layer of the tire. The lower stiffness and large deformation recovery properties of the rubber are utilized to damp impact loads and to provide soft contacts with wheel steel structures and with the ground. When other materials are embedded within the rubber (such as steel wire,

steel belt, fabric, etc.), the mechanical performance of the tire will be totally different from a pure rubber tire. To simplify the modelling in this study, rubber was not modelled as a separate entity. Instead, the tire was discretized into several regions, as shown in Figure 5.2. Discretization was based on the physical tire's approximate cross-sectional structure as well as the deformation behaviour of the tire observed under loading conditions. Simplifications and assumptions were made to reduce modeling effort and computation costs; however, special care was taken not to introduce inaccuracies into the model. To simplify the implementation process of a material model, an elastic material model was assigned to all regions of the tire FE model, with a value of 0.33 assigned for Poisson's ratio. However, different regions of the tire were assigned different elastic moduli, which were related to the observed specific mechanical material behaviour of the tire during loading. Details on the assignment of the elastic moduli are presented in subsequent sections. This approach enables the numerical model to better capture the non-linear behaviour inherent to the tire while allowing for effective simplification for modelling purposes given the difficulty of performing traditional material tests on such a large tire. The mass density of the tire,  $1428 \text{ kg/m}^3$ , was calculated based on the total mass of the tire (1304 kg) and the meshed total solid element volume of the tire, which represents the actual tire volume.

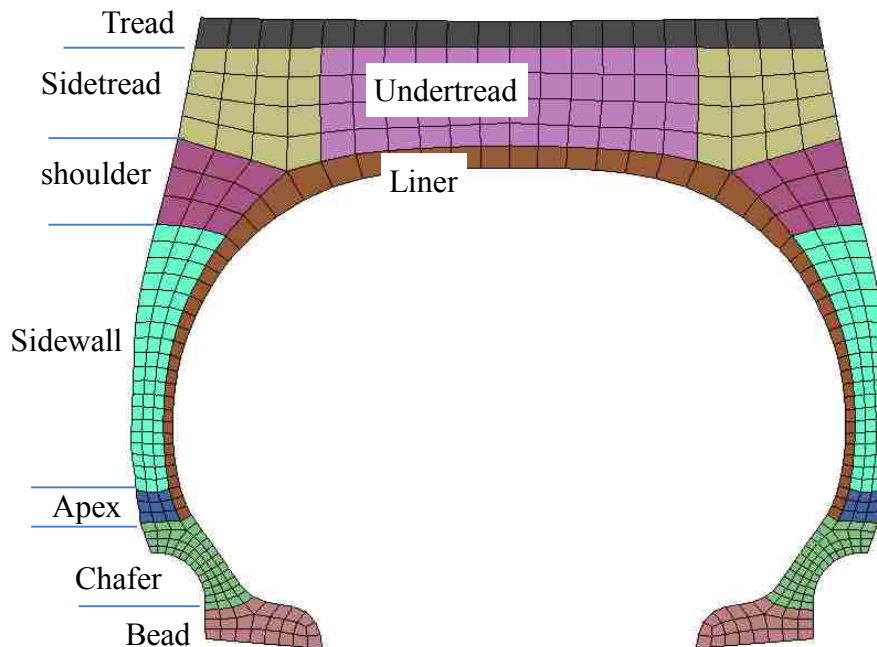


Figure 5.2 Tire region definitions and discretization.

#### **5.1.2.1.1. The Bead**

The bead region of the tire is made of highly stiff rubber and steel cords which essentially ‘locks’ the tire to the rim restraining relative movement under normal conditions. It is used to carry the interface force between the tire and the wheel and also provides a seal to maintain tire pressure. In real-world operation, the bead region experiences little deformation as a result of its high elastic modulus. To accommodate this behaviour, a number of preliminary simulations were performed. During simulations it was observed that an elastic modulus that exceeded 5000 MPa caused difficulty for the bead to slide along the BS band and rim base, which have a small taper (an angle of approximately 5 degrees), during the inflation process. Therefore, this value was assigned as modulus of elasticity for the bead area.

#### **5.1.2.1.2. The Chafer**

The Chafer region is relatively flexible compared to the bead region. This mechanical behaviour allows the tire to wrap tightly around the flanges of the wheel during operation, maintaining a good seal between the tire and wheel, permitting consistent tire pressure. Additionally, the portion of the chafer that contacts the flanges of the wheel is also responsible for transmitting loads and assists with ensuring a mechanically stable tire condition. A number of trial simulations preferred the selection of 500 MPa as the elastic modulus for this region. Lower values of the elastic modulus resulted in the formation of separation between the chafer and flanges. Higher values of the elastic modulus did not permit the chafer to tightly wrap around the flanges since the stiffer chafer did not allow a suitable degree of flexibility to permit tire deformation along the contour of the flanges.

#### **5.1.2.1.3. The Apex, Sidewall, Shoulder, Sidetread, Undertread, Tread, and Liner**

The apex, sidewall, shoulder, sidetread, undertread, tread, and liner interact together to dictate the performance and deflection of the tire. Preliminary simulations indicated that if the sidetread was too soft relative to the shoulder, the sidetread would experience excessive deformation (Figure 5.3 (a)). Similarly, if the shoulder was too soft relative to the sidetread, elements within the vicinity of this region would undergo unrealistic deformation (Figure 5.3 (b)). These observations served to illustrate the dependence of a region’s deformation behaviour on the relative elastic moduli of surrounding regions, and were considered for the assignment of elastic moduli for the sidetread, shoulder, sidewall and apex. Furthermore, the elastic moduli of these regions were also selected such that vertical and lateral tire deflections were reached simultaneously. Final values, for the sidetread, shoulder, sidewall and apex were assigned as 4.0 MPa, 0.8 MPa, 1.0 MPa and 5.0 MPa, respectively, which served to produce tire deformation

highly similar to that which has been observed in practice and based on Goodyear engineering data.

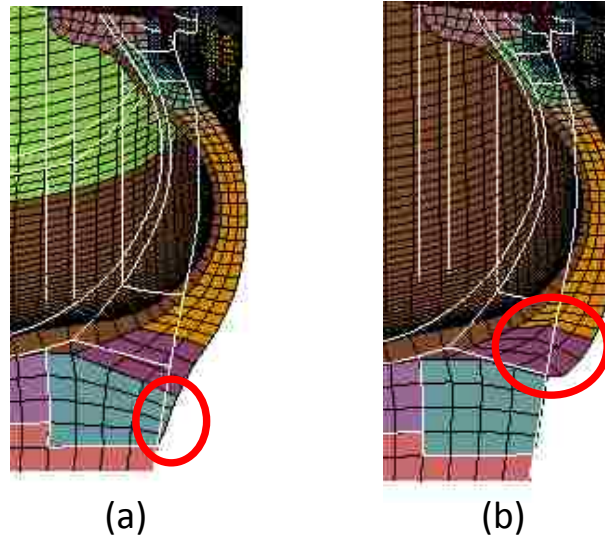


Figure 5.3 Deformed tire (a) sidewall too soft, (b) shoulder too soft.

The liner plays an important role in ensuring that realistic vertical and lateral tire deflections are attained simultaneously where both vertical and lateral deflections of the tire are highly sensitive to changes in the elastic modulus of the liner. Table 5.1 summarizes the different deflection values for a given liner elastic modulus, provided that the stiffness of other regions remain constant. Finally, an elastic modulus of 40 MPa (highlighted in the table) was selected for the liner.

Table 5.1 Liner elastic modulus change effects

Liner Elastic Modulus	20 MPa	40 MPa	50 MPa	80 MPa	120 MPa
Vertical Deflection (mm)	90.1	82.6	79.5	71.8	64.2
Lateral Deflection (mm)	38.7	36.5	35.5	32.5	29.3

The tread and undertread primarily contribute to the vertical deflection of the tire. Furthermore, the tread controls the deformed shape of the tire in the contact patch region. These critical aspects were accommodated within the model by proper selection of elastic moduli. This was accomplished through multiple iterations where relative values of the elastic moduli were modified. The initial values assigned were based on the relative stiffness characteristics of the

tread and undertread with respect to the sidetread and shoulder, and iterations involved altering properties until a sufficiently realistic behaviour was achieved.

#### **5.1.2.1.4. The Body Plies**

The body plies act to reinforce the sidewall rubber and increase the lateral load capacity of the tire. They are generally made of a polyester material that runs perpendicular to the direction of the tread and steel belts. In the work of Reid et al. [120], beam elements were successfully used to model the bead, steel belts and body plies, to achieve accurate prediction of tire performance. Similarly, the work of Orengo et al. [121] also used beam elements to model the radial reinforcement of the tire in the shoulder areas. In this FE tire model, beam elements were implemented along the transverse direction of the tire on the inner edge of the solid elements that composed the liner (Figure 5.4 (a)). The addition of beam elements was necessary to circumvent issues in preliminary model simulations which showed excessive tire expansion during inflation. Its purpose served to provide a variable that was used to refine the behaviour of the model during inflation, without negatively affecting the performance of the model during the application of static loads.

For the FE simulations, lateral deflection was calculated as the difference in lateral positions of the tire's outer surface between two tire conditions (e.g. pressurized and pressurized with static loads applied). After the addition of beam elements, the lateral deflection of the tire during the pressurization process was reduced from 40.5 mm to 13.3 mm, which was more representative of physical behaviour. This decrease is attributable to the tension developed in the beam elements during the pressurization process. Conversely, the lateral deflection of the tire between pressurization and static loading increased from 24 mm to 36.6 mm, after the addition of beam elements. This behaviour is attributed to the fact that with beam elements the tire deforms much less during pressurization; thus allowing it to deform during the application of static loads, more representative of the behaviour of real tires. The beam elements used in the model were discrete beams with a circular cross-section radius of 1.0 mm, an elastic modulus of 10,000 MPa, an initial tension of 50 N, and a mass density of 7800 kg/m<sup>3</sup>. The radius of 1.0 mm does not represent physical dimension and this value was selected for calculation convenience. The value of the elastic modulus was selected in consideration with the number of beam elements and diameter to obtain desirable tire deflections (tire stiffness). In total, there were 64 beam elements in the radial direction of each row, resulting in a total of 9,024 beam elements in the entire half tire model. Figure 5.4(b) illustrates deformation of the tire at the contact patch, which resembles that which has been observed in practice.



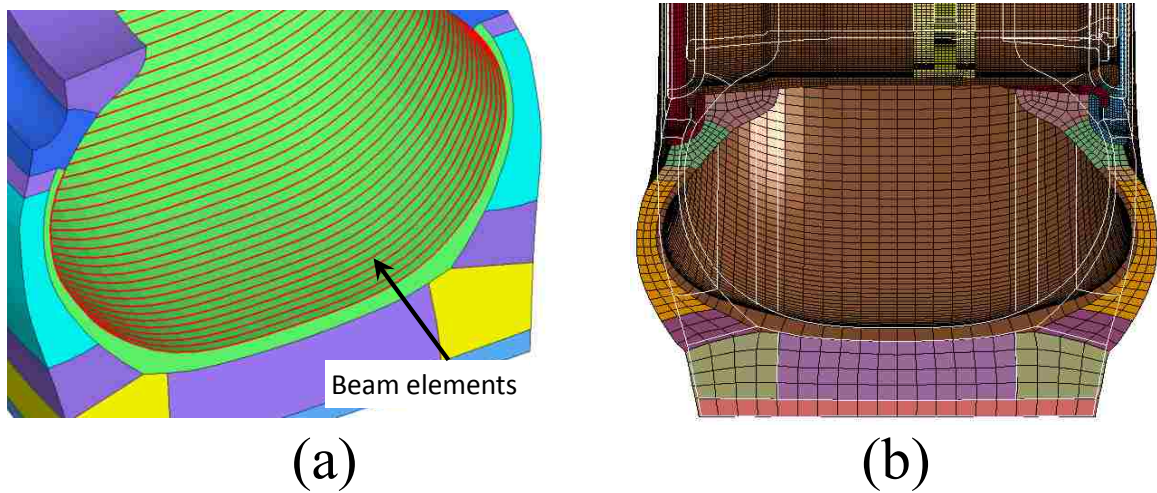


Figure 5.4 (a) beam elements added and (b) deformation of the tire at the bottom contact patch.

Based upon the details provided in the previous sections, assignment of the elastic moduli for the various regions of the tire was completed as presented in Figure 5.5.

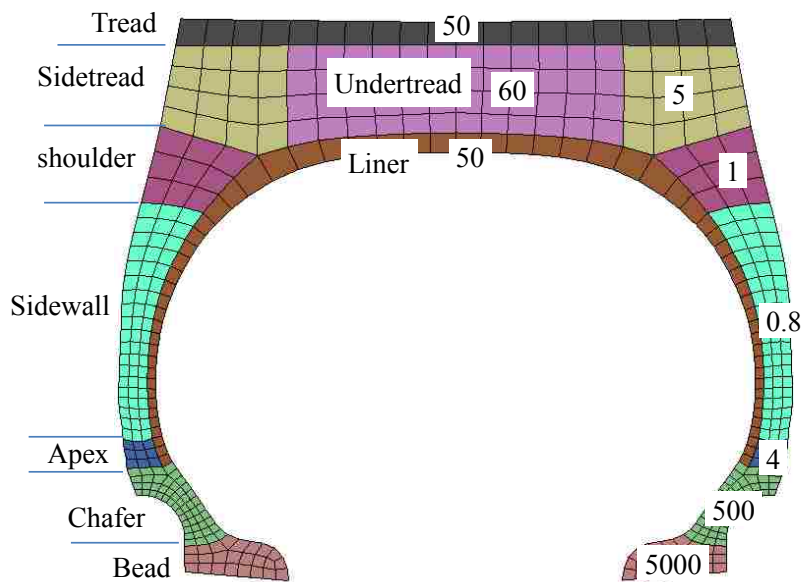


Figure 5.5 Tire region definitions and the associated elastic moduli assigned (in MPa).

Another aspect to note is that the selection of the material properties for modeling the tire in this research is not unique. If alternate material properties (Poisson's ratio, elastic modulus) are chosen for a region of the discretized tire model, it is possible to potentially determine the same predictability of the tire model with the variation of the material properties in other regions.

### 5.1.2.2. Tire Pressure Modelling

To model the inflation process observed in practice, the initial positions of the tire beads were offset 30 mm on the inside of both sides of the tire, relative to their final seating positions, as shown in Figure 5.6. Two rigid virtual discs (with the same shape and size as the flanges) were added to reduce the speed of bead motion due to the rapid pressure increase used in the model. Since they were only used to slow the movement of the bead regions and to properly seat them during initial pressurization, they were created to not interface with other components in the FE model. Furthermore, when the bead regions were within contact range of the front and back flanges, the contacts between the virtual discs and the beads were deactivated, such that the beads could freely make contact with the flanges in the lateral direction.

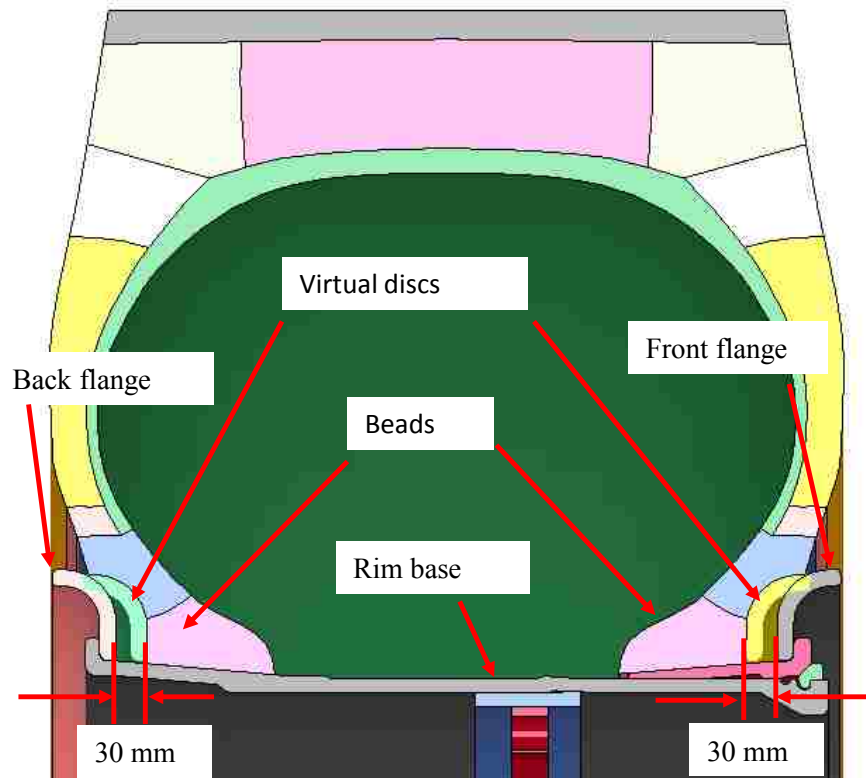


Figure 5.6 Set-up for simulating tire inflation.

Often in tire modelling, the internal pressure is implemented as a pressurized control volume within LS-DYNA. This definition requires a set of parts to form a closed boundary in the model. One benefit of using a control volume is that as the volume changes, the pressure will also adjust based upon the characteristics of the control volume. However, during the tire pressure initialization process, the areas forming the closed volume of the tire change due to the movement of the tire beads. If the control volume method was used to model the internal

pressure, it would be difficult to define the control volume due to the inconsistent enclosed boundary resulting from large bead movement. Under load conditions considered in this study, the enclosed volume was assumed to experience negligible volume change and the temperature of air inside the tire was similarly assumed constant, therefore the pressure inside the tire was assumed unchanged. In an effort to reduce the complexity of the tire model in this study, the tire pressure was modelled with constant surface pressure applied on the tire inner surface.

### 5.1.2.3. Other Critical Modelling Features

A penalty based surface to surface contact definition was applied to model the interaction between all tire and wheel components. For contacts amongst wheel components, which were modelled as steel, a coefficient of static friction of 0.35 was used. A coefficient of static friction of 0.2 was applied to contact areas between the bead region and the BS band and rim, to reflect the fact that in practice a lubricant is applied to the bead region to ensure it can slide along the BS band/rim with ease during the inflation process.

At the interface between the chafer and the front/back flanges, where no lubricant was applied and to ensure the tight contact within this region, a coefficient of friction varying from 0.85 to 1.0 was considered in the model development. Observations regarding the relative movement of this portion of the tire and the wheel indicated no separation at this interface throughout all testing. This range of the coefficient of friction was realistic given that the coefficient of static friction between rubber and solids has been noted to range from 1.0 to 4.0 under dry conditions [123] and from 0.6 to 0.9 between steel and rubber [124]. A final value of unity for the coefficient of friction was used within this investigation.

A stationary rigid wall was created below the bottom of the tire to model the contact between the tire and the ground, with a friction of coefficient of 1.0 to prevent tire slip.

During early model development, the application of static forces resulted in tire deformation hysteresis and tire vibrations. These traits are attributable to the interior pressure of the tire. To address the presence of deformation hysteresis and tire vibrations within the model, mass weighted nodal damping and second order objective stress updates were applied to the model [120]. The force vector ( $F_{damp}$ ) due to system damping was determined from Equation (5.1) according to LS-DYNA [114].

$$\{F_{damp}\} = 2 \cdot \omega \cdot \{m\} \cdot \{v\} \quad (5.1)$$

In the equation,  $\omega$  is the natural frequency (given in radians per unit time),  $m$  is the nodal mass, and  $v$  is the nodal velocity. This is done to achieve the effect of damping both rigid body motion as well as tire vibration. To assess the amount of damping required for the model, an eigenvalue analysis was conducted to find the natural frequency of the model. This allowed determination of damping constants suitable for the tire pressurization process and static force application which were selected as 35 and 39, respectively. With these damping constants, the damping energy was less than 25% of the internal energy of the model, thus validating the use of damping.

To circumvent hourglass deformation, the Flanagan-Belytschko stiffness hourglass control with a coefficient of 0.1 was employed for the entire tire [114]. Hourglass modes are nonphysical, zero-energy modes of deformation that produce zero strain and no stress. Hourglass modes occur only in under-integrated solid, shell, and thick shell elements. LS-DYNA has various algorithms for inhibiting hourglass modes. Hourglass control introduces non-physical energy in the FE analysis and this energy is referred to as hourglass energy. Hourglass energy should be kept as low as possible, typically less than 10% of the system's peak internal energy. For the simulations conducted in this research, the maximum hourglass energy was found to be 6.29% of the peak internal energy of the simulation.

Mass scaling and time scaling techniques were used to improve the computational efficiency of the model. The time periods of the excitations of the tire during the experimental deflection testing were approximately 10 seconds. These time durations were reduced by one order of magnitude when used in the FE model in order to expedite the simulations, without affecting the acceptable levels of accuracy. In order to maximize the time step during simulations, a constant time step of  $1.8 \mu\text{s}$  was used, with the majority of the mass added to the lock ring portion of the wheel, as most of the small elements are located in this part due to geometric constraints. Trial simulations without mass scaling were conducted and compared to simulations with mass scaling where results indicated a negligible difference in model behaviour. The FE keywords used in tire modeling was illustrated in Appendix E.1, with important parameters of FE modeling included.

#### **5.1.2.4. Static and Quasi-static Deflection Testing Simulations**

Due to the symmetry of geometry and boundary conditions, only half of the wheel assembly was modelled and symmetric boundary conditions were applied along the plane of symmetry, for static load simulations. The half wheel assembly model contained 65,520

hexahedral elements and 9,024 beam elements for the tire, while 222,528 hexahedral and pentagonal elements were used for the wheel components.

#### 5.1.2.4.1. Static Loading Simulations

Static loading simulations were performed to numerically reproduce the experimental testing protocol detailed in Chapter 4 (Scale Testing) and two loading phases were employed. First, the tire model was loaded under its own weight (gravity) and air pressure was applied to the inner surface of the tire liner. Subsequently, forces consistent with the scale readings were applied to the centre node of the wheel, which was constrained to the rigid mounting disc. The forces due to gravity and the vehicle loads were ramped up from zero to full load in 0.05 seconds, while the pressure in the tire was ramped up from zero to full load 0.593 MPa (86 psi) in 0.1 seconds. Figure 5.7 shows the load application time history. While the technique of applying gravity and pressure in a more rapid fashion than in practice (time scaling) was applied, the ratios of kinetic energy to internal energy of the entire system indicated small values (less than 3.6%); thus validating the use of time scaling.

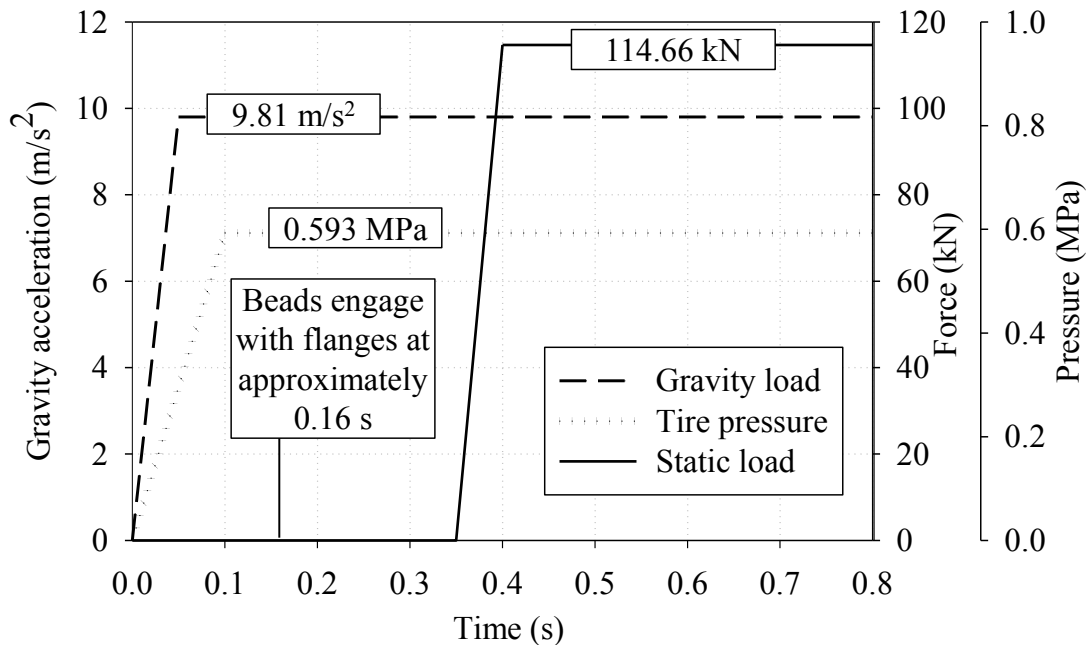


Figure 5.7 Load applications for static load simulation.

#### 5.1.2.4.2. Quasi-Static Loading Simulations

Quasi-static loading simulations were performed to numerically reproduce the experimental protocol described in Chapter 4 (Deflection Testing). In these FE simulations, the first two phases of static loading FE simulations (gravity and pressure loads) were applied,

followed by a third phase. During the third phase, a prescribed motion was applied to the centre of the wheel. The motion prescribed encompassed the planar motion of the wheel which was observed from the experimental tests. The translational and rotational degrees of freedom of the wheel (in the plane of motion), which were obtained from the analysis of acquired high speed camera footage using ProAnalyst, were applied to the wheel within the numerical model. This allowed for better simulation of the entire system consistent with the experimental testing, as both horizontal and vertical displacements as well as the rotation of the wheel were observed during experimental testing. The load application process to simulate test event 3 is shown in Figure 5.8.

It is important to note that time scaling technique was used to simulate the test events in order to save CPU calculation time. The simulated time was the time period of each experimental test event divided by 10. When comparing the simulation results with the test results in Section 6.1.1, time scaling was applied to the simulated results by multiplying the time by 10.

Given that the full planar motion of the wheel was considered in these simulations, the full tire was modelled. This was accomplished by removing the symmetric boundary conditions initially prescribed to the half tire model and mirroring the tire and wheel about its plane of symmetry. The detailed modelling information is listed in Appendix E.2.

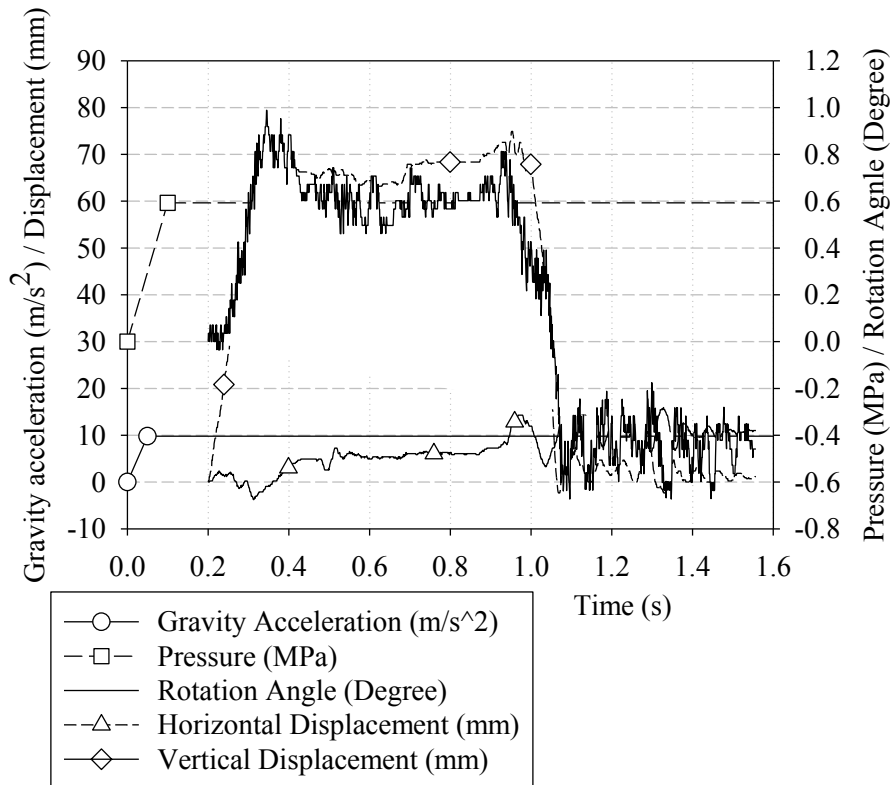


Figure 5.8 Load applications for quasi-static simulation.

### 5.1.2.5. The Computer Used for the Simulations and Simulation Time

The computer used for the simulations is a Dell desktop computer model Precision T7500, with twelve processors (Intel(R) Xeon(R) CPU, X5675@3.07GHz). One simulation was conducted at a time and all simulations were conducted using all the 12 CPUs. For the static load simulations, half of the wheel assembly was modelled with a simulation time of 0.7 seconds and the each simulation finished in approximately 7 hours; for quasi-static load conditions, the whole wheel assembly was modelled and the simulation time was between 1.3 seconds and 2.1 seconds, according to different test events, and the computation time for 1.3 seconds simulation time was approximately 22.5 hours. LS-DYNA version 971, revision 7600.398 was used to run the simulations.

## 5.2. Numerical Rim Base Model Development

Numerical testing was conducted under conditions identical to experimental testing, where an external load was applied to the system. Due to the symmetric nature of the geometry and loading only one half of the rim base structure was modelled, as illustrated in Figure 5.9. Symmetric boundary constraints were applied on the plane of symmetry ( $x/z$  plane).

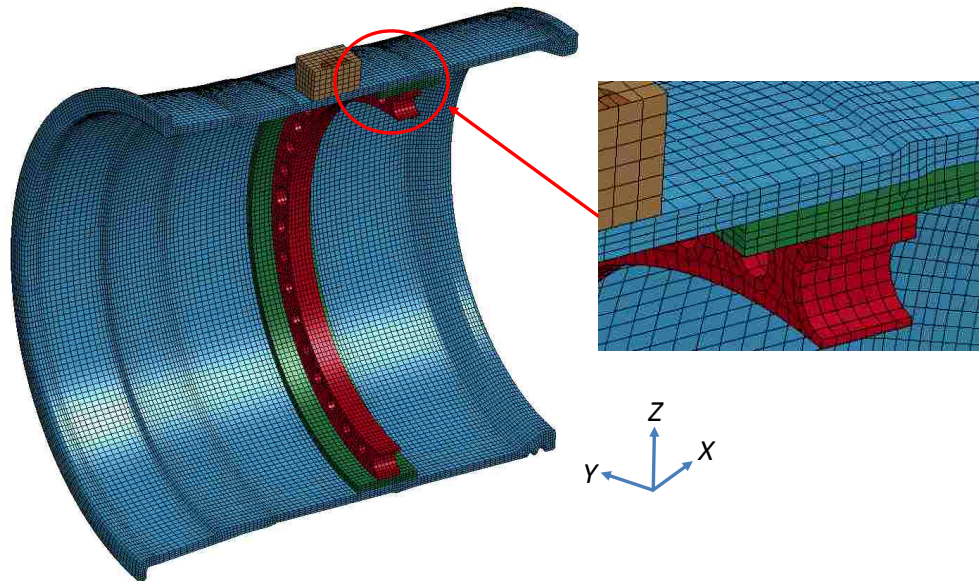


Figure 5.9 Half rim base model illustrating mesh discretization.

Rigid shell elements were used to model the support surfaces of the steel support blocks since they experienced negligible deformation during the experimental loading process. Full boundary constraints were applied to the support blocks. Although a rigid material model was invoked for the support surfaces, material properties consistent with steel (elastic modulus,

density, and Poisson's ratio equal to 210 GPa, 7800 kg/m<sup>3</sup> and 0.28, respectively) were applied within the rigid material definition. Although no deformation of the elements occurs, such information is needed for the contact definitions which contain the support surfaces.

The 50.8 mm diameter aluminum pad was modelled with rigid shell elements and used to apply the external load to the system. Single point boundary constraints were applied to the aluminum pad to permit motion in only the *z*-axis direction. The rigid material model utilized for the aluminum pad incorporated material properties consistent with aluminum (elastic modulus, density, and Poisson's ratio equal to 72 GPa, 2700 kg/m<sup>3</sup> and 0.33, respectively).

The rectangular aluminum block, which conformed to the curved profile of the rim base, was modelled using single point quadrature solid elements having elastic material properties. The elastic modulus, density, and Poisson's ratio of the rectangular aluminum block was prescribed as 72 GPa, 2700 kg/m<sup>3</sup> and 0.33, respectively. No permanent deformations of the block were noted in any of the experimental tests. Under-integrated solid elements were utilized for the aluminum block, with 384 elements used to discretize this structure. The aspect ratio of the elements within this portion of the model was approximately 1.2.

Surface to surface contact definitions were used to establish interfaces between (1) the rigid disc and the aluminum block, (2) the aluminum block and the rim, and (3) the rim and support blocks. The coefficient of friction, within these contact algorithms, is a function of the static and dynamic coefficients of friction as well as the relative sliding velocity between surfaces and a decay coefficient as expressed in Equation (5.2) [114].

$$\mu = \mu_D + (\mu_S - \mu_D) \cdot e^{-DC \cdot |v_{rel}|} \quad (5.2)$$

No relative motion was noted to occur within the experimental testing and thus a consistent coefficient of friction equal to 0.3 was applied. This occurs if  $\mu_S = \mu_D = 0.3$  and  $DC = 0$  as was implemented into the model. This coefficient of friction was determined from simple experimental testing completed between the interacting surfaces. Gravity was also applied to the system, with a local acceleration due to gravity of 9.807 m/s<sup>2</sup> prescribed.

The cross-section of the rim base (within the *x/z* plane), excluding the mounting ring, was first meshed using shell elements, which were then revolved about the centreline of the rim to form the three dimensional FE model of the structure. Careful discretization of the cross-section was completed to ensure that a suitably sized mesh was constructed with interior angles approximately equal to 90 degrees. Furthermore, a uniform and consistent mesh through the cross-section was developed. Following this process the shell elements were revolved about the



centreline of the rim through 180 degrees (1/2 of the model) utilizing 140 increments in the circumferential direction. Great care was taken to ensure that the hexahedron elements were maintained as close to cubes as possible. The smallest element length ranged from 2.2 mm to 11.0 mm, with an average of 4.5 mm. The maximum aspect ratio of all solid elements was 3.6 and the average aspect ratio was 1.92. Four hexahedronal elements were used through the thickness of the rim base to appropriately capture bending stiffness. The mounting ring was meshed by constructing a shell section in the  $y/z$  plane where appropriate holes for fasteners were incorporated into the model. Following the creation of these shell elements, extrusion along the  $x$ -axis direction was completed with 6 increments to form the solid elements to represent the mounting ring. All solid elements were modelled using one point constant stress integration formulation within the rim base and support band. In some regions of the mounting ring, four elements through the thickness could not be obtained, as illustrated in the inset within Figure 5.9, correspondingly, this region of the rim base model incorporated a selective reduced solid element formulation. The rim base was meshed with 71,680 hexahedrons elements, the support band contained 9,800 hexahedrons, and the mounting ring was discretized using 5,064 hexahedrons and 144 pentahedrons.

As a result of the linear observations obtained from the experimental tests, an elastic material model was assigned to the rim base. The elastic modulus, density, and Poisson's ratio, equal to 210 GPa, 7800 kg/m<sup>3</sup> and 0.28, respectively, were utilized in this material model.

To measure the surface strain of the rim base, 36,120 shell elements having a thickness of 0.01 mm, were extracted from the outer surface of the structure. This approach is common in FE modeling for durability analysis of solid structures to accurately capture surface stresses and strains. This data is critical in fatigue and engineering analyses which involve crack formation at exterior surfaces. The effect on the rim stiffness by adding this thin layer of shell elements was assumed to be negligible. The Belytschko-Tsay shell element formulation was used for these shell elements with three integration points through the thickness. The strains output from the midpoint of the shell elements were used for comparison with the experimental tests.

Explicit time integration was applied in this numerical model with a time step scale factor of 0.9 applied to the Courant condition necessary for stability of the explicit time integration scheme. A shared memory parallel (SMP) version of LS-DYNA, incorporating single precision was invoked. The simulation took 3 hours 30 minutes using 12 CPUs on a Dell T7500 workstation having Intel X5675 Xeon processors with an internal clock speed of 3.07 GHz and 12 Mbytes of level 3 cache. To reduce simulation CPU costs, time scaling was invoked for the

structural analyses. Loading was prescribed to the 50.8 mm diameter aluminum pad starting from zero to 100 kN, in a manner consistent with the experimental tests. However, within the numerical simulation, the time which the load was increased from zero to 100 kN was over a period of 1 second. Following the completion of the simulation two critical observations were investigated to ensure the appropriateness of the time scaled (quasi-static) solution. Firstly, it was determined that the kinetic energy was found to be negligible (less than 1%) when compared to the internal energy. Secondly, no significant differences between the applied external load at the top of the rim base and the sum of the support loads at the two support bases was found. Correspondingly, a quasi-static simulation was completed and the use of time scaling was appropriately justified. Detailed modelling information is listed in the input file of Appendix E.3.

## Chapter 6. Stress and Fatigue Life Analyses

The tire and rim base models were validated based on the comparisons of the results between experimental tests and numerical simulations. The validated tire/wheel assembly model was used to conduct stress and fatigue life assessment of the wheel components at critical regions under severe loading conditions and the further design improvements of the multi-piece wheels were based on the validated tire/wheel assembly model.

### 6.1. FE Model Validation

#### 6.1.1. FE Model Validation for Tire 29.5-29

##### 6.1.1.1. Validation Procedures

###### 6.1.1.1.1. Static Loading Behaviour Validation

Validation of the numerical tire model was performed in three steps. First, the ability of the tire model to correctly predict centre wheel deflection and maximum lateral sidewall deflection for a prescribed centre wheel load was verified based on Goodyear engineering data. As previously discussed (Table 4.2 and 4.3), the Goodyear data indicated that for tire 29.5-29, under a static load equivalent to approximately 230 kN at wheel centre, the tire would experience a vertical deflection of 80 mm and a maximum lateral sidewall deflection of 36.5 mm (one side), when pressurized to 627 kPa (91 psi).

In the next step of validation, the static deflections of the simulated tire model under various loads were compared with the experimentally obtained scale testing deflection measurements in Chapter 4. This step is considered a comparison of static load deflection behaviour of the tire, in which the gross vehicle weight was input into the FE model and the vertical and maximum lateral sidewall deflections were output for comparison. Furthermore, as the experimental tire pressure was 86 psi (0.593 MPa), this step is also used to validate the effectiveness of the model at simulating pressure different from that which is referenced in the Goodyear data.

The percentage error, calculated using Equation (6.1), was used to assess the predictive capabilities of the numerical model relative to the experimental observation. In Equation (6.1) 'Nv' represents the value of the numerical variable and 'Ev' represents the corresponding experimental measurement.

$$\% \text{ error} = \left( \frac{N_v - E_v}{E_v} \right) \cdot 100 \quad (6.1)$$

#### 6.1.1.1.2. Quasi-Static Loading Behaviour Validation

The final step in the tire model validation consisted of comparing the deflections of the model under the quasi-static loading conditions against the measurements recorded during the deflection testing. In this step, two separate comparisons were able to be made, due to the amount of data collected during the deflection testing; thus allowing for a more thorough validation of the model in the most computationally intensive simulation regime of this study.

In the first comparison, the maximum lateral sidewall deflections of the tire were compared to those experimentally obtained using the 100 mm Acuity AR700 series displacement transducer. Data points were first plotted in the time domain to illustrate the lateral deflection as a function of time and were subsequently plotted as a function of the vertical deflection of the wheel centre.

In the physical tests, the laser displacement transducer was supported by a fixed height tripod positioned on the ground. Due to the vertical deflections of the tire during loadings, the measured lateral sidewall deflections were not of a fixed point on the tire, but instead of a continuous vertical line, based on the amount of vertical tire deflection experienced at the maximum lateral sidewall points. To account for these measurement variations, three nodal points in the FE tire model were tracked within the vicinity of the area which was recorded by the transducer. Results from tracking the three nodes indicated a difference in lateral deflection of 2-3 mm per node. Therefore, the average of the three nodal measurements was taken for each simulation, and was used to compare with the experimental testing data.

In the second comparison, the vertical ( $z$ -direction) and longitudinal ( $y$ -direction) deflections of selected points on the tire was compared. As previously discussed, the experimental deflection of these points were determined through acquisition of high speed photographs, using a Fastec high speed camera followed by motion tracking of the various highlighted locations in Figure 6.1(H-in, H-out, D-in, D-out, V-in, and V-out) using ProAnalyst. The locations of the tracked points on the physical tire and the corresponding nodes tracked in the FE model are illustrated in Figures 6.1 (a) and 6.1 (b).

For the quasi-static comparisons, maximum relative errors calculated using Equation (6.1) and more rigorous accumulative errors and validation metrics using Equations (4.1) and (4.2) were conducted.

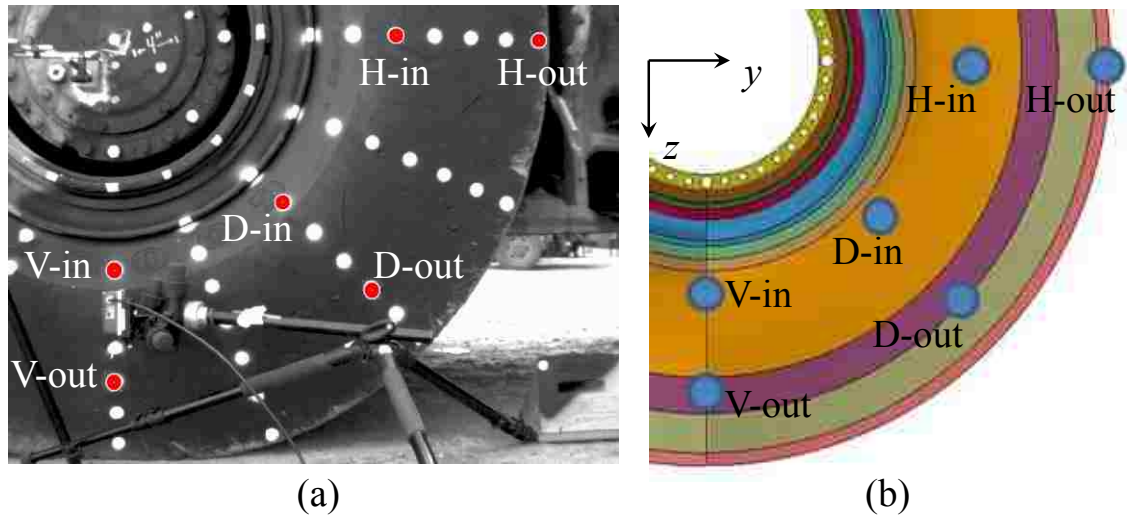


Figure 6.1 Location of points tracked on the physical test apparatus (a) and numerical model (b).

### 6.1.1.2. Results and Discussions

Before quantitative comparisons between experimental tests and simulations are presented, qualitative comparisons were assessed in terms of general tire deflection behaviour. It was observed that the tire bulged at the lower portions of the tire for both experimental tests and simulations. The shapes of deformed tire and the extent of deformation were observed very similar between the experimental tests and simulations. For quasi-static conditions, the tire deformed at the same fashion in the time domain between the experimental tests and simulations.

#### 6.1.1.2.1. Static Loading Behaviour

The resulting vertical deflection and sidewall deflection of the tire model for a tire pressure of 627 kPa (91 psi) and a centre wheel loading of approximately 230 kN are presented in Table 6.1, along with the equivalent engineering data from Goodyear Off-The-Road Tires. As can be observed, the model appears to correlate well with the engineering data, with a maximum vertical deflection error of 3.3%, and a negligible lateral deflection error.

Table 6.1 Vertical and Lateral Deflections for static loading condition.

	Vertical Deflection	% Error	Lateral Deflection	% Error
Engineering data	80.0 mm	3.3%	36.5 mm	0.3%
FE simulation	82.6 mm		36.6 mm	

Observations from the scale testing described in Chapter 4 are included in Figure 6.2, as are those of the static loading simulations. In both instances, a tire pressure of 593 kPa (86 psi) was implemented. Linear regression was performed on each dataset, and the resulting fits were

plotted in Figure 6.2. The correlation coefficient ( $R^2$ ) for the regression analysis from experimental findings for the vertical and lateral deflections was observed to be 0.945 and 0.898, respectively. Correlation coefficients for the regression analysis based upon numerical observations were equal to unity for both vertical and lateral deflections. The slopes of vertical deflection versus load are 0.356 mm/kN and 0.341 mm/kN for scale tests and simulations, respectively. The slopes of lateral deflection versus load are 0.147 mm/kN and 0.155 mm/kN, respectively. As can be observed, the numerical model correlates well with data obtained in the field, with an error of -4.2% for vertical deflections and an error of 5.4% for lateral deflections, as summarized in Table 6.2. Furthermore, both experimental and numerical testing shows that the load-deflection behaviour of the tire is essentially linear for the range of static loading conditions performed in this study. This linearity correlates with data provided by the tire manufacturer 0.346 mm/kN and 0.158 mm/kN, respectively for vertical displacement and lateral tire deflection.

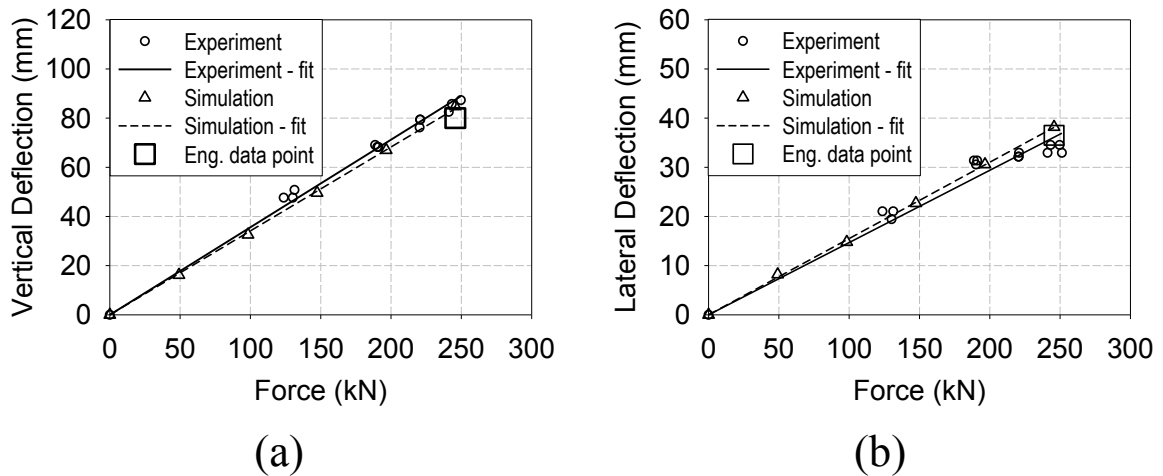


Figure 6.2 (a) Vertical deflection/load response and (b) lateral deflection/load response for tire 29.5-29.

Table 6.2 Slope comparisons for vertical and lateral deflections versus load.

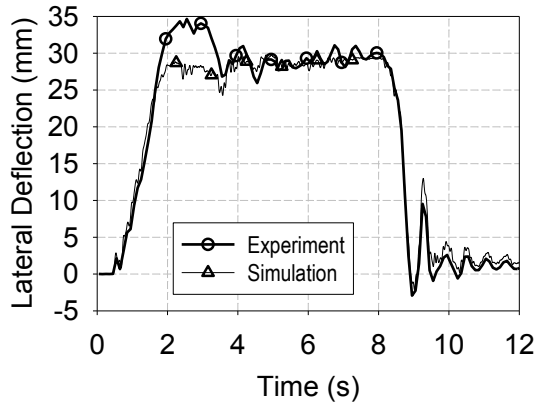
	Vertical Deflection	% Error	Lateral Deflection	% Error
Experiment	0.356 mm/kN	-4.2%	0.147 mm/kN	5.4%
Simulation	0.341 mm/kN		0.155 mm/kN	

#### **6.1.1.2.2. Quasi-Static Loading Behaviour**

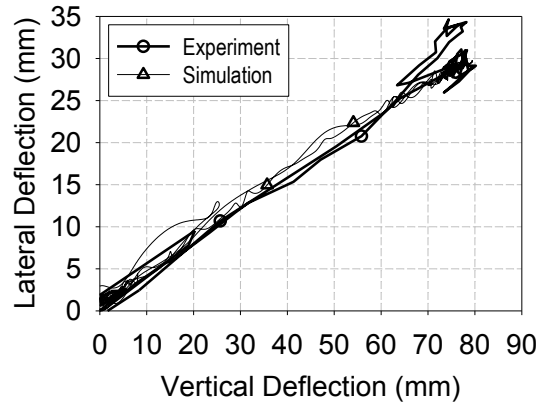
##### **Maximum Lateral Sidewall Deflection**

The results from experimental deflection test events as described in Chapter 4 are presented in in Figures 6.3 to 6.6, as well as the numerical results from the quasi-static loading simulations described in Chapter 5. Event 1, with observations presented in Figure 6.3 (a) and 6.3 (b), was the most severe loading condition on the tire, resulting in a maximum vertical deflection of approximately 80 mm. The corresponding lateral deflection for this event was noted to be maximized, having a value of approximately 35 mm, when the vertical deflections were most significant. A linear relationship between lateral and vertical deflections was noted for all events for both experimental and numerical findings. A regression analysis of the lateral/vertical deflection relationship resulted in slopes for event 1, 2, and 3, of 0.396 mm/mm, 0.359 mm/mm, and 0.346 mm/mm, respectively. This finding indicates that the lateral deflections were typically 37% of the vertical deflections and consistency amongst all tests was noted. Differences in the slopes of the lateral/vertical deflection relationship from experimental findings to numerical predictions were typically less than 13%, with the average slope for numerical findings being equal to 0.39 mm/mm. A minor degree of hysteresis was noted in both testing methods, with the experimental observations being slightly greater on this aspect of the lateral/vertical deflection relationship.

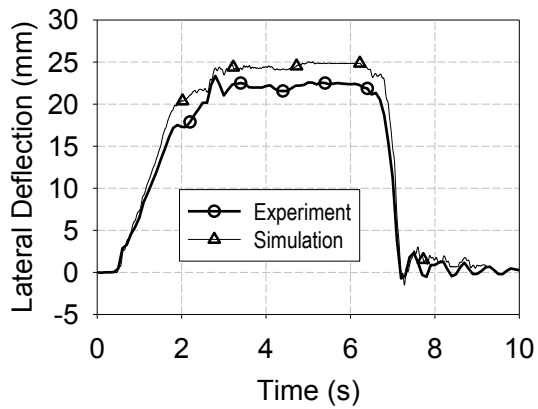
For the time domain comparisons, the numerical results demonstrate good correlation with tire deflections obtained experimentally for all test events. For event 1, there exists a difference of approximately 17% between the numerical and experimental findings, from 1.8 s to 3.5 s. However, for the remainder of the simulation, the percentage error is almost negligible between the two responses. Results from events 2 and 3 also demonstrate good correlation between numerical and experimental findings, with the numerical models only over-predicting the experimental findings by a maximum of 10% during the entire duration of each event.



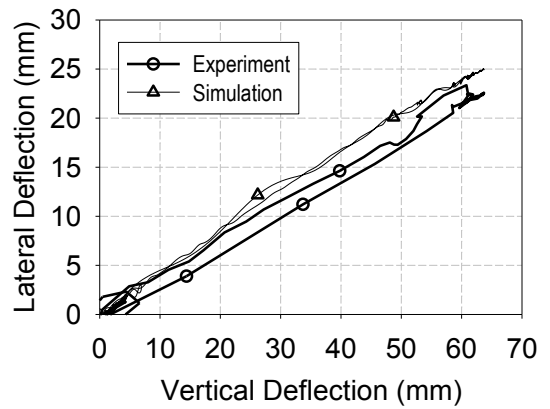
(a)



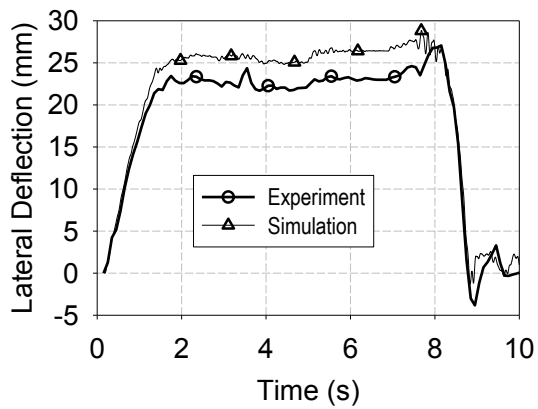
(b)



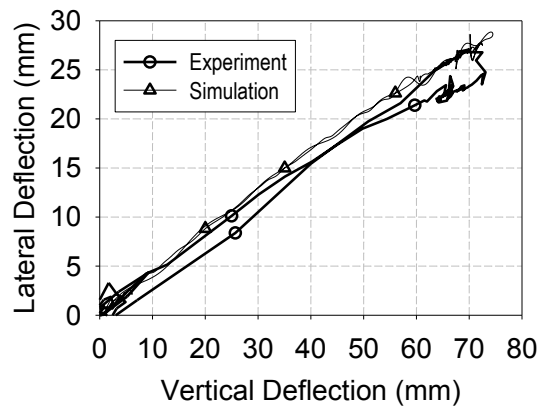
(c)



(d)



(e)



(f)

Figure 6.3 (a) Lateral deflection versus time for event 1, (b) lateral versus vertical deflection for event 1, (c) lateral deflection versus time for event 2, (d) lateral versus vertical deflection for event 2, (e) lateral deflection versus time for event 3, (f) lateral versus vertical deflection for event 3.



## Vertical and Horizontal Deflection Comparisons for the Quasi-Static Testing

Comparison of the vertical ( $z$ -direction) and horizontal ( $y$ -direction) deflections at selected points between experimental findings and numerical simulations show acceptable correlations for all events. For brevity only the findings from the most severe testing condition, event 1, are presented in Figure 6.4 through 6.6. Comparisons for test event 2 and 3 are listed in Appendix D.

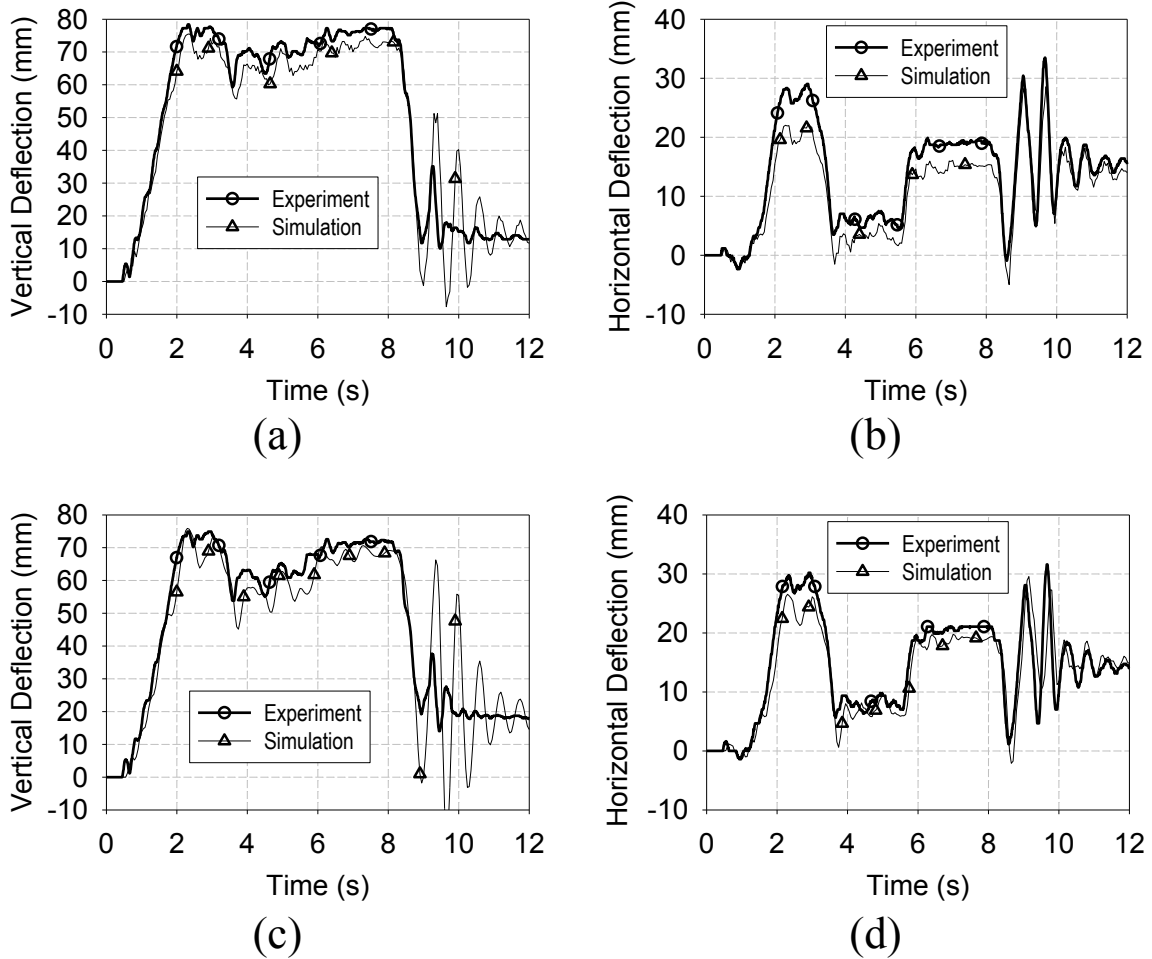


Figure 6.4 Deflection comparisons at H points for event 1, (a) Vertical deflection versus time for H-in location, (b) horizontal deflection versus time for H-in location, (c) vertical deflection versus time for H-out location, (d) horizontal deflection versus time for H-out location.

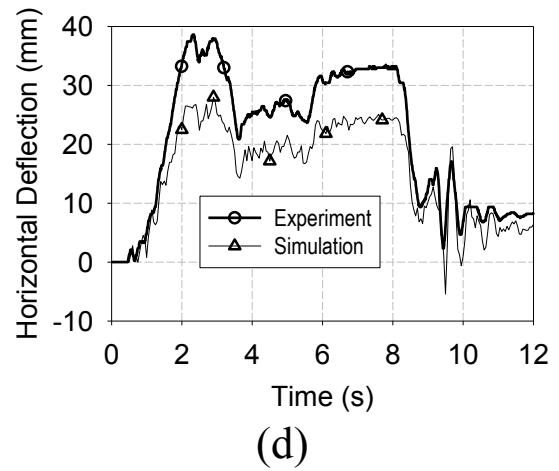
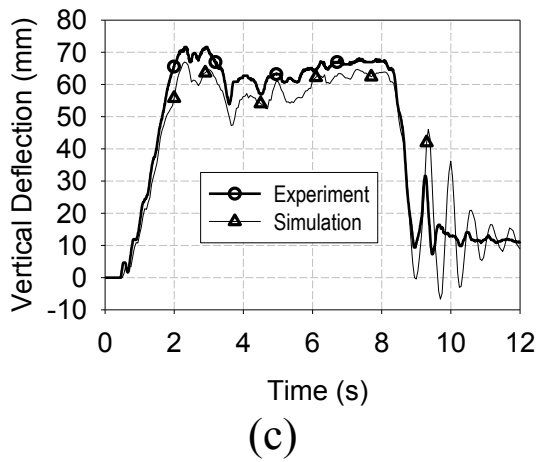
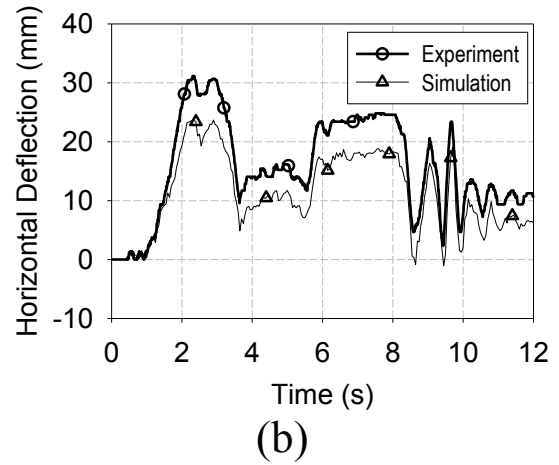
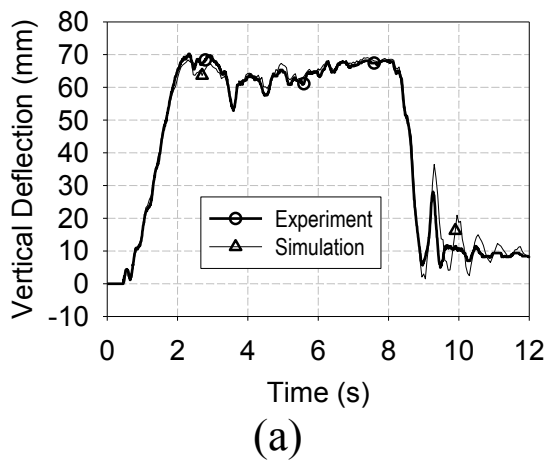


Figure 6.5 Deflection comparisons at D points for event 1, (a) Vertical deflection versus time for D-in location, (b) horizontal deflection versus time for D-in location, (c) vertical deflection versus time for D-out location, (b) horizontal deflection versus time for D-out location.

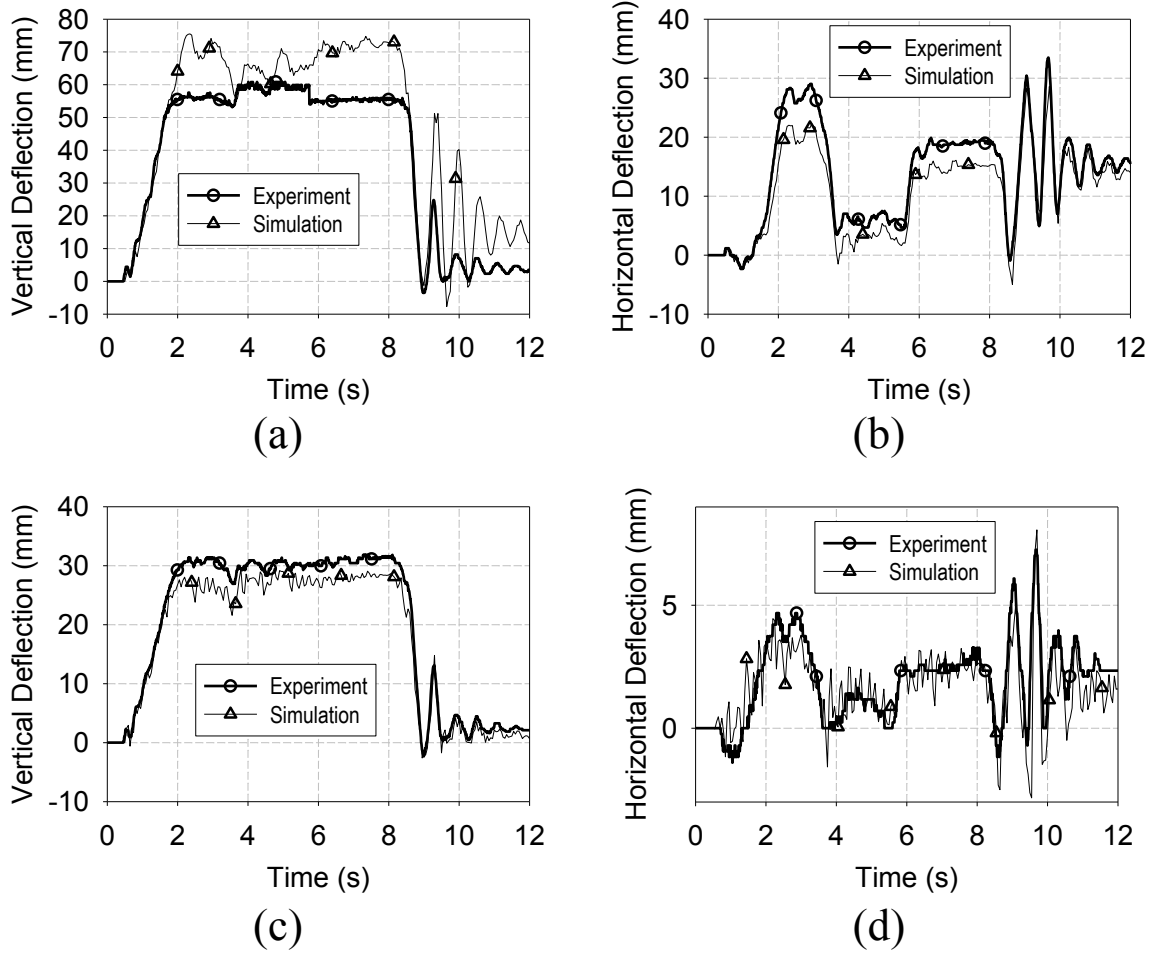


Figure 6.6 Deflection comparisons at V points for event 1, (a) Vertical deflection versus time for V-in location, (b) horizontal deflection versus time for V-in location, (c) vertical deflection versus time for V-out location, (b) horizontal deflection versus time for V-out location.

The various responses presented in Figures 6.4 through 6.6 demonstrate the deformation behaviour of the tire in the vertical and horizontal directions for the various locations considered. Generally consistent findings between the vertical and horizontal measurements are noted for both experimental and numerical testing schemes. The greatest percentage error was calculated to be approximately 27% and is a result of the differences in the experimentally measured and numerical predicted vertical deflections occurring from approximately 6 seconds to 8 seconds at the V-in point location. It was noted that near the vicinity of the V-in point location, the vertical deflection observations were highly sensitive based on the location of the point selected in the FE model, since the vertical deformation changes rapidly at the transition between the tread and

sidewall. The element size in this region of the tire is roughly 15 mm and the vertical deflections at neighbouring points exhibit significant variation as a result of the displacement field transition.

For vertical deflection comparisons in Figures 6.4 to 6.6, significant oscillations in the FE simulations were observed from 9 seconds to 12 seconds, compared to horizontal deflection comparisons. The oscillations were caused due to the applications of gravitational acceleration in the vertical direction in a short time of period by time scaling in the FE model.

### Accumulated Errors and Validation Metrics for Quasi-static Testing

Using Equations (4.1) and (4.3), accumulative errors and validation metrics were calculated for lateral deflection and other in-plane deflections of the points illustrated in Figure 6.1. The calculated values are listed in Table 6.3 for event 1. Within the table, “V” represents vertical direction and “H” represents horizontal direction. The average accumulative error was calculated to be 9.7% and the average validation metric was 0.96. For the other two events, the accumulated errors and validation metrics are similar to event 1, which are not presented here for brevity.

Table 6.3 Errors and validation metrics between experimental test and simulation for event 1.

		Accumulative error	Validation Metric
Lateral		2.7%	0.97
H-in	V	7.8%	0.92
	H	12.3%	0.77
H-out	V	7.5%	0.93
	H	8.2%	0.89
D-in	V	3.0%	0.97
	H	26.5%	0.74
D-out	V	5.0%	0.94
	H	29.8%	0.71
V-in	V	10.1%	0.90
	H	6.8%	0.93
V-out	V	4.3%	0.95
	H	2.3%	0.98
Average		9.7%	0.96

### 6.1.2. Rim Base FE Model Validation

Validation of the rim base FE model is completed using both vertical and lateral displacement measurements at locations ‘A’ and ‘B’ as well as circumferential strain measurements at locations ‘1’ through ‘5’, as illustrated in Figure 4.11. Graphical comparison of the model predictions and experimental findings (for Test #1 only) are presented in Figure 6.7 for the displacement measurements. Furthermore, Figure 6.8 illustrates the comparison of the predictions to findings for all circumferential strain measurement locations. To quantify the validity of the model predictions to experimental findings the relative error (Equation 6.1), accumulated relative error (Equation 4.1), and the validation metric (Equation 4.2) are utilized. These model validation metrics are presented in Table 6.4.

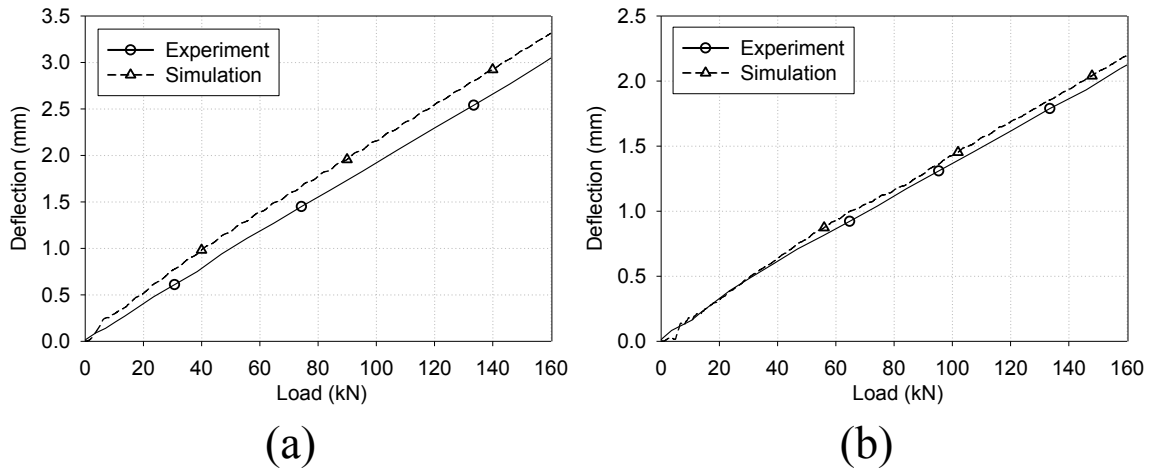


Figure 6.7 Comparison of experimental and numerical (a) vertical displacements and (b) lateral displacements measured from locations ‘A’ and ‘B’, respectively.

The displacement/load responses obtained from the numerical predictions correlate very well to the experimental findings. The maximum value of the relative error, for vertical and lateral displacement measurements was found to be approximately 10.5% and 4.8%, respectively. The cumulative relative error and validation metric were found to be 8.78% and 0.91 for vertical displacements. In the case of lateral displacement measurements a cumulative relative error and validation metric of 6.38% and 0.94 were noted, respectively. For the two locations considered for comparison, the numerical predictions generally overestimated the physical measurements.

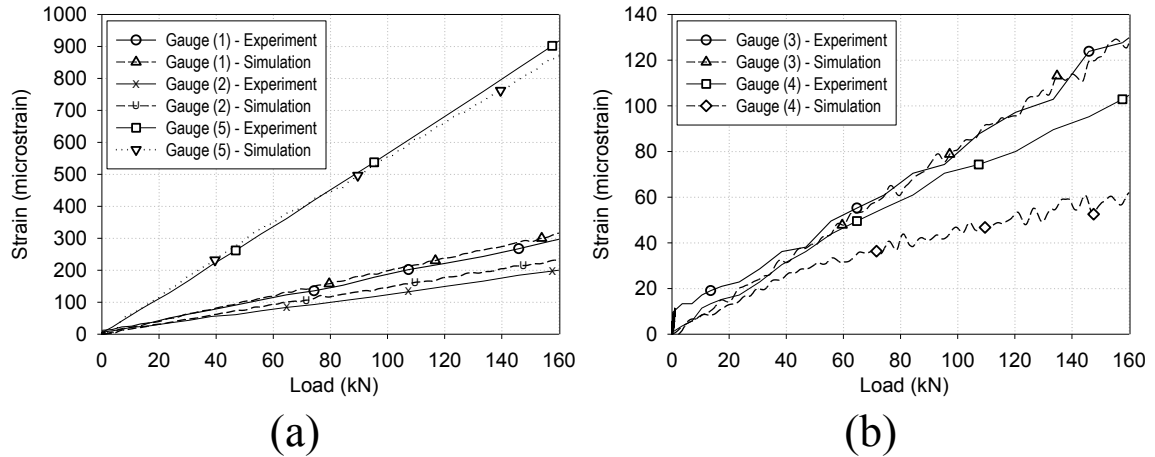


Figure 6.8 Comparison of experimental and numerical circumferential strains at (a) locations 1, 2 and 5 and (b) locations 3 and 4.

Table 6.4 Deflection (mm), strain (microstrain,  $\mu\epsilon$ ), errors, and validation metrics for simulations and experimental tests under static load condition.

Location	Displacement (mm)		Circumferential strain ( $\mu\epsilon$ )				
	Vertical (location 'A')	Lateral (Location 'B')	Gauge (1)	Gauge (2)	Gauge (3)	Gauge (4)	Gauge (5)
Experiment	3.00	2.10	292.19	197.26	127.62	102.86	901.90
Simulation	3.32	2.20	316.21	232.64	130.14	62.42	872.31
Relative error at maximum	10.54%	4.80%	8.22%	17.94%	1.97%	-39.31%	-3.28%
Accumulated relative error	8.78%	6.38%	7.98%	15.76%	4.96%	31.24%	3.81%
Validation metric	0.91	0.94	0.92	0.84	0.96	0.70	0.96

Figure 6.8 illustrates the circumferential strain versus load responses, which demonstrates favourable correlation for all gauges, with the exception of gauge (4), in which the simulation under-predicted the strain. The experimental and numerical observations for gauge (4) demonstrate a linear behaviour up to approximately 60 kN load. After this load was obtained, deviation of the simulation result from the experimental observation was noted. It is worth noting that percentage errors for gauge (4) at 40 kN and 60 kN applied loads are approximately 15% and 20%, respectively, which are considerably less than at maximum load. Differences in the apparatus setup and locations of the supports between the FE model and experimental test may be responsible for the difference in the discrepancies. Additionally, slight variation in the positioning and orientation of the strain gauges, when mounted to the rim, may also have

contributed to the observed variations. For all gauge locations other than (4), all relative errors at maximum strains were noted to be less than 18% with an average relative error of 7.85%. The accumulative relative error also illustrates similar findings for these strain gauge locations.

## **6.2. Geometry Degradation Modeling**

Though traditional automotive wheels are not considered consumable items and typically survive the life of a vehicle, OTR wheel components require replacement due to wear, corrosion, and cracks. This necessitates routine wheel inspection and maintenance to ensure proper conditions are satisfied for safe operation as well as dictating replacement when repairs are unfeasible. The failure of OTR wheels typically originates from three main factors: the multi-piece wheel structure, the exposure to high working loads, and the harsh operating conditions in which the wheels are used.

This section investigates the fatigue life of wheels under geometry degradations due to wear. The wheels considered are all five-piece designs and three different varieties are compared: a new OEM (original equipment manufacturer) wheel, a worn OEM wheel, and a heavy duty model HT2000 wheel manufactured by North Shore Industrial Wheel Mfg. (NSIW). In these three varieties, the steel material properties of the wheels are assumed to be as-received (not used). The worn OEM wheel represents geometry degradation from the new OEM wheel. The wheels considered have the same size 29-25.00 /3.5 (Diameter-width/flange height), which are commonly used for 29.5-29 or 29.5R29 OTR tires on underground Caterpillar R2900G load-haul-dumps (LHDs) and Caterpillar AD45B dump trucks.

### **6.2.1. The OEM Wheel Information and Wear Conditions**

During service, the lock ring groove can be worn out due to fretting and galling at the contact area between the locking ring and the groove as shown in Figure 2.16. Loss of material in this region is a serious concern as the lock ring may be insecurely engaged with the rim base and may fail under high loads. Additionally, with less material in this region, highly fluctuating impacting forces between the lock ring and lock ring groove will accelerate the development of fatigue cracks in the groove region, therefore reducing the fatigue life of the rim base.

Considering the back section of the wheel, this area can become worn thinner in the axial direction and deeper in the circumferential direction due to sliding wear from the flange. The loss of material in this region will similarly accelerate crack development and growth, and shorten the service life of the wheel.

In order to ensure the safety of OTR wheels, NSIW tracks most in-service wheels at mine sites and carries out routine check-ups and maintenance as required. To facilitate inspections, tolerance “GO/NO-GO” gauges were designed and used to check critical regions of the wheel. Figure 6.9 shows the use of these gauges in the back section of the rim base. A “GO” condition signifies the wear is not significant enough to warrant repair or replacement, whereas “NO-GO” conditions means the wear in the particular region is too large and out of tolerance, meaning the region has to be replaced or repaired in order to maintain safe working conditions. In Figure 6.9(a), the gauge checks the thickness of the back section; in Figure 6.9(b), the gauge checks the wear in the radial direction.

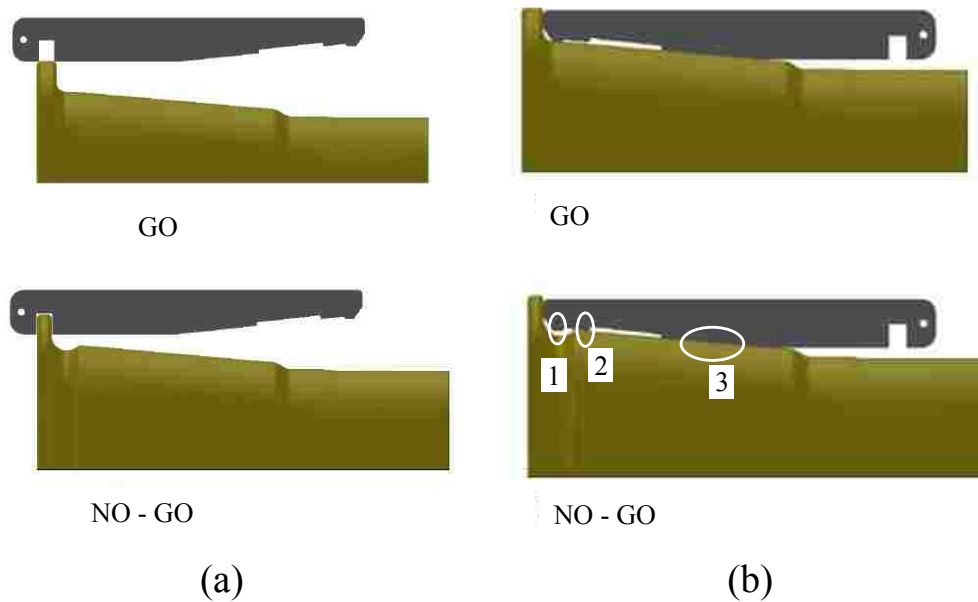
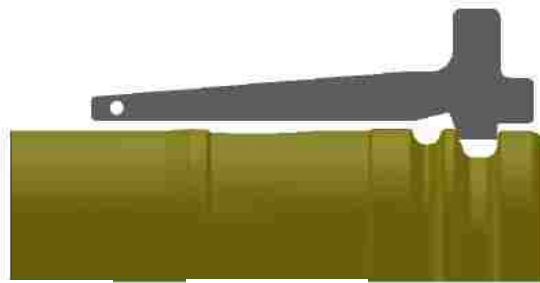


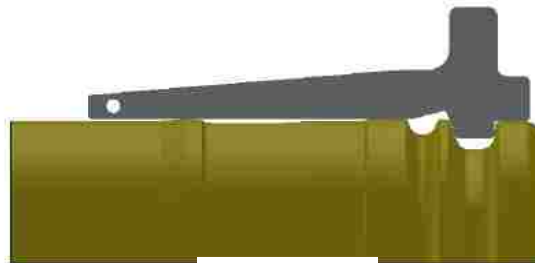
Figure 6.9 Gauges are used to check the back section.

Figure 6.10 illustrates the use of a gauge in the front gutter region of the rim. Given a “GO” condition, the wear in the groove is negligible whereas a “NO-GO” condition indicates wear is significant enough for the gauge to fit in the groove. In this condition, the gutter region must be replaced or the whole rim base must be discarded.





GO



NO - GO

Figure 6.10 Gauges is used to check front gutter region.

### 6.2.2. New and Worn Wheel Dimensions

In this study, the wear (or material loss) at the back section and front groove region is referred to as “geometry degradation”. The focus of this study is on geometrical degradation and its effects on fatigue life of the rim base. Two conditions of the OEM manufactured rim bases are considered for comparison, namely, (1) a new rim base and (2) a worn rim base demonstrating “NO-GO” conditions.

The dimensions of the back section and front groove region for worn rim bases were based on the gauge dimensions provided by NSIW. For the back section, the thickness is the gap dimension of the gauge. The severe radial wear (as shown in Figure 6.9 (b)) is the condition when the sections (2) and (3) of the gauge touch the rim base profile, while section (1) barely touches the rim base profile. For the front gutter region, the groove wear condition is defined such that the gauge fully fits into the groove with the front step touching the bottom of the lock ring groove. Figure 6.11 illustrates the dimension differences of the back section and front groove region between the new and worn rim bases. The blue colour represents the profiles of the new rim base and the red colour the worn rim base.

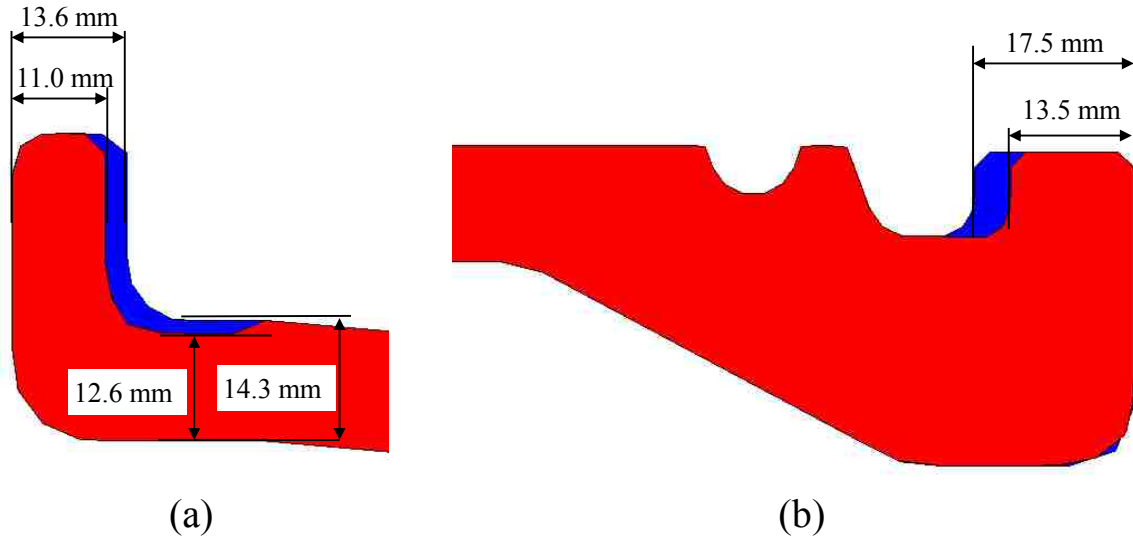


Figure 6.11 Profiles of back (a) and front (b) section of rim base – new (blue) and worn (red).

### 6.2.3. The Heave-duty HT2000 Rim Base

In order to address specific wear and cracking issues, a special HT2000 five-piece wheel was proposed by NSIW. The most significant difference between the HT2000 rim and the OEM rim are located at the back section and front gutter region as shown in Figure 6.12.

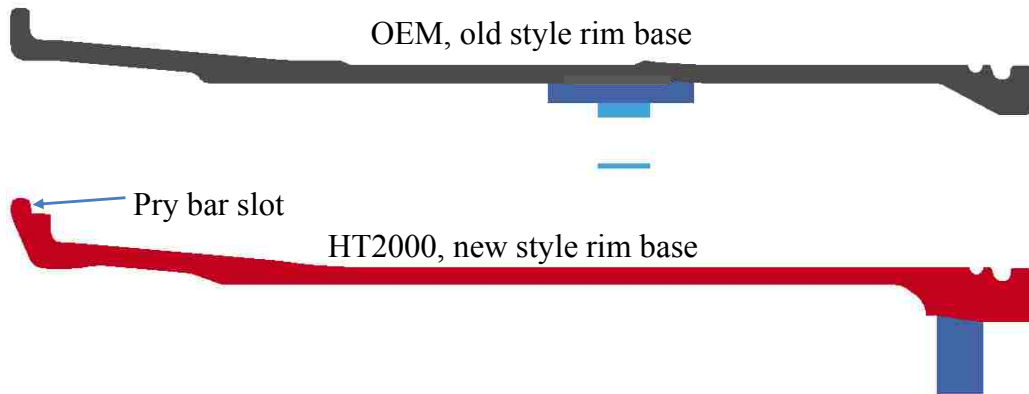


Figure 6.12 Cross section comparison between the OEM rim base and the HT2000 rim base.

The OEM design utilizes 2 to 4 pry bar pockets formed into the back section to break the tire off the tire bead area during demounting. The problem with this design is that if the tire is seized up tight and the rim base is sufficiently fatigued, the pry bar pockets can be broken off. The HT2000 style uses a continuous pry bar slot around the entire circumference of the rim. This slot is used with a hydraulic tool for forcing the flange back and to push a mounted tire off the tire bead area of the rim, providing much greater ease when dismantling the wheel assembly and

replacing tires. In the design, another difference is that more material is added in the back section, in an attempt to improve the strength in this region.

The front gutter region is also modified. Figure 6.13 illustrates the comparison between the OEM (shaded grey color) and the HT2000 profiles (red feature lines) at the front gutter region. The HT2000 rim base has an integrated gutter and bolt flange and more material was added in the neck region. This design provides a stronger and more durable disk attachment than a conventional flat plate disk installation. The gutter of this rim base is manufactured as a forged ring from alloy steel and is completely machined.

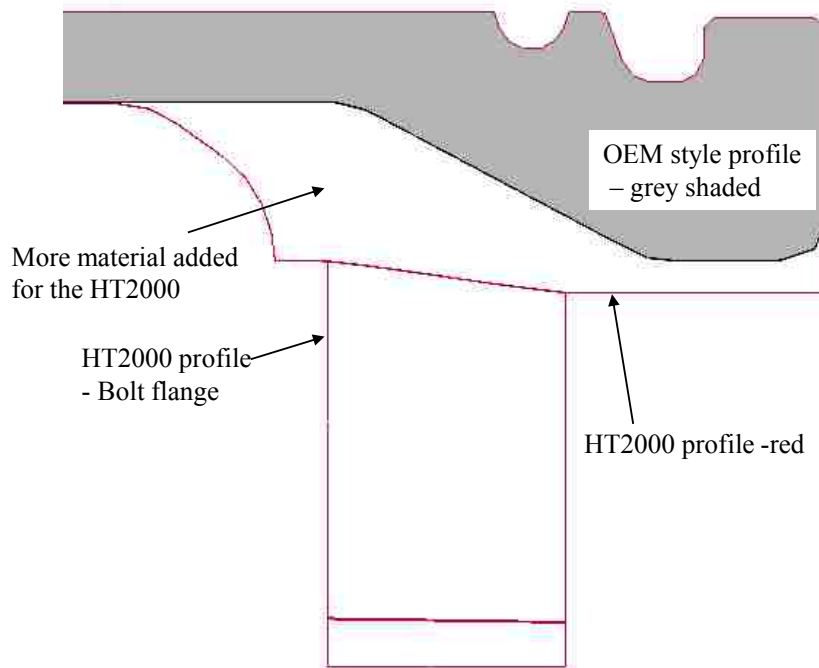


Figure 6.13 Front gutter region comparisons between the OEM rim base and the HT2000 rim base.

The design of the gutter region of the HT2000 rim base was further justified by computer simulations of “push out” testing. Computer simulations were performed to check the lock ring engagement of the traditional OEM design and the HT2000 design. In the simulations, the wheels were modeled using previously validated method and only the front beads of the tires were included in the FE models. The back sections of the rim bases were fully constrained and the front gutter regions were allowed to deform freely. Linear increasing forces were applied on the tire bead region pushing outwards in the axial direction until failures occurred. In these two simulations, similar failure modes were observed in the gutter regions: the neck regions deformed

so it buckled inward, causing the lock ring to dislodge from the lock ring grooves, resulting in tire blow-outs as shown in Figure 6.14 for the OEM wheel. The forces needed to cause failures were 4,476 kN and 13,605 kN respectively, for the OEM wheel and the HT2000 wheel. The simulated failure forces indicate that the HT2000 is more than 3 times stronger than the OEM design in the gutter region in respect to preventing the dislodge of lock rings.

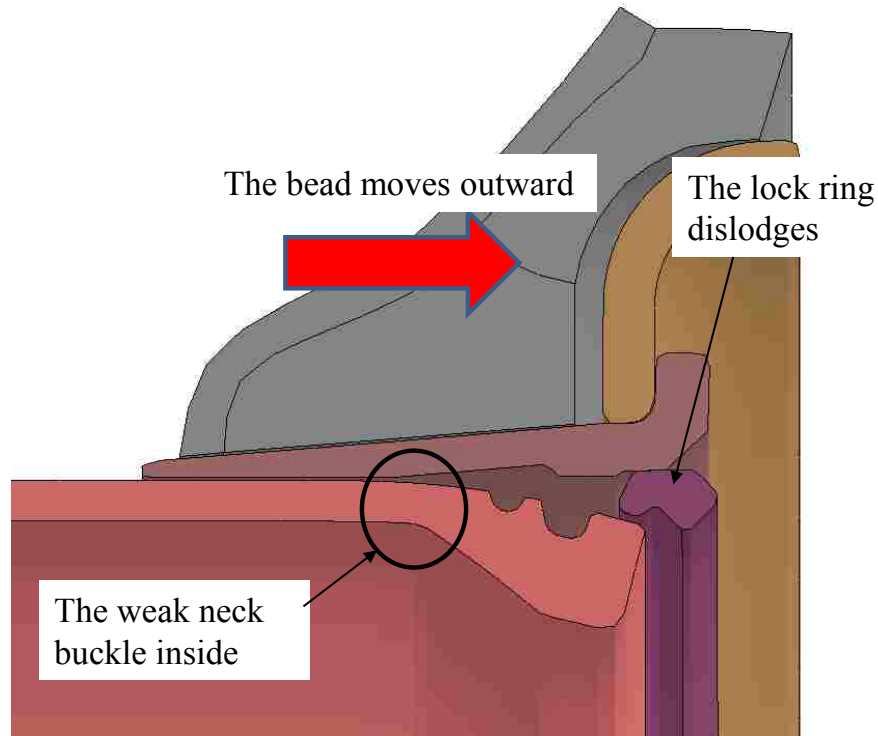


Figure 6.14 The lock ring dislodged under “push out” simulation for the OEM rim.

#### 6.2.4. FE Model Development

In order to compare which wheel design/condition (the new OEM wheel, the worn OEM wheel, and the HT2000 design) has a greater fatigue life, computer simulations were conducted under identical boundary and loading conditions. It is important to note only geometrical differences are considered and the analysis will be focused on the rim base component only. Other factors, such as manufacturing methods, surface treatment, and material property degradation are not considered and are beyond the scope of this study.

In the FE computer models, the tire model of the Goodyear 29.5-29, which was validated using experimental static and quasi-static tests data, was incorporated into the wheel assemblies of the three different wheel structures. Due to symmetry of the loading and boundary conditions, only half of the wheel assemblies were modeled. Identical modeling approaches as detailed in

Chapter 5 were used to model the three different rims. Figure 6.15 illustrates the FE model of the OEM wheel/tire assembly. The wheel components were meshed using 140,000 solid elements. For the wheel components, elastic steel material properties were applied, with elastic modulus of 210, 000 MPa. To reduce vibration and artificial (numerical) noise, mass-weighted damping was utilized in LS-DYNA with a constant of 37 radian/s for the tire (damping force was calculated using Equation (5.1)). Stiffness damping, which is better suited to deal with high frequencies [114], with a percentage coefficient of 20%, was applied to all wheel (metal) components. Different damping coefficients were tried and 0.2 was found the smallest one to give stabilized stress values in the wheel components after the maximum loads were applied. The damping matrix  $[C]$  is computed from the stiffness matrix  $[K_s]$  as indicated in Equation (6.2).

$$[C] = \beta \cdot [K_s] \quad (6.2)$$

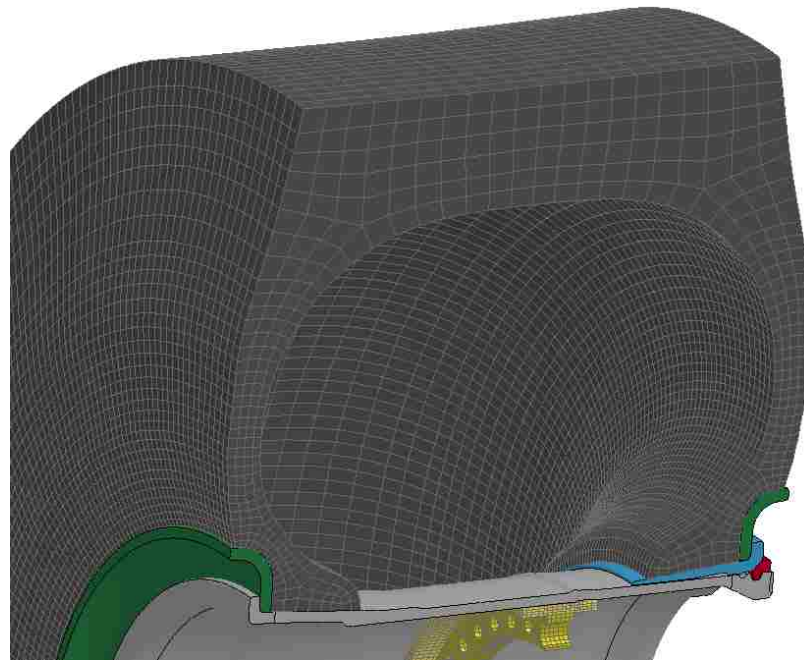


Figure 6.15 The FE model of the rim/tire assembly of the OEM new rim.

A maximum vertical wheel displacement of 82.5 mm, as observed in the quasi-static tests, was applied to the wheel centerline in the FE model. This magnitude of vertical displacement was applied to the hub of the wheel in the FE model and represents a severe loading condition. Vehicle and tire weight was included in the model as well as a tire pressure of 0.593 MPa (86 psi). The loading histories and loading application are shown in Figure 6.16. Consideration of the mechanical response was focused on two regions of the rim base, namely, the back section and the front gutter region.

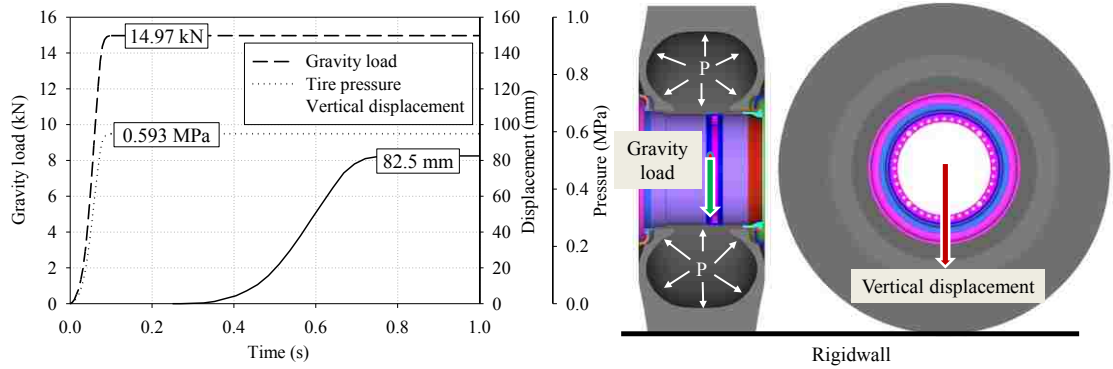


Figure 6.16 Load application histories and illustrations of applied loads for fatigue life analysis – the OEM wheel assembly.

The LS-DYNA Massively Parallel Processor (MPP) solver was used to run the simulations. The MPP solver uses a more robust method to deal with contact between components and more accurate contact stresses can be predicted. In the FE model, LS-DYNA contact definitions (\*contact\_surface\_to\_surface) were used with coefficients of friction of 0.35 and 0.25 respectively for static and dynamic frictions to model the interactions among the rim components.

### 6.3. Determination of Cyclic Fatigue Properties.

To conduct fatigue life analysis from FE-based stress/strain results, the cyclic fatigue properties are needed. These properties were obtained through monotonic tensile testing and cyclic stress-based fatigue testing, which were conducted by Sante DiCecco, another member of this research team at the University of Windsor.

#### 6.3.1. Mechanical Properties of the Rim Base from Monotonic Tensile Tests

##### 6.3.1.1. Tensile Test Results of Specimens Extracted from Rim Base

The rim base and all other wheel components are manufactured using a high strength low alloy (HSLA) structural steel, equivalent to ASTM A572 Grade 50. Mechanical performance expectations of this material, as listed within the ASTM specification [125], are a minimum yield strength of 345 MPa, a minimum tensile strength of 450 MPa, and a minimum percentage elongation to failure of 21% (over a 50 mm gauge region). To verify that the wheel material conformed to these specifications, tensile tests were performed on specimens extracted from gutter region (with and without specimen corrosion considered) and the back region of the rim base of a conventional five-piece wheel sized 29-25.00/3.5, which was geometrically identical to

the five-piece wheel under investigation in this study. Tensile testing was performed in accordance to ASTM E8 [126], for sub-sized tensile specimens, with a 25 mm gauge region. The average engineering stress versus engineering strain curves are plotted in Figure 6.17 for the three test conditions. Three specimens were tested in each condition.

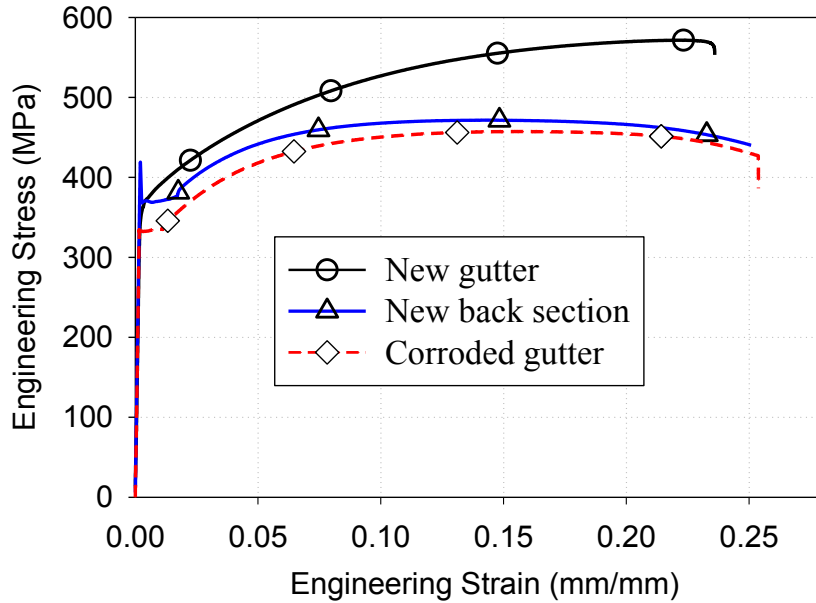


Figure 6.17 Engineering stress/strain behavior of the 29-25.00/3.5 rim base.

From Figure 6.17, the elastic moduli were noted to be almost identical. After yielding, the stress levels are much higher in the gutter region than the back region. The difference may be caused by the different fabrication process between the gutter region and the back region. The stress levels for the corroded gutter were noted to be lower than the back region as would be expected.

Assuming constant volume of the specimens during the tensile tests, the true stress and true strain can be calculated using Equation (2.11). Due to plasticity, the true stresses are greater than corresponding engineering stresses and true strains smaller than the corresponding engineering strains.

The elastic modulus is the slope of the stress-strain curve before yielding, which resembles a straight line. The yield stress was obtained by offsetting the linear portion of the stress/strain response by 0.2%. The intersection of this straight line and the stress-strain curve is reported as the yield point. Table 6.5 summaries the elastic moduli and engineering and true data for the three tests.

Table 6.5 Elastic moduli, engineering and true data for the three tests.

	Elastic modulus (GPa)	Yield stress (MPa)	Tensile stress (MPa)		Elongation at failure (%)	
			Engineering	True	Engineering	True
<i>Gutter</i>	208	368.00	571.50	706.37	23.60	21.19
<i>Back section</i>	208	368.00	471.50	589.75	25.08	22.38
<i>Corroded gutter</i>	206	336.24	461.10	578.13	25.38	22.62

### 6.3.1.2. Yield Criteria under Multiaxial Loading

The yield stress in Table 6.5 is the tensile stress under static uniaxial loading conditions. For multiaxial loading conditions, there are two commonly accepted criteria to decide if the material yields under static loading conditions.

#### 6.3.1.2.1. Maximum Shear Stress Yield Criterion (Tresca)

According to maximum shear stress yield criterion (Tresca), a ductile material will yield once the largest principal shear stress on any plane reaches a critical value  $\tau_o$  [85]. The Tresca yield criterion can be written as:

$$\tau_o = \text{MAX}(\tau_1, \tau_2, \tau_3) \quad (6.3)$$

$$\text{with: } \tau_1 = \frac{|\sigma_2 - \sigma_3|}{2} \quad \tau_2 = \frac{|\sigma_1 - \sigma_3|}{2} \quad \tau_3 = \frac{|\sigma_1 - \sigma_2|}{2} \quad (6.4)$$

where  $\tau_1$ ,  $\tau_2$ , and  $\tau_3$  are the first, second, and third principal shear stress, respectively, and  $\sigma_1$ ,  $\sigma_2$ , and  $\sigma_3$  are the first, second, and third principal normal stress, respectively.

The critical value  $\tau_o$  is actually the yield stress in simple shear which can be calculated from the yield stress in uniaxial tension  $\sigma_o$ , which is readily available from the tensile test. From Equation (6.4), it can be deduced that:

$$\tau_o = \frac{\sigma_o}{2} = 0.5 \cdot \sigma_o \quad (6.5)$$

#### 6.3.1.2.2. Maximum Distortion-Energy or von Mises Criterion

This theory states that yielding starts when the maximum distortion energy in the material equals the maximum distortion energy at yielding in a simple tension test [85]. The general form of von Mises Criterion is:

$$\sigma_{vm} = \frac{1}{\sqrt{2}} \cdot \sqrt{(\sigma_x - \sigma_y)^2 + (\sigma_y - \sigma_z)^2 + (\sigma_z - \sigma_x)^2 + 6 \cdot (\tau_{xy}^2 + \tau_{yz}^2 + \tau_{zx}^2)} = \sigma_o \quad (6.6)$$



Where  $\sigma_{vm}$  is the von Mises stress or effective stress,  $\sigma_x$ ,  $\sigma_y$ ,  $\sigma_z$  and  $\tau_{xy}$ ,  $\tau_{yz}$ ,  $\tau_{zx}$  are the normal stresses and shear stresses in the generalized coordinates system.

For the case of pure shear as encountered in pure torsional loading, all the stress components are zero except  $\tau_{xy}$ , so the shear yield stress can be deduced:

$$\tau_o = \tau_{xy} = \frac{\sigma_o}{\sqrt{3}} = 0.577 \cdot \sigma_o \quad (6.7)$$

### 6.3.1.2.3. Determination of Yield Shear Stress under Multiaxial Loading

At present there is no theoretical way of deducing the relationship between the stress components to correlate yielding for a multiaxial stress state with yielding in the uniaxial tension test. Therefore, yield criteria are empirical relationships. However, a yield criterion must be consistent with a number of experimental observations. For ductile materials, the majority of the experimental data correlated well with von Mises criterion and therefore it provides a theoretically more accurate result [85]. The maximum shear theory provides a more conservative criterion.

In this research, the von Mises criterion was used to assess yielding under multiaxial loading conditions. Therefore the yield shear stress was taken as 212 MPa.

## 6.3.2. Cyclic Fatigue Properties for Stress-life Approach

### 6.3.2.1. Introduction of the Stress-Based Fatigue Tests

The stress-based fully reversed fatigue tests were conducted on an Instron R.R. Moore high speed rotating beam fatigue testing machine as illustrated in Figure 6.18. The fatigue specimen was clamped in the fixture and hung by a weight in the middle. This allowed a constant-magnitude, pure-bending moment to be applied to the specimen. Specimen rotating action (at 6000 rpm) was driven by a motor on the right, resulting in tensile stresses in the lower portion of the specimen and compressive stresses in the upper portion of the specimen gauge region. Therefore, along the gauge length, the specimen was subjected to alternating tensile and compressive stresses similar to the fully reversed cyclic loading. The specimen was tested at one particular stress level until it failed, and the number of cycles to failure and the applied stress were recorded. This test was repeated with multiple specimens of the same material loaded at different stress levels. The collected data were then plotted as stress against number of cycles,  $N$ , (typically on log coordinates) to obtain an  $S-N$  diagram.

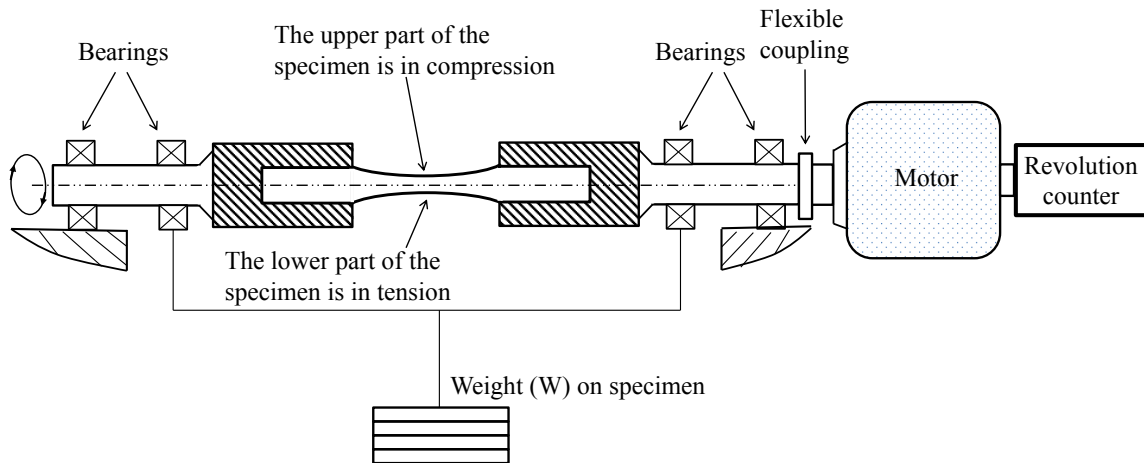


Figure 6.18 R. R. Moore rotating beam fatigue testing machine.

Specimens were extracted from the gutter region and the back section of the rim base. The specimens were polished with an arithmetical mean roughness ( $R_a$ ) of  $0.39\ \mu\text{m}$ , a maximum peak roughness ( $R_y$ ) of  $3.44\ \mu\text{m}$ , a maximum valley roughness ( $R_z$ ) of  $3.44\ \mu\text{m}$ , and a root mean squared roughness ( $R_q$ ) of  $0.48\ \mu\text{m}$ . The specimens were polished to a test diameter (diameter at centre of specimen) of  $5.842\ \text{mm}$  ( $0.23\ \text{inch}$ ). For corroded fatigue testing, the specimens extracted from gutter region were immersed in salt water (with 3.5% salt) at room temperature for approximate forty days.

To do the test, the specimen was subjected to a predetermined stress by applying a calculated load. Three specimens were tested at different stress levels. The stress range was approximately between the yield stress and half of the tensile strength so that the numbers of cycles to failure of  $10^4$  to  $5 \times 10^6$  were observed. Within the tested stress ranges, 14, 17, and 17 specimens were tested for the new gutter region, back section, and corroded gutter respectively, with tested stresses approximately evenly distributed within the ranges. For all the three conditions, the transition lives (the life from finite life to infinite life) were assumed to be  $5 \times 10^6$ . The fatigue tests were stopped before failure when the numbers of cycles reached or passed the transition life.

### 6.3.2.2. Cyclic Fatigue Properties for Stress-Based Tests

Figure 6.19 illustrates the tested data points and their power equation fitting lines. Under an identical number of cycles to failure, the corroded specimens illustrated a 15% to 30% reduction in fatigue strength, compared to the un-corroded specimens from same region. Specimens from the back section illustrated a 7% to 11% reduction in fatigue strength than the

gutter region. This finding is consistent with the monotonic tensile testing results of the three different specimens. In addition, the fatigue strength decreases faster for the corroded specimens than the un-corroded specimens, with the increase of the number of cycles to failure.

Figure 6.19 also illustrates the data points when the fatigue life exceeded  $5 \times 10^6$ . It is important to note that the numbers of cycles beyond the transition life do not represent the cycles to failure. They were the numbers of cycles the specimens experienced when the tests were stopped. The stresses at the transition life were found to be close to half of the tensile stresses of the testing materials separately.

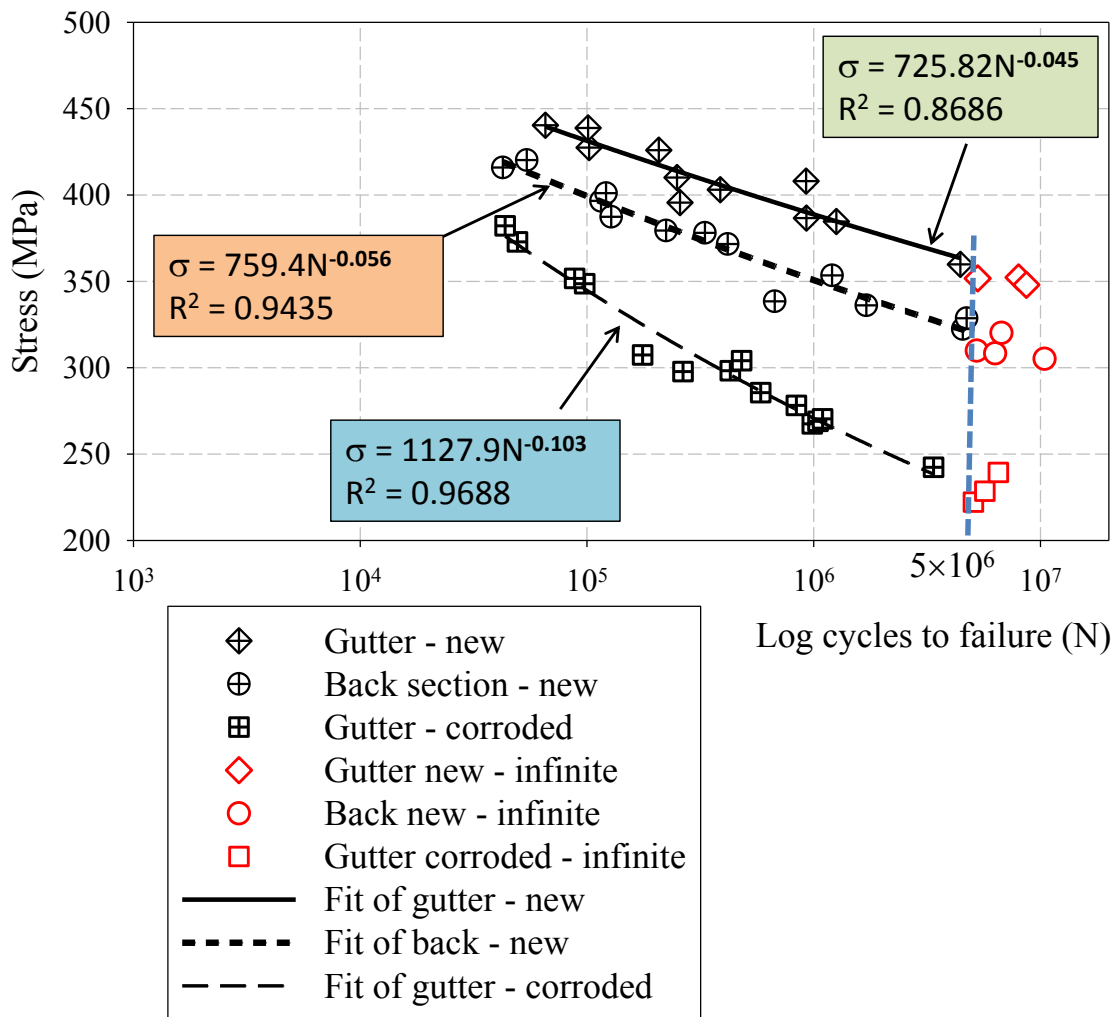


Figure 6.19 High cycle fatigue (HCF) behaviors for specimens extracted from new gutter, back section, and corroded gutter regions.

Using a power equation curve fit, with  $R^2$  values illustrated in Figure 6.19, the stresses (in MPa) versus the numbers of cycle to failure can be expressed as follows:

$$S(N)_{gutter-new} = 725.8 \cdot N^{-0.0452} \quad (6.8)$$

$$S(N)_{back-new} = 759.4 \cdot N^{-0.056} \quad (6.9)$$

$$S(N)_{gutter-corroded} = 1127.9 \cdot N^{-0.103} \quad (6.10)$$

Combining the information from tensile tests and fatigue tests, the Stress-life ( $S-N$ ) fatigue properties were calculated (as listed in Table 6.6) and used within nCode DesignLife to assess fatigue life based on the linear FE simulation stress/strain results.

Table 6.6  $S-N$  fatigue properties generated from fatigue tests.

	<i>Gutter - new</i>	<i>Back section - new</i>	<i>Gutter - corroded</i>	<i>Description</i>
<i>YS</i>	368.00	368.00	336.24	Yield Strength (MPa)
<i>UTS</i>	571.50	471.50	461.10	Ultimate Tensile Strength (MPa)
<i>E</i>	$2.076 \times 10^5$	$2.076 \times 10^5$	$2.059 \times 10^5$	Elastic Modulus (MPa)
<i>SRII</i>	725.82	759.4	1127.90	Stress Range Intercept (MPa)
<i>b1</i>	-0.045	-0.056	-0.103	First Fatigue Strength Exponent
<i>Nc1</i>	$5 \times 10^6$	$5 \times 10^6$	$5 \times 10^6$	Fatigue Transition Point (cycles)
<b><i>b2</i></b>	<b>-0.045</b>	<b>-0.056</b>	<b>-0.103</b>	<b>Second Fatigue Strength Exponent</b>
<i>SE</i>	0.1	0.1	0.1	Standard Error of Log (N)
<i>RR</i>	-1	-1	-1	R-ratio of Test
<i>Nfc</i>	$1 \times 10^{30}$	$1 \times 10^{30}$	$1 \times 10^{30}$	Fatigue CutOff

For steel materials, the fatigue life is assumed infinite beyond the transition life on the  $S-N$  life profile and the second portion of the  $S-N$  relationship is a straight horizontal line with the second fatigue strength exponent (the slope  $b2$ ) equivalent to zero. If the predicted lives for the original design and the proposed design are both infinite, then the two designs are not quantitatively comparable. To circumvent this issue, the second slope  $b2$  was assumed to be equivalent to the first slope  $b1$ , as highlighted in Table 6.6. These modifications were recommended by DesignLife [127] and allowed for a comparison on the fatigue lives of the different wheel designs. Obviously, the fatigue life estimated beyond transition life does not reflect real fatigue life. It is used for comparison only between different design iterations. If the predicted life is greater than the Fatigue CutOff ( $Nfc$ ), an infinite fatigue life will be given.

### 6.3.3. Cyclic Fatigue Properties for Strain-life Approach

Due to the unavailability of the strain-life fatigue testing equipment, the fatigue properties were initially estimated using Manson's universal slopes listed in Table 6.7, based on the tensile strength and elongation at break.

Table 6.7 Estimation of material cyclic properties for strain-life using Manson's universal slopes.

<i>Parameters</i>	<i>Universal Slopes</i>	<b>Gutter - new</b>	<b>Back section - new</b>	<b>Gutter - corroded</b>
$S_{ut}$		571.50 MPa	471.50 MPa	461.10 MPa
$\varepsilon_f$		21.19%	22.38%	22.62%
$\sigma'_f$	$1.9 \cdot S_{ut}$	1085.85 MPa	895.85 MPa	876.09 MPa
$b$	$-0.12$	-0.12	-0.12	-0.12
$\varepsilon'_f$	$0.76 \cdot \varepsilon_f^{0.6}$	0.30	0.31	0.31
$c$	$-0.6$	-0.6	-0.6	-0.6
$K'$	$\sigma'_f / (\varepsilon'_f)^{0.2}$	1381.48 MPa	1132.30 MPa	1106.23 MPa
$n'$	$0.2$	0.2	0.2	0.2

Based on stain-life fatigue theory and Equation (2.18) and Equation (2.20), the elastic strain-life and total strain-life equations for the new gutter specimen can be written as:

$$\varepsilon_e(N_f) = \frac{1085.85 \cdot (2N_f)^{-0.12}}{3.08 \times 10^5} \quad (6.11)$$

$$\varepsilon_a(N_f) = \frac{1085.85 \cdot (2N_f)^{-0.12}}{3.08 \times 10^5} + 0.3 \cdot (2N_f)^{-0.6} \quad (6.12)$$

Changing the stress-life Equation (6.8) into a strain-life format by dividing the elastic modulus on the right side, it can be written as:

$$\varepsilon(N_f)_{gutter-new} = \frac{725.8}{2.08 \times 10^5} \cdot (N_f)^{-0.0452} \quad (6.13)$$

The three Equations (6.11), (6.12), and (6.13) were plotted together as illustrated in Figure 6.20. Theoretically, the profile of elastic strain-life approximated from universal slopes (Equation (6.11)) should be a very good approximation of that transformed from the tested stress-life (Equation (6.13)). However, Figure 6.20 displays great deviation between the two lines. The slopes (exponent coefficients) are -0.12 and -0.0452 respectively for the two different curves. When the reversals are greater  $2.5 \times 10^4$ , the fatigue life is much lower for the approximated strain life than the transformed strain-life. Similar issues were found for the strain life profiles for the two conditions: specimens from the back section and the corroded gutter region.

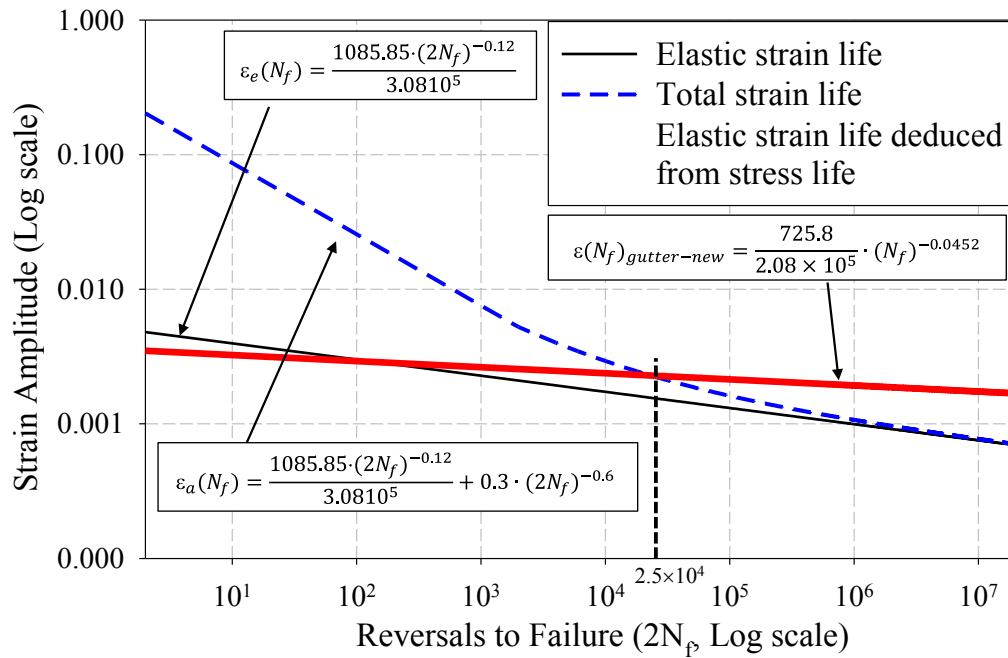


Figure 6.20 Total strain-life curve and elastic strain-life curve deduced using universal slope approximations, and elastic strain-life curve transformed from stress-life testing.

Assuming valid stress-life testing results, based on the above analysis, Manson's universal slope method is not suitable to approximate the strain life of the high strength low alloy (HSLA) steel used on the multi-piece wheel, at high cycle fatigue (greater than  $2.5 \times 10^4$ ). To make the strain life consistent with the stress-life testing results at HCF, the elastic strain life was modified by directly using the stress-life test results, making  $b = b1$ , and  $\sigma_f \cdot (2)^b = SRII$ . In the low cycle fatigue (LCF), Manson's method was still used. The modified parameters are listed in Table 6.8.

Table 6.8 Modified parameters for the strain life approach.

Parameters	Formula	Gutter - new	Back section - new	Gutter - corroded
$S_{ut}$		571.5 MPa	471.5 MPa	461.10 MPa
$\epsilon_f$		21.19%	22.38%	22.62%
$\sigma_f$	$SRII/(2^{b1})$	748.9 MPa	789.5 MPa	1211.4 MPa
$b$	$b1$	-0.0452	-0.056	-0.103
$\epsilon'_f$	$0.76 \cdot \epsilon_f^{0.6}$	0.30	0.31	0.31
$c$	-0.6	-0.6	-0.6	-0.6
$K'$	$\sigma_f/(\epsilon'_f)^{0.2}$	1381.48 MPa	1132.30 MPa	1106.23 MPa
$n'$	0.2	0.2	0.2	0.2

Based on the parameters in Table 6.8, the strain-life equations for the three materials can be written as:

$$\varepsilon_{a-gutter-new} = \frac{748.9 \cdot (2N_f)^{-0.0452}}{3.08 \times 10^5} + 0.3 \cdot (2N_f)^{-0.6} \quad (6.14)$$

$$\varepsilon_{a-back-new} = \frac{789.5 \cdot (2N_f)^{-0.056}}{3.08 \times 10^5} + 0.31 \cdot (2N_f)^{-0.6} \quad (6.15)$$

$$\varepsilon_{a-gutter-corroded} = \frac{1211.4 \cdot (2N_f)^{-0.103}}{3.06 \times 10^5} + 0.31 \cdot (2N_f)^{-0.6} \quad (6.16)$$

Figure 6.21 illustrate the curves of total strain life, elastic strain life, and plastic strain life for the gutter-new specimens. The transition between HCF and LCF is about  $3 \times 10^3$  reversals ( $1.5 \times 10^3$  cycles).

Figure 6.22 illustrates the profiles of the total strain lives for the specimens in different conditions. In the plastic (LCF) region, the three curves almost overlap one another, which is anticipated since the fatigue ductility coefficients  $\varepsilon'_f$  are almost identical (from 0.3 to 0.31) and the fatigue ductility exponents  $c$  are all the same (-0.6). The differences in the elastic (HCF) region correspond well with the tested stress-life curves.

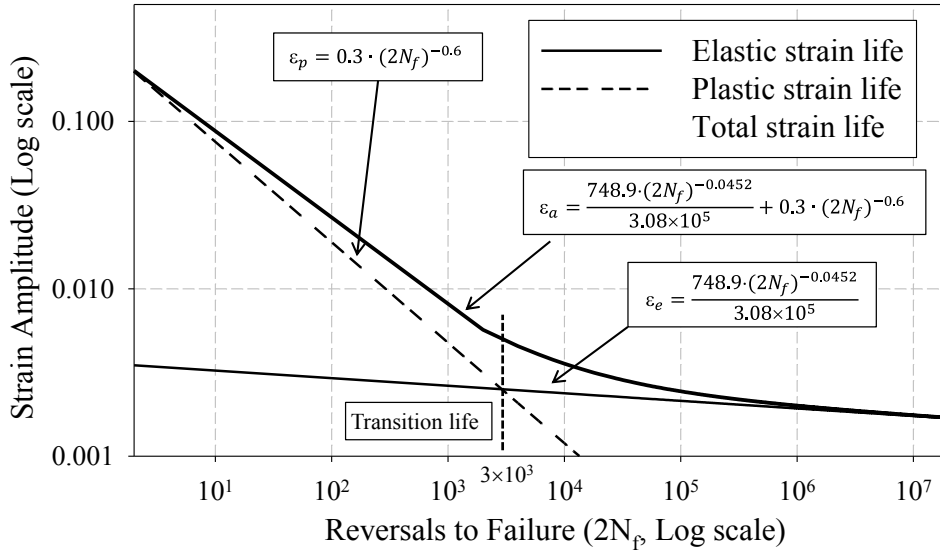


Figure 6.21 The curves of total strain life, elastic strain life and plastic strain life for the new gutter region.

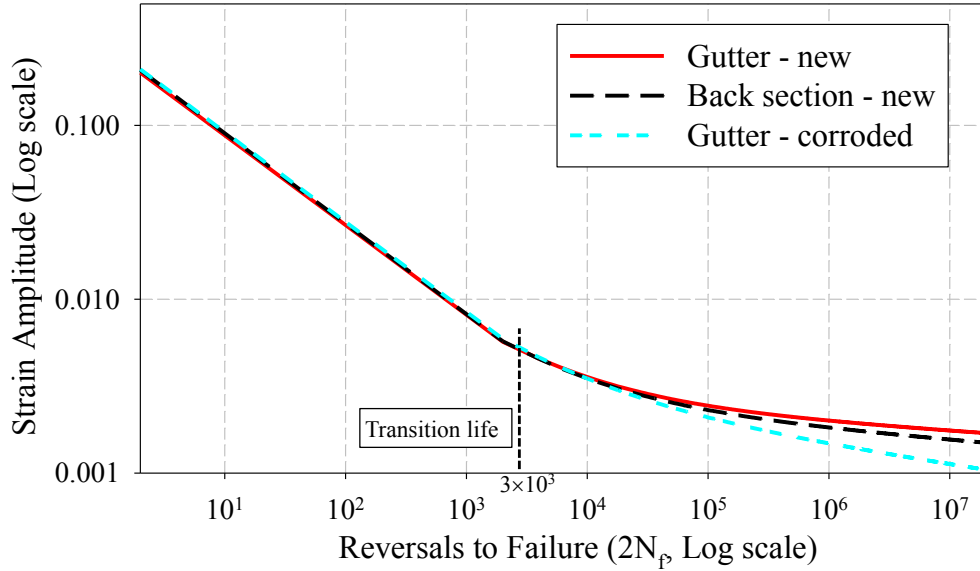


Figure 6.22 The total strain life curves for the three conditions.

The calculated parameters in Table 6.8 were input into DesignLife to create the fatigue life material models for strain-life analysis. Additionally, the infinite fatigue life cut-off criterion was modified from  $10^8$  to  $10^{25}$  in the  $\varepsilon-N$  based analysis. These modifications were recommended by DesignLife [127] and allowed for a comparison on the fatigue lives of the different wheel designs.



## Chapter 7. Discussions on Simulation Results

von Mises stress is widely accepted to assess the stress levels of structures. However, von Mises stress is a scalar and does not show the directions of the stresses. In fatigue life analysis associated with multiaxial loadings, the critical plane method is the most acceptable approach. In this research, all fatigue life analyses (including  $S-N$  approach and  $\varepsilon-N$  approach) were conducted using the critical plane method. Typically the critical plane is the plane with the maximum shear stress/strain. Therefore, both von Mises stresses and the maximum shear stresses are assessed to compare the stress levels among different wheel designs or conditions.

### 7.1. Geometry Degradation

#### 7.1.1. Maximum von Mises and Maximum Shear Stress Analyses

Figure 7.1 illustrates the maximum von Mises stress contours at the surface shell elements of the front gutter regions for the HT 2000 new wheel, the OEM new wheel, and the OEM worn wheel. The contours show that the maximum von Mises stresses are 133.6 MPa, 155.3 MPa, and 358.7 MPa respectively for the three different wheels. The contours show that at the gutter regions, the OEM worm rim base has the highest stress levels and the HT2000 has the lowest stress levels.

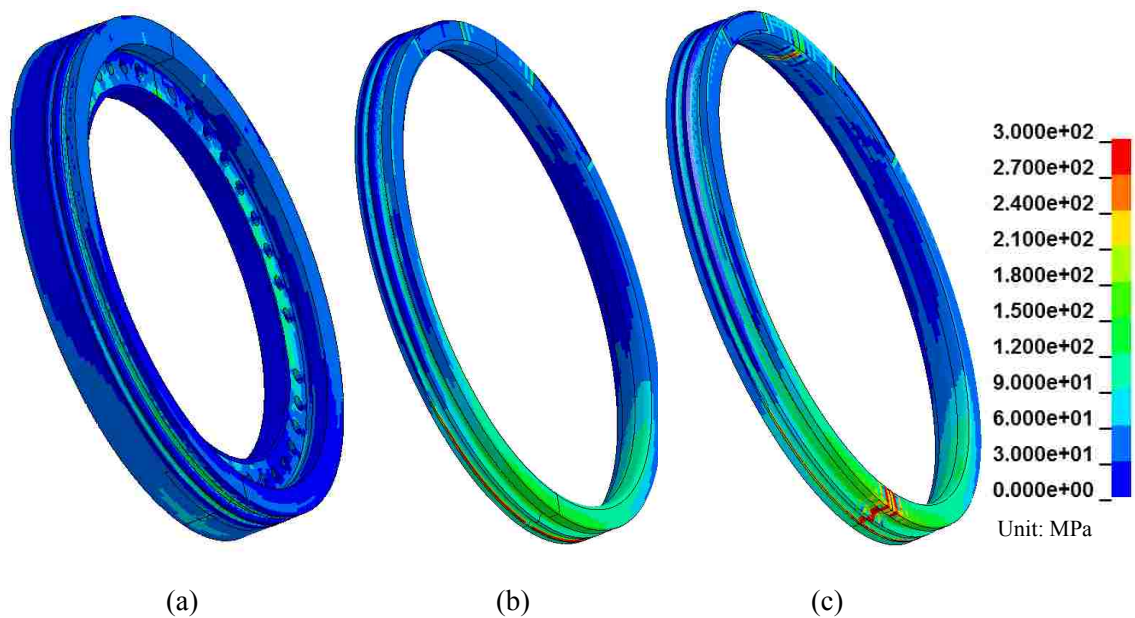


Figure 7.1 Maximum von Mises stress contours for the three different rims, (a) the HT2000 new, (b) the OEM new, and (c) the OEM worn.

Table 7.1 summarizes the maximum stress values at the back section and gutter regions for the HT2000 wheel, the new OEM wheel, and the worn OEM wheel. The stress differences were calculated relative to the stresses of the OEM new rim base using Equation (7.1).

$$Relative\ Error = \frac{Stress\ value\ of\ other\ rim\ condition}{Stress\ value\ for\ the\ OEM\ new\ rim} - 1 \quad (7.1)$$

Table 7.1 Maximum von Mises stresses/maximum shear stresses (MPa) on the shell elements at the front gutter and back section regions.

Region	HT2000 New		OEM New	OEM Worn	
	Stress	Difference	Stress	Stress	Difference
Gutter	133.6/83.8	-14.0% / -6.1%	155.3/89.2	358.7/189.2	131.0% / 112.1%
Back	110.8/69.3	-8.5% / -11.5%	121.1/78.3	258.9/103.2	113.8% / 31.8%

Relative stress difference calculations show that for the HT2000 new rim base, the maximum von Mises stresses were approximately 14.0% and 8.5% lower than the new OEM rim base, at front gutter region and back section region respectively. For the worn OEM rim base, the maximum von Mises stress were increased by approximately 131.0% and 113.8%, respectively. The maximum shear stresses were decreased by 6.1% and 11.5%, respectively in the front and back regions for the HT2000 new wheel, and increased by 112.1% and 31.8% for the OEM worn wheel, respectively.

### 7.1.2. Fatigue Life Analyses

Table 7.2 presents the fatigue life comparisons amongst the three wheel types, using both the  $S-N$  approach and the  $\varepsilon-N$  approach. For all regions, the  $\varepsilon-N$  approach predicted higher lives than the  $S-N$  approach, since the  $\varepsilon-N$  approach conducted plastic stress/strain correction before calculating fatigue life when the linear FE-based stresses are above the yield stress. The corrected stresses are lower than the FE-based stresses and plastic deformations were accounted for in  $\varepsilon-N$  approach.

Table 7.2 Fatigue life comparisons.

Method	Region	The HT2000 New		The OEM New	The OEM Worn	
		Life	Increase	Life	Life	Increase
$S-N$	Gutter	$7.065 \cdot 10^{13}$	75.8%	$4.019 \times 10^{13}$	$6.053 \cdot 10^5$	-100.0%
	Back	$1.768 \cdot 10^{15}$	103.4%	$8.692 \cdot 10^{14}$	$2.562 \cdot 10^7$	-100.0%
$\varepsilon-N$	Gutter	$4.698 \cdot 10^{23}$	19377.6%	$2.412 \times 10^{21}$	$1.395 \cdot 10^{10}$	-100.0%
	Back	$5.908 \cdot 10^{24}$	55426.3%	$1.064 \cdot 10^{22}$	$7.628 \cdot 10^{11}$	-100.0%

Based on the fatigue life prediction using  $S-N$  approach, finite fatigue lives were predicted at the gutter region ( $6.053 \times 10^5$ ) of the OEM worn wheel. Infinite lives (greater than transition life  $5 \times 10^6$ ) were predicted for other regions using  $S-N$  approach and all the regions using  $\varepsilon-N$  approach. Using Equation 7.1, the calculated relative differences of the fatigue life between different situations are also listed in Table 7.2. The predicted fatigue lives for the OEM worn wheel were over several orders of magnitude lower than the predicted lives for the OEM new wheel, on the corresponding regions. On the other hand, the predicted fatigue lives for the HT2000 new wheel were over 75% higher than the lives of the OEM new wheel, on the corresponding regions.

## 7.2. Material Degradation

It was initially planned to compare the fatigue lives between OEM new wheel and OEM used wheel, in order to investigate the material degradation effects. Tensile and fatigue tests were conducted on specimens extracted from new OEM wheel and used OEM wheel and the testing results showed almost identical yield stresses, tensile stresses, elongations, and fatigue data between the specimens. For the used wheel, the material property degradations mostly happened on the outer surfaces of the wheel components. After polishing the specimens before testing, the degraded materials were removed, which explains why the testing results were almost identical between the specimens extracted from the two different wheels. In this study, therefore, the material property degradation effects were investigated using material properties of specimens extracted from the new OEM wheel, corroded in salted water and non-corroded.

In order to investigate the effects of material degradation, fatigue life estimations were conducted on the OEM new wheel base structure without considering geometry degradation. The fatigue life estimations were only focused on the gutter region of the rim base since the gutter region is the most critical region. The FE stress/strain results were obtained with the loading conditions illustrated in Figure 6.16. The cyclic fatigue properties (listed in Table 6.6 and 6.8) from specimens of new gutter and corroded gutter were used to compare the fatigue life. Table 7.3 lists the fatigue life calculation results using nCode DesignLife.

Table 7.3 Fatigue life comparisons between new gutter and corroded gutter materials.

Method	Region	New gutter	Corroded gutter	Increase
$S-N$	Gutter	$4.019 \times 10^{13}$	$6.197 \cdot 10^5$	-100.0%
$\varepsilon-N$	Gutter	$2.412 \times 10^{21}$	$9.735 \cdot 10^8$	-100.0%

It is observed that both  $S-N$  and  $\varepsilon-N$  methods predicted higher fatigue life for the new specimen than the corroded specimen in the gutter region, with the  $\varepsilon-N$  method predicting much longer fatigue life than the  $S-N$  method. No matter what methods were used, the fatigue lives of the corroded materials were significantly reduced by several orders of magnitude.

From a microscopic point of view, corrosion takes away the external material and creates highly irregular micro-structure on the surface of the component. Significant stress concentrations are induced in localized areas of the component during service. Therefore, massive fatigue life reductions were predicted. This is an important finding which was hypothesized by Vijayan et al. [6, 14].

## Chapter 8. Innovative Multi-piece Wheel Designs

Using previously validated FE models of the 29.5-29 tire and the associated five-piece wheel, two design modifications were considered to increase the integrity and the fatigue life of the wheel component, specifically on the front gutter region.

### 8.1. The Threaded-connection Design

The incident analyses and summary in Section 2.2.4 reveals that the majority of multi-piece wheel blow out happened in the lock ring region (front gutter region) of the rim base. Therefore, structural performance enhancement of the multi-piece wheel must increase the effectiveness of the locking mechanism, while also reducing the complexity of the overall design and improving the ease of assembly. This will serve to reduce the failure rate of multi-piece wheels and correspondingly to improve workplace safety and the efficiency of mining operations.

The proposed design is based on a conventional five-piece wheel assembly, but the traditional lock ring was replaced with a more robust threaded locking mechanism. The approach taken to quantify the mechanical behaviour of the modified design involved the structural performance comparison of the new design and the conventional five-piece wheel design using two different criteria simulated through FE modelling methods. The two different testing criteria included (i) the maximum force required to cause wheel component disengagement during a “pull-out” test and (ii) the assessment of the stress field associated with an extreme loading condition under quasi-static and fatigue loading. The lack of any viable structural testing methods for multi-piece wheel assemblies required the researchers to consider these two aspects of possible loading. A high degree of modelling accuracy was maintained throughout the entire process by validating the numerical model of the conventional five-piece wheel and associated tire against experimental data obtained from ancillary physical testing.

#### 8.1.1. The Proposed Threaded-Connection Locking Mechanism

The proposed wheel design under investigation in this study is based on a conventional five-piece wheel sized 29-25.00/3.5, as shown in Figure 8.1. In practice, this assembly is paired with a 29.5-29 bias or 29.5R29 radial OTR tire.

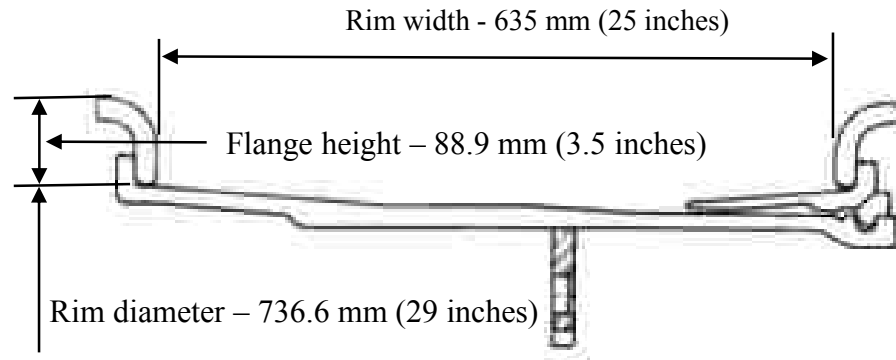


Figure 8.1 Schematic of a 29-25 five-piece rim, illustrating rim width, flange height, and rim diameter.

In the proposed design, the lock ring and the BS band of the conventional rim were combined into one entity. The combined BS band engages the modified rim base by threads, as shown in Figure 8.2(a). Figure 8.2(b) illustrates the threads on the rim base and BS band. During installation, the O-ring would be first positioned as shown in Figure 8.2(a), followed by rotational motion of the threaded BS band to the rim base. The O-ring would be tightly squeezed between the rim base and the threaded BS band to form an appropriate air seal. Critical geometries and dimensions (rim width, diameter, and flange height) of the proposed rim were maintained to ensure compatibility with the tire used for the conventional five-piece wheel. The feature line profiles in the front region of rim bases of the two designs are illustrated in Figure 8.3(a), in which the grey line represents the conventional design and the red line the proposed design. Figure 8.3(b) illustrates the critical dimensions of the threaded BS band. The exterior dimensions and profile of the threaded BS band are identical to the conventional BS band except within the thread and front end regions. This was required so the proposed BS band would be compatible with conventional flange and tire bead. The threads have a pitch of 20 mm and a tooth depth of approximately 8.5 mm.

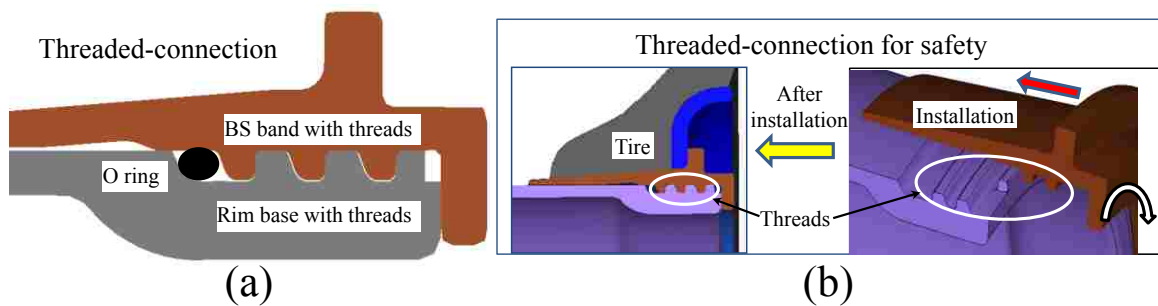


Figure 8.2 Illustrations of (a) O-ring placement and the BS band mating with the threaded rim base and (b) the threaded rim base and BS band, and the installation process.

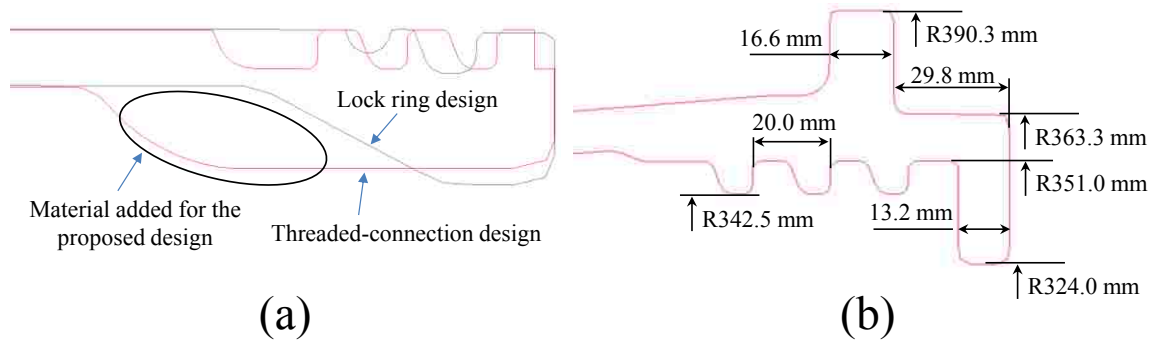


Figure 8.3 (a) Feature lines of a conventional rim base and a threaded rim base and (b) critical dimension of the threaded BS band region.

In the threaded-connection design, at least three full threads are engaged after proper installation to increase the effective locking contact area. Correspondingly, in contrast to the conventional lock ring design, the proposed threaded-connection is expected to experience reduced magnitudes of stress in the locking region due to increased contact area. The proposed design employs more material along the axial direction for construction of the threads as material was added at the internal side of the rim base to strengthen this region. It is anticipated that the added material will also contribute to strengthening the engagement between the BS band and rim base. Given that the threads on the BS band will only be capable of mating to a rim base with matching threads, failures related to mismatched wheel components will be reduced. This design consideration is important as failures resulting from mismatched locking components also contribute to a significant number of injuries and fatalities.

### 8.1.2. Assessment Approaches for the Proposed Design

To assess the performance of the conventional and the proposed threaded-connection locking mechanisms, it is essential that extensive testing be conducted. Several barriers exist to accomplish effective physical testing. These include, but are not limited to, cost, availability of the proposed wheel components, physical difficulty of handling large assemblies, as well as the potential dangers of experimental wheel/tire assembly failure testing. Therefore, for the initial design and testing stages, numerical analysis, paired with ancillary physical testing, where possible, was implemented.

Considering the challenges of completing experimental prototype testing listed in the previous paragraph, the strategy for investigating the structural performance of the proposed threaded wheel design, relative to the conventional design, was carefully selected. Firstly, significant efforts were completed to develop and validate the FE model of the OTR tire (29.5-29)

and wheel (29-25.00/3.5) assembly as stated in Chapter 4, 5, and 6. For the proposed threaded-connection design, identical modelling approaches to the five-piece wheel were applied. Therefore the predictability of the FE model of the proposed design can be justified. Subsequent to achieving a well-developed and validated FE model of both the tire and wheel, structural loading of the wheel/tire assembly were performed using two different numerical testing conditions. Firstly, to investigate the ability of the wheel's capability to contain its components during extreme loading on the tire, a pull-out test of the locking assembly for both the conventional and proposed designs was completed. Secondly, stress and fatigue analyses of the conventional and proposed wheel components were performed when the wheel/tire assembly was subjected to significant loading conditions as tested and documented in Chapter 4. Through these two testing conditions, the structural performances of both the conventional and proposed wheel designs were compared.

#### 8.1.2.1. BS Band Pull-out Simulations

The numerical simulation of the BS band pull-out testing incorporated a subset of all components of the multi-piece wheel; only the rim base, lock ring, BS band and a portion of the front tire were utilized in the FE models. In the model, the back section of the rim base was fully constrained. A prescribed linearly varying displacement on the portion of the tire was applied with a constant speed of 200 mm/s in order to make the lock ring move out of the groove in the selected simulation time of 0.5 second. This motion was prescribed in the outward axial direction as shown in Figure 8.4. This prescribed motion is intended to push the flange and BS band outward thus simulating a pull-out condition where the structure's ability to contain the BS band, flange, and tire can be investigated. Throughout the entire simulation, contact forces within the region of the locking mechanism were recorded. For the conventional five-piece wheel assembly, this entailed the contact forces between the BS band and the lock ring, whereas for the threaded-connection design, the contact forces between the BS band and the rim base in the threaded region were recorded.

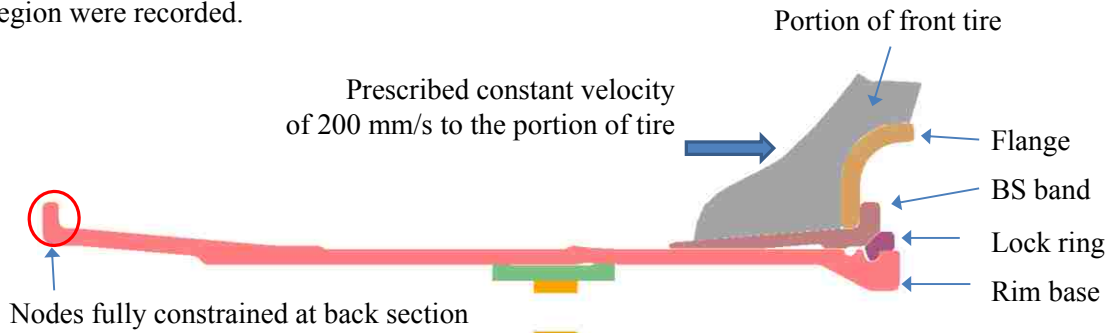


Figure 8.4 Cross-section of the wheel/tire FE model illustrating the BS band pull-out simulation for the five-piece wheel/tire assembly.



Since this simulated testing condition involves plasticity of the wheel component, an elastic-plastic material model was developed and incorporated into all portions of the wheel FE model. The model selected was type 24 within LS-DYNA [114] which incorporates the von Mises yield criterion, and the equivalent von Mises stress is calculated in terms of the deviatoric stress tensor as presented in Equation (8.1). Furthermore, the equivalent plastic strain is calculated through time integration of the rate of deformation tensor as presented in Equation (8.2).

$$\bar{\sigma} = \left( \frac{3}{2} \cdot S_{ij} \cdot S_{ij} \right)^{1/2} \quad (8.1)$$

$$\bar{\epsilon}_p = \int_0^t \left( \frac{2}{3} \cdot D^p_{ij} \cdot D^p_{ij} \right)^{1/2} dt \quad (8.2)$$

To be conservative in the numerical analyses, the minimum values of the yield strength (345 MPa), ultimate tensile strength (450 MPa) and percent elongation (21%) of the ASTM A572 Grade 50 steel were used within the development of the material model. Failure of finite elements was considered by implementing a simple effective plastic strain failure criterion where any elements which the effective plastic strain exceeded 0.21 would be removed from the calculations and no longer able to support any stress. No material strain rate effects were considered in the model since the load was applied in a slow fashion.

Contact between the rim components as well as between the tire and wheel components (specifically the flange and BS band) was modelled using a surface to surface contact algorithm within LS-DYNA. The coefficients of static and dynamic friction as well as the decay coefficient for contact associated with the wheel components was defined as 0.35, 0.25 and 1000, respectively. This large value of the decay coefficient results in a very abrupt change from the static to the dynamic coefficient of friction as shown in Equation (5.2). The coefficients of static and dynamic friction and the decay coefficient for contact between the tire portion and the flange and BS band were specified as 0.35, 0, and 0, respectively. These values resulted in a constant coefficient of friction between interacting surfaces regardless of whether or not relative motion occurs. The input file used for the pull-out testing is listed in Appendix E.4.

#### **8.1.2.2. Wheel Stress and Fatigue Life Assessments**

As previously identified, an anticipated benefit of the proposed threaded-connection wheel design is reduced magnitudes of stress within the locking region resulting from an increase

in the overall contact area between the rim base and the BS band. Through numerical simulation efforts, the effective (von Mises) stress and the 1<sup>st</sup> principal stress magnitudes were compared between the conventional five-piece wheel and the proposed wheel under identical loading conditions. Subsequently, the fatigue life of each wheel was evaluated based on FE simulated stress/strain results using the commercial software DesignLife. In these simulation conditions a complete wheel/tire assembly was considered.

#### **8.1.2.2.1. Simulated Loading and Boundary Conditions for Stress and Fatigue Life Assessments**

The quasi-static loading condition considered in the numerical simulation was based upon the previously detailed experimental testing in Chapter 4. This loading condition was identified by mine operators and supervisors as representing an extreme loading condition on the wheel/tire assembly. In this condition the centre of the wheel obtained a maximum vertical displacement of 82.5 mm.

The numerical implementation of this loading condition involved the application of a vertical (downward) displacement of the centre of the wheel as well as the application of internal pressure within the tire and the appropriately distributed vehicle weight to one of the wheel/tire assemblies. Therefore, within the numerical simulations application of gravity (14.97 kN) and internal pressure (86 psi) were first applied and allowed to reach a steady state deformation condition. Following this loading, a vertical downward displacement (82.5 mm) was prescribed to the centre of the wheel/tire assembly. The load applications were identical to the load application as in the geometry degradation study described shown in Figure 6.16. The FE input file is in Appendix E.5.

## **8.2. The Two-piece Wheel Design**

### **8.2.1. The Proposed Two-piece Wheel Design**

The Kalmar ContChamp 42-45 tonnes container handler uses five-piece wheels, as shown in Figure 8.5 (a). The numbers in the brackets show the mounting sequence, which is the same as conventional five-piece wheels. Figure 8.5 (b) shows the container handler on which the five-piece wheels are installed [128]. This five-piece wheel has the similar structures of the HT 2000 enhanced mining wheel.

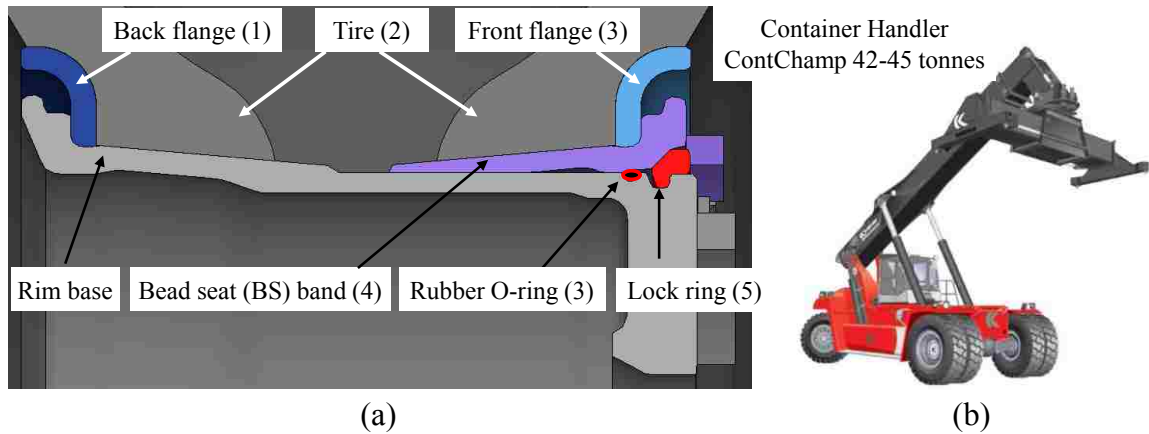


Figure 8.5 (a) five-piece wheel structure and (b) Kalmar ContChamp 42-45 tonnes container handler [128].

It has been reported within the industry [129] that considerable fatigue cracks and wear can develop within the lock ring groove region of a five-piece wheel assembly. These cracks and wear (as illustrated in Figure 2.22) are caused by the lock ring moving or vibrating in the lock ring groove and high side wall stress, which is more prevalent during steering. If these issues go unnoticed, a failure of the wheel assembly will occur, propelling wheel components away from the failure zone, resulting in serious injuries and, in some instances, fatalities [5].

A prominent wheel manufacturer, North Shore Industrial Wheels (NSIW), attempted to remedy the aforementioned issue by applying a 0.076 mm – 0.127 mm thick HVOF tungsten carbide nickel (Rc 78 hardness) coating to the lock ring grooves of a select number of five-piece wheel assemblies. However, it was found that the coating would be almost fully removed from the grooves within a year of application, thus making the solution not feasible for long term use [129].

To ensure workplace safety and wheel longevity, it is essential that a solution be developed to address the premature failure of multi-piece wheels due to wear and crack propagation within the lock ring groove. In this study, a new wheel design is proposed with the purpose of eliminating the current potential for wheel failure. The new design is a two-piece wheel, which has combined the front and rear flanges of a five-piece wheel with the rim base, while eliminating the BS band and lock ring. In place of the lock ring locking mechanism, a 20-bolt pattern is utilized to fasten the wheel portions together after tire mounting, as illustrated in Figure 8.6. The proposed design maintains all critical dimensions of the conventional five-piece wheel in an effort to ensure compatibility with current OTR tires.

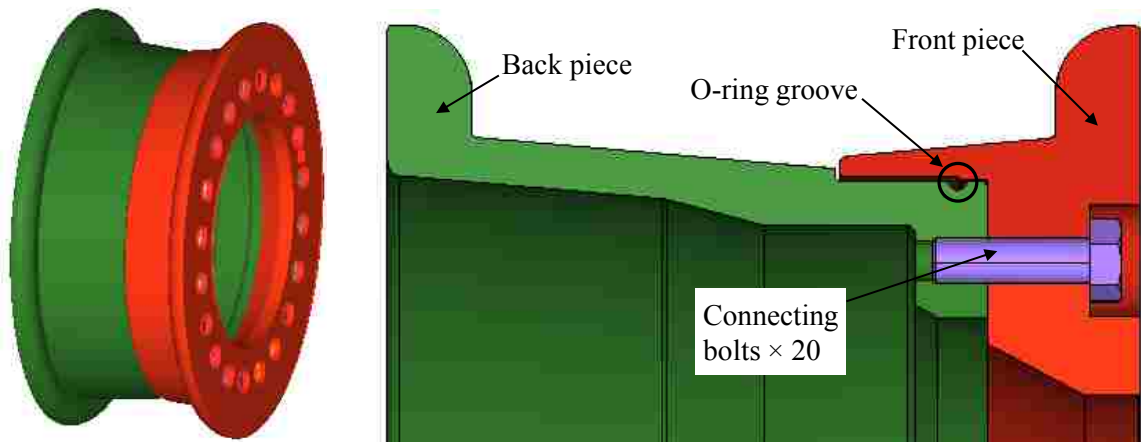


Figure 8.6 The proposed two-piece wheel design.

Given that the majority of the five-piece wheel failures have been associated with the wear and cracks in the lock ring groove and the incorrect installation of a lock ring, as stated in section 2.2.4, the benefit of the proposed two-piece design is obvious, it completely removes the possibility of wheel failure due to incorrect wheel component installations. Additionally, it is expected that the two-piece wheel design should have superior longevity if implemented within industry. Nevertheless, it is essential that with any new design, the benefits be quantitatively assessed relative to previous designs, where possible. Thus, in this study, a conventional 33-13.00/2.5 five-piece wheel will serve as a baseline for comparison against the proposed two-piece wheel of comparable dimensions.

Comparison of the wheels will consist of numerically analyzing the stress levels the wheels experience during severe operating conditions. These stress levels will then serve as input parameters for a fatigue analysis of the wheels to evaluate their respective fatigue lives. Additionally, the load bearing capacity of the bolt pattern will be evaluated for conditions of severe loading. The FE method is implemented for all wheel analyses, given that no prototype of the two-piece wheel currently exists.

## 8.2.2. The Tire and Wheel Model Development

### 8.2.2.1. The Tire Model Development

Based on previous experience modelling the OTR tire 29.5-29, a simplified approach was applied in this study. Figure 8.7 shows the FE model of the tire/wheel assembly and its cross-section views. Before the tire model was validated, a basic wheel model was developed based on previous experience modelling a 29.5-25 five-piece wheel used for a R2900G underground loader.

The tire mounted on the 33-13.00/2.5 five-piece wheel is a Goodyear port & container handler tire, sized 18.00-33, type ELV-4B, 40 ply rating, and with a bias structure. The tire has an overall width of 516 mm and an overall diameter of 1864 mm with a weight of 379 kg and a volume of 553 litres [28]. Other size information, such as tire thicknesses along the radial directions was unknown and there was not a physical tire of this size available for measurements. The tire shape (cross-sectional profile) and thicknesses in radial directions were estimated based on knowledge of other OTR tire structures and previous modelling experience. This approach will be sufficient for wheel analysis, given that the tire model will be validated with the appropriate material models. The tire/wheel assembly with the conventional lock ring structure was modelled and validated by comparing the static load versus deflection data provided by Goodyear OTR [28] and that the output of the numerical simulations.

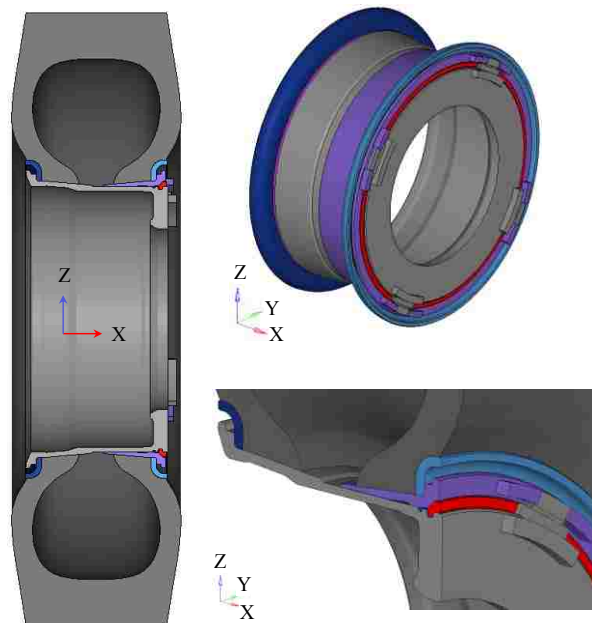


Figure 8.7 The FE model of the five-piece tire/wheel assembly.

Based on the Goodyear OTR tire engineering data [28], with a static load of approximately 33,300 kg acting at the wheel centre, the static load radius of the tire decreases from 932 mm to 874 mm and the section width increases from 516 mm to 564 mm, under an inflation pressure of 150 psi (1000 kPa). These load-deflection characteristics were used as a primary reference point for model creation and validation.

#### 8.2.2.1.1. Tire Discretization

The majority of the material comprising the tire structure is rubber, especially on the outer layer of the tire. In order to simplify the modelling in this study, the rubber was not

modelled as a single entity. Instead, the tire was discretized into several regions, as shown in Figure 8.8. Discretization was based on the physical tire's approximate cross-sectional structure as well as the deformation behaviour of the tire observed under loading. In the FE model, the mass density of the tire,  $683 \text{ kg/m}^3$ , was calculated based on the total mass of the tire (379 kg) and the meshed total solid element volume of the tire (554.8 litres, close to the actual tire volume of 553 litres). The details of tire tread and other structures were ignored for modelling simplifications.

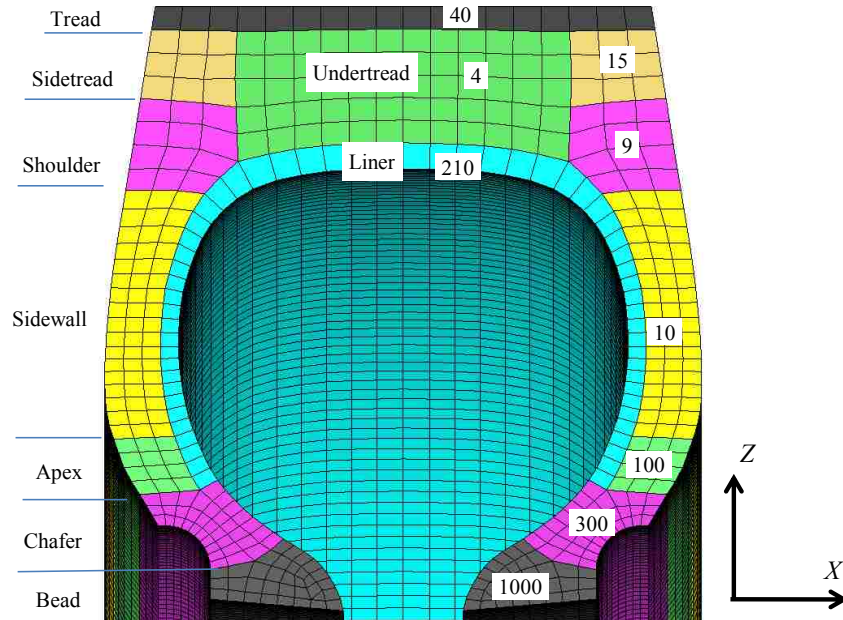


Figure 8.8 Discretization of the tire showing elastic moduli (MPa) at different regions.

To simplify the implementation process of a material model, an elastic material model was assigned to all regions of the tire FE model, with a value of 0.33 assigned for Poisson's ratio. However, different regions of the tire were assigned different elastic moduli (the values are shown as numbers in Figure 8.8), which were related to the observed specific mechanical material behaviour of the tire during loading. Details on the determination of the elastic modulus can be referred in the Section 5.1.2 about the modelling of the tire 29.5-29. This approach enables the numerical model to better capture the non-linear behaviour inherent to tires while allowing for effective simplification for modelling purposes, given the difficulty of performing traditional material tests on such a large tire. For the physical tire, the bead region is the hardest among other regions of the tire. Therefore, the largest elastic modulus of 1,000 MPa was assigned to this region in the FE model. Due to the symmetric nature of the tire geometry and loading conditions, only one half of the tire/wheel assembly was modelled during tire validation.

Generally, the thickness of the real-world OTR tire is highly non-uniform. This non-uniformity would result in geometric characteristics that are not suitable for shell element implementation. Consequently, the tire was meshed with solid elements.

The cross-section of the tire (within the  $x/z$  plane) was first meshed using shell elements, which were then revolved about the centre line of the wheel to form the three dimensional FE model of the structure. The quality of the solid elements can be easily controlled by adjusting the quality of the shell elements before generating the solid elements. Two hundred increments in the circumferential direction were utilized to generate solid elements from the shell elements for the half tire model. The average element side length was approximately 10 mm. The average aspect ratio of all solid elements was approximately 2.5. Four hexahedral elements were used through the thickness of the sidewall to appropriately capture bending stiffness. The hexahedron elements can better capture the large deformation of structures. For the tire model, hexahedral elements were maintained as close to cubic as possible in most regions, with only a small amount of wedge elements used in the bead regions. The curved geometry in the bead region brings difficulty to mesh using only hexahedral elements. The small amount of wedge elements used will have negligible effects on the deformation of the beads since these regions were very stiff and experienced very small deformation during the loading process. A constant stress solid element formulation was used for all elements. The tire was meshed with 88,800 hexahedron elements and 400 pentahedron elements total.

#### **8.2.2.1.2. Modelling of Steel Bead Coils and Body Pliers**

If the tire was modelled with only the aforementioned discretized regions using elastic solid elements, it would not be able to capture the deflection characteristics of the physical tire, in which steel bead coils and body plies play an important role in controlling the tire deflection. Body plies act to reinforce the sidewall rubber and increase the lateral load capacity of the tire. They are generally made of a polyester material that runs perpendicular to the direction of the tread and steel belts. Steel coils in the bead regions are used to help the tire strongly grip the rim base during service even under heavy loading conditions to seal the tire pressure, to provide stable and smooth deflection, and to enhance the life of the tire and wheel components.

Reid et al. [120] and Orengo et al. [121] used beam elements in simplified tire modelling and successfully developed tire models for impact simulations. In this study, beam elements were used to model these structures to control the tire deflection in the desired way. The beam elements were added in three regions of the tire with the same material model but different material properties as shown in Figure 8.9. The beams in the liner region (Figure 8.9(a)) were

along the transverse direction; the beams in the bead and chafer regions (Figure 8.9(b)) were in the circumferential direction, which was the same direction as the steel coils used in the physical tire. The beam elements were built along the edge of the solid elements, one beam element was built along the edge of one solid element. The two end nodes of each beam element were merged with the nodes of the solid element. The beam elements were built in the internal edges of the solid elements at the bead and chafer regions, in order to maintain the deformation characteristics of rubber in these regions so the tire can maintain tight contact with the rim base and flanges. Two hundred and one (201) lines of beam elements (58 beam elements in each line) were added in the liner region, since there were 200 solid elements along the circumferential direction for the half model; 9 lines of beam elements in the bead region and 6 lines of beam elements in the chafer region were added on each side of the tire, with 200 beam elements in each line. The beam elements used in the model were discrete beams with a circular cross-section of 2.0 mm in diameter. These elements utilized an elastic material definition having a mass density equivalent to steel and an initial tension of 50 N. The elastic moduli of the beams were, respectively, 20 GPa, 2000 GPa, 1000 GPa in the liner region, bead region, and chafer region to reflect the different stiffness in these regions. It is important to note that very high elastic moduli were used in bead and chafer regions since the diameters of the beams used were much smaller than the diameters of steel cords in the physical tire.

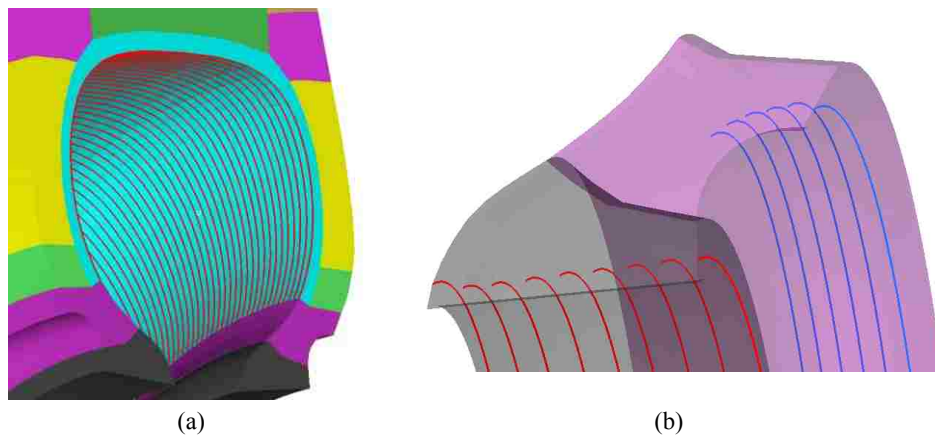


Figure 8.9 (a) Beam elements in the liner region and (b) beam elements in bead and chafer regions.

### 8.2.2.1.3. Other Critical Modelling Features

Penalty based surface to surface contact definitions were applied to model the interactions between the tire and all wheel components. The coefficient of friction, within these contact algorithms, is a function of the static and dynamic coefficients of friction as well as the relative sliding velocity between surfaces and a decay coefficient as expressed in Equation (5.2)



The static coefficients of friction ( $\mu_S$ ), the dynamic coefficients of friction ( $\mu_D$ ), and the decay coefficients (DC) were defined as 0.35, 0.25, and 1.0, respectively, for all the contacts among wheel metal parts; 0.2, 0.15, and 1.0 respectively for the contacts between tire beads and rim base/BS band; 0.5, 0.45, and 1.0, respectively between the tire and flanges.

Gravity was applied to the system using a local acceleration  $9.807 \text{ m/s}^2$ . A stationary rigid wall was created at the bottom of the tire to model the contact between the tire and the ground. To circumvent hourglass deformation, the Flanagan-Belytschko stiffness hourglass control with a coefficient of 0.1 was employed for the entire tire.

During early model development, the application of static forces resulted in tire deformation hysteresis and tire vibrations. These traits are attributable to the interior pressure of the tire. In an effort to reduce vibration and artificial (numerical) noise, mass-weighted damping was utilized in LS-DYNA for the tire. The force vector due to system damping was determined from Equation (5.1).

To assess the amount of damping required for the model, an eigenvalue analysis was conducted to find the natural frequency of the model. This allowed determination of damping constants ( $\omega$ ) suitable for the tire pressurization process and static force application process, which were selected as 39 radian/second and 71 radian/second, respectively. With use of these damping constants, the damping energy was found to be less than 6% of the internal energy of the system; thus ensuring that the application of damping did not significantly influence model behaviour.

#### **8.2.2.2. Wheel Model Development**

This section focuses on the FE model development of half of the five-piece wheel model used for the tire model validation and the modelling of the bolt connection of the two-piece wheel. Other modelling aspects, such as rotating and steering of the wheels, and discretization of analysis focused regions in the numerical testing scenarios, are explained in the following sections.

##### **8.2.2.2.1. Five-piece Wheel Model Development**

Identical approaches to meshing the tire were taken to create the solid mesh for the wheel components. After creating cross-section shell element meshes, 200 solid elements were created along circumferential direction in the half model for all the wheel components. Four hexahedral elements were used through the thickness of the rim base to appropriately capture bending stiffness since the rim base is a critical component. Three elements were used through

the thicknesses of the flanges and BS band due to the geometric size constraints. In contact regions among the components, hexahedral elements were implemented with an approximate cubic geometry. A constant stress solid element formulation was utilized for all elements. The element length ranged from 12.6 mm to 2.9 mm, with an average of 5.0 mm. The maximum aspect ratio of all solid elements was 2.8 and the average aspect ratio was 2.0. The five-piece wheel was meshed with 108,191 hexahedron elements and 4,800 pentahedron elements, and 384 rigid shell elements for the driver keys.

For computation efficiency and modeling simplicity, elastic steel material properties were used for tire validation purpose since the deformation of the steel wheel components were negligible compared to the deformations of the tire. Elastic steel material properties (density of  $7.8 \cdot 10^{-9}$  tonne/mm<sup>3</sup>, elastic modulus of 210 GPa, and Poisson's ratio of 0.28) were assigned to all the components, except the inner ring of elements of the mounding disc, which were modelled as rigid elements. The mounting disc would experience negligible deformation under loading and the rigid modelling was assumed to cause minimal effect on the stresses/strains on other regions of the rim base, far away from the rigid elements. Since the axle of the wheel was not included in the FE model, an artificial node at the axial centre line of the wheel was created. This node was constrained to the rigid ring so the node and the ring act as one rigid entity. The static load and boundary conditions were applied on this node, as a simplified representation of the axle of the wheel. The detailed model of the wheel for validation of the tire is shown in Figure 8.10.

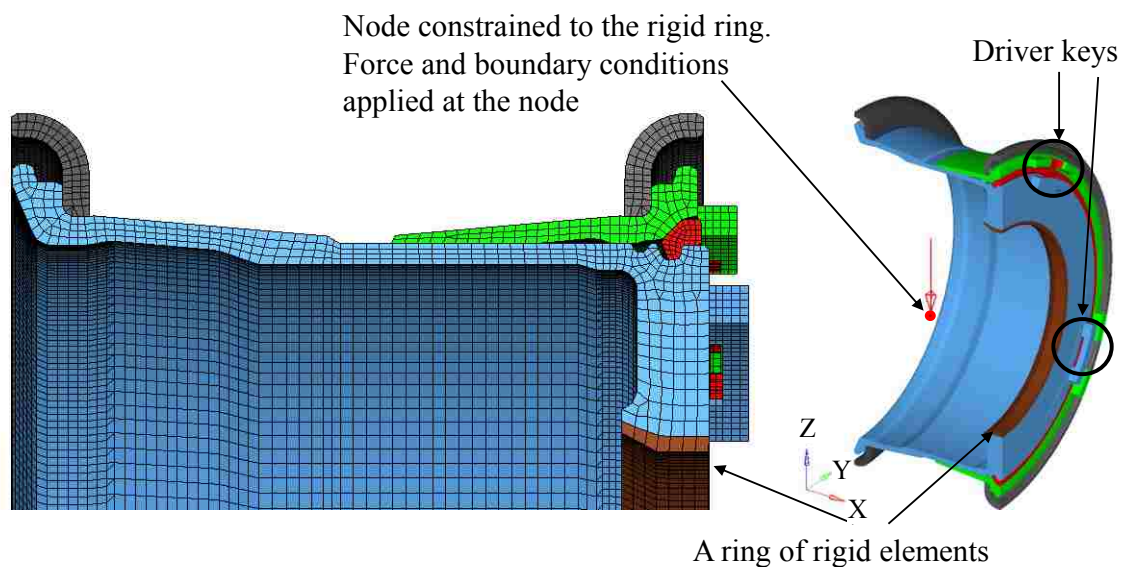


Figure 8.10 Modelling of the five-piece rim for tire validation purpose.

#### 8.2.2.2.2. Two-piece Wheel Model Development

The same approaches used in modelling the five-piece wheel were applied during the model development of the two-piece wheel. Figure 8.11 shows the cross section view of the full wheel model. The meshed element size was selected to be 5.0 mm. The two pieces were joined together with 20 bolts ( $\phi 25.4 \text{ mm} \times 106.68 \text{ mm}$  long). In the FE model, the threaded connection between the bolt and wheel was modelled as one rigid link, under the assumption that the threaded connection will not fail. The bolt head and the nearby contacting wheel area were modelled as another rigid link, assuming no relative motion between the head and the connecting wheel. The bolt shaft was modelled using one beam element, with two ends connecting to the centre nodes of the aforementioned two rigid links. The beams had a nominal diameter of 25.4 mm, with elastic steel material properties assigned. The axial and transverse forces of the beam elements were output to allow the maximum forces of the bolts to be assessed for proper bolt selection. Contacts identical to those used in modelling the five-piece wheel were implemented during modelling of the two-piece proposed wheel.

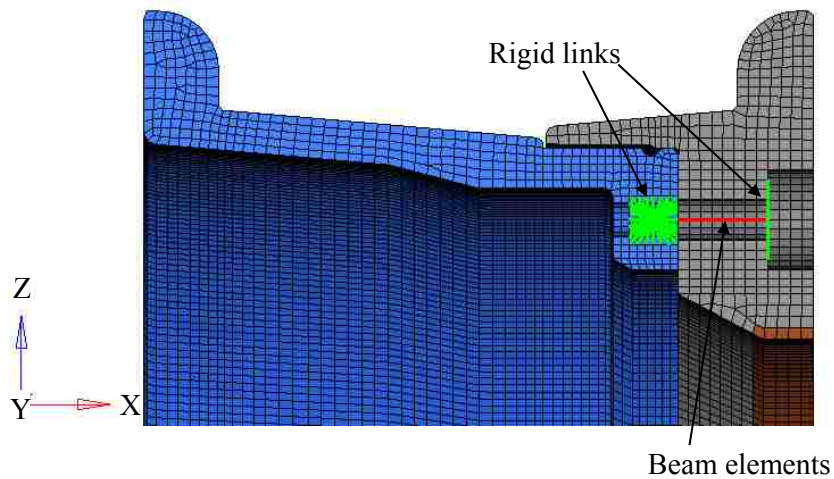


Figure 8.11 Modelling of bolt connection for two-piece rim.

#### 8.2.3. Loading and Boundary Conditions for Tire Validation

Under the static load conditions specified in the Goodyear OTR tire engineering data [28] (33,300 kg load and 1 MPa tire pressure), the tire's static radius (vertical distance from wheel center to ground) decreases 58 mm and the cross section (tire maximum width in lateral direction) increases 48 mm. In the FE model, two loading phases were employed. First, the tire model was loaded under its own weight (gravity) and air pressure (1MPa) was applied to the inner surface of

the tire liner. Subsequently, a static load was applied to the centre node of the wheel, which was constrained to the mounting disc. Since only half of the assembly was modelled, only half of the static load (163.28 kN) was applied. Symmetric boundary constraints were applied on the plane of symmetry. The gravity and pressure loads were ramped up from zero to full load in 0.05 seconds and 0.1 seconds, respectively. The static load was ramped up from zero at 0.3 seconds to full load at 0.4 seconds. Figure 8.12 illustrates the load application time histories and the sketch of load applications. A comparison of the kinetic energy and internal energy of the entire system was performed to ensure that the time scaling of the applied loads did not influence the behaviour of the model. Overall, it was found that the kinetic energy was only 5.5% of the internal energy of the system; thus justifying the use of the time scaling technique.

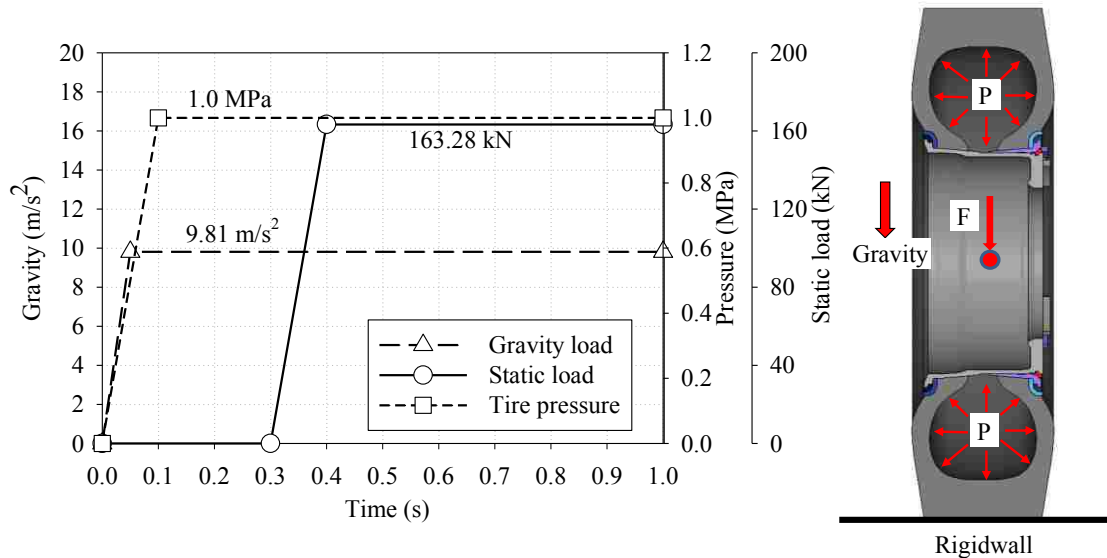


Figure 8.12 Load application histories for tire FE model validation.

#### 8.2.4. Tire Model Validation through Static Load Simulation

Figure 8.13 illustrates the simulated tire deformation under the maximum applied load, which exhibits qualitatively similar deformation behaviour to that of the real tire. The white lines represent the pressurized tire profile before static load was applied.

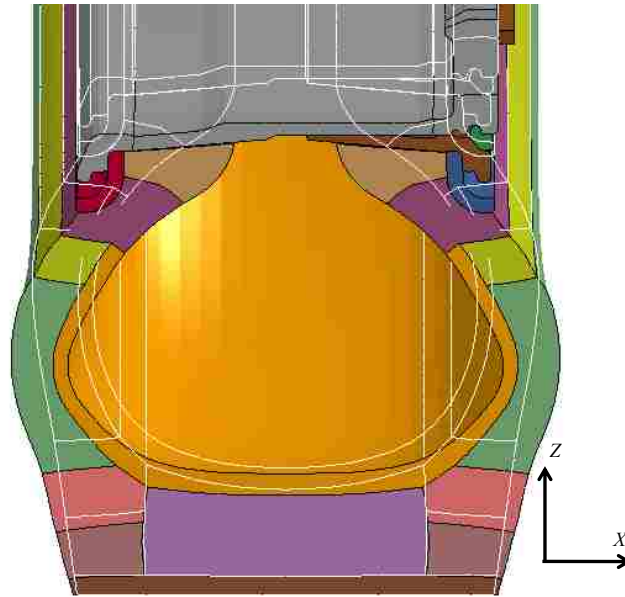


Figure 8.13 Simulated tire deformation of the half model at 163.28 kN static load.

The deformation comparison between the simulated and the engineering data is listed in Table 8.1.

Table 8.1 Tire deflection comparisons.

	Vertical Deflection	% Error	Lateral Deflection	% Error
Engineering data	58 mm		48 mm	
FE simulation	58.36 mm	0.6	47.28 mm	1.5

The percentage error, calculated using Equation (6.1), was used to assess the predictive capabilities of the numerical model relative to the engineering data. The small relative errors (less than 1.5%) indicate that the FE model can predict the static deformation of the tire with considerable accuracy. However, it is uncertain how the model may perform under quasi-static loading conditions. Nevertheless, given that the same modelling practices were applied in this work as in Section 5.1.2, in which a 29.5-29 tire was successfully developed for both static and quasi-static loading conditions, it is expected that the model will adequately capture the quasi-static loading behaviour of the tire. The FE model of the tire/wheel assembly will be used to assess mechanical performances of the five-piece and two-piece wheels.

Once the tire model is validated, it can be used on the two-piece wheel without questioning the fidelity of the model, since the five-piece wheel and the two-piece wheel are geometrically equivalent along regions which contact the mounted tire.

## 8.2.5. Numerical Testing of the Multi-Piece Wheel Assemblies

### 8.2.5.1. Loading and Bounding Conditions for FE Simulations

Based on the observations of the five-piece wheel during service, the wheel and tire have high side wall stresses which are more prevalent during cornering. This results in the lock ring moving or vibrating relative to the lock ring groove during operation, which leads to premature fatigue, fretting and wear of the lock ring groove. Accordingly, in the FE model, similar conditions were simulated. First, the static load, representing vehicle weight and payload, was applied. Subsequently, the application of gravity and tire pressure were applied to the wheel and tire assembly. Finally, to simulate the relative motion of the lock ring and groove interface, rotation of the wheel and tire was prescribed, while the assembly was numerically steered at an angle of approximately  $82^\circ$ .

To simplify the FE model, only the tire/wheel assemblies were included in the model. In order to keep balance (avoid rolling of the tire/wheel assembly around the y-axis), two identical tire/wheel assemblies were joined together by one axle as shown in Figure 8.14.

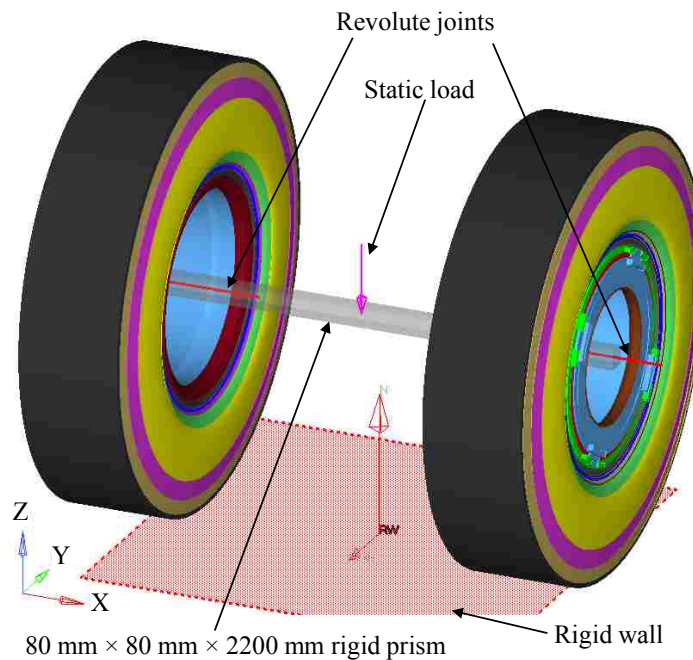


Figure 8.14 FE model set-ups for travelling (rotation) and steering (turning) simulation.

In the FE model, the two tire/wheel assemblies were parallel to each other and separated by 1,740 mm, which was meant to represent the axle spacing of the wheels. The two tires stand on a rigid wall, which represents the flat ground. A rigid 80 mm × 80 mm × 2200 mm square prism was created in the middle of the two tire/wheel assemblies to represent the axle. At both ends of the prism, a revolute joint was created to constrain the prism to the wheels, using a kinematic constraint [114]. In each of the joints, two nodal pairs (n1, n2) and (n3, n4) were created with a separation of 860 mm. The nodal points within the nodal pairs (n1, n2) and (n3, n4) coincided in the initial configuration. Nodes n1 and n3 were constrained to the inner ring of rigid elements on the wheel; nodes n2 and n4 were constrained to the rigid prism, using a kinematic rigid coupling. The static load (double of the maximum static load for each tire at specific travelling speed) was applied at the centre node of the prism, which would be transferred to the tires through the joints. After the tire assemblies achieved their maximum respective static loads and the tire deflections became stabilized, a prescribed translational motion in the y-direction was applied to the prism, which caused the tires to rotate on the rigid wall. Finally the prism was prescribed a turning movement along the vertical axis, z, which resulted in the two tire/wheel assemblies turning left (counter clockwise direction viewed from above), at approximately 82° to simulate steering movement.

Two load and speed conditions were simulated for the five-piece tire/wheel assemblies and the two-piece tire/wheel assemblies. These two conditions were severe loading conditions specified within the Goodyear OTR tire Engineering Data Book [28]. For each tire, the recommended maximum travelling speeds of 24.14 km/h at a load of 23,100 kg, and 8.05 km/h at 26,900 kg were considered. The load application time histories are shown in Figure 8.15 for the 24.14 km/h condition. All simulations were terminated at 1.65 seconds.

The static coefficients of friction between the tires and rigid wall were selected as 0.65. Preliminary simulations were conducted to allow for the appropriate selection of the coefficients of friction. If the coefficient was reduced, excess slippage would occur between the tire and the rigid wall. Larger values of the friction coefficient caused excessive hourglass deformation of the tires and simulation would terminate before reaching the termination time of simulation. In order to control hourglass deformation of the tire, a Flanagan-Belytschko stiffness form with exact volume integration for solid elements hourglass control type was used with an hourglass coefficient 1.0 [114].

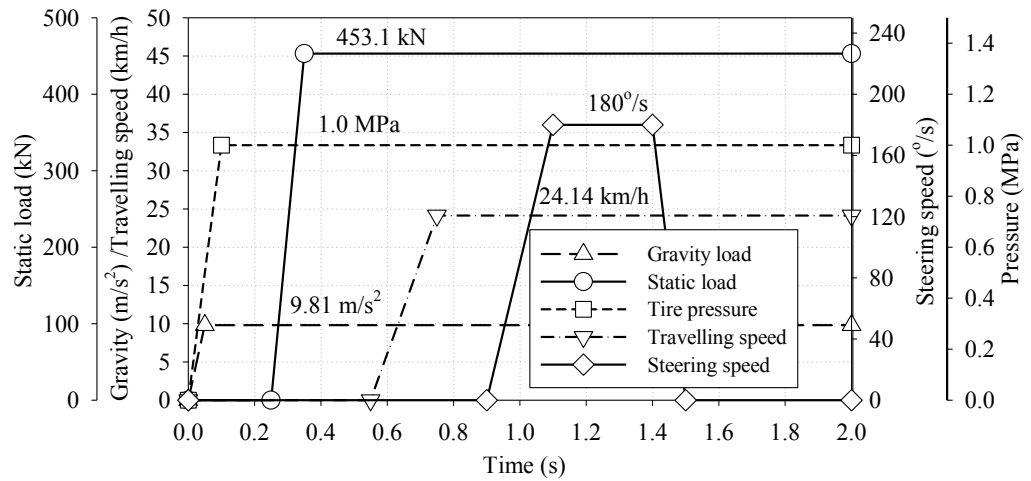


Figure 8.15 Load application histories for 24.14 km/h transverse travelling condition.

For the five-piece wheel, four drive keys were used to prevent the relative rotation between the rim base and BS band and to evenly distribute the reaction forces at the driver key regions. In conditions of rotation, there is a greater tendency for the BS band to rotate relative to the rim base, compared to static load conditions. The modeling technique for the driver key using rigid shell elements in the static load condition did not work efficiently for the rotation condition, causing contact penetration between the driver key and wheel, and between the driver key and BS band, resulting in excess relative rotation of the components. In the rotation loading condition, the driver keys were modeled as solid elements as one entity with the rim base and contacts were established between the rim base and BS band at driver key locations. The relative rotation between the two components was prevented using this approach. To prevent the relative rotation between the flange and BS band/rim base, a static coefficient of friction of 0.80 was used for the contacts between these parts. The static coefficients of friction between the tire and wheel components were selected as 0.95. The static coefficients of friction among the wheel components were selected as 0.35.

To reduce the artificial (numerical) noise effects on stress levels, stiffness damping was implemented. This type of damping is more effective for high frequencies [114]. The damping coefficient ( $\beta$ ) of 20% was applied to all wheel (metal) components. The damping matrix was computed from the stiffness matrix as indicated in Equation (6.2). Detailed modelling parameters are included in Appendix E.5.

As pointed out by Conle et al. [130], plastic modeling gives poor quality of stress/strain assessment when faced with reversals in loading direction. In this research, a linear elastic model



was created to simulate the aforementioned loading conditions. Using linear elastic FEA to obtain stress/strain data is a common acceptable practice for durability studies. During fatigue life analyses, linear elastic stresses/strains were converted to elastic-plastic stresses/strains using modified Neuber method [98] within nCode DesignLife.

### 8.2.5.2. Modelling Approaches for the Focused Regions

For the conventional five-piece wheel design, the concerned region is located at the lock ring groove region on the rim base, where wear and premature fatigue failure generally occur. The stress and fatigue life analyses will focus on the lock ring groove region (FR1-1 as shown in Figure 8.16). As an alternative to the five-piece wheel, the two-piece wheel is constructed by bolting the two separate pieces together. For comparison purposes, the potential wear and premature fatigue failure regions on this wheel are located at the transition areas between the bead contacting region and flanges (FR2-1 and FR2-2 as shown in Figure 8.16), and at the inner faces where the two wheel pieces make contact (FR2-3 in Figure 8.16).

Another region of focus for the two-piece wheel is the connecting bolts (FR2-4 in Figure 8.16). The bolts are expected to be strong enough to withstand the axial and transverse forces under severe load conditions. Therefore, beam elements were used to model the bolt connections and the element's forces were calculated as a reference for bolt selection.

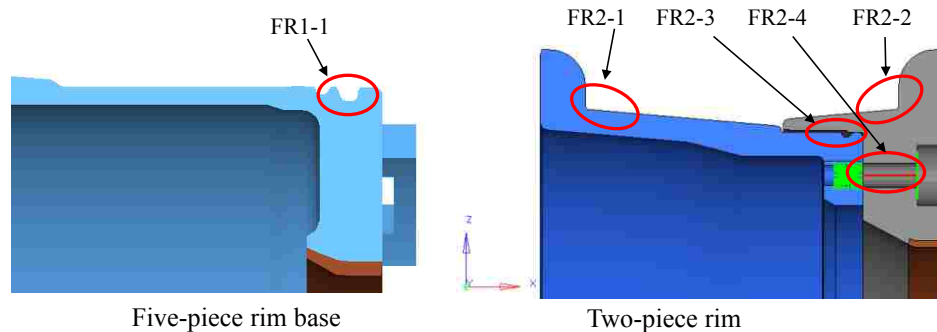


Figure 8.16 Analysis focused regions for the five-piece and two-piece wheels.

Fatigue failures primarily initiate at the surfaces of structures. The stresses of solid elements are calculated from the centroids (integration point) of solid elements [114], which do not accurately reflect the stress levels at the outer surface. When calculating the fatigue life using FE stress/strain results, the fatigue results will only be as accurate as the stress information in the model, and a 5% error in stresses can result in a factor of 2 errors in the calculated fatigue life [131]. In order to accurately capture the surface stresses on the structure, a thin layer of shell

elements (0.01 mm thick) were extracted from the solid elements for the focused areas and the simulated shell element stresses will be used to assess the fatigue life.

#### **8.2.5.3. Selection of Material Properties for Numerical Fatigue Assessment**

For the five-piece wheel, the fatigue life in the gutter region was investigated using the cyclic fatigue properties of the specimens extracted from the gutter without corrosion. For the two-piece wheel, the cyclic fatigue properties of the specimens extracted from the middle region of the rim base was used, as listed in Section 6.3. Using of lower fatigue strength properties in the two-piece wheel is more conservative for this innovative design, considering the fabricating process of the two-piece wheel may make its fatigue strength lower than the gutter region of the five-piece wheel.

## Chapter 9. Discussions on Innovative Designs

### 9.1. Discussions on Threaded-connection Design

#### 9.1.1. BS Band Pull-out Simulation Results

Figure 9.1 illustrates cross-section cut view of the simulated deformation characteristics when the BS bands of both respective wheels were pulled out and engagement between the BS bands and rim bases failed. In the lock ring design, the mechanism of failure was buckling of the rim base at the transition between the reduced and thick walled regions of this portion of the wheel. For the proposed threaded design, the deformation mode during failure was noted to be a combination of buckling deformation of the rim base and the BS band, and thread failures on the BS band resulting from high localized plastic strains at the base of the threads. It is also worthy to note that the increased material thickness, along the axial direction of the rim base, results in a lower degree of buckling in the proposed threaded connection.

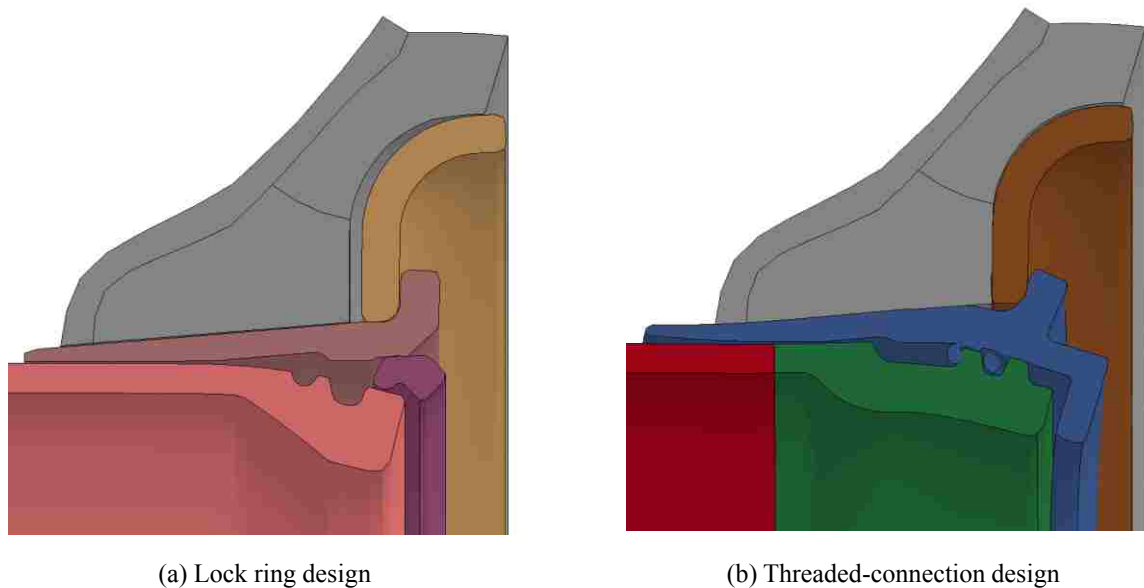


Figure 9.1 Simulation deformation predictions of the BS band disengagements of (a) the lock ring design and (b) the threaded-connection design.

Figure 9.2(a) illustrates the predicted axial force versus displacement responses during the pull-out simulations. Very large pull-out forces exist for both designs with maximum forces for the proposed threaded locking design being 9,552 kN and 4,476 kN for the conventional lock design. Such a significant increase in pull-out load is expected due to the increased contact area resulting from the threads designed into the rim base and BS band, and added material in the neck

region. An increase in pull-out force of 113% was noted over the conventional design. This finding, as one would expect, demonstrates stronger and more thorough engagement between the BS band and the rim base.

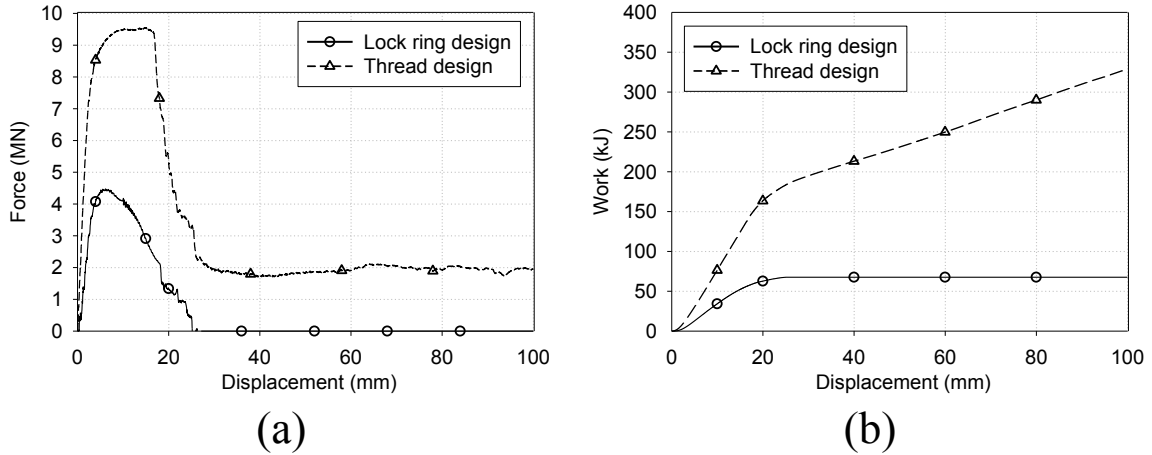


Figure 9.2 Predicted pull-out (a) force/displacement response and (b) energy/displacement response of the conventional and proposed wheel designs.

For the proposed threaded connection design, elastic loading occurs until approximately 7,500 kN and a stiffer response is noted over the conventional wheel design. Localized plasticity within the threads occurs over a displacement of approximately 15 mm, where the maximum pull-out force is obtained (9,552 kN) until material shearing at the root of the threads initiates, resulting in a rapid reduction in the pull-out force. Localized material rupture occurs within the threaded region in a progressive fashion and a constant load during pull-out is observed to occur over the displacement range of 25 mm to 100 mm. The combination of material failure at the threads and contact between the wheel entities results in the approximate constant load of 2,000 kN to occur during pull-out. This failure mechanism is far more conservative in design over the conventional wheel as retention forces continue to exist after the maximum force has been obtained and deformation (pull-out) continues. In a practical implementation of the proposed wheel design the maintained retention force would allow for gradual reduction in air pressure within a tire during blow-out and/or disengagement of the wheel components; thus potentially resulting in a safer mode of failure.

Figure 9.2 (b) illustrates an approximation to the work necessary to pull-out the wheel components. This information was obtained by integrating, using a trapezoidal numerical integration scheme, the force/displacement response observed for each wheel design. Another superior characteristic of the proposed threaded connection is the ability of the structure to

continue to require work, or dissipate energy, during deformation. At approximately 20 mm displacement the conventional design illustrates a maximum energy dissipation of approximately 67 kJ. However, the proposed design demonstrates a level of approximately 170 kJ at the same displacement which continues to increase linearly during deformation. The proposed design dissipates approximately 4.8 times more energy than the conventional design under the prescribed displacement of 100 mm.

### 9.1.2. Wheel Stress and Fatigue Life Analyses

Figure 9.3 illustrates the contours of effective stress (von Mises stress) of the front regions of the rim bases for the proposed threaded-connection design and the conventional five-piece lock ring design for the prescribed quasi-static loading condition. These stress contours are from the shell elements of the out layers. The front regions exhibited the greatest magnitude of stresses. Simulation predictions indicate that the highest stressed region of the rim base are located at the bottom of the structure, which are expected given the vertical (downward) loading condition prescribed. The maximum von Mises stresses were 129.3 MPa for the proposed threaded-connection design and 155.3 MPa for the conventional five-piece lock ring design, on the out layer of shell elements. These findings indicate a decrease of approximately 16.7% in the magnitude of the von Mises stress for the threaded-connection design. Furthermore, the extent of the region of the structure which experiences higher stresses is much broader for the conventional design.

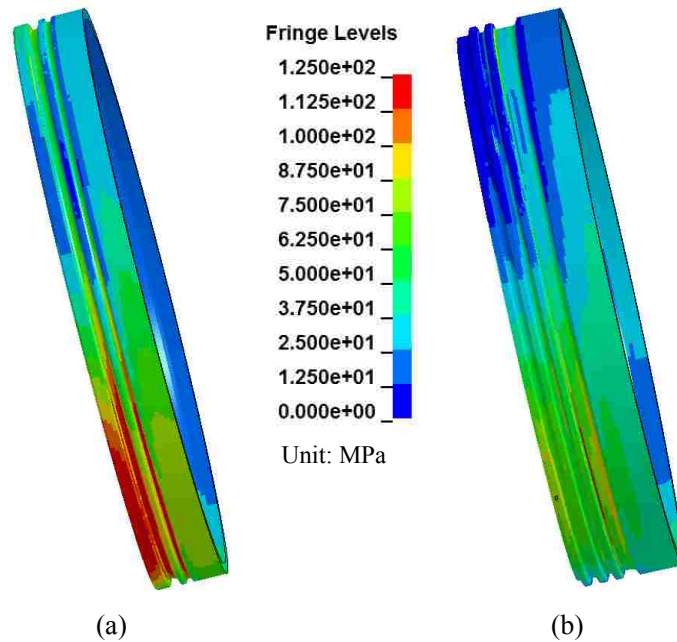


Figure 9.3 von Mises stress contours of the lock ring design (a) and the threaded-connection design (b) during quasi-static loading simulations.

Table 9.1 lists the maximum von Mises stresses/maximum shear stresses on the front regions of the shell elements. All stresses are below the halves of the yield stresses. The maximum shear stress is 16.5% lower for the threaded-connection design than the lock ring design.

Table 9.1 The maximum von Mises stress/maximum shear stress at the front regions of shell elements for the lock ring design and the threaded-connection design.

Lock ring design	Threaded-connection design	difference
155.3/89.2	129.3/74.5	-16.7%/-16.5%

Cyclic fatigue properties of the specimens extracted from the gutter without corrosion were used to assess the fatigue lives of both designs. Table 9.2 summarizes the findings from the fatigue analyses. Predictions of the fatigue life, using both  $S-N$  and  $\varepsilon-N$  methods, are presented. In both cases, large numbers of the cycles to failure are observed, which is consistent to the findings of Vijayan et al. [5, 14], where infinite fatigue lives were found to exist for undamaged mining wheel assemblies. It is important to note, regardless of the method used to predict the fatigue life of the wheel assemblies, the proposed threaded-connection increased the fatigue life of the mining wheel approximately by two orders of magnitude.

Table 9.2 Fatigue life predictions (cycles) and comparisons.

Fatigue life estimate method	Conventional lock ring design	Proposed threaded connection design	Relative difference between designs
$S-N$	$4.019 \times 10^{13}$	$2.3472 \times 10^{15}$	5740.3%
$\varepsilon-N$	$2.412 \times 10^{21}$	$8.582 \times 10^{22}$	3458.0%

## 9.2. Discussions on Two-piece Wheel Numerical Testing

### 9.2.1. Stress Analysis

For all simulations, the five-piece and two-piece tire/wheel assemblies travelled and turned approximately the same distance and angles, separately, under identical loading conditions. Figure 9.4 illustrates the travelling paths of the assemblies under the 8.05 km/h and 24.14 km/h conditions, in which the red lines represent the moving traces of the nodes on the axles. The identical traces of motion indicate that the wheel components of the five-piece wheel and two-piece wheel experienced identical external loads and the stresses the two wheels experienced are comparable.

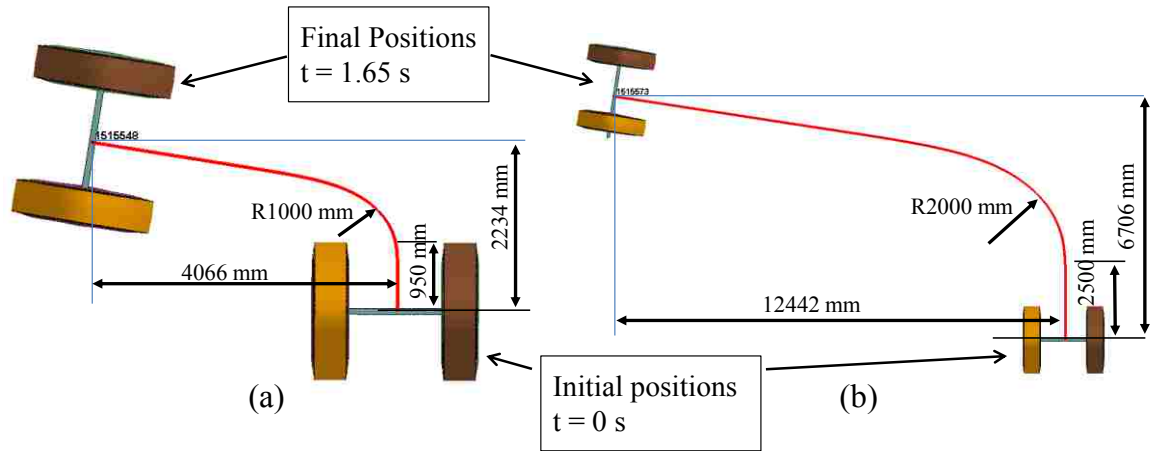


Figure 9.4 Initial and final positions of the tires, and moving traces of the axles with approximate dimensions (a) 8.05 km/h and (b) 24.14 km/h.

Stresses on the wheel components were examined on both the left side and right side of the wheels and it was found that the stress levels were generally higher on the wheel components on the left side than the corresponding wheel components on the right side. The differences were possible due to the small cornering radii in the left side (inner side) than the right side (external side). Therefore, in this study, the left side wheels were selected for comparison between five-piece wheel and two-piece wheel.

For all simulations, the stresses at different regions along the circumferential direction varied according to their locations and load applications. Figure 9.5 shows the time histories of effective stress (von Mises) of the four shell elements at the lock ring groove for the 24.14 km/h condition. These elements were located at the lower valley of the lock ring groove, and were spaced equally apart by approximately  $90^\circ$  in the circumferential direction. Prior to the load applications, element 1 was located at the bottom of the wheel and element 2 was positioned at the top of the wheel. From the stress histories, it is observed that the stresses ramped up linearly with the loading of gravity and tire pressure. Then, the stresses are seen to plateau at different stress levels for different elements (at different locations). With the application of the static force at 0.25 seconds, the stress levels changed again until a new constant stress level was reached for respective elements. During this period, element 1 had the highest von Mises stress (approximately 150 MPa) since it was located at the bottom of the wheel. When the wheel began rotation at 0.55 seconds, the stresses of the elements began fluctuating based on their initial circumferential positions. The steering manoeuvre ramped up from 0.9 seconds and reached the maximum angular speed of  $180^\circ/\text{s}$  at 1.1 seconds. At 1.4 seconds, the steering speed was

decreased linearly, until 1.5 seconds, at which steering motion stopped while the tire/wheel assemblies continued to rotate. From approximately 1.4 seconds, the stresses of some elements increased very quickly. The high stresses were caused by the change of steering speed. These findings are consistent with observations of the wheel during service, indicating that the steering condition represents a severe loading condition for the wheel.

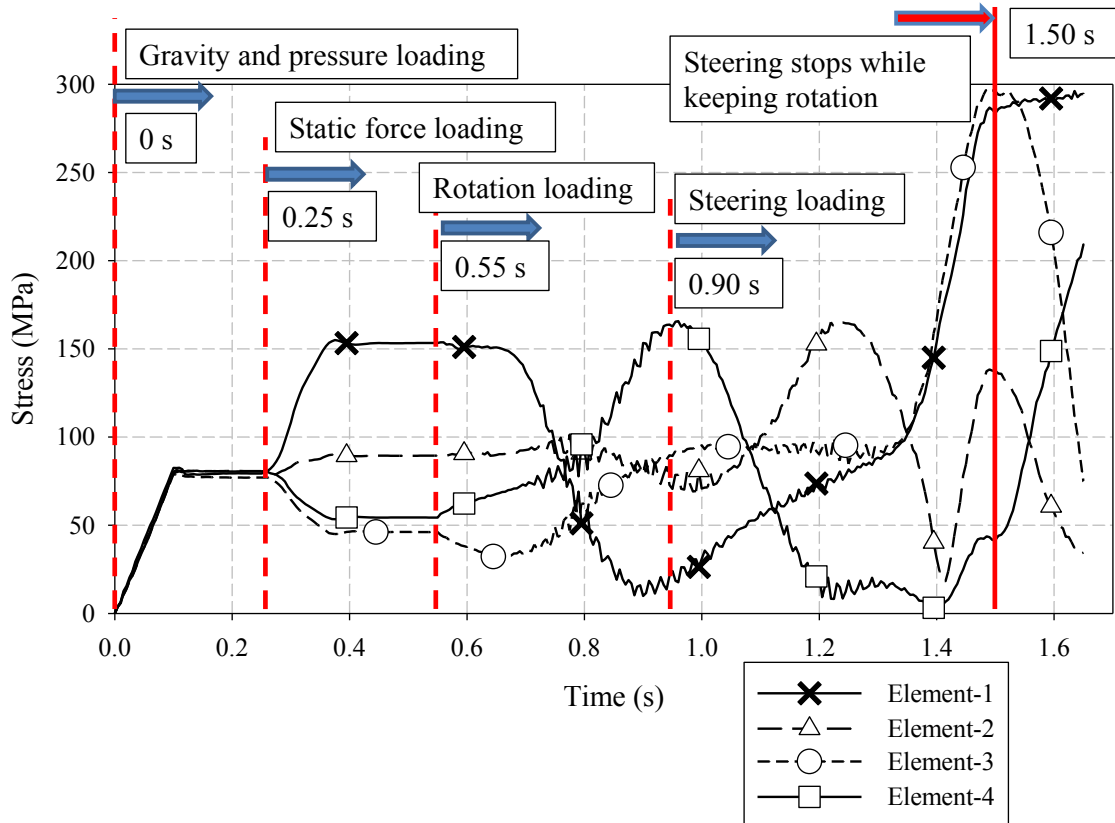


Figure 9.5 von Mises stress time histories for the shell elements on lock ring groove – 24.14 km/h.

Figure 9.6 shows the maximum shear stress contours for the shell elements at the lock ring region (FR1-1) and at the FR2-1 and F2-3 regions of the two-piece wheel at  $t = 1.65$  second, under the 24.14 km/h condition. Figure 9.6 (b) shows the maximum shear stress contour of the piece of the rim base with the O-ring groove on it. The stress levels are lower on the other piece of the rim without the O-ring groove. From the stress contours it can be seen that both the maximum shear stress and the average shear stress are much higher in the FR1-1 region than FR2-1 and FR2-3 regions. The maximum shear stresses in the FR2-2 region were found lower than in the FR1-1 region as well.



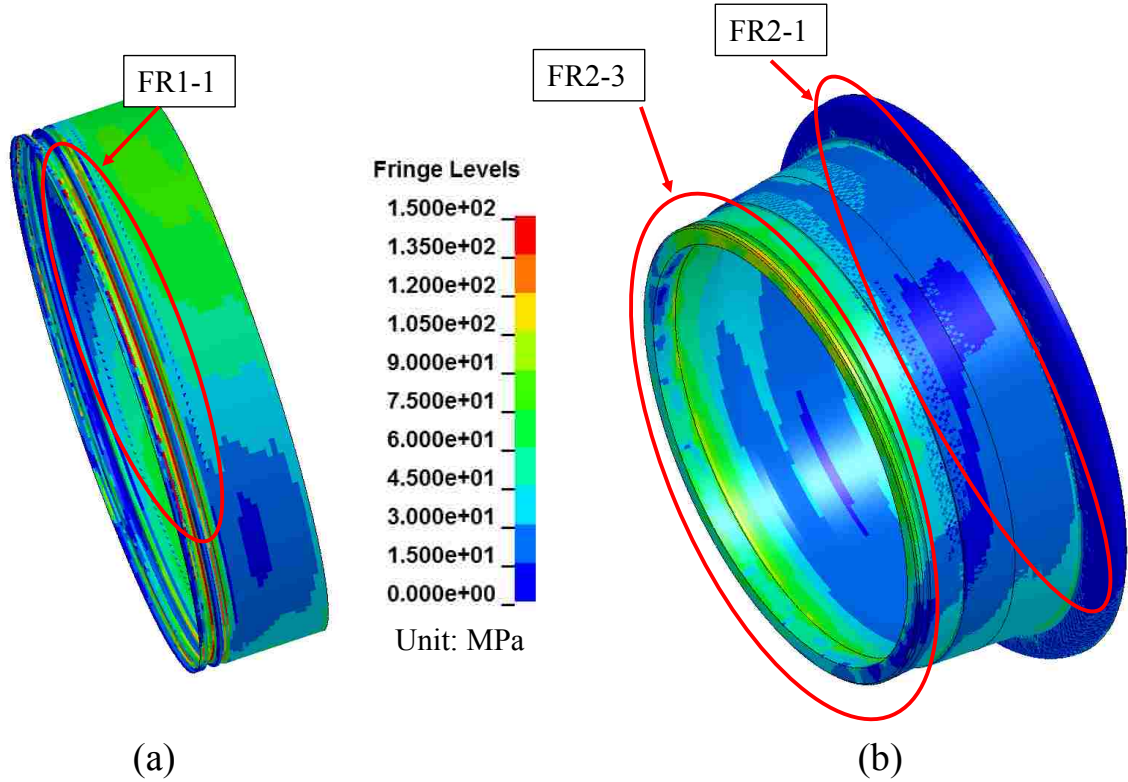


Figure 9.6 Maximum shear stress contours at lock ring groove (FR1-1) (a) and at the FR2-1 and FR2-3 regions of the two-piece rim (b) at  $t = 1.65$  s under 24.14 km/h condition.

Table 9.3 summarizes the maximum von Mises stresses and maximum shear stresses for the two load conditions. The values in the brackets are the relative stress increases compared with the five-piece wheel, calculated using Equation (6.1). For the five-piece wheel, the maximum von Mises stresses are above the yield strength under both loading conditions; the maximum shear stress is above the shear yield strength under the 24.14 km/h condition. The stresses above the yield strengths are highlighted in red colour. Comparing to the five-piece wheel, the two-piece wheel decreased the maximum von Mises stresses by a minimum of 56.3% and a minimum of 52.5% respectively, and the maximum shear stresses by a minimum of 55.0% and a minimum of 52.1% respectively, for the 8.05 km/h and 24.14 km/h conditions.

Table 9.3 Maximum effective/maximum shear stresses (MPa) at different focused regions.

	8.05 km/h		24.14 km/h	
Five-piece	381.1/190.7 (lock ring groove)		498.9/250.0 (lock ring groove)	
Two-piece	130.2/65.9 (-65.8%/-65.4%) (FR2-3)	166.7/85.9 (-56.3%/-55.0%) (FR2-2)	237.0/120.2 (-52.5%/-52.1%) (FR2-3)	179.6/94.1 (-64.0%/-62.5%) (FR2-2)

Comparing the stresses between the 8.05 km/h and 24.14 km/h conditions, the maximum von Mises stress increased by 30.9% (from 381.1 MPa to 498.9 MPa) for the five-piece wheel and 82.0% (from 130.2 MPa to 237.0 MPa on FR2-3 regions) for the two-piece wheel. The maximum shear stresses increased by 31.1% (from 190.7 MPa to 250.0 MPa) for the five-piece wheel and 82.4% (from 65.9 MPa to 120.2 MPa) for the two-piece wheel on FR2-3 region.

Examining the stress histories of the five-piece wheel, it was observed that the maximum von Mises stresses were only 5% higher for 24.14 km/h than for 8.05 km/h before travelling speeds were applied to the model at 0.55 seconds. After rotation and steering motions were applied, the stress levels increased dramatically, especially in the 24.14 km/h simulation. Therefore, it can be concluded that the travelling and steering speeds of the vehicles are the key contributors of the stress levels on wheel components.

It is important to note that the predicted stresses were based on elastic material properties used in the FE simulations. The predicted effective stresses (shown in red colour in Table 9.3) for the five-piece wheel at both the 8.05 km/h and 24.14 km/h conditions are significantly higher than the yield strength of the physical wheel material (368 MPa). In practical situations, highly localized plastic deformations at the surfaces of the wheel components would occur when the stress levels are above the yield stress. This would result in localized yielding (plasticity) and reduced stresses compared to the FE predicted stresses. The maximum 1st principal stresses are much lower than the corresponding effective stresses and this implies that the higher effective stresses are mainly compression stresses. Nevertheless, the predicted stress/strain fields within the wheels were converted to elastic-plastic stresses/strains in nCode DesignLife before calculating fatigue lives.

### **9.2.2. Connecting Beam Element Forces**

During the static loading, tire rotation and steering processes, the ends of the two wheel pieces were found to maintain contact. Therefore, no separation was observed under the specified loading conditions.

The beam element forces were used to assess the forces the bolts would experience. These forces were monitored and output in the FE simulation. During rotation and steering processes, each beam element did not experience the same axial and transverse forces for a given instant in time since their instantaneous positions were different. Figure 9.7 shows the histories of axial forces of the four beam elements for the 8.05 km/h condition. These four beams were equally apart, resulting in a 90 ° separation of each beam in the circumferential direction. Prior to

the load applications, beam element 1 was located at the bottom of the wheel and beam 2 was positioned at the top of the wheel. The patterns of the curves of the axial forces versus time in Figure 9.7 are similar as to those of the curves of the stresses versus time in Figure 9.5. During the application of the maximum static load (between 0.3 seconds and 0.6 seconds), beam 1 had the highest axial force (approximately 88 kN), which is expected since it was located at the bottom of the wheel. The steering manoeuvre created very high tension forces in the beam elements. A maximum tension force of 111.3 kN was observed at  $t = 1.62$  seconds, when the wheel was turn at approximately  $82^\circ$ . The shear forces (transverse forces across the cross section of the beam elements) of all the beam elements were observed to be negligible. This indicates that the connecting bolts are primarily loaded under axial tension and shear forces are not a concern.

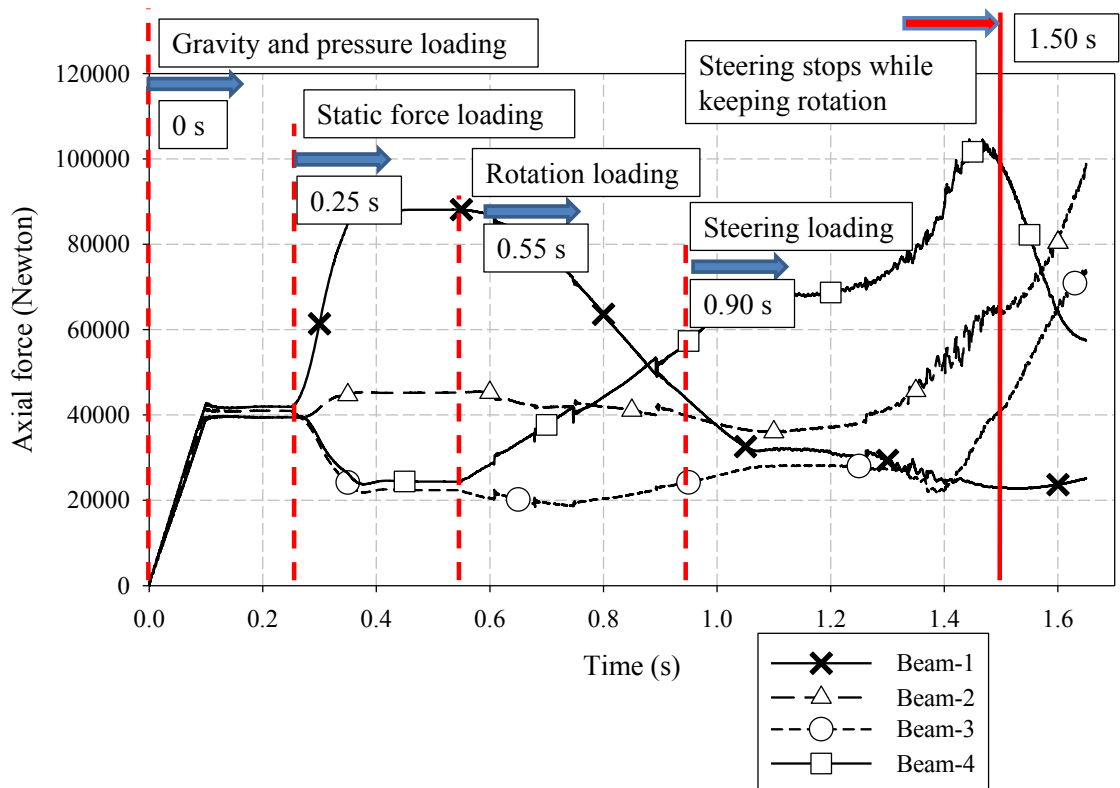


Figure 9.7 Axial forces on the 4 beam elements – 8.05 km/h condition.

The maximum axial beam forces for the 8.05 km/h and 24.14 km/h conditions were 111.4 kN and 195.6 kN, respectively. The maximum bolt force in the 24.14 km/h condition is 75.7% higher than that in the 8.05 km/h condition. This observation is consistent with the finding that travelling and steering speeds have a significant effect on stress levels of wheel components. These estimated forces may be used as a reference for bolt selection.

### 9.2.3. Fatigue Life Simulation Results.

Table 9.4 summarizes the findings from the fatigue life analyses. Predictions of the fatigue life, using both  $S-N$  and  $\varepsilon-N$  methods, are presented. In both cases, a large number of cycles are observed except on the five-piece wheel under the 24.14 km/h condition, which indicates a finite number of cycles ( $8.346 \times 10^5$ ), lower than the transition life ( $5 \times 10^6$ ). For all the regions considered, due to the consideration of plasticity and stress correction from linear FE results, the  $\varepsilon-N$  approach predicted higher fatigue life than the  $S-N$  method. For the five-piece wheel under the 8.05 km/h condition, although the maximum von Mises stress is above yield, a very large number of cycles to failure was predicted. This implies that the stresses are typically under compressive state.

Table 9.4 Minimum fatigue  $S-N/\varepsilon-N$  life (cycle) comparisons on focused regions.

Fatigue life estimate method	Wheel	8.05 km/h		24.14 km/h	
$S - N$	Five-piece	$4.946 \times 10^{10}$ (lock ring groove)		$8.346 \times 10^5$ (lock ring groove)	
	Proposed two-piece	$1.091 \times 10^{14}$ (FR2-3)	$2.843 \times 10^{12}$ (FR2-2)	$7.203 \times 10^{11}$ (FR2-3)	$1.941 \times 10^{11}$ (FR2-2)
$\varepsilon - N$	Five-piece	$2.834 \times 10^{17}$ (lock ring groove)		$3.828 \times 10^{12}$ (lock ring groove)	
	Proposed two-piece	$6.861 \times 10^{19}$ (FR2-3)	$2.620 \times 10^{17}$ (FR2-2)	$4.918 \times 10^{17}$ (FR2-3)	$7.805 \times 10^{15}$ (FR2-2)

Corresponding to the stress levels, the fatigue lives for the five-piece wheel are over four orders of magnitude higher under the 8.05 km/h condition than those under the 24.14 km/h condition, and ten times higher for the two-piece wheel. Under identical steering condition, high traveling speed caused much high stresses, consequently much lower fatigue live were predicted on the wheel components. Using the  $S-N$  approach, the fatigue lives for the two-piece are at least two orders of magnitude higher than the five-piece wheel under both loading conditions. Using the  $\varepsilon-N$  approach, the fatigue lives are almost identical between the five-piece and the proposed two-piece wheel under the 8.05 km/h condition, and the fatigue life for the two-piece wheel is at least two orders of magnitude higher than the five-piece wheel under the 24.14 km/h condition.

Due to the similar structure between the mining vehicle five piece wheel (29-25) and the port container handler vehicle five-piece wheel, the proposed two-piece wheel can be used in mining industry without compromising its advantages described above.

## Chapter 10. **Summaries and Conclusions**

A thorough research investigation was conducted on safety issues of multi-piece wheels for OTR vehicles, especially for heavy-duty mining vehicles. The wheel and tire performance of a five-piece wheel was tested both experimentally and numerically. The fatigue lives of the wheel base were investigated in different conditions, namely, new condition, geometry degradation condition, and material degradation condition. Two innovative designs were proposed to enhance the performance and durability of the multi-piece wheels. The following conclusions can be drawn from this research.

### **10.1. Summary on the Analyses of the Fatality Reports**

Forty-nine fatality reports, associated with multi-piece wheel failure in Canada, the United States, and Australia during 2008-2012, were analyzed. Multi-piece wheel/tire assembly failures can be classified in three failure modes, namely, tire explosion, tire rupture, and tire blow-out. Of the forty-nine fatality incidents, two incidents were caused due to tire explosion and another two incidents were caused due to tire zipper rupture. The remaining fatality incidents were caused due to tire blow-outs, which were associated with failure of multi-piece wheels to hold the tire pressure.

Blow-outs are usually caused by incorrect assembly, metal fatigue, corrosion, wear, impact damage, over inflation, and under inflation. In those situations, the sudden separation of the engaged wheel components under high pressure can cause property damages and human injuries. The majority of the blow-outs were a result of the incorrect use of the split lock ring; either by incorrect installation in the gutter region or by corrosion, wear, and fatigue cracks in the gutter region. This discovery reveals the appropriate direction of design improvement to enhance the safety of multi-piece wheel wheels through the removal of the lock ring locking mechanism.

### **10.2. Conclusions on Experimental Tire Testing and Rim Base Testing**

#### **10.2.1. Experimental Tire Testing**

This study investigated the deflection response of a five-piece wheel and tire assembly on a heavy mining vehicle HLD R2900G when subjected to excitation. The Goodyear tire 29.5-29 was experimentally tested to determine its deflection performance and planar deformation characteristics. Based upon the work completed within this study the following conclusions can be made:

- 1) For each quasi-static test, linear relationships were experimentally observed between tire lateral deflections versus wheel vertical displacements. The average proportionality constant between the two measurements of 0.3678 mm/mm for the tire 29.5-29 was determined.
- 2) For the most aggressive loading conditions considered within this study, maximum wheel vertical displacement and tire sidewall lateral deflection were observed to be approximately equal to 80 mm and 35 mm, respectively.
- 3) For each static test, linear relationships were observed for the vertical wheel displacement and the lateral tire deflection versus tire load. Approximate values of 2.81 kN/mm and 6.81 kN/mm were observed for the vertical displacement and the lateral deflection respectively.
- 4) Based on a static loading condition, good correlation between engineering data and the experimental findings was found with respect to load versus vertical displacement and lateral deflection with errors of 2.7% and 8.1% respectively.

### **10.2.2. Laboratory Rim Base Testing**

Static load tests were conducted on the rim base of a five-piece wheel, sized 29-25.00/3.5 and commonly used for 29.5-29 or 29.5R29 OTR tires. The applied load was controlled so the rim base experienced elastic deformation. Based on experimental observations, the following conclusions can be drawn:

- 1) The measured deflection and strain data from experimental tests showed approximately identical results for multiple tests under identical boundary and testing conditions. Consistency in testing observations was obtained.
- 2) Linear relationships were observed for the deflection/load and strain/load responses of the rim base for all regions monitored during the testing.
- 3) Maximum rim deflections at the top and side locations were experimentally observed to be 3.0 mm and 2.1 mm, respectively. Maximum strain measurements at gauge locations (1) through (5) were found to be  $292.2 \times 10^{-6}$ ,  $197.3 \times 10^{-6}$ ,  $127.6 \times 10^{-6}$ ,  $102.9 \times 10^{-6}$ , and  $901.9 \times 10^{-6}$ , respectively.

### **10.3. Conclusions on the FE Model Developments**

#### **10.3.1. Tire Model Development**

Validation of the tire model to experimental findings was completed through examination of the displacement field of various regions on the tire. The relative errors of the simulation results were within 5.4% compared with the experimental findings under static loading condition. The average accumulative error and average validation metric were 9.7% and 0.96 respectively under quasi-static condition. Based upon the work completed in this study, it can be concluded that The FE model of the tire 29.5-29 can predict the tire deflection characteristics with acceptable accuracies, which are normally 15%.

#### **10.3.2. Rim Base Model Development**

The very good degree of predictability of the displacement and circumferential strain from the numerical model and the thorough error analyses of these observations provide a strong degree of confidence in model capabilities. Correspondingly, the numerical model of the rim base combined with the rest of the wheel components, which were modeled following consistent discretization procedures, as well as the numerical model of the tire were used for subsequent structural analyses.

### **10.4. Geometry Degradation Analysis of the Rim Base**

In this study, the geometrical differences and fatigue lives were compared amongst a new OEM rim base, a worn OEM rim base, and a new heavy duty HT2000 rim base, which have the same rim size. The dimensions of the worn OEM rim base were established based on the “NO GO” gauges invented by NSIW to facilitate the inspection of the wheel components. Computer simulations were used to assess the stress levels and fatigue lives in critical regions. Under identical loading conditions (displacing the rim base 82.5 mm downward quasi-statically), the predicted fatigue lives for the OEM worn wheel are 100% lower than the predicted lives for the OEM new wheel, on the corresponding regions; the predicted fatigue lives for the HT2000 new wheel are over 75% higher than the lives of the OEM new wheel, on the corresponding regions.

The simulation results suggest the dimensions determined by the NSIW “GO/NO-GO” gauges are effectively designed to identify wheel geometries which exhibit a reduced fatigue life condition and should be considered for maintenance. The use of the gauges or similar methodologies to facilitate the inspection of wheel components is highly recommended to ensure

the safety. The stress and fatigue life comparisons among the three different wheels suggest that material wear (geometry degradation) is a significant concern in the wheel's fatigue life.

### **10.5. Material Degradation Analysis of the Rim Base**

Using tested stress-based cyclic material properties and estimated strain-based cyclic material properties for the new and corroded gutter specimens, the material property degradation effect on the fatigue life was investigated. It was found the fatigue lives of the corroded materials were significantly reduced by at least six (6) orders of magnitude.

### **10.6. Conclusions on Innovative Design Improvements to Enhance Safety**

Based on the validated FE model of the five-piece wheel/tire assembly, two innovative design improvements were proposed and their mechanical performance and fatigue lives were numerical assessed.

#### **10.6.1. Conclusions on the Threaded-connection wheel Design**

This study proposed a threaded-connection locking design between wheel components in place of the conventional lock ring mechanism, in an effort to improve the engagement capability of wheel components and thus enhance structural performance and safety. The proposed threaded-connection was incorporated into the validated FE model of the wheel/tire assembly and two structural tests were conducted to evaluate the mechanical performance in the regions where the locks of the wheel components occur. The following conclusions regarding the proposed threaded-connection design can be made:

- 1) The numerical BS band pull-out tests showed that the maximum force required to pull out the BS band of the threaded-connection was 9,552 kN, or nearly double (113%) the force required to pull out the BS band of the conventional five-piece design (4,476 kN). This finding demonstrates the enhanced engagement ability of the threaded-connection locking mechanism. Additionally, the simulation predictions illustrated a safer failure deformation mode for the proposed thread locking mechanism.
- 2) The quasi-static load simulations demonstrated that the maximum von Mises stresses were 129.3 MPa and 155.3 MPa, the maximum shear stresses 89.2 MPa and 72.5 MPa, respectively at the front regions of the threaded-connection design and conventional lock ring design respectively. Furthermore, a much broader region of the conventional wheel



structure experiences higher magnitudes of stress compared to the proposed threaded connection design.

- 3) The fatigue analyses predicted a significant enhancement in the fatigue life of the proposed threaded wheel design over the conventional lock ring structure. The fatigue life was noted to increase at least by two orders of magnitude when utilizing a threaded connection design.

### **10.6.2. Conclusions on the Two-piece Wheel Design**

In this study, the FE model of a tire sized 18.00-33, used for the container handler vehicle, was developed and validated using engineering data obtained from the tire manufacturer's engineering data. The conventional five-piece wheel and proposed two-piece wheel, sized 33-13.00/2.5, compatible with the tire, were modeled using previously validated approaches. Using the validated FE models, the rims were numerically investigated under severe loading and manoeuvre conditions – static loading followed by rotation travelling and steering of the rims. The two simulated conditions encompassed the wheel and tire assemblies travelling at speeds of 8.05 km/h with 26,900 kg load and 24.14 km/h with 23,100 kg load, respectively. The performances of the wheel components were assessed in terms of stresses, fatigue lives, and, for the two-piece wheel, bolt connection forces. Based on the analyses, the following conclusions were drawn.

- 1) Comparing to the conventional five-piece wheel, the proposed two-piece wheel decreased the maximum von Mises stresses by over 56.3% and 52.5%, the maximum shear stresses by over 55.0% and 52.1%, respectively, for the 8.05 km/h and 24.14 km/h conditions. Consequently, the fatigue lives for the two-piece wheel were increased by over two orders of magnitude except under the 8.05 km/h condition using  $\epsilon$ - $N$  approach, where almost identical fatigue life was predicted to the five-piece wheel.
- 2) Comparing the stresses between the 8.05 km/h and 24.14 km/h conditions, the maximum von Mises stress increased by 30.9% (from 381.1 MPa to 498.9 MPa) for the five-piece wheel and 82.0% (from 130.2 MPa to 237.0 MPa on FR2-3 regions) for the two-piece wheel. The maximum shear stresses increased by 31.1% (from 190.7 MPa to 250.0 MPa) for the five-piece wheel and 82.4% (from 65.9 MPa to 120.2 MPa) for the two-piece wheel on FR2-3 region. The durability analysis shows that the fatigue life was significantly decreased under the 24.14 km/h condition for both the five-piece wheel and the two-piece wheel, using both  $S$ - $N$  and  $\epsilon$ - $N$  approaches, compared to the 8.05 km/h condition.

- 3) The bolt forces were assessed from the beam elements in the FE model of the two-piece wheel. The shear forces (transverse direction) were found to be negligible. The maximum axial forces were 111.4 kN and 195.7 kN, for the 8.05 km/h and 24.14 km/h conditions, respectively.
- 4) Although the magnitude of the static load contributes to increasing the stresses on the wheel components and the bolt connecting forces, driving and steering speeds are the key factors in high stresses and high bolt connection forces. This is most notable during hard cornering of the wheels.

## Chapter 11. **Limitations of the Study and Future Work**

### **11.1. Limitations of the Study**

In this study, all materials were assumed isotropic and homogenous. In the practical situation, the material properties may very well be different in different directions, resulting in anisotropy caused by forming and product manufacturing processes.

Structural fatigue is a statistic phenomenon, due to inconsistency of the material fatigue properties and the existence of micro-cracks in any structure. There are considerable scatter in values in multiple tests of the same material under the same test conditions. The standard deviations of endurance strengths of steels seldom exceed 8% of their mean values [85]. The fatigue test data presented in this study represents the mean values of the steel fatigue strength and has a reliability of 50%. If a 99.99% reliability is desired, the tested fatigue strength values have to be reduced by a factor of 0.702. Correspondently, the calculated fatigue lives will be reduced based on this 99.99% reliability.

### **11.2. Future work**

#### **11.2.1. Future Work on the Threaded-connection Design**

In the threaded-connection design, the combined BS band is screwed onto the rim base. To prevent over-screwing or loose during driving forward or backward conditions of the vehicle, a lock mechanism needs to be incorporated into the design to prevent the relative rotation between the BS band and the rim base. The function of this device is similar to the drive keys, currently used in multi-piece wheels, which prevent relative rotation between BS band and rim base.

#### **11.2.2. Future Work on the Two-piece Wheel Design**

The proposed two pieces are bolted together using twenty bolts. Another way to join the two pieces together is thread connection, similar to the proposed threaded-connection four-piece wheel design. The threaded-connections replace the bolt connections, avoiding the occurrences of bolt failures or accidental removal of the bolts. In the future, the durability performance of the threaded-connected two-piece wheel may be investigated.

### **11.2.3. Experimental Testing of Prototype Wheels for the New Designs**

Any product design must experience the validation of final prototype testing before putting into mass production. The prototype testing for the threaded-connection four-piece wheel and the bolted-together two-piece wheel can be conducted by collaboration with industry partners.

### **11.2.4. Geometry Optimization of the Multi-piece Wheels**

Using advanced computer software, the shapes of wheel components can be optimized to minimize weight of the wheel and maximize the fatigue life, especially on the front gutter regions of multi-piece wheels with a lock ring.

## References

- [1] The Mining Association of Canada (2013). Facts and Figures of The Canadian Mining Industry 2012.  
<[http://www.mining.ca/www/media\\_lib/MAC\\_Documents/Publications/2013/Facts%20and%20Figures/FactsandFigures2012Eng.pdf](http://www.mining.ca/www/media_lib/MAC_Documents/Publications/2013/Facts%20and%20Figures/FactsandFigures2012Eng.pdf)> accessed on May 13, 2013.
- [2] Ontario Mining Association, Facts & Figures (2013).  
<[http://www.oma.on.ca/en/ontariomining/facts\\_figures.asp](http://www.oma.on.ca/en/ontariomining/facts_figures.asp)> accessed on May 14, 2013.
- [3] Workplace Safety North, Injury and Occupational Disease Trends in the Mining industry, Workplace Safety North Mining Health and Safety Conference, April 16 - 18, 2013, Sudbury, Ontario.  
<<http://www.workplacesafetynorth.ca/sites/default/files/Injury%20and%20Occupational%20Disease%20Trends%20in%20the%20Mining%20Industry%202013.pdf>> accessed on May 15, 2013.
- [4] Jewel, Elizabeth (2006). The Pocket Oxford Dictionary and Thesaurus. Oxford University Press. pp. 722. ISBN 978-0-19-530715-3.
- [5] North Shore Industry Wheel Manufacturing (2010). Wheel Safety, Maintenance and Inspection, Presentation on the Technical Advisory Committee meeting, June, 2010, Sudbury, Ontario, Canada.
- [6] Vijayan V. (2008). Numerical model development of a heavy mining vehicle multi-piece wheel assembly for structural analysis, M.A.Sc.thesis, University of Windsor, Windsor, Ontario, Canada.
- [7] < <http://www.caterpillar.com/>> accessed on June 13, 2013.
- [8] WORK SAFE ALBERTA (2004). Workplace Health and Safety Bulletin - Servicing Tires Safely, Alberta Human Resources and Employment, Canada, GS003 – General Safety, 7 pages.
- [9] U.S. Department of Labor, Mine Safety and Health Administration, National Mine Health and Safety Academy (1996). Tire and Rim Safety Awareness Program, Instruction Guide Series, MSHA IG 60. <<http://www.msha.gov/S&HINFO/IG60.PDF>> accessed on June 5, 2013.
- [10] Fatality Assessment and Control Evaluation (FACE) Program, U.S. Department of Health and Human Services (2007). Mechanic Dies while Changing a Tire Mounted on a Multi-piece Split Rim Wheel, Massachusetts Case Report: 07-MA-058.  
<<http://www.cdc.gov/niosh/face/stateface/ma/07ma058.html>> accessed on June 5, 2013.
- [11] Workplace Safety North (2000). Multi-piece Rim – Controlling the Hazards.  
<<http://www.workplacesafetynorth.ca/sites/default/files/resources/Multi-Piece%20Rims%20Presentation.pdf>> accessed on June 17, 2013.
- [12] Workplace Safety North, Ontario, Fatality Reports.  
<[http://www.masha.on.ca/fatality\\_details.aspx?fatality\\_id=9](http://www.masha.on.ca/fatality_details.aspx?fatality_id=9)> accessed on September 7, 2012.

- [13] Ministry of The Solicitor General, Office of the Chief Coroner, Canada (2003). Verdict of Coroner's jury serving on the inquest into the death of Jerome Burns.
- [14] Vijayan V., Altenhof W., and Banting R. (2010). A finite element approach to estimation of fatigue life for a three-piece mining vehicle wheel, *International Journal of Heavy Vehicle Systems*, Vol. 17, No. 2, pp. 159 - 178.
- [15] Society of Automotive Engineers (1993). Wheel Cornering Fatigue Test Standard - SAE J1992 Nov. 93, SAE Handbook, 2000, 400 Commonwealth Drive, Warrendale, PA.
- [16] <<http://www.secondchancegarage.com/public/265.cfm>> accessed on June 12, 2013.
- [17] <[http://en.wikipedia.org/wiki/File:Tire\\_code\\_-\\_en.svg](http://en.wikipedia.org/wiki/File:Tire_code_-_en.svg)> accessed on June 12, 2013.
- [18] Topy Industries Limited (2008). Multi-piece Rims for Industrial and Construction Vehicles RIM INSTRUCTION MANUAL, vision 1, 2008. <<http://www.topy.co.jp/english/dept/wheel/pdf/71424250-e.pdf>> accessed on June 13, 2013.
- [19] Fatality Assessment and Control Evaluation (FACE) Program, U.S. Department of Health and Human Services (2003). Worker Struck by Multi-piece Rim during Wheel Installation, Alaska Case Report: 03AK006. <<http://www.cdc.gov/niosh/FACE/stateface/ak/03ak006.html>> accessed on June 7, 2013.
- [20] Occupational Health and Safety, Alberta Employment and Immigration (2004). Servicing Tires Safely, *Workplace Health and Safety Bulletin*. <[http://humanservices.alberta.ca/documents/WHS-PUB\\_gs003.pdf](http://humanservices.alberta.ca/documents/WHS-PUB_gs003.pdf)> accessed on June 7, 2013.
- [21] North Shore Industry Wheel Mfg. (2011). Earthmover and Construction Products Catalog. <<http://www.nsiw.com/UploadedFiles/File/nsiw%20em%20catalogue.pdf>> accessed on June 10, 2011.
- [22] North Shore Industry Wheel Mfg. (2013). QC7 – 7-piece quick changing wheel. <<http://www.nsiw.com/UploadedFiles/File/qc7%20quick%20change%20wheel%20broc.pdf>> accessed on June 12, 2013.
- [23] Workplace Safety North (2000). Take Ten for Safety, Multi-piece Rims Controlling The Hazards, Version 2.0. <[http://www.workplacesafetynorth.ca/sites/default/files/resources/Multi-Piece%20Rims%20Leader%20Guide\\_0.pdf](http://www.workplacesafetynorth.ca/sites/default/files/resources/Multi-Piece%20Rims%20Leader%20Guide_0.pdf)> accessed on June 17, 2013.
- [24] The Goodyear Tire & Rubber Company (2008). Goodyear off-the-road Tire Maintenance Manual. <[http://www.goodyearotr.com/cfm/web/otr/info/pdf/otr\\_MaintenanceManual.pdf](http://www.goodyearotr.com/cfm/web/otr/info/pdf/otr_MaintenanceManual.pdf)> accessed on June 10, 2010.
- [25] deCastro J. (Goodyear Canada Inc.) (2010). ABC's of OTR, presentation on the Technical Advisory Meeting of Workplace Safety North (MSN), Sault Ste. Marie, Ontario, June 1, 2010.

- [26] The Goodyear Tire & Rubber Company (2003). Radial Truck Tire & Retread Service Manual. <[http://www.goodyear.ca/truck/pdf/radialretserv/Retread\\_All\\_V.pdf](http://www.goodyear.ca/truck/pdf/radialretserv/Retread_All_V.pdf)> accessed on June 13, 2013.
- [27] The Tire and Rim Association (2013). 2013 Year Book. <<http://www.gobookee.net/tire-and-rim-yearbook/>> accessed on June 17, 2013.
- [28] The Goodyear Tire & Rubber Company (2008). Goodyear OTR Tire Engineering Data Book. <<http://www.goodyearotr.com/cfm/web/otr/info/pdf/otrdatobook.pdf>> accessed on June 17, 2013.
- [29] Albert Government (2012). Workplace Incident Fatalities Accepted by the Workers' Compensation Board in 2012. <<http://www.humanservices.alberta.ca/documents/2012-workplace-fatalities-accepted-wcb.pdf>> and <<http://www.edmontonsun.com/2012/02/26/exploding-tire-kills-worker>> accessed on June 22, 2013.
- [30] Occupational Health and Safety, Alberta Employment and Immigration (2009). WORKER FATALLY INJURED WHEN TIRE COMPONENTS SEPARATE, Occupational Health and Safety Fatality Report, File #: F-256084. <<http://humanservices.alberta.ca/documents/FR-2009-08-28.pdf>> accessed on June 22, 2013.
- [31] WorkSafeBC, Workers' Compensation Board of BC (2006). Hazard Alert - Removing inflated tire leads to fatal explosion, Alert #: Fatality 06-03. <<http://www2.worksafebc.com/i/posters/pdfs/2006/ha0603.pdf>> accessed on June 13, 2013.
- [32] WorkSafety BC, Workers' Compensation Board of BC (2005). Welding on assembled wheel results in explosion, Incident Investigation Report, 2005. <<http://www2.worksafebc.com/PDFs/investigations/IIR2005108320019.pdf>> accessed on June 15, 2013.
- [33] Occupational health and safety, Saskatchewan Labour (2004). Truck tire explosions claim two more lives, November 2004. <<http://www.lrws.gov.sk.ca/truck-tire-explosions-claim-two-more-lives>> accessed on September 5, 2012.
- [34] Alberta Human Resources and Employment, Workplace Health & Safety, Alberta (2002). Occupational Health & Safety Magazine, Work Struck by Tire Rim. Volume 25, Number 3, September 2002. <[http://humanservices.alberta.ca/documents/WHS-PUB\\_ohsmag\\_0902.pdf](http://humanservices.alberta.ca/documents/WHS-PUB_ohsmag_0902.pdf)> accessed on June 20, 2013.
- [35] Occupational Health and Safety, Saskatchewan Ministry of Labor Relations and Workplace Safety (1999). Hazard Alerts – Tire Mound/Demound on Heavy Vehicles. <<http://www.lrws.gov.sk.ca/tire-mount-demount-heavy-vehicles>> accessed on June 28, 2013.

- [36] Occupational Safety & Health Administration, U.S. Department of Labor (2011). Mechanic Dies After Wheel Failure During Tire Inflation, Report ID: 0729300. <[http://www.osha.gov/pls/imis/accidentsearch.accident\\_detail?id=200012912](http://www.osha.gov/pls/imis/accidentsearch.accident_detail?id=200012912)> accessed on June 20, 2013.
- [37] Occupational Safety and Health Administration, U.S. Department of Labor (2010). Exploding Multi-piece Wheel Rim Kills Auto Dealer Worker, Report ID: 0524700. <[http://www.osha.gov/pls/imis/accidentsearch.accident\\_detail?id=202089462](http://www.osha.gov/pls/imis/accidentsearch.accident_detail?id=202089462)> accessed on June 11, 2013.
- [38] Occupational Safety & Health Administration, U.S. Department of Labor (2010). Employee Is Killed From Head Injury While Inflating Tire, Report ID: 0950633. <[http://www.osha.gov/pls/imis/accidentsearch.accident\\_detail?id=202609129](http://www.osha.gov/pls/imis/accidentsearch.accident_detail?id=202609129)> accessed on June 11, 2013.
- [39] Occupational Safety and Health Administration, U.S. Department of Labor (2009). Tire Service Worker Is Killed In Rim Wheel Explosion, Report ID: 0452110. <[http://www.osha.gov/pls/imis/accidentsearch.accident\\_detail?id=201859931](http://www.osha.gov/pls/imis/accidentsearch.accident_detail?id=201859931)> accessed on June 11, 2013.
- [40] Occupational Safety and Health Administration, U.S. Department of Labor (2009). Worker Is Killed When Multi-Piece Rim Explodes, Report ID: 0521700. <[http://www.osha.gov/pls/imis/accidentsearch.accident\\_detail?id=200033496](http://www.osha.gov/pls/imis/accidentsearch.accident_detail?id=200033496)> accessed on June 11, 2013.
- [41] Occupational Safety & Health Administration, U.S. Department of Labor (2008). Employee Is Killed When Struck In The Head By Tire Rim, Report ID: 0521100. <[http://www.osha.gov/pls/imis/accidentsearch.accident\\_detail?id=200651529](http://www.osha.gov/pls/imis/accidentsearch.accident_detail?id=200651529)> accessed on June 11, 2013.
- [42] Fatality Assessment and Control Evaluation (FACE) Program, U.S. Department of Health and Human Services (2007). Equipment Operator Killed by a Lock Ring Propelled from a Multi piece Rim Wheel, New York State Case Report: 07NY137. <<http://www.health.ny.gov/environmental/investigations/face/07ny137.htm>> accessed on June 7, 2013.
- [43] Occupational Safety & Health Administration, U.S. Department of Labor (2007). Employee Killed When Struck By Exploding Multi-Piece Wheel, Report ID: 0524200. <[http://www.osha.gov/pls/imis/accidentsearch.accident\\_detail?id=201262177](http://www.osha.gov/pls/imis/accidentsearch.accident_detail?id=201262177)> accessed on June 11, 2013.
- [44] Occupational Safety & Health Administration, U.S. Department of Labor (2007). Employee Is killed By Exploding Split Rim Tire, Report ID: 0418300. <[http://www.osha.gov/pls/imis/accidentsearch.accident\\_detail?id=201272689](http://www.osha.gov/pls/imis/accidentsearch.accident_detail?id=201272689)> accessed on June 11, 2013.



- [45] Occupational Safety & Health Administration, U.S. Department of Labor (2006). Employee IS Killed When Split Ring Rim Blows Off Tire, Report ID: 0453710. <[http://www.osha.gov/pls/imis/accidentsearch.accident\\_detail?id=200355576](http://www.osha.gov/pls/imis/accidentsearch.accident_detail?id=200355576)> accessed on June 11, 2013.
- [46] Fatality Assessment and Control Evaluation (FACE) Program, U.S. Department of Health and Human Services (2006). An apprentice mechanic died when the truck tire he was standing over exploded, FACE 05CA007. <<http://www.cdc.gov/niosh/face/stateface/ca/05ca007.html>> accessed on June 13, 2012.
- [47] Occupational Safety & Health Administration, United States Department of Labor (2004). Employee Is Killed While Repairing Multi-Piece Wheel, Report ID: 0316700. <[http://www.osha.gov/pls/imis/accidentsearch.accident\\_detail?id=14319248](http://www.osha.gov/pls/imis/accidentsearch.accident_detail?id=14319248)> accessed on June 11, 2013.
- [48] Occupational Safety & Health Administration, United States Department of Labor (2004). Employee Is Killed During Tire Rim Failure, Report ID: 0751910. <[http://www.osha.gov/pls/imis/accidentsearch.accident\\_detail?id=200528883](http://www.osha.gov/pls/imis/accidentsearch.accident_detail?id=200528883)> accessed on June 11, 2013.
- [49] Occupational Safety & Health Administration, U.S. Department of Labor (2004). Tire Explosion Kills Employee, Report ID: 0420600. <[http://www.osha.gov/pls/imis/accidentsearch.accident\\_detail?id=202344396](http://www.osha.gov/pls/imis/accidentsearch.accident_detail?id=202344396)> accessed on June 11, 2013.
- [50] Occupational Safety & Health Administration, U.S. Department of Labor (2004). Employee Is Killed When Struck By Wheel Ring Shot From Wheel, Report ID: 0950625. <[http://www.osha.gov/pls/imis/accidentsearch.accident\\_detail?id=201086105](http://www.osha.gov/pls/imis/accidentsearch.accident_detail?id=201086105)> accessed on June 11, 2013.
- [51] Occupational Safety & Health Administration, United States Department of Labor (2003). Employee Killed After Tire He Was Inflating Exploded, Report ID: <0453720. [http://www.osha.gov/pls/imis/accidentsearch.accident\\_detail?id=200071850](http://www.osha.gov/pls/imis/accidentsearch.accident_detail?id=200071850)> accessed on June 11, 2013.
- [52] Occupational Safety & Health Administration, U.S. Department of Labor (2003). Employee Died After Explosion While Recapping Truck Tire, Report ID: 0453710. <[http://www.osha.gov/pls/imis/accidentsearch.accident\\_detail?id=200352896](http://www.osha.gov/pls/imis/accidentsearch.accident_detail?id=200352896)> accessed on June 11, 2013.
- [53] FACE Facts, Massachusetts Department of Public Health (2004). Worker Killed While Inflating a Tire Mounted on a Multi-Piece Rim - Massachusetts Fatality Investigation Report, August 2004, Vol. 7, No. 2. <<http://www.mass.gov/eohhs/docs/dph/occupational-health/face-facts/face-fact-rim.pdf>> accessed on June 7, 2013.
- [54] Occupational Safety & Health Administration, U.S. Department of Labor (2003). One Employee Died, One Injured When Struck By Truck Tire Rim, Report ID: 0729700.

- <[http://www.osha.gov/pls/imis/accidentsearch.accident\\_detail?id=201343381](http://www.osha.gov/pls/imis/accidentsearch.accident_detail?id=201343381)> accessed on June 11, 2013.
- [55] Occupational Safety & Health Administration, U.S. Department of Labor (2004). Multi-Piece Rim Wheel Explodes Killing Employee, Report ID: 0950621.  
<[http://www.osha.gov/pls/imis/accidentsearch.accident\\_detail?id=201174026](http://www.osha.gov/pls/imis/accidentsearch.accident_detail?id=201174026)> accessed on June 13, 2013.
- [56] Occupational Safety & Health Administration, U.S. Department of Labor (2003). Employee Killed When Struck In The Head By Flying Split Rims, Report ID: 1050210.  
<[http://www.osha.gov/pls/imis/accidentsearch.accident\\_detail?id=201681376](http://www.osha.gov/pls/imis/accidentsearch.accident_detail?id=201681376)> accessed on June 11, 2013.
- [57] Occupational Safety & Health Administration, U.S. Department of Labor (2002). Employee Killed When Tire And Rim Assembly Exploded, Report ID: 0214200.  
<[http://www.osha.gov/pls/imis/accidentsearch.accident\\_detail?id=200022697](http://www.osha.gov/pls/imis/accidentsearch.accident_detail?id=200022697)> accessed on June 11, 2013.
- [58] Occupational Safety & Health Administration, United States Department of Labor (2002). Employee Struck By A Flying Wheel Rim, Report ID: 0257230.  
<[http://www.osha.gov/pls/imis/accidentsearch.accident\\_detail?id=202260584](http://www.osha.gov/pls/imis/accidentsearch.accident_detail?id=202260584)> accessed on June 11, 2013.
- [59] Occupational Safety & Health Administration, U.S. Department of Labor (2002). Employee Killed When Struck By Multipiece Tire Rim, Report ID: 0522300.  
<[http://www.osha.gov/pls/imis/accidentsearch.accident\\_detail?id=200101319](http://www.osha.gov/pls/imis/accidentsearch.accident_detail?id=200101319)> accessed on June 11, 2013.
- [60] Occupational Safety & Health Administration, U.S. Department of Labor (2002). Employee Struck By A Split Rim Tire, Report ID: 0418100.  
<[http://www.osha.gov/pls/imis/accidentsearch.accident\\_detail?id=201281334](http://www.osha.gov/pls/imis/accidentsearch.accident_detail?id=201281334)> accessed on June 11, 2013.
- [61] Occupational Safety & Health Administration, U.S. Department of Labor (2002). Employee Dies When Struck In His Head By Exploding Wheel Rim, Report ID: 0420600.  
<[http://www.osha.gov/pls/imis/accidentsearch.accident\\_detail?id=202327854](http://www.osha.gov/pls/imis/accidentsearch.accident_detail?id=202327854)> accessed on June 11, 2013.
- [62] Occupational Safety & Health Administration, U.S. Department of Labor (2001). Employee Killed When Struck By A Ring And Wheel, Report ID: 0627400.  
<[http://www.osha.gov/pls/imis/accidentsearch.accident\\_detail?id=200811081](http://www.osha.gov/pls/imis/accidentsearch.accident_detail?id=200811081)> accessed on June 11, 2013.
- [63] Occupational Safety & Health Administration, U.S. Department of Labor (2001). Employee Killed When Struck By A Piece From Tire Rim, Report ID: 0418300.  
<[http://www.osha.gov/pls/imis/accidentsearch.accident\\_detail?id=201271368](http://www.osha.gov/pls/imis/accidentsearch.accident_detail?id=201271368)> accessed on June 11, 2013.

- [64] Occupational Safety & Health Administration, U.S. Department of Labor (2000). Employee Dies After Tire Assembly Accident, report ID: 1054116. <[http://www.osha.gov/pls/imis/accidentsearch.accident\\_detail?id=201620374](http://www.osha.gov/pls/imis/accidentsearch.accident_detail?id=201620374)> accessed on June 11, 2013.
- [65] Division of Occupational Safety and Health, Department of Labour, North Carolina (2000). Hazard Alert – Multi-piece Rims. <[http://www.nclabor.com/osha/etta/hazard\\_alerts/MultiRims.pdf](http://www.nclabor.com/osha/etta/hazard_alerts/MultiRims.pdf)> accessed June 8, 2013.
- [66] Occupational Safety & Health Administration, U.S. Department of Labor (2000). Employee Killed When Struck By Tire Rim Lock Ring, report ID: 0453730. <[http://www.osha.gov/pls/imis/accidentsearch.accident\\_detail?id=202074530](http://www.osha.gov/pls/imis/accidentsearch.accident_detail?id=202074530)> accessed on June 11, 2013.
- [67] Mine Safety and Health Administration (MSHA), U.S. Department of Labor (2002). MSHA's Accident Prevention Program Miner's Tip - Multi-Piece Rim Wheels. <[http://www.msha.gov/accident\\_prevention/Tips/rimwheel.pdf](http://www.msha.gov/accident_prevention/Tips/rimwheel.pdf)> accessed on June 26, 2013.
- [68] Occupational Safety & Health Administration, U. S. Department of Labor (1998). Employee Killed When Truck Crane Tire Explodes, report ID: 0316400. <[http://www.osha.gov/pls/imis/accidentsearch.accident\\_detail?id=200630259](http://www.osha.gov/pls/imis/accidentsearch.accident_detail?id=200630259)> accessed on June 11, 2013.
- [69] Occupational Safety & Health Administration, U. S. Department of Labor (1998). Employee Killed Tire Explodes During Mounting, report ID: 0627100. <[http://www.osha.gov/pls/imis/accidentsearch.accident\\_detail?id=200260495](http://www.osha.gov/pls/imis/accidentsearch.accident_detail?id=200260495)> accessed on June 11, 2013.
- [70] Occupational Safety & Health Administration, U. S. Department of Labor (1998). Employee Killed When Wheel Rim Blows Apart, Report ID: 0728500. <[http://www.osha.gov/pls/imis/accidentsearch.accident\\_detail?id=200000495](http://www.osha.gov/pls/imis/accidentsearch.accident_detail?id=200000495)> accessed on June 11, 2013.
- [71] Occupational Safety & Health Administration, U. S. Department of Labor (1998). Employee Killed When Struck By Split Rim Tire Locking Ring, report ID: 0419400. <[http://www.osha.gov/pls/imis/accidentsearch.accident\\_detail?id=201360518](http://www.osha.gov/pls/imis/accidentsearch.accident_detail?id=201360518)> accessed on June 11, 2013.
- [72] Natural Resources and Mines, Queensland Government (2005). Fatal Injury To Prime Mover Operator As Rim Assembly Fails, Safety Alert No. 136, 2005. <[http://mines.industry.qld.gov.au/assets/inspectorate/safety\\_alert136.pdf](http://mines.industry.qld.gov.au/assets/inspectorate/safety_alert136.pdf)> accessed on June 7, 2013.
- [73] Mineral Resources, New South Wales (2004). Safety Alert - QUEENSLAND FATALITY DURING WHEEL REMOVAL, Report No: SA 04 01.

- <[http://www.dpi.nsw.gov.au/data/assets/pdf\\_file/0010/66853/Safety-Alert-04-01-QLD-fatality-during-wheel1.pdf](http://www.dpi.nsw.gov.au/data/assets/pdf_file/0010/66853/Safety-Alert-04-01-QLD-fatality-during-wheel1.pdf)> accessed on June 7, 2013.
- [74] Natural Resources and Mines, Queensland Government (2002). Safety Alert - Violent Tire Rupture on Dump Truck, Alert No. 83, 2002.  
<[http://mines.industry.qld.gov.au/assets/inspectorate/safety\\_alert083.pdf](http://mines.industry.qld.gov.au/assets/inspectorate/safety_alert083.pdf)> accessed on June 13, 2012.
- [75] Natural Resources and Mines, Queensland Government (2000). Tire Rim Assembly Blew Apart, Mines Inspectorate Safety Alert No. 29, 2000.  
<[http://mines.industry.qld.gov.au/assets/inspectorate/safety\\_alert029.pdf](http://mines.industry.qld.gov.au/assets/inspectorate/safety_alert029.pdf)> accessed on June 8, 2013.
- [76] Rasche T. and Lkinge T. (2006). Review and Analysis of tire Related Accidents and Incidents – an ACARP Study to Improve tire & Rim Maintenance and Operational Safety of Rubber tired Earthmover Equipment.  
<[http://www.qrc.org.au/conference/\\_dbase\\_upl/rasche\\_Tyre%20Related%20Accidents%20and%20Incidents.pdf](http://www.qrc.org.au/conference/_dbase_upl/rasche_Tyre%20Related%20Accidents%20and%20Incidents.pdf)> accessed on June 26, 2013.
- [77] Workplace Safety North, Ontario (2013). Tires and Rims - MOL Guideline-Section 107 – Working With Tires and Wheel Assemblies.  
<<http://www.workplacesafetynorth.ca/resources/multi-piece-rims-controlling-hazards>> accessed on June 5, 2013.
- [78] Cutler T. (2004). Final Report to Hamersley Iron on Catastrophic Tire Incident on Haultruck 06H1 at Channar on April 10, 2004.  
<[http://www.otraco.com.au/Libraries/Technical\\_Papers/Tyre\\_Explosion\\_Investigation\\_-\\_Lightning\\_Strike.sflb.ashx](http://www.otraco.com.au/Libraries/Technical_Papers/Tyre_Explosion_Investigation_-_Lightning_Strike.sflb.ashx)> accessed on June 26, 2013.
- [79] Workers' Compensation Board of British Columbia, Canada (2003). Hazard Alert – Tire explodes when truck contacts overhead power line.  
<[http://www2.worksafebc.com/i/posters/2003/ha0317\\_tire.htm](http://www2.worksafebc.com/i/posters/2003/ha0317_tire.htm)> accessed on June 26, 2013.
- [80] Kocabicak U. and Firat M. (2001). Numerical analysis of wheel cornering fatigue tests. Engineering Failure Analysis, vol. 8, pp. 339 - 354.
- [81] SAE (Society of Automotive Engineers) International (2005). SURFACE VEHICLE RECOMMENDED PRACTICE - Wheels - Passenger Car and Light Truck Performance Requirements and Test Procedures- SAE J328, Rev. Feb. 2005, 400 Commonwealth Drive, Warrendale, PA. <[http://standards.sae.org/j328\\_200502/](http://standards.sae.org/j328_200502/)> accessed on July 11, 2013.
- [82] SAE (Society of Automotive Engineers) International (2007). SURFACE VEHICLE RECOMMENDED PRACTICE - Wheels/Rims - Performance Requirements and Test Procedures - Truck and Bus- SAE J267, Rev. Dec. 2007, 400 Commonwealth Drive, Warrendale, PA. <[http://standards.sae.org/j328\\_200502/](http://standards.sae.org/j328_200502/)> accessed on July 11, 2013.

- [83] SAE (Society of Automotive Engineers) International (2007). SURFACE VEHICLE RECOMMENDED PRACTICE -Wheels/Rims—Military Vehicles—Test Procedures and Performance Requirements- SAE J1992, Rev. Mar. 2001, 400 Commonwealth Drive, Warrendale, PA.  
<<http://www.autoparts-standard.org/index/images/userfiles/media/SAE%20J1992-2001.pdf>> accessed on July 11, 2013.
- [84] <[http://en.wikipedia.org/wiki/Fatigue\\_\(material\)](http://en.wikipedia.org/wiki/Fatigue_(material))> accessed November 1, 2012.
- [85] Norton R. L. (2006). Machine Design-An Integrated Approach, third edition, Pearson Prentice Hall, pp. 302.
- [86] J. W. Fischer and B. T. Yen (1972). Design, Structural details, and Discontinuities in Steel, Safety and Reliability of Metal Structures, American Society of Civil Engineers, Nov. 2.
- [87] HBM-nCode United Kingdom Limited (2012). nCode Book of Fatigue Theory.
- [88] Chu C. (1997). Multiaxial fatigue life prediction method in the ground vehicle industry, International Journal of Fatigue, Vol. 19, No. 1, pp. S325 - S330.
- [89] Conle F.A. and Chu C.-C. (1997). Fatigue analysis and the local stress-strain approach in complex vehicular structures, International Journal of Fatigue, Vol. 19, Supp. No. 1, pp. S317 - S323.
- [90] Grujicic M., Arakere, G., Bell W.C., Harvi H., Yalavarthy H. V., Pandurangan B., Haque I., and Fadel G. M. (2010). Reliability-Based Design Optimization for Durability of Ground Vehicle Suspension System Components, ASM International, Journal of Material Engineering and Performance, vol. 19, pp.301 - 313.
- [91] Mitchell M. R. (1996). Fundamentals of modern fatigue analysis for design, In: Lampman Steven R., editor, ASM Handbook, Materials Park: ASM International, pp. 229 - 49.
- [92] Basquin OH. (1910). The exponential law of endurance tests, Proceedings – American Society for Testing Materials, Vol. 10, pp. 625 - 30.
- [93] Manson SS. (1965). Fatigue: a complex subject – some simple approximation, Experimental Mechanics, Vol. 5, pp. 193 - 226.
- [94] Coffin LF. (1954). A study of the effect of cyclic thermal stresses on a ductile metal, Transactions of the American Society of Mechanical Engineers, Vol. 76, pp. 931 - 950.
- [95] Morrow J. (1968). Fatigue properties of metals, section 3.2., In: Fatigue Design Handbook, Pub. No. AE-4, SAE, Warrendale, PA.
- [96] Muralidharan U, Manson SS. (1988). Modified universal slopes equation for estimation of fatigue characteristics, Journal of Engineering Materials and Technology - Transactions of the American Society of Mechanical Engineers, Vol. 10, pp. 55 - 58.

- [97] Smith, K. N., Watson, P. and Topper, T. H. (1970). A stress-strain function for the fatigue of materials, *Journal of Materials*, Vol. 5, pp. 767 - 778.
- [98] HBM-nCode United Kingdom Limited (2013). *DesignLife Theory Guide*.
- [99] Collins, J. A. (1993). *Failure of Material in Mechanical Design*, 2nd edition, John Wiley & Sons Inc., New York, pp. 238 - 254,.
- [100] Mercer I., Malton G., and Draper J. (2003). Investigating fatigue failures using analysis and testing – some do's and don'ts, *Safe Technology Limited, EIS Seminar*.
- [101] Tipton S. M. and Nelson D. V. (1985). Fatigue Life Predictions for a Notched Shaft in Combined Bending and Torsion, in *Multiaxial Fatigue*, K. J. Miller and M. W. Brown, Editors. SATM: Philadelphia, PA. pp. 514 - 550.
- [102] Nishihara T. and Kawamoto M. (1945). The strength of Metals under Combined Alternating Bending and Torsion with Phase Difference, *Memoirs College of Engineering, Kyoto Univ., Japan*, 11(85).
- [103] McDiarmid D. L. (1991). A general criterion for high cycle multiaxial fatigue failure, *Fatigue and Fracture of Engineering Materials and Structures*, Vol. 14(4), pp. 429 - 453.
- [104] Brown M. W. and Miller K. J. (1973). A theory for fatigue failure under multiaxial stress strain conditions, *Proceeding of the Institute of Mechanical Engineers*, Vol. 187, pp. 745 - 755.
- [105] HBM-nCode United Kingdom Limited (2012). *Practical Fatigue Theory*.
- [106] Wang X. and Zhang X. (2010). Simulation of dynamic cornering fatigue test of a steel passenger car wheel, *International Journal of Fatigue*, Vol. 32, pp. 434 - 442.
- [107] Shang R, Altenhof W, Hu H, Li N. (2008). Rotary fatigue analysis of forged magnesium road wheels, *SAE technical paper*, No. 2008-01-0211.
- [108] Topac M.M., Ercan S., and Kuralay N.S. (2012). Fatigue life prediction of a heavy vehicle steel wheel under radial loads by using finite element analysis, *Engineering Failure Analysis*, Vol. 20, pp. 67 - 79.
- [109] Firat M., Kozan R., Ozsoy M., and Mete O.H. (2009). Numerical modeling and simulation of wheel radial fatigue tests, *Engineering Failure Analysis*, Vol. 16, pp. 1533 - 1541.
- [110] Llano-Vizcaya L., Rubio-González C., Mesmacque G., and Cervantes-Hernández T. (2006). Multiaxial fatigue and failure analysis of helical compression springs, *Engineering Failure Analysis*, Vol. 13, pp. 1303 - 1313.
- [111] Conle F.A. and Chu C.-C. (1997). Fatigue analysis and the local stress-strain approach in complex vehicular structures, *International Journal of Fatigue*, Vol. 19, Supp. No. 1, pp. S317 - S323.

- [112] Kocabicak U. and Firat M. (2001). Numerical analysis of wheel cornering fatigue tests, *Engineering Failure Analysis*, Vol. 8, pp. 339 – 354.
- [113] Altair Incorporated (2006). *HyperMesh 8.0 User's Guide*, July 2006.
- [114] Livermore Software Technology Corporation (LSTC), *LS-DYNA Keyword User's Manual*, Version 971/Rev5, May 2010.
- [115] Livermore Software Technology Corporation (LSTC) (2012). *Introduction to LS-PrePost 3.2*, July 31, 2012.
- [116] Burke A.M. and Olatunbosun O.A. (1997). *Static tire/Road Interaction Modelling*, *Meccanica*, Vol. 32, pp. 472 - 479.
- [117] Neves R.R. V., Micheli G.B., Alves, M. (2010). An experimental and numerical investigation on tire impact, *International Journal of Impact Engineering*, Vol. 37, pp 685 - 693.
- [118] Nguyen S., Greenhalgh E.S., Iannucci L., Longstaff S., Olsson R. and Curtis P. T. (2011). Experimental Characterisation of tire Indentation by Simulated Runway Debris, *Strain: An International Journal for Experimental Mechanics*, Vol. 47, pp. 343 - 350.
- [119] Oberkampf W. and Trucano T. (2002). Verification and validation in computational fluid dynamics, *Progress in Aerospace Science*, Vol. 38, pp. 209 - 272.
- [120] Reid J. D., Boesch D. A. and Bielenberg R.W. (2007). Detailed tire modeling for crash applications, *International Journal of Crashworthiness*, Vol. 12, No. 5, pp. 521 - 529.
- [121] Orengo F., Ray M. H., and Plaxico C.A. (2003). Modeling tire blow-out in roadside hardware simulations using LS-DYNA, *Proceedings of IMECE'03, 2003 ASME International Mechanical Engineering Congress & Exposition*, Washington, DC, November 16 - 21.
- [122] Shiraishi M., Iwasaki N., Saruwatari T., and Hayashi K. (2002). Developing FE-Tire Model Library for Durability and Crash Simulations, the 7th International LS-DYNA Users Conference, Dearborn, Michigan, Vol. 13, pp.29 - 36.
- [123] Coefficient of Friction –RoyMech.  
<[http://www.roymech.co.uk/Useful\\_Tables/Tribology/co\\_of\\_friact.htm](http://www.roymech.co.uk/Useful_Tables/Tribology/co_of_friact.htm)> accessed on June 15, 2010.
- [124] Burton, W.E. (1949). *Engineering With Rubber*, McGraw Hill Book Company Inc., New York, New York.
- [125] ASTM Standard A572/A572M – 12a, Standard Specification for High-Strength Low-Alloy Columbium Vanadium Structural Steel, ASTM International, West Conshohocken, PA, 2013, DOI: 10.1520/A0572\_A0572M-12A, [www.astm.org](http://www.astm.org).

- [126] ASTM Standard E8/E8M – 11, Standard Test Methods for Tension Testing of Metallic Materials1, ASTM International, West Conshohocken, PA, 2012, DOI: 10.1520/E0008\_E0008M-11, [www. astm.org](http://www.astm.org).
- [127] Mentley J. (2013). nCode DesignLife, personal communication.
- [128] Kalmar Industries, Technical Information – Container Handler – ContChamp 42-45 Tonnes (2012).  
<<http://www.kalmarind.nl/source.php/38881/Products%20Tech%20doc%20DRF%20Toplift.pdf>> accessed on October 15, 2013.
- [129] Zhang Y. (2008). Metallurgical Failure Analysis of Cracked Wheel Rim, Bodycote Materials Testing Canada Inc., Ref #: G807288.
- [130] Conle F.A. and Chu C. (1997). Fatigue analysis and the local stress–strain approach in complex vehicular structures, International Journal of Fatigue, Vol. 19-1, pp. 317 - 323.
- [131] Draper J. and Aveline R., (2004). How to achieve valid results in durability analysis from FEA software, ANSYS World User Conference, Bergamo, Italy, pp. 8 - 14.



## Appendix A: Fatigue Analysis within nCode DesignLife

As mentioned in the aforementioned section, there are three approaches to estimate the fatigue life of a structure, corresponding to fatigue process. Regardless of the particular analysis technique applied in analytical fatigue life assessments, similar types of inputs are required; these can be described by means of the "5-Box Trick" shown in Figure 2.36 [87]. In each case, some form of geometry factor or description must be made: the Geometry box; the loading environment of the structure under consideration must be defined: the Loading box. Finally, the response of the material to cyclic loading must be defined: the fatigue material properties; an S-N curve, Strain-life and cyclic stress-strain curve is appropriate. These three inputs are then combined in a cycle-by-cycle fatigue analysis and a fatigue life result is presented.

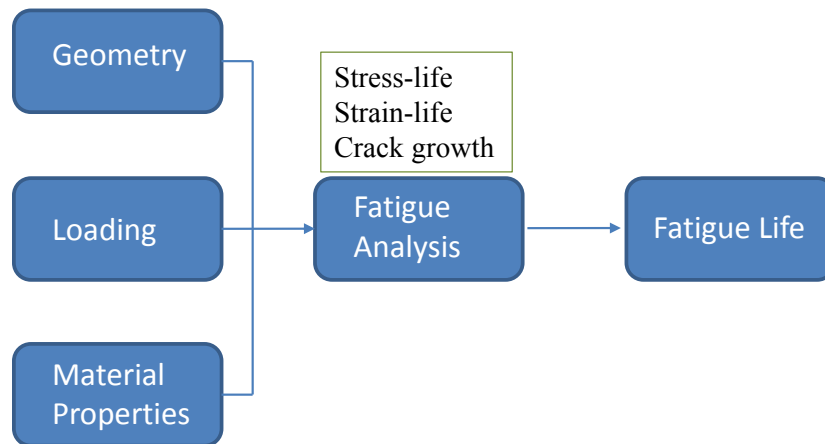


Figure A.1 The fatigue analysis "5-Boxes Trick" [105].

With the advancement of computer technology, numerical modeling and estimating the fatigue life prevails in practice. One kind of such software for fatigue life analysis is DesignLife from HBM nCode, a software company. DesignLife is a process oriented, FE-based fatigue analysis package which identifies critical locations and calculates fatigue lives.

In the case of FE simulated fatigue life analysis, the geometry and loading histories (stresses/strains) can be directly imported to DesignLife from FE simulation result files. If LS-DYNA is used for the FE simulations, the d3plot files will be used to input to the DesignLife, with geometry and stress/strain loading history attached to the d3plot files. The strength reduction factor or compliance functions are not needed since all these factors are accounted for in the previous FE simulation. The users just need to input or select appropriate fatigue material properties. In the course of setting up fatigue life analysis, different approaches (S-N,  $\epsilon$ -N, or

LEFM) can be selected. In each different approach, different correction methods can be selected, such as mean stress correction, elastic-plastic correction, multi-axial stress consideration. The user may just select the concerned part for fatigue life analysis from the FE model to save time. The estimated fatigue life (damage) can be viewed graphically with contour plot to identify the hot spot region (low fatigue life region), or the fatigue life can be tabulated by element or node number.

The GUI (graphical user interface) of DesignLife is very user-friendly. The DesignLife analysis process is a flow process, which is composed of glyphs connected by pipes. Glyphs are the basic analysis building blocks, which contain the data that pass between glyphs and can be edited accordingly. Pipes are attached to glyph pads. In DesignLife, processes are defined graphically by dragging, dropping, connecting and configuring glyphs on the Analysis Workspace. The FE result input glyph is used to input FE results, including geometry and loading histories (stress and strain data). The fatigue analysis engine can be configured to select different analysis approach (S-N,  $\epsilon$ -N), fatigue material properties, and other fatigue analysis properties. The hot spot detection glyph is used to identify the critical areas of the model. The fatigue result glyph is used to display fatigue contours. The fatigue results can also be tabulated by elements or nodes.

Figure 2.37 shows a simple example of DesignLife fatigue life analysis process, which is explained as follows: (1) start DesignLife and define working directory; (2) select, drag, and drop the necessary glyphs from glyph palette into the workspace, and join the glyphs with pipes to form a flow; (3) drag and drop FE results from working directory into the FE result input glyph; (4) configure the material mapping and modify other analysis properties in fatigue analysis engine glyph; (5) click the “run” button; (6) after the run finishes, the fatigue life results will be displayed by contours and table. In the FE result input and fatigue result glyphs, display can be modified to show the interested components only.

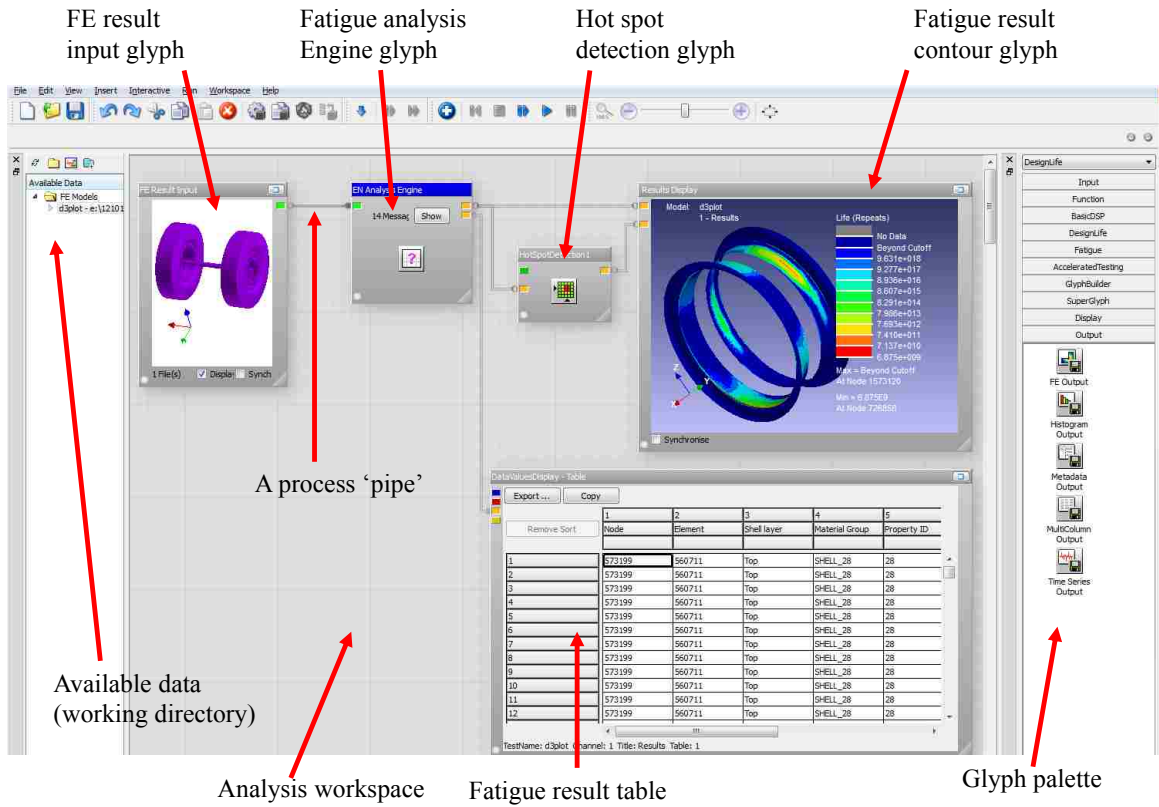


Figure A.2 A simple example of DesignLife-based fatigue life analysis process.

## Appendix B: Quasi-static Testing Observations for Event 2 and Event 3

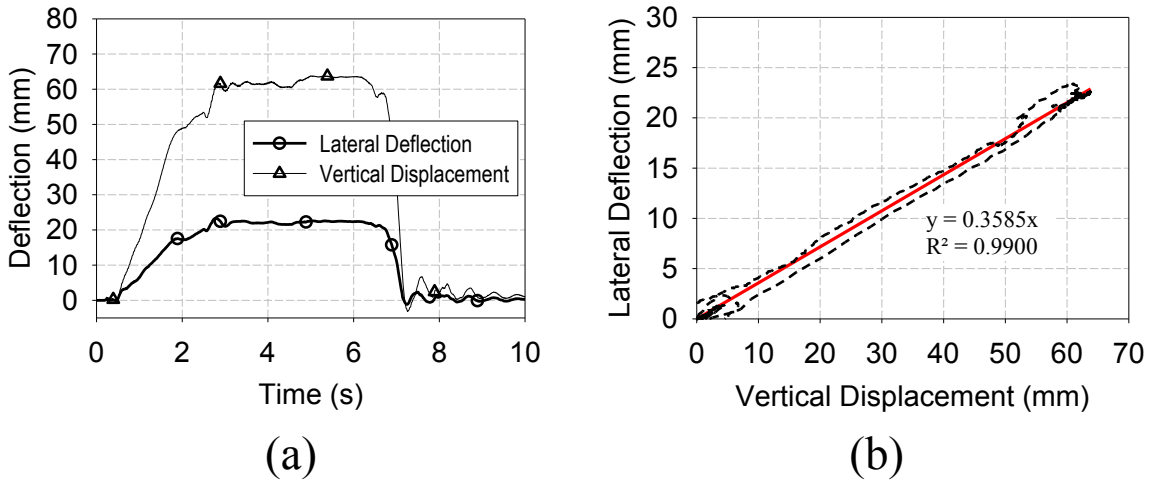


Figure B.1 Quasi-static testing tire responses for test event 2 (a) vertical and lateral directions as well as (b) lateral deflection versus vertical deflection.

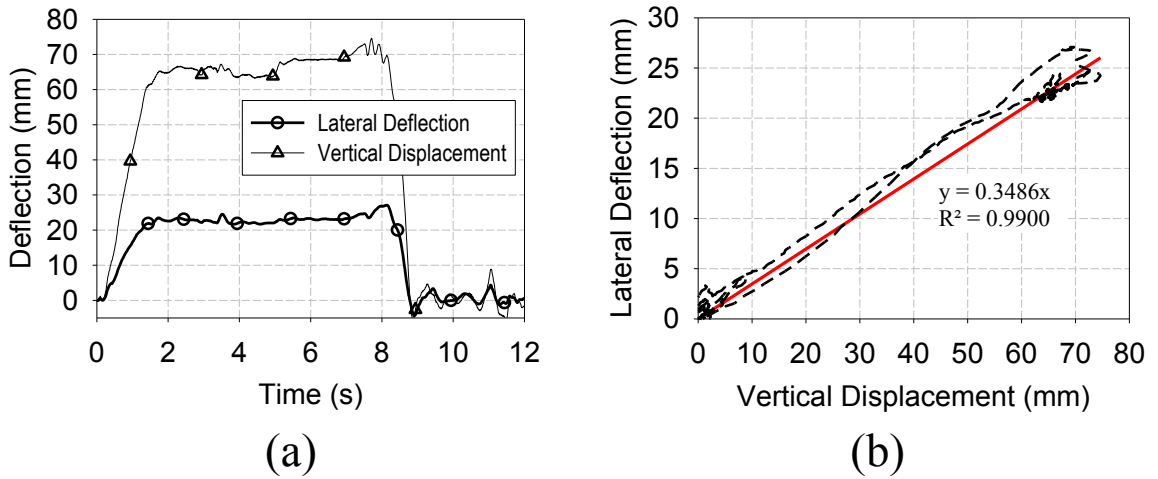
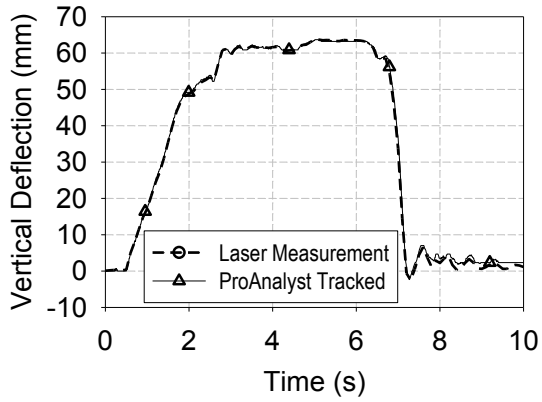
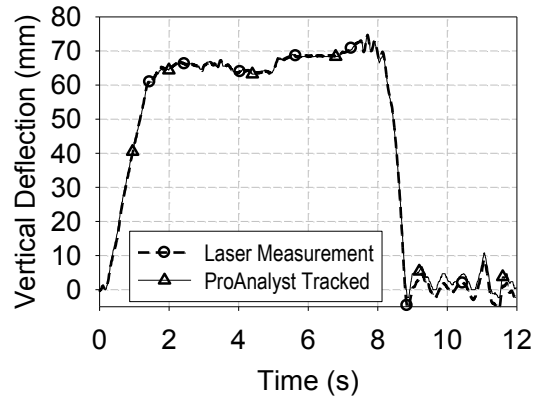


Figure B.2 Quasi-static testing tire responses for test event 3 (a) vertical and lateral directions as well as (b) lateral deflection versus vertical deflection.

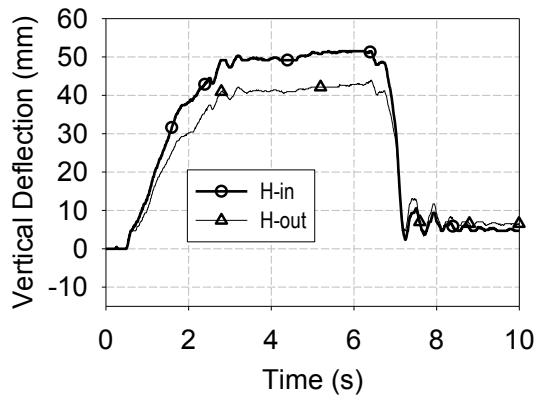


(a)

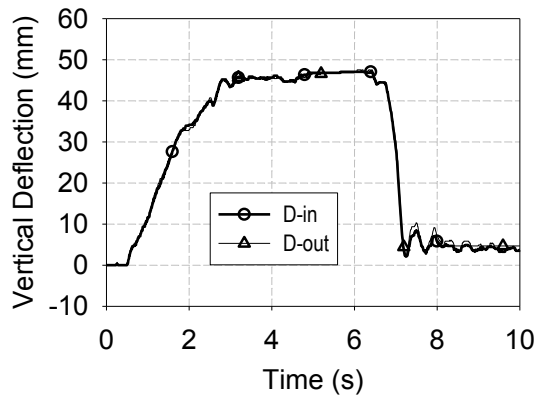


(b)

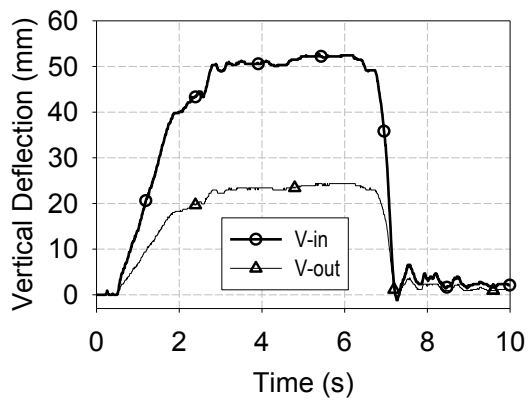
Figure B.3 Vertical displacement comparisons between laser displacement transducer measurements and high-speed camera image tracking using ProAnalyst (a) test event 2 and (b) test event 3.



(a)

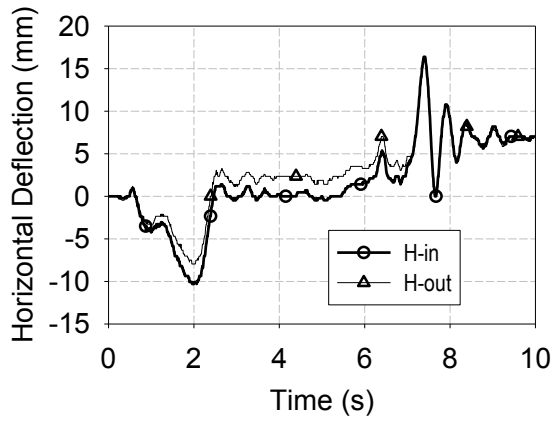


(b)

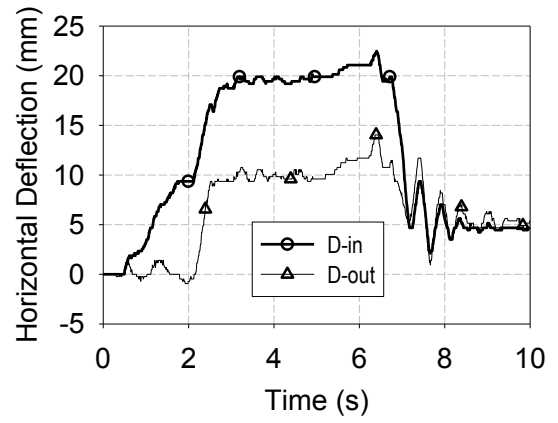


(c)

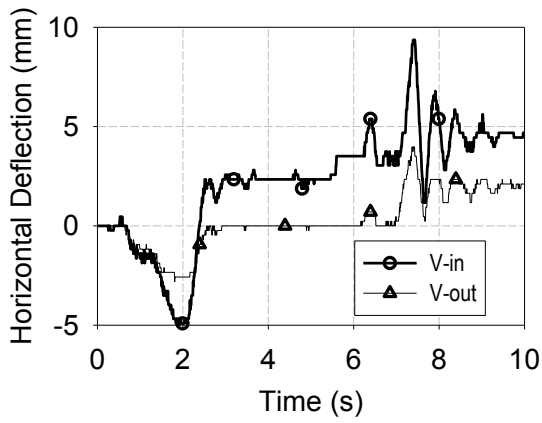
Figure B.4 Vertical deflection responses for tracked nodes for test event 2.



(a)

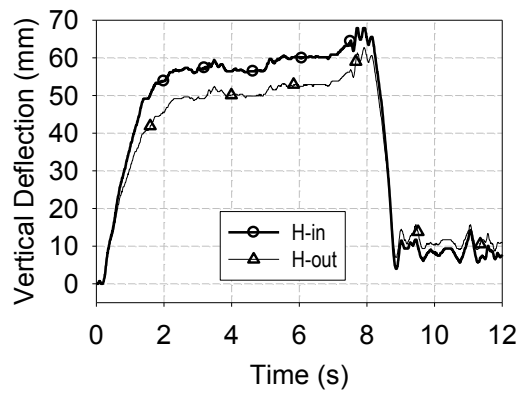


(b)

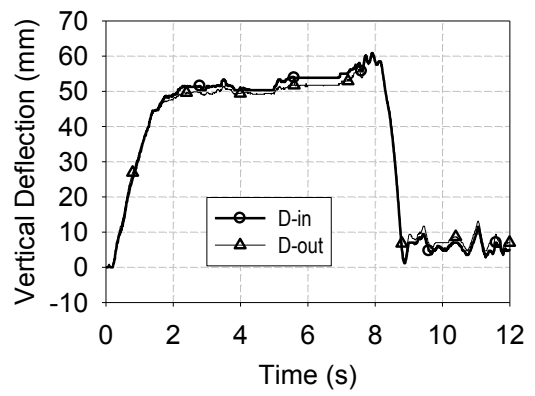


(c)

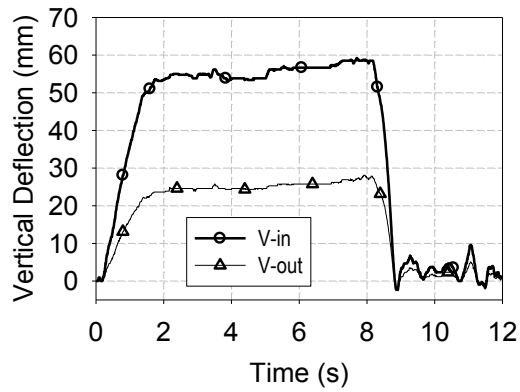
Figure B.5 Horizontal deflection responses for tracked nodes for test event 2.



(a)

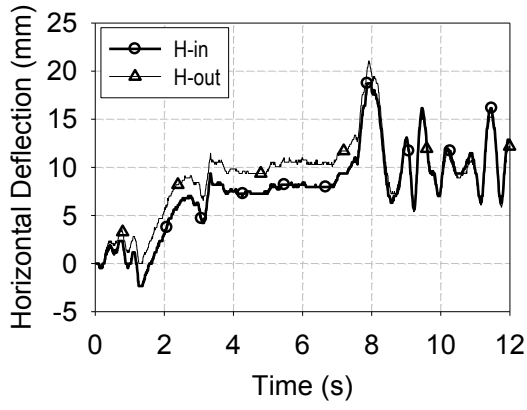


(b)

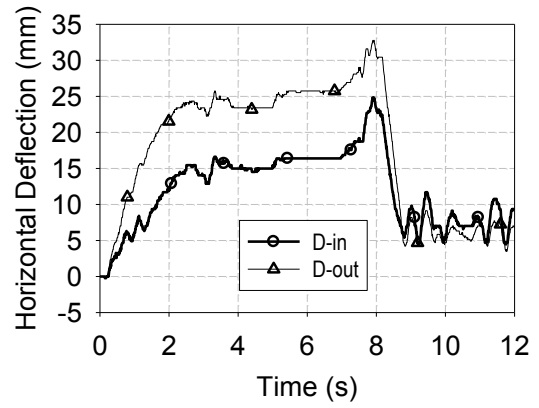


(c)

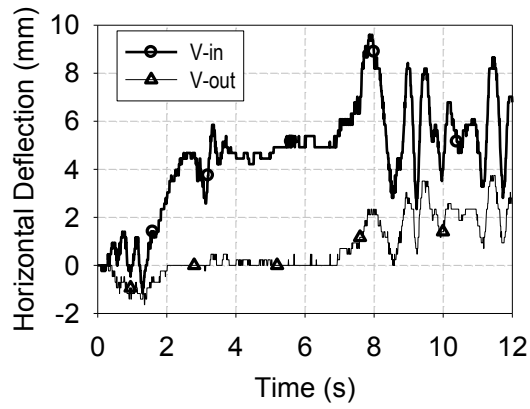
Figure B.6 Vertical deflection responses for tracked nodes for test event 3.



(a)



(b)



(c)

Figure B.7 Horizontal deflection responses for tracked nodes for test event 3.



## Appendix C: Experimental Observations from the Rim Base Testing

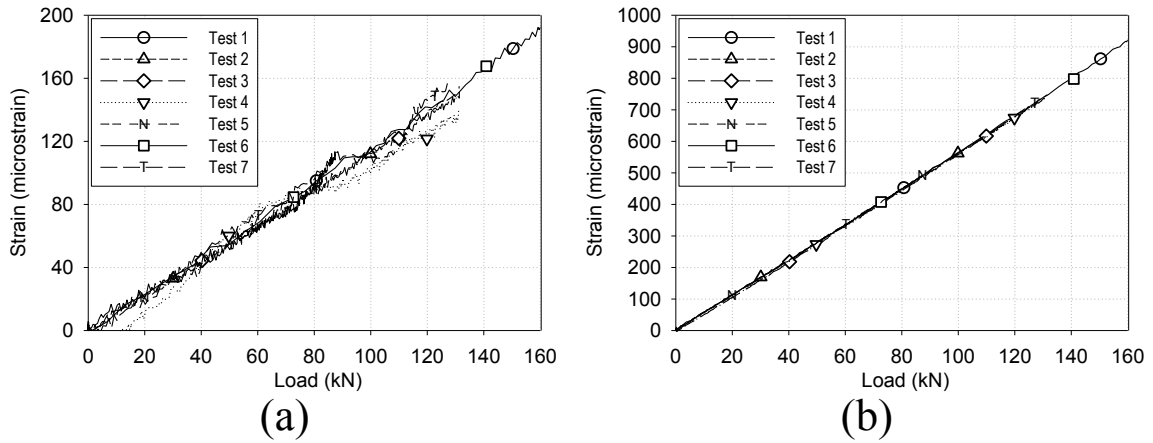


Figure C.1 Experimental observations (a) circumferential strain at location '2' and (b) circumferential strain at location '5'.

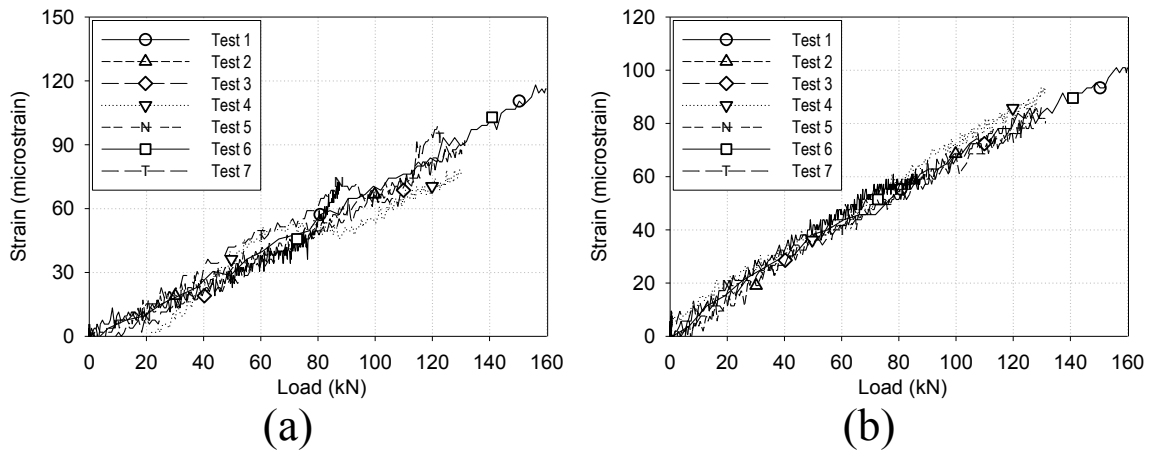


Figure C.2 Experimental observations (a) circumferential strain at location '3' and (b) circumferential strain at location '4'.

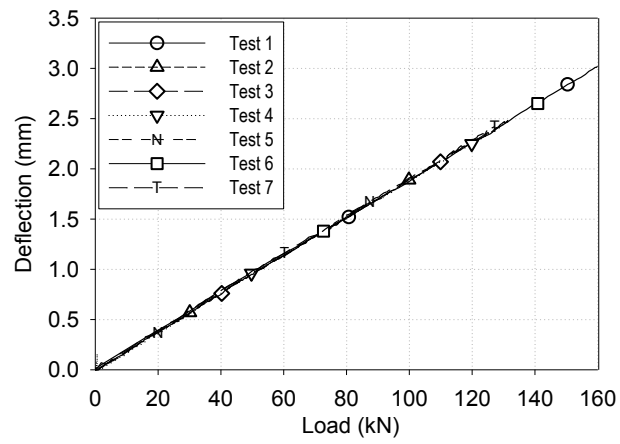


Figure C.3 Experimental observations - vertical deflections at location 'A'.

## Appendix D: Tire Quasi-static Testing Results Comparisons between Experimental Tests and Computer Simulations for Test Event 2 and Event 3 Conditions

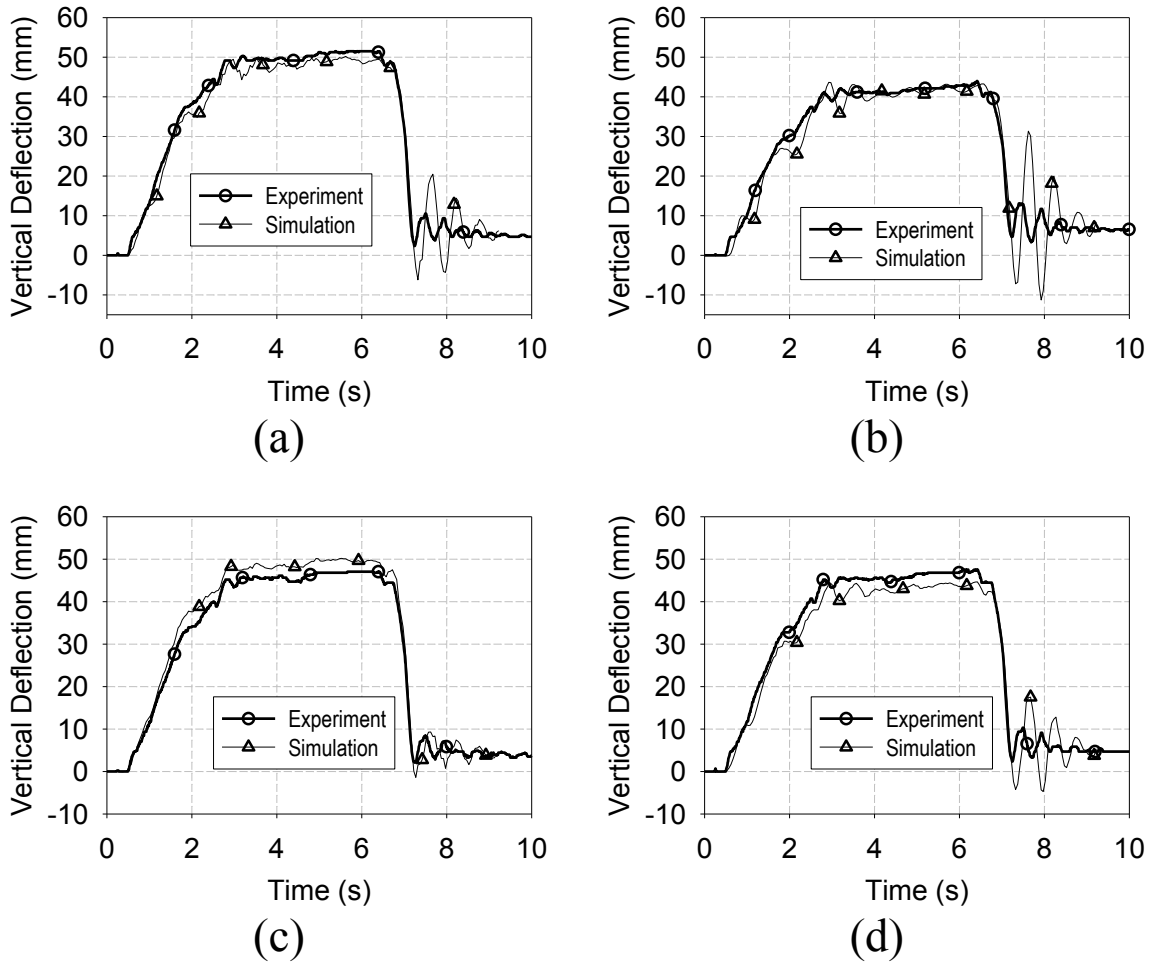
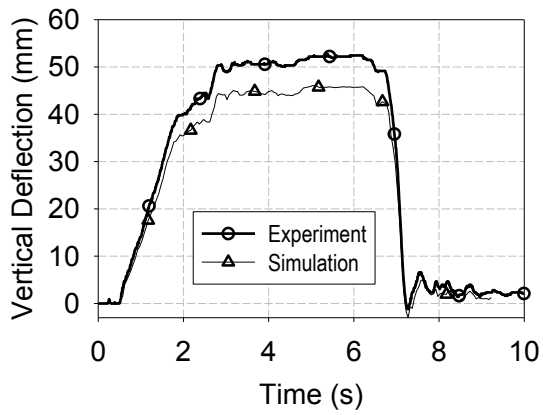
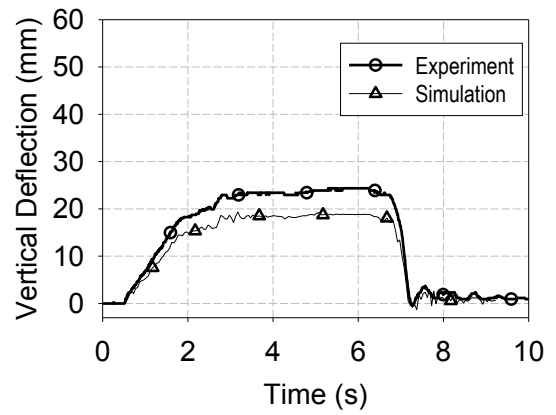


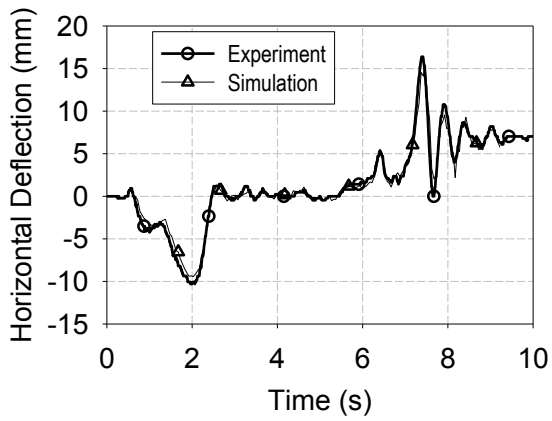
Figure D.1 Deflection comparisons at H points for event 2, (a) Vertical deflection versus time for H-in location, (b) horizontal deflection versus time for H-in location, (c) vertical deflection versus time for H-out location, (b) horizontal deflection versus time for H-out location.



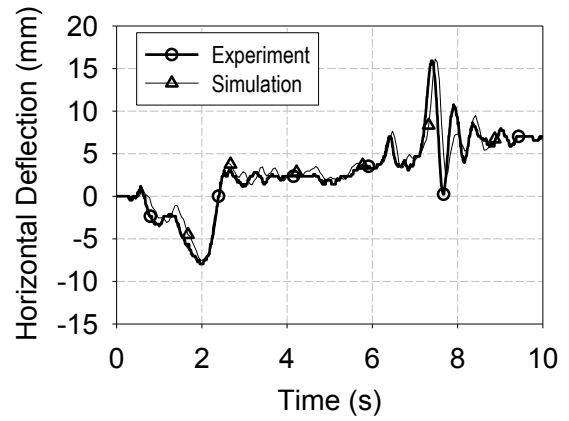
(a)



(b)



(c)



(d)

Figure D.2 Deflection comparisons at D points for event 2, (a) Vertical deflection versus time for D-in location, (b) horizontal deflection versus time for D-in location, (c) vertical deflection versus time for D-out location, (d) horizontal deflection versus time for D-out location.

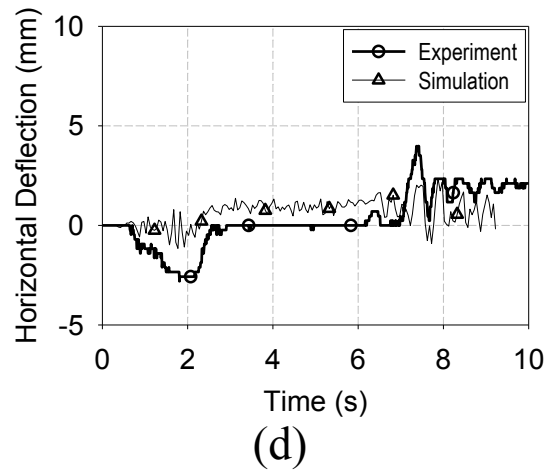
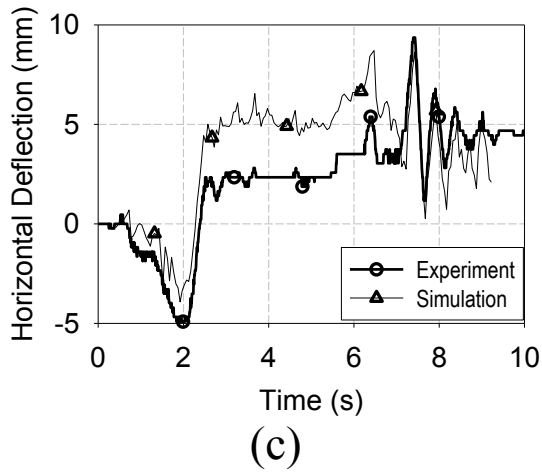
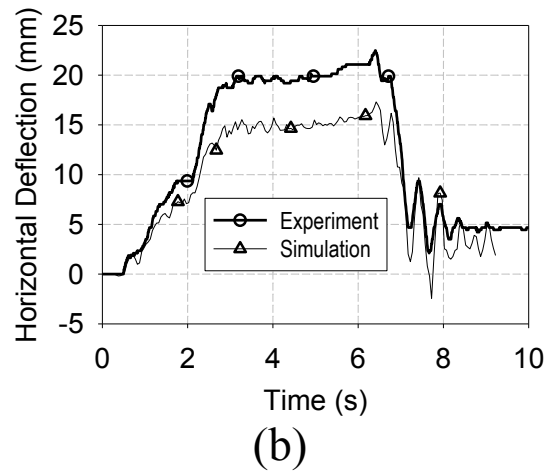
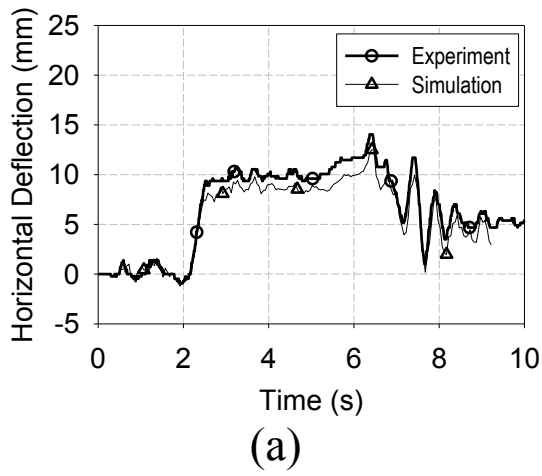


Figure D.3 Deflection comparisons at D points for event 2, (a) Vertical deflection versus time for V-in location, (b) horizontal deflection versus time for V-in location, (c) vertical deflection versus time for V-out location, (b) horizontal deflection versus time for V-out location.

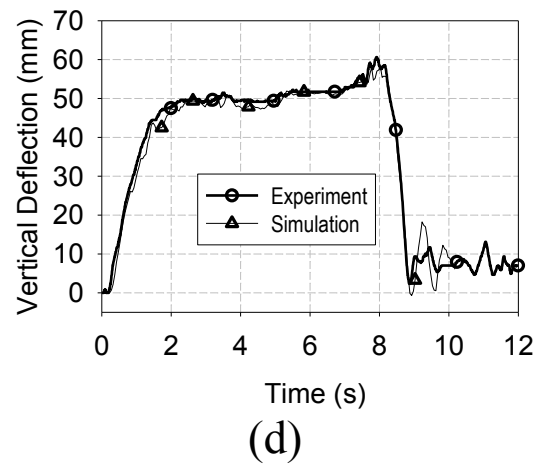
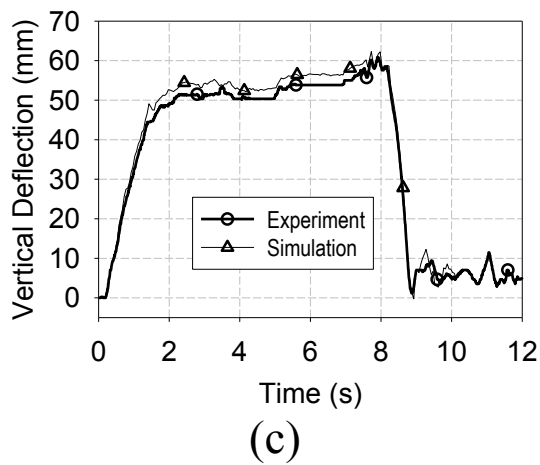
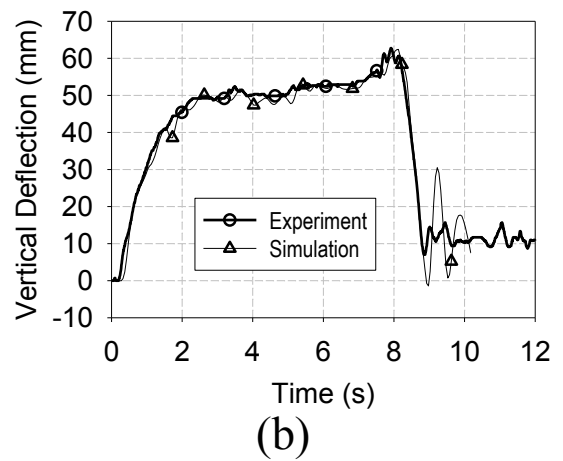
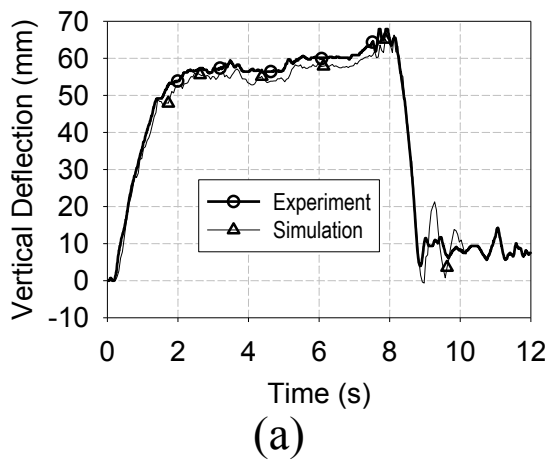
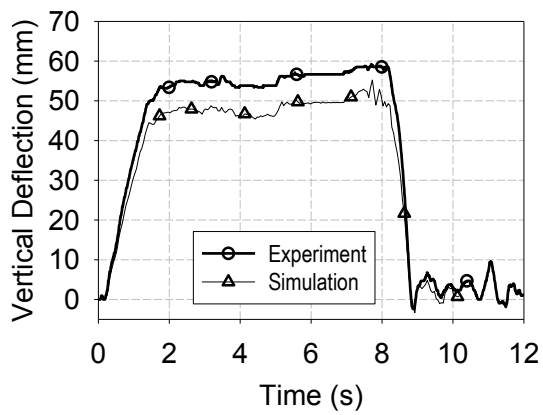
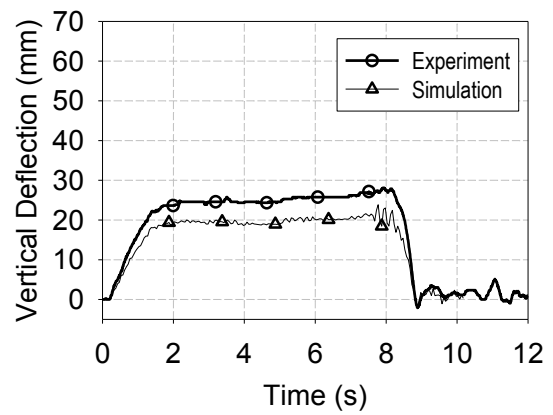


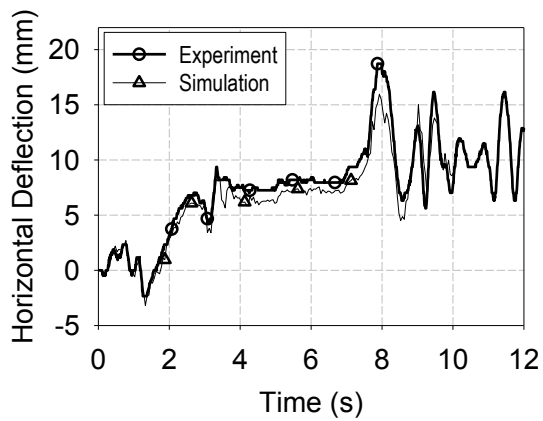
Figure D.4 Deflection comparisons at H points for event 3, (a) Vertical deflection versus time for H-in location, (b) horizontal deflection versus time for H-in location, (c) vertical deflection versus time for H-out location, (b) horizontal deflection versus time for H-out location.



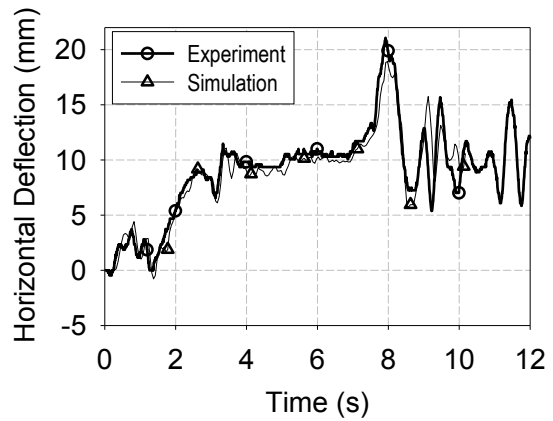
(a)



(b)



(c)



(d)

Figure D.5 Deflection comparisons at D points for event 3, (a) Vertical deflection versus time for D-in location, (b) horizontal deflection versus time for D-in location, (c) vertical deflection versus time for D-out location, (d) horizontal deflection versus time for D-out location.

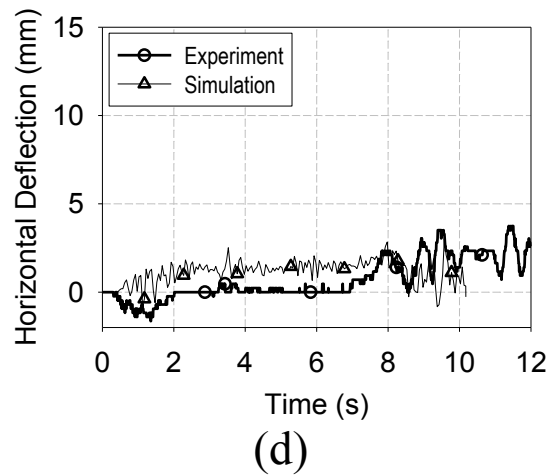
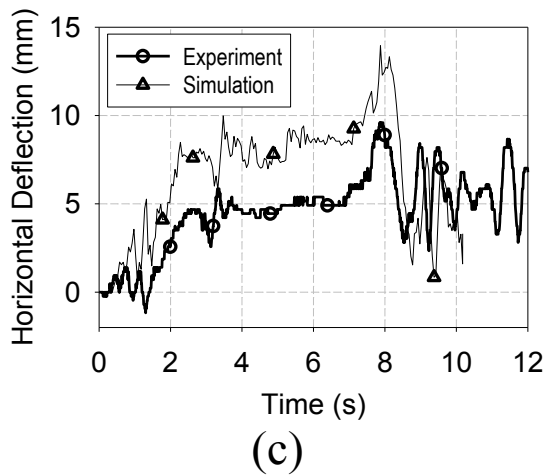
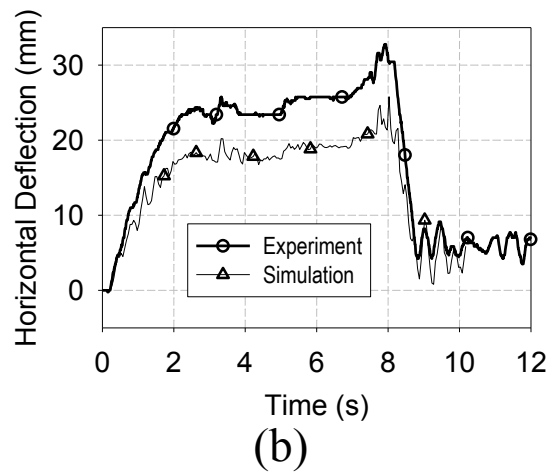
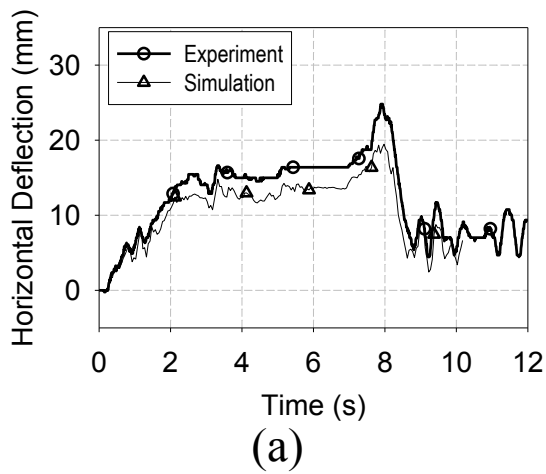


Figure D.6 Deflection comparisons at D points for event 3, (a) Vertical deflection versus time for V-in location, (b) horizontal deflection versus time for V-in location, (c) vertical deflection versus time for V-out location, (b) horizontal deflection versus time for V-out location.



# Appendix E: Partial Input Files Used for FE Simulations

## E.1 Partial Input File Used of Tire Model Validation

```

$-----1-----2-----3-----4-----5-----6-----7-----8
$          CONTROL CARDS AND DATA OUTPUT CARDS          $
$-----1-----2-----3-----4-----5-----6-----7-----8
*CONTROL_ACCURACY
$$ OSU      INN      PIDOSU
$#   osu      inn      pidosu
    1         2         0
*CONTROL_BULK_VISCOSITY
$$      Q1      Q2      IBQ
$#     q1      q2      type      btype
    1.500000  0.060000      -2         0
*CONTROL_CONTACT
$$ SLSFAC  RWPNAL  ISLCHK  SHLTHK  PENOPT  THKCHG  ORIEN  ENMASS
    0.000    0.000    0         1         0         0         0         0
$$ USRSTR  USRFRS  NSBCS  INTERM  XPENE  SSTHK  ECDT  TIEDPRJ
    0         0         0         0         0.000    1         0         0
$#  sfric  dfric    edc    vfc    th    th_sf  pen_sf
    0.000    0.000    0.000    0.000    0.000    0.000    0.000
$#  ignore  frceng  skiprwg  outseg  spotstp  spotdel  spothin
    0         0         0         0         0         0         0.000
$#  isym  nserod  rwgaps  rwgpth  rwsf  icov  swradf  ithoff
    0         0         0         0.000  1.000000  0         0.000    0
$#  shledg
    0
*CONTROL_ENERGY
$$  HGEN      RWEN      SLNTEN      RYLEN
    2         2         2         0
*CONTROL_HOURLASS
$$  IHQ      QH
    6         0.000
*CONTROL_SOLID
$$  ESORT  FMATRX  NIPTETS  SWLOCL
    1         1         0         0         0
$$  PM1    PM2    PM3    PM4    PM5    PM6    PM7    PM8    PM9    PM10
    0         0         0         0         0         0         0         0         0         0
*CONTROL_TERMINATION
$$  ENDTIM  ENDCYC  DTMIN  ENDENG  ENDMAS
    0.700000  0         0.000  0.000  0.000
*CONTROL_TIMESTEP
$$  DTINIT  TSSFAC  ISDO  TSLIMIT  DT2MS  LCTM  ERODE  MSIST
    0.000  0.900000  0         0.000  -2.000E-6  0         0         0
$#  dt2msf  dt2mslc  imsc1
    0.000  0         0
*DAMPING_GLOBAL
$$  LCID  VALDMP  STX  STR  STZ  SRX  SRY  SRZ
    3     0.000  0.000  0.000  0.000  0.000  0.000  0.000
*DATABASE_ELOUT
$#  dt  binary  lcur  ioopt
    0.001000  0         0         1
*DATABASE_GLSTAT
$#  dt  binary  lcur  ioopt
    1.0000E-4  0         0         1
*DATABASE_MATSUM
$#  dt  binary  lcur  ioopt
    1.0000E-4  0         0         1
*DATABASE_NODOUT
$#  dt  binary  lcur  ioopt  dthf  binhf
    1.0000E-4  0         0         1  0.000  0
*DATABASE_RCFORC
$#  dt  binary  lcur  ioopt
    1.0000E-4  0         0         1
*DATABASE_RWFORC
$#  dt  binary  lcur  ioopt

```

```

1.0000E-4      0      0      1
*DATABASE_SLEOUT
$#      dt      binary      lcur      iopt
1.0000E-4      0      0      1
*DATABASE_BINARY_D3PLOT
$$ DT/CYCL      LCDT      BEAM      NPLTC
0.005000      0      0      0      0
$#      iopt
0
*DATABASE_EXTENT_BINARY
$#      neigh      neips      maxint      strflg      sigflg      epsflg      rltflg      engflg
0      0      0      0      0      0      0      0      0
$#      cmpflg      ieverp      beamip      dcomp      shge      stssz      n3thdt      ialemat
0      1      0      0      0      0      0      0      0
$#      nintsld      pkp_sen      sclp      unused      msscl      therm      intout      nodout
0      0      0.000      0      0      0      0      0
$-----1-----2-----3-----4-----5-----6-----7-----8
$-----1-----2-----3-----4-----5-----6-----7-----8
$-----1-----2-----3-----4-----5-----6-----7-----8
*MAT_ELASTIC
$HMNAME MATS      1Tire side center
$#      mid      ro      e      pr      da      db      not used
1 1.4280E-9 0.800000 0.330000 0.000 0.000 0
*MAT_ELASTIC
$HMNAME MATS      2Tire-Inner 1
$#      mid      ro      e      pr      da      db      not used
2 1.4280E-9 40.000000 0.330000 0.000 0.000 0
*MAT_ELASTIC
$HMNAME MATS      3Tire-bead
$#      mid      ro      e      pr      da      db      not used
3 1.4280E-9 5000.0000 0.330000 0.000 0.000 0
*MAT_ELASTIC
$HMNAME MATS      4Tire-tread-side
$#      mid      ro      e      pr      da      db      not used
4 1.4280E-9 5.000000 0.330000 0.000 0.000 0
*MAT_ELASTIC
$HMNAME MATS      5Tire-tread-bottom
$#      mid      ro      e      pr      da      db      not used
5 1.4280E-9 50.000000 0.330000 0.000 0.000 0
*MAT_ELASTIC
$HMNAME MATS      6Elastic steel
$#      mid      ro      e      pr      da      db      not used
6 7.8000E-9 2.1000E+5 0.280000 0.000 0.000 0
*MAT_ELASTIC
$HMNAME MATS      7tire side outer
$#      mid      ro      e      pr      da      db      not used
7 1.4280E-9 1.000000 0.330000 0.000 0.000 0
*MAT_ELASTIC
$HMNAME MATS      8tire side inner
$#      mid      ro      e      pr      da      db      not used
8 1.4280E-9 4.000000 0.330000 0.000 0.000 0
*MAT_ELASTIC
$HMNAME MATS      9Tire-bead-side
$#      mid      ro      e      pr      da      db      not used
9 1.4280E-9 500.00000 0.330000 0.000 0.000 0
*MAT_ELASTIC
$HMNAME MATS      10Tire-tread-inner
$#      mid      ro      e      pr      da      db      not used
10 1.4280E-9 60.000000 0.330000 0.000 0.000 0
*MAT_RIGID
$HMNAME MATS      11Rigid
$#      mid      ro      e      pr      n      couple      m      alias
11 7.8500E-9 2.1000E+5 0.300000 0.000 0.000 0.000
$#      cmo      con1      con2
1.000000 4 7
$#      lco or a1      a2      a3      v1      v2      v3
0.000 0.000 0.000 0.000 0.000 0.000
*MAT_RIGID
$HMNAME MATS      12Rigid dummy flange
$#      mid      ro      e      pr      n      couple      m      alias
12 7.8000E-9 1000.0000 0.300000 0.000 0.000 0.00021000

```

```

$#      cmo      con1      con2
      1.000000      5      7
$# lco or a1      a2      a3      v1      v2      v3
      0.000      0.000      0.000      0.000      0.000      0.000
*MAT_CABLE_DISCRETE_BEAM
$HMNAME MATS      13MATL71_2
$#      mid      ro      e      lcid      f0      tmaxf0      tramp      iread
      13 7.8300E-9 10000.000      0 50.000000      0.000      0.000      0
$-----1-----2-----3-----4-----5-----6-----7-----8
$
$          SECTION CARDS
$-----1-----2-----3-----4-----5-----6-----7-----8
*SECTION_BEAM
$HMNAME PROPS      1SectBeam_3
      1      6      1.0      2.0      1.0      0.0
      100.0      7.8      3.14      0.0      0.0      1.0      0.0
*SECTION_SHELL
$HMNAME PROPS      20.01
      2      16      0.833      3      0.0
      0.01      0.01      0.01      0.01
*SECTION_SOLID
$HMNAME PROPS      3Solid_under integratd
      3
*HOURGLASS
$HMNAME PROPS      4Solid Hourglass-tire
      4      4      0.1
$$ Base Accelerations and Angular Velocities
$-----1-----2-----3-----4-----5-----6-----7-----8
$          LOAD AND BOUNDARY CARDS
$-----1-----2-----3-----4-----5-----6-----7-----8
*LOAD_BODY_Z
$HMNAME LOADCOLS      6LoadBody_6
$HWCOLOR LOADCOLS      6      3
      5      9800.0
*BOUNDARY_PRESCRIBED_MOTION_RIGID
$HMNAME LOADCOLS      1Right dummy flange
$HWCOLOR LOADCOLS      1      3
      7      1      2      4      1.0      0
*BOUNDARY_PRESCRIBED_MOTION_RIGID
$HMNAME LOADCOLS      2Left dummy flange
$HWCOLOR LOADCOLS      2      46
      8      1      2      4      -1.0      0
*LOAD_SEGMENT_SET
$HMNAME LOADCOLS      3Pressure-0.625MPa-tire
$HWCOLOR LOADCOLS      3      3
      21      1      0.625
$-----1-----2-----3-----4-----5-----6-----7-----8
$          CONTACT CARDS
$-----1-----2-----3-----4-----5-----6-----7-----8
*CONTACT_SURFACE_TO_SURFACE_ID
$HMNAME GROUPS      1BS-Band-Flange
$HWCOLOR GROUPS      1      4
      1BS band to flange
      13      14      0      0      1      1
      0.35      0.25      1.0      300.0      20.0
      10.0      10.0
      0
      0.0
      1      1
*CONTACT_SURFACE_TO_SURFACE_ID
$HMNAME GROUPS      2BS-Band-Lock-ring
$HWCOLOR GROUPS      2      37
      2BS-lock ring
      16      15      0      0      1      1
      0.35      0.25      1.0      300.0      20.0
      10.0      10.0
      0
      0.0
      1      1
*CONTACT_SURFACE_TO_SURFACE_ID
$HMNAME GROUPS      3Lock-ring to Rim

```

```

$HWCOLOR GROUPS          3          3
  3Lock ring to Rim
  17          18          0          0          1          1
  0.35        0.25        1.0        300.0        20.0
  10.0        10.0
  0
  0.0
  1          1
*CONTACT_SURFACE_TO_SURFACE_ID
$HMNAME GROUPS          4BS-Band to Rim
$HWCOLOR GROUPS          4          5
  4BS to Rim
  19          4          0          0          1          1
  0.35        0.25        1.0        300.0        20.0
  1.0
  0
  0.0
  1          1
*CONTACT_SURFACE_TO_SURFACE_ID
$HMNAME GROUPS          5Rear Flange to Rim
$HWCOLOR GROUPS          5          3
  5Rear Flange to Rim
  20          6          0          0          1          1
  0.35        0.25        1.0        300.0        20.0
  10.0        10.0
  0
  0.0
  1          1
*CONTACT_SURFACE_TO_SURFACE_ID
$HMNAME GROUPS          6Mid-plate to Rim
$HWCOLOR GROUPS          6          3
  6Mid-plate to Rim
  1          2          0          0          1          1
  0.35        0.25        1.0        300.0        20.0
  1.0
  0
  0.0
  1          1
*CONTACT_SURFACE_TO_SURFACE_ID
$HMNAME GROUPS          7Rear-bead_Rim-base
$HWCOLOR GROUPS          7          3
  7Rear bead-rim
  9          12          0          0          1          1
  0.2         0.15        1.0         50.0        20.0
  1.0         1.0
  0
  0.0
  1          1
*CONTACT_SURFACE_TO_SURFACE_ID
$HMNAME GROUPS          8Front-bead_BS-band
$HWCOLOR GROUPS          8          21
  8Front bead- BS band
  8          11          0          0          1          1
  0.2         0.15
  1.0
  0
  0.0
  1          1
*CONTACT_SURFACE_TO_SURFACE_ID
$HMNAME GROUPS          9Ft Bead side - Dummy Flange-Slide
$HWCOLOR GROUPS          9          4
  9Ft Beadside to Dummy flange - Slide
  7          10          3          0          1          1
  0.35        0.3         0.0         0.16
  10.0        10.0

  1
*CONTACT_SURFACE_TO_SURFACE_ID
$HMNAME GROUPS          12Rr Bead side - Dummy Flange-Slide
$HWCOLOR GROUPS          12          5

```

12Rr Beadsid	to Dummy flange	-Slide				
8	24	3	0		1	1
0.35	0.3				0.0	0.16
10.0	10.0					

1							
*CONTACT_SURFACE_TO_SURFACE_ID							
\$HMNAME	GROUPS	14Rr Bead side - Flange-No-Slide					
\$HWCOLOR	GROUPS	14	7				
14Rr Bead side - Flange-No-Slide							
13	24	3	0		1	1	
1.0	0.9						
10.0	10.0						

1							
*CONTACT_SURFACE_TO_SURFACE_ID							
\$HMNAME	GROUPS	15Ft Bead side - Flange-No-Slide					
\$HWCOLOR	GROUPS	15	7				
15Ft Bead side - Flange-No-Slide							
11	10	3	0		1	1	
1.0	0.9						
10.0	10.0						

1							
*CONTACT_NODES_TO_SURFACE_ID							
\$HMNAME	GROUPS	20Ft Bead side - Flange-Slide					
\$HWCOLOR	GROUPS	20	36				
20Ft Bead side - Flange-Slide							
2	25	4	0		1	1	
0.1	0.05						
100.0	100.0						

1							
*CONTACT_NODES_TO_SURFACE_ID							
\$HMNAME	GROUPS	19Rr Bead side - Flange-Slide					
\$HWCOLOR	GROUPS	19	4				
19Rr Bead side - Flange-Slide							
3	26	4	0		1	1	
0.1	0.05						
100.0	100.0						

1							
*CONTACT_NODES_TO_SURFACE_ID							
\$HMNAME	GROUPS	22Ft flange to chafer					
\$HWCOLOR	GROUPS	22	4				
22Ft flange to chafer							
4	22	4	0				
0.1	0.05						
100.0	100.0						

*CONTACT_NODES_TO_SURFACE_ID							
\$HMNAME	GROUPS	23bk flange to chafer					
\$HWCOLOR	GROUPS	23	4				
23bk flange to chafer							
5	23	4	0				
0.1	0.05						
100.0	100.0						

*CONSTRAINED_EXTRA_NODES_NODE							
\$HMNAME	GROUPS	21load center					
\$HWCOLOR	GROUPS	21	4				
4	179915						

```

*RIGIDWALL_PLANAR_FORCES_ID
$HMNAME GROUPS      17Ground
$HWCOLOR GROUPS    17      5
      17
      1
721.0049364.2432E-05-994.50025721.0049363.2308E-04-993.50025
      0      0      0      0      0      0
$-----1-----2-----3-----4-----5-----6-----7-----8
$
                                     DEFINE CURVE CARDS
$-----1-----2-----3-----4-----5-----6-----7-----8
*DEFINE_CURVE
$HMNAME CURVES      1LoadCurve_1
$HWCOLOR CURVES    1      3
$HMCURVE          2      2 LoadCurve1
      1      0      1.0      1.0      0.0      0.0      0
      0.0      0.0
      0.1      1.0
      10.0      1.0

*DEFINE_CURVE
$HMNAME CURVES      2LoadCurve_2
$HWCOLOR CURVES    2      4
$HMCURVE          3      3 LoadCurve2
      2      0      1.0      1.0      0.0      0.0      0
      0.0      0.0
      0.35      0.0
      0.4      1.0
      10.0      1.0

*DEFINE_CURVE
$HMNAME CURVES      3LoadCurve_3
$HWCOLOR CURVES    3      3
$HMCURVE          1      1 LoadCurve3
      3      0      1.0      1.0      0.0      0.0      0
      0.0      35.0
      0.35      35.0
      0.36      39.0
      10.0      39.0

*DEFINE_CURVE
$HMNAME CURVES      4curve1
$HWCOLOR CURVES    4      3
$HMCURVE          1      2 curve1
      4      0      1.0      1.0
      0.0      0.0
      0.15      30.0
      10.0      600.0

*DEFINE_CURVE
$HMNAME CURVES      5curve2
$HWCOLOR CURVES    5      3
$HMCURVE          1      3 curve2
      5      0      1.0      1.0
      0.0      0.0
      0.05      1.0
      10.0      1.0

```

## E.2 Partial Input File Used for Tire Quasi-static Loading

```

$-----1-----2-----3-----4-----5-----6-----7-----8
$                                LOAD AND BOUNDARY CARDS                                $
$-----1-----2-----3-----4-----5-----6-----7-----8
*LOAD_BODY_Z
$HMNAME LOADCOLS          7LoadBody_9
$HWCOLOR LOADCOLS          7      4
          5      9800.0
*BOUNDARY_PRESCRIBED_MOTION_RIGID
$HMNAME LOADCOLS          1Right dummy flange
$HWCOLOR LOADCOLS          1      7
          7      1      2      4      1.0      0
*BOUNDARY_PRESCRIBED_MOTION_RIGID
$HMNAME LOADCOLS          2Left dummy flange
$HWCOLOR LOADCOLS          2      46
          8      1      2      4      -1.0      0
*BOUNDARY_PRESCRIBED_MOTION_RIGID_LOCAL
$HMNAME LOADCOLS          3rotation
$HWCOLOR LOADCOLS          3      38
          4      5      2      8      1.0      0      0.7
*LOAD_SEGMENT_SET
$HMNAME LOADCOLS          6Pressure=0.593MPa-tire
$HWCOLOR LOADCOLS          6      24
          19      1      0.593
*LOAD_NODE_POINT
$HMNAME LOADCOLS          8LoadNode_3
$HWCOLOR LOADCOLS          8      63
          179915      3      2 -130000.0      0
*BOUNDARY_PRESCRIBED_MOTION_NODE
$HMNAME LOADCOLS          4Vertical movement
$HWCOLOR LOADCOLS          4      3
          179915      3      2      6      1.0      0.7
*BOUNDARY_PRESCRIBED_MOTION_NODE
$HMNAME LOADCOLS          5Longitudinal movement
$HWCOLOR LOADCOLS          5      51
          179915      2      2      7      1.0      0.7
$-----1-----2-----3-----4-----5-----6-----7-----8
$                                DEFINE CURVE CARDS                                $
$-----1-----2-----3-----4-----5-----6-----7-----8
*DEFINE_CURVE
$HMNAME CURVES          1LoadCurve_1
$HWCOLOR CURVES          1      3
$HMCURVE          2      2 LoadCurve1
          1      0      1.0      1.0      0.0      0.0      0
          0.0      0.0
          0.1      1.0
          10.0      1.0
*DEFINE_CURVE
$HMNAME CURVES          2LoadCurve_2
$HWCOLOR CURVES          2      4
$HMCURVE          3      3 LoadCurve2
          2      0      1.0      1.0      0.0      0.0      0
          0.0      0.0
          0.35      0.0
          0.4      1.0
          10.0      1.0
*DEFINE_CURVE
$HMNAME CURVES          3LoadCurve_3
$HWCOLOR CURVES          3      3
$HMCURVE          1      1 LoadCurve3
          3      0      1.0      1.0      0.0      0.0      0
          0.0      35.0
          0.35      35.0
          0.36      39.0
          10.0      39.0
*DEFINE_CURVE
$HMNAME CURVES          4curve1
$HWCOLOR CURVES          4      3
$HMCURVE          1      2 curve1

```

```

4          0          1.0          1.0
          0.0          0.0
          0.15         30.0
          10.0         600.0

*DEFINE_CURVE
$HMNAME CURVES          5curve2
$HWCOLOR CURVES          5          3
$HMCURVE 1          3 curve2
          5          0          1.0          1.0
          0.0          0.0
          0.05         1.0
          10.0         1.0

*DEFINE_CURVE
$HMNAME CURVES          6LoadCurve_6
$HWCOLOR CURVES          6          3
$HMCURVE 1          1 LoadCurve6
          6          0          1.0          -1.0          0.0          0.0          0
          0.0          0.0
          0.007         0.2341
          0.015         1.405
          0.023         2.809
          0.031         3.511
          0.039         4.214
          0.047         5.384
          0.055         6.086
          0.063         6.555
          0.071         6.555
          0.079         8.427
          0.087         8.427
          0.095         8.896
          0.103         10.07
          0.111         10.77
          0.119         10.77
          0.127         11.7
          0.135         12.64
          0.143         11.94
          0.151         11.7
          0.159         11.7
          0.167         11.94
          0.175         11.94
          0.183         14.05
          0.191         16.39
          0.199         18.03
          0.207         20.13
          0.215         22.24
          0.223         24.35
          0.231         26.69
          0.239         28.56
          0.247         30.43
          0.255         31.84
          0.263         33.48
          0.271         35.11
          0.279         36.75
          0.287         38.39
          0.295         40.26
          0.303         41.2
          0.311         42.37
          0.319         43.54
          0.327         44.48
          0.335         44.71
          0.343         44.95
          0.351         44.95
          0.359         44.71
          0.367         45.18
          0.375         45.88
          0.383         45.88
          0.391         46.35
          0.399         48.22
          0.407         50.56
          0.415         50.1
          0.423         51.27

```



0.431	54.08
0.439	53.37
0.447	52.44
0.455	54.08
0.463	53.37
0.471	51.5
0.479	52.44
0.487	52.91
0.495	51.97
0.503	51.5
0.511	51.97
0.519	51.73
0.527	51.5
0.535	51.97
0.543	51.73
0.551	51.5
0.559	50.8
0.567	51.5
0.575	51.27
0.583	51.27
0.591	51.5
0.599	51.5
0.607	51.03
0.615	51.03
0.623	51.03
0.631	51.03
0.639	51.03
0.647	51.03
0.655	51.03
0.663	51.03
0.671	51.03
0.679	51.03
0.687	51.03
0.695	51.03
0.703	50.56
0.711	50.8
0.719	50.8
0.727	50.8
0.735	50.56
0.743	50.56
0.751	50.56
0.759	50.56
0.767	50.56
0.775	50.56
0.783	50.56
0.791	50.56
0.799	50.56
0.807	50.56
0.815	50.56
0.823	50.56
0.831	50.56
0.839	50.56
0.847	50.56
0.855	50.56
0.863	50.56
0.871	50.56
0.879	50.56
0.887	50.56
0.895	50.56
0.903	50.56
0.911	50.56
0.919	50.56
0.927	50.56
0.935	50.56
0.943	50.56
0.951	50.56
0.959	50.56
0.967	49.63
0.975	48.22
0.983	47.76
0.991	46.35

0.999	44.95
1.007	41.9
1.015	39.8
1.023	36.52
1.031	31.6
1.039	26.69
1.047	22.71
1.055	19.2
1.063	14.05
1.071	11.7
1.079	9.598
1.087	6.086
1.095	2.809
1.103	2.575
1.111	3.043
1.119	3.746
1.127	4.448
1.135	4.682
1.143	3.746
1.151	2.575
1.159	2.575
1.167	3.277
1.175	3.511
1.183	2.809
1.191	2.809
1.199	1.639
1.207	1.405
1.215	2.107
1.223	2.809
1.231	2.809
1.239	2.107
1.247	1.639
1.255	1.405
1.263	1.873
1.271	3.043
1.279	2.809
1.287	2.341
1.295	1.405
1.303	1.405
1.311	1.405
1.319	1.405
1.327	1.873
1.335	2.107
1.343	1.405
1.351	1.17
1.359	1.405
1.367	1.405
1.375	1.405
1.383	1.639
1.391	1.405
1.399	0.9364

```

*DEFINE_CURVE
$HMNAME_CURVES      7LoadCurve_7
$HWCOLOR_CURVES    7      4
$HMCURVE           2      2 LoadCurve7
                    7      0      1.0      1.0      0.0      0.0      0
                    0.0      0.0
                    0.007      0.2341
                    0.015      0.9364
                    0.023      0.4682
                    0.031      0.0
                    0.039      -0.4682
                    0.047      -0.7023
                    0.055      -0.2341
                    0.063      -0.4682
                    0.071      -0.4682
                    0.079      0.0
                    0.087      0.7023
                    0.095      2.341
                    0.103      3.98
                    0.111      4.448

```

0.119	3.511
0.127	2.341
0.135	2.341
0.143	2.341
0.151	2.341
0.159	2.341
0.167	2.341
0.175	2.341
0.183	2.575
0.191	2.341
0.199	2.341
0.207	2.107
0.215	1.405
0.223	0.7023
0.231	0.0
0.239	-0.9364
0.247	-0.7023
0.255	-0.9364
0.263	-1.17
0.271	-1.17
0.279	-1.405
0.287	-1.639
0.295	-1.873
0.303	-2.341
0.311	-2.341
0.319	-2.341
0.327	-2.341
0.335	-3.043
0.343	-2.341
0.351	-2.341
0.359	-2.575
0.367	-3.043
0.375	-2.341
0.383	-2.341
0.391	-4.682
0.399	-4.682
0.407	-3.511
0.415	-4.682
0.423	-6.555
0.431	-5.384
0.439	-4.682
0.447	-4.682
0.455	-4.916
0.463	-5.15
0.471	-4.682
0.479	-4.448
0.487	-4.682
0.495	-4.682
0.503	-4.682
0.511	-4.682
0.519	-4.682
0.527	-4.682
0.535	-4.682
0.543	-4.916
0.551	-4.682
0.559	-4.682
0.567	-4.682
0.575	-5.15
0.583	-5.15
0.591	-4.682
0.599	-4.682
0.607	-5.15
0.615	-5.15
0.623	-5.15
0.631	-5.15
0.639	-5.15
0.647	-5.15
0.655	-5.15
0.663	-5.15
0.671	-5.15
0.679	-5.15

0.687	-5.15
0.695	-5.15
0.703	-4.916
0.711	-5.618
0.719	-5.618
0.727	-5.618
0.735	-5.618
0.743	-5.618
0.751	-5.618
0.759	-5.618
0.767	-5.618
0.775	-5.618
0.783	-5.618
0.791	-5.618
0.799	-5.618
0.807	-5.618
0.815	-5.618
0.823	-5.618
0.831	-5.618
0.839	-5.618
0.847	-5.618
0.855	-5.852
0.863	-5.852
0.871	-5.852
0.879	-5.852
0.887	-5.852
0.895	-5.852
0.903	-5.852
0.911	-5.852
0.919	-5.852
0.927	-5.852
0.935	-5.852
0.943	-5.852
0.951	-5.852
0.959	-5.852
0.967	-6.789
0.975	-7.959
0.983	-10.53
0.991	-14.05
0.999	-17.32
1.007	-20.37
1.015	-18.73
1.023	-14.28
1.031	-11.94
1.039	-10.53
1.047	-8.427
1.055	-6.555
1.063	-5.384
1.071	-4.682
1.079	-3.511
1.087	-2.341
1.095	-2.107
1.103	-0.9364
1.111	-0.7023
1.119	-1.639
1.127	-2.809
1.135	-2.341
1.143	-1.639
1.151	-0.4682
1.159	-0.4682
1.167	-1.17
1.175	-2.341
1.183	-2.107
1.191	-1.405
1.199	-0.9364
1.207	-0.9364
1.215	-0.9364
1.223	-1.639
1.231	-1.873
1.239	-1.873
1.247	-1.405

```

1.255      -0.9364
1.263      -0.9364
1.271      -1.405
1.279      -2.341
1.287      -2.341
1.295      -1.17
1.303      -0.2341
1.311      -0.2341
1.319      -1.17
1.327      -1.873
1.335      -1.873
1.343      -1.17
1.351      -1.17
1.359      -0.2341
1.367      -0.9364
1.375      -1.405
1.383      -1.405
1.391      -1.17
1.399      -1.17

*DEFINE_CURVE
$HMNAME CURVES      8LoadCurve_8
$HWCOLOR CURVES      8      4
$HMCURVE      2      2 LoadCurve7
                8                0      1.0      1.0      0.0      0.0      0
                0.0                0      0.0
0.007 -6.221000000000E-04
0.015 -6.040000000000E-04
0.023  6.169000000000E-04
0.031 -3.672000000000E-10
0.039      0.002452
0.047      0.001826
0.055      0.001226
0.063      0.002452
0.071      0.002452
0.079  6.169000000000E-04
0.087      0.00121
0.095      -0.001231
0.103      -0.002452
0.111      -0.001842
0.119 -6.040000000000E-04
0.127 -2.936000000000E-09
0.135 -6.161000000000E-04
0.143      -0.001231
0.151      -0.001846
0.159      -0.001846
0.167      -0.001231
0.175      -0.00246
0.183      -0.001842
0.191 -4.404000000000E-09
0.199  6.169000000000E-04
0.207      0.001226
0.215      0.00305
0.223      0.003656
0.231      0.003667
0.239      0.003667
0.247      0.004298
0.255      0.004286
0.263      0.006131
0.271      0.006131
0.279      0.006116
0.287      0.006721
0.295      0.009187
0.303      0.009151
0.311      0.009771
0.319      0.009771
0.327      0.009771
0.335      0.01097
0.343      0.01039
0.351      0.01039
0.359      0.009771
0.367      0.01222

```

0.375	0.01101
0.383	0.009771
0.391	0.01037
0.399	0.01037
0.407	0.01349
0.415	0.01164
0.423	0.01346
0.431	0.01282
0.439	0.01342
0.447	0.01164
0.455	0.01162
0.463	0.01284
0.471	0.01162
0.479	0.01284
0.487	0.01286
0.495	0.01101
0.503	0.01164
0.511	0.01164
0.519	0.01101
0.527	0.0116
0.535	0.01164
0.543	0.01099
0.551	0.01164
0.559	0.01039
0.567	0.01101
0.575	0.01097
0.583	0.01222
0.591	0.01164
0.599	0.01164
0.607	0.01222
0.615	0.01222
0.623	0.01222
0.631	0.01222
0.639	0.01222
0.647	0.01222
0.655	0.01222
0.663	0.01222
0.671	0.01222
0.679	0.01222
0.687	0.01222
0.695	0.01222
0.703	0.01099
0.711	0.01279
0.719	0.01279
0.727	0.01279
0.735	0.01217
0.743	0.01217
0.751	0.01279
0.759	0.01217
0.767	0.0122
0.775	0.0122
0.783	0.0122
0.791	0.01282
0.799	0.01282
0.807	0.0116
0.815	0.01222
0.823	0.01222
0.831	0.01222
0.839	0.01222
0.847	0.01284
0.855	0.01222
0.863	0.01222
0.871	0.01344
0.879	0.01344
0.887	0.01222
0.895	0.01284
0.903	0.01222
0.911	0.01162
0.919	0.01224
0.927	0.01346
0.935	0.01224

0.943	0.01224
0.951	0.01224
0.959	0.01164
0.967	0.0116
0.975	0.01097
0.983	0.01464
0.991	0.01714
0.999	0.01905
1.007	0.01776
1.015	0.01654
1.023	0.01349
1.031	0.01226
1.039	0.009828
1.047	0.007978
1.055	0.009187
1.063	0.006736
1.071	0.005511
1.079	0.004274
1.087	0.001234
1.095	0.002443
1.103	0.001835
1.111	0.001218
1.119	0.001835
1.127	0.003071
1.135	0.002472
1.143	0.001835
1.151	6.094000000000000E-04
1.159	0.001835
1.167	0.001835
1.175	0.002452
1.183	0.001844
1.191	0.001844
1.199	0.002443
1.207	0.002443
1.215	0.002462
1.223	0.00306
1.231	0.003071
1.239	0.003667
1.247	0.002452
1.255	0.001835
1.263	0.001844
1.271	0.001235
1.279	0.001835
1.287	0.002452
1.295	0.001226
1.303	0.001226
1.311	0.001226
1.319	6.169000000000000E-04
1.327	0.002452
1.335	0.00306
1.343	0.001226
1.351	0.001826
1.359	0.001235
1.367	0.001835
1.375	0.001226
1.383	0.001844
1.391	0.001226

### E.3 Partial Input File Used for Rim Base Model Validation

```

Rim base static load test
$-----1-----2-----3-----4-----5-----6-----7-----8
$
$
CONTROL CARDS
$
$-----1-----2-----3-----4-----5-----6-----7-----8
*CONTROL_TERMINATION
$$ ENDTIM ENDCYC DTMIN ENDENG ENDMAS
1.0
*CONTROL_TIMESTEP
$$ DTINIT TSSFAC ISDO TSLIMIT DT2MS LCTM ERODE MSIST
0.0 0.9 -2.000E-06
*CONTROL_HOURLASS
$$ IHQ QH
6
*CONTROL_BULK_VISCOSITY
$$ Q1 Q2 IBQ
1.5 0.06 -2
*CONTROL_CONTACT
$$ SLSFAC RWPNAL ISLCHK SHLTHK PENOPT THKCHG ORIEN ENMASS
1
$$ USRSTR USRFRC NSBCS INTERM XPENE SSTHK ECDD TIEDPRJ
1
*CONTROL_ENERGY
$$ HGEN RWEN SLNTEN RYLEN
2 2 2 2
*CONTROL_ACCURACY
$$ OSU INN PIDOSU
1 2
*DATABASE_EXTENT_BINARY
$$ NEIPH NEIPS MAXINT STRFLG SIGFLG EPSFLG RLTF LG ENGFLG
1
$$ CMPFLG IEVERP BEAMIP DCOMP SHGE STSSZ N3THDT IALEMAT
1
$$ NINTSLD PKP_SEN SCLP MSSCL THERM
$-----1-----2-----3-----4-----5-----6-----7-----8
$
$
MATERIAL CARDS
$
$-----1-----2-----3-----4-----5-----6-----7-----8
*MAT_ELASTIC
$HMNAME MATS 1Elastic steel
17.8000E-09 210000.0 0.28
*MAT_ELASTIC
$HMNAME MATS 2Aluminum
22.7000E-09 70000.0 0.33
*MAT_RIGID
$HMNAME MATS 3Rigid
32.7000E-09 70000.0 0.3
1.0 4 7
0
*MAT_RIGID
$HMNAME MATS 4rigid support
47.8000E-09 210000.0 0.28
1.0 7 7
0
$-----1-----2-----3-----4-----5-----6-----7-----8
$
$
SECTION CARDS
$
$-----1-----2-----3-----4-----5-----6-----7-----8
*SECTION_SHELL
$HMNAME PROPS 10.01
1 0.833 3 0.0
0.01 0.01 0.01 0.01
*SECTION_SHELL
$HMNAME PROPS 2Plate-4.0mm
2 0.833 2 0.0
2.0 2.0 2.0 2.0
*SECTION_SOLID
$HMNAME PROPS 3Solid_under integratd
3
ALL ALL
$-----1-----2-----3-----4-----5-----6-----7-----8

```



```

$
                                LOAD CARDS
$-----1-----2-----3-----4-----5-----6-----7-----8
*LOAD_BODY_Z
$HMNAME LOADCOLS          3LoadBody_3
$HWCOLOR LOADCOLS        3      3
      2      9800.0
*LOAD_RIGID_BODY
$HMNAME LOADCOLS          1Load-rigid-body
$HWCOLOR LOADCOLS        1      3
      5      3      1 -100000.0
$-----1-----2-----3-----4-----5-----6-----7-----8
$
                                CONTACT CARDS
$-----1-----2-----3-----4-----5-----6-----7-----8
*CONTACT_SURFACE_TO_SURFACE_ID
$HMNAME GROUPS          1pad to Aluminum
$HWCOLOR GROUPS        1      29
      1pad to Aluminum
      5      3      3      0
      0.3      0.0
      1      1

      1      1
*CONTACT_SURFACE_TO_SURFACE_ID
$HMNAME GROUPS          2Rim to stands
$HWCOLOR GROUPS        2      29
      2Rim to Support 2
      5      6      0      3
      0.2      0.1
      20      20
      1      1

      1      1
*CONTACT_SURFACE_TO_SURFACE_ID
$HMNAME GROUPS          3Aluminum to Rim
$HWCOLOR GROUPS        3      29
      3Aluminum to Rim
      4      1      0      0
      0.6      0.15
      1      1

      1      1
*CONTACT_SURFACE_TO_SURFACE_ID
$HMNAME GROUPS          4Rim to support 1
$HWCOLOR GROUPS        4      29
      4Rim to support 1
      2      11      0      3
      0.2      0.1
      20.0      20.0
      1      1

      1      1
$-----1-----2-----3-----4-----5-----6-----7-----8
$
                                DEFINE CURVE CARDS
$-----1-----2-----3-----4-----5-----6-----7-----8
*DEFINE_CURVE
$HMNAME CURVES          1LoadCurve_2
$HWCOLOR CURVES        1      4
$HMCURVE          3      3 LoadCurve2
      1      0      1.0      1.0      0.0      0.0      0
      0.0      0.0
      1.0      1.0
*DEFINE_CURVE
$HMNAME CURVES          2curve2
$HWCOLOR CURVES        2      3
$HMCURVE          1      3 curve2
      2      0      1.0      1.0
      0.0      0.0
      0.05      1.0

```

## E.4 Partial Input File Used for BS Band Pull-out Simulation

```

$-----1-----2-----3-----4-----5-----6-----7-----8
$                                     MATERIAL CARDS                                     $
$-----1-----2-----3-----4-----5-----6-----7-----8
*MAT_ELASTIC
$HMNAME MATS          16Tire-bead.1
    161.4280E-09      1000.0      0.33
*MAT_ELASTIC
$HMNAME MATS          17Tire-bead-side
    171.4280E-09      1000.0      0.33
*MAT_RIGID
$HMNAME MATS          15Rigid inner
    151.4280E-09      2000.0      0.3
    1.0      5      7
    0
*MAT_PIECEWISE_LINEAR_PLASTICITY
$HMNAME MATS          6Elastic steel
    67.8000E-09      210000.0      0.28      345.0      550.0      0.21

$$ HM Entries in Stress-Strain Curve =

*MAT_PIECEWISE_LINEAR_PLASTICITY
$HMNAME MATS          18front flange
    187.8000E-09      210000.0      0.28      345.0      550.0

$$ HM Entries in Stress-Strain Curve =
$-----1-----2-----3-----4-----5-----6-----7-----8
$                                     SECTION CARDS                                     $
$-----1-----2-----3-----4-----5-----6-----7-----8
*SECTION_BEAM
$HMNAME PROPS          3Beam
    3
    3.14      1.0      2      1.0      2.0      2.0      1.0
    1.0      2.0      0.0
*SECTION_SHELL
$HMNAME PROPS          10.01
    1
    0.01      0.01      0.01      1      0.0
*SECTION_SOLID
$HMNAME PROPS          2Solid_under integratd
    2
$HMNAME PROPS          4Solid_under integratd.1
    4
*HOURGLASS
$HMNAME PROPS          5Solid Hourglass-tire
    5      4      0.1
$-----1-----2-----3-----4-----5-----6-----7-----8
$                                     BOUNDARY CARDS                                     $
$-----1-----2-----3-----4-----5-----6-----7-----8
*BOUNDARY_PRESCRIBED_MOTION_RIGID
$HMNAME LOADCOLS      1Prescribed displacement
$HWCOLOR LOADCOLS      1      3
    33      1      2      1      50.0      0
*DEFINE_CURVE
$HMNAME CURVES          1LoadCurve_1
$HWCOLOR CURVES          1      3
$HMCURVE          2      2 LoadCurve1
    1      0      1.0      1.0      0.0      0.0      0
    0.0
    0.5      2.0

```

## E.5 Partial Input File Used for Threaded-connection Design at Quasi-static Loading Condition

```

$---+---1---+---2---+---3---+---4---+---5---+---6---+---7---+---8
$                                     MATERIAL CARDS                                     $
$---+---1---+---2---+---3---+---4---+---5---+---6---+---7---+---8
*MAT_ELASTIC
$HMNAME MATS          1Tire side center
    11.4280E-09      0.8      0.33
*MAT_ELASTIC
$HMNAME MATS          2Tire-Inner 1
    21.4280E-09     40.0      0.33
*MAT_ELASTIC
$HMNAME MATS          3Tire-bead
    31.4280E-09    5000.0     0.33
*MAT_ELASTIC
$HMNAME MATS          4Tire-tread-side
    41.4280E-09     5.0      0.33
*MAT_ELASTIC
$HMNAME MATS          5Tire-tread-bottom
    51.4280E-09     50.0     0.33
*MAT_ELASTIC
$HMNAME MATS          6Elastic steel
    67.8000E-09   210000.0     0.28
*MAT_ELASTIC
$HMNAME MATS          7tire side outer
    71.4280E-09     1.0      0.33
*MAT_ELASTIC
$HMNAME MATS          8tire side inner
    81.4280E-09     4.0      0.33
*MAT_ELASTIC
$HMNAME MATS          9Tire-bead-side
    91.4280E-09     500.0     0.33
*MAT_ELASTIC
$HMNAME MATS         10Tire-tread-inner
   101.4280E-09     60.0     0.33
*MAT_RIGID
$HMNAME MATS         11Rigid
   117.8500E-09   210000.0     0.3
    1.0      1      4
    0
*MAT_RIGID
$HMNAME MATS         12Rigid dummy flange
   127.8000E-09   1000.0     0.3
    1.0      5      7
    0
*MAT_RIGID
$HMNAME MATS         13rigid driver key
   137.8000E-09   210000.0     0.28
    0.0
    0
*MAT_CABLE_DISCRETE_BEAM
$HMNAME MATS         14MATL71_2
   147.8300E-09   10000.0     0     50.0     0
$---+---1---+---2---+---3---+---4---+---5---+---6---+---7---+---8
$                                     SECTION CARDS                                     $
$---+---1---+---2---+---3---+---4---+---5---+---6---+---7---+---8
*SECTION_BEAM
$HMNAME PROPS        1SectBeam_3
    1          6          1.0          2.0          1.0          0.0
   100.0      7.8          3.14          0.0          0.0          1.0          0.0
*SECTION_SHELL
$HMNAME PROPS        20.01
    2          0.833          3          0.0
    0.01      0.01      0.01      0.01
*SECTION_SHELL
$HMNAME PROPS        3Driver key
    3          0          0.833          2          0.0

```

```

2.0      2.0      2.0      2.0
*SECTION SOLID
$HMNAME PROPS      4Solid_under integratd
4
*HOURGLASS
$HMNAME PROPS      5Solid Hourglass-tire
5      4      0.1
$-----1-----2-----3-----4-----5-----6-----7-----8
$
$              LOAD AND BOUNDARY CARDS
$-----1-----2-----3-----4-----5-----6-----7-----8
*LOAD_BODY_Z
$HMNAME LOADCOLS      6LoadBody_6
$HWCOLOR LOADCOLS      6      3
1      9800.0
*BOUNDARY_PRESCRIBED_MOTION_RIGID
$HMNAME LOADCOLS      1Right dummy flange
$HWCOLOR LOADCOLS      1      7
8      1      2      4      1.0      0
*BOUNDARY_PRESCRIBED_MOTION_RIGID
$HMNAME LOADCOLS      2Left dummy flange
$HWCOLOR LOADCOLS      2      46
9      1      2      4      -1.0      0
*LOAD_SEGMENT_SET
$HMNAME LOADCOLS      4Pressure-0.593MPa-tire
$HWCOLOR LOADCOLS      4      24
15      1      0.593
$HMNAME LOADCOLS      5Pressure-rim base
$HWCOLOR LOADCOLS      5      3
3      1      0.593
*SET_SEGMENT
$HMNAME CSURFS      1Mid plate
$HWCOLOR CSURFS      1      4
1
368      370      224862      224863
*BOUNDARY_PRESCRIBED_MOTION_NODE
$HMNAME LOADCOLS      3Vertical movement
$HWCOLOR LOADCOLS      3      3
69812      3      2      6      -82.5
*DATABASE_HISTORY_NODE
$HMNAME OUTPUTBLOCKS      1TimeHistory1
69812      71479      90144      90166      90168      90169      90184      90187
90191      90192      103050      74468      96701      111654      113436      90174
90141      113440
$-----1-----2-----3-----4-----5-----6-----7-----8
$
$              CONTACT CARDS
$-----1-----2-----3-----4-----5-----6-----7-----8
*CONTACT_SURFACE_TO_SURFACE_ID
$HMNAME GROUPS      1BS-Band-Flange
$HWCOLOR GROUPS      1      4
1BS band to flange
11      12      0      0      1      1
0.35      0.25      1.0      300.0      20.0
10.0      10.0
0
0.0
1      1
*CONTACT_SURFACE_TO_SURFACE_ID
$HMNAME GROUPS      2BS END - Rin front end
$HWCOLOR GROUPS      2      37
2BS END - Rin front end
22      24      0      0      1      1
0.35      0.25      1.0      300.0      20.0
10.0      10.0
0
0.0
1      1
*CONTACT_SURFACE_TO_SURFACE_ID
$HMNAME GROUPS      3Rim thread - BS thread
$HWCOLOR GROUPS      3      3
3Rim thread - BS thread
21      23      0      0      1      1

```

0.35	0.25	1.0	300.0	20.0		
10.0	10.0					
0						
0.0						
1	1					
*CONTACT_SURFACE_TO_SURFACE_ID						
\$HMNAME	GROUPS	4BS-Band to Rim				
\$HWCOLOR	GROUPS	4	5			
4BS to Rim						
13	4	0	0		1	1
0.35	0.25	1.0	300.0	20.0		
10.0	10.0					
0						
0.0						
1	1					
*CONTACT_SURFACE_TO_SURFACE_ID						
\$HMNAME	GROUPS	5Rear Flange to Rim				
\$HWCOLOR	GROUPS	5	3			
5Rear Flange to Rim						
14	5	0	0		1	1
0.35	0.25	1.0	300.0	20.0		
10.0	10.0					
0						
0.0						
1	1					
*CONTACT_SURFACE_TO_SURFACE_ID						
\$HMNAME	GROUPS	6Mid-plate to Rim				
\$HWCOLOR	GROUPS	6	3			
6Mid-plate to Rim						
1	2	0	0		1	1
0.35	0.25	1.0	300.0	20.0		
1.0						
0						
0.0						
1	1					
*CONTACT_SURFACE_TO_SURFACE_ID						
\$HMNAME	GROUPS	7Rear-bead Rim-base				
\$HWCOLOR	GROUPS	7	3			
7Rear bead-rim						
7	10	0	0		1	1
0.35	0.25	1.0	50.0	20.0		
1.0	1.0					
0						
0.0						
1	1					
*CONTACT_SURFACE_TO_SURFACE_ID						
\$HMNAME	GROUPS	8Front-bead_BS-band				
\$HWCOLOR	GROUPS	8	21			
8Front bead- BS band						
6	9	0	0		1	1
0.35	0.25					
1.0						
0						
0.0						
1	1					
*CONTACT_SURFACE_TO_SURFACE_ID						
\$HMNAME	GROUPS	9Ft Bead side - Dummy Flange-Slide				
\$HWCOLOR	GROUPS	9	4			
9Ft Beadside to Dummy flange - Slide						
8	8	3	0		1	1
0.35	0.3				0.0	0.16
10.0	10.0					
1						
*CONTACT_SURFACE_TO_SURFACE_ID						
\$HMNAME	GROUPS	10Rr Bead side - Dummy Flange-Slide				
\$HWCOLOR	GROUPS	10	5			
10Rr Beadside to Dummy flange -Slide						
9	18	3	0		1	1
0.35	0.3				0.0	0.16

10.0 10.0

```

1
*CONTACT_SURFACE_TO_SURFACE_ID
$HMNAME GROUPS 11Rr Bead side - Flange-No-Slide
$HWCOLOR GROUPS 11 7
11Rr Bead side - Flange-No-Slide
13 18 3 0 1 1
1.0 0.9
10.0 10.0

```

```

1
*CONTACT_SURFACE_TO_SURFACE_ID
$HMNAME GROUPS 12Ft Bead side - Flange-No-Slide
$HWCOLOR GROUPS 12 7
12Ft Bead side - Flange-No-Slide
12 8 3 0 1 1
1.0 0.9
10.0 10.0

```

```

1
*CONTACT_NODES_TO_SURFACE_ID
$HMNAME GROUPS 13Ft Bead side - Flange-Slide
$HWCOLOR GROUPS 13 36
13Ft Bead side - Flange-Slide
2 19 4 0 1 1
0.1 0.05
100.0 100.0

```

```

1
*CONTACT_NODES_TO_SURFACE_ID
$HMNAME GROUPS 14Rr Bead side - Flange-Slide
$HWCOLOR GROUPS 14 4
14Rr Bead side - Flange-Slide
3 20 4 0 1 1
0.1 0.05
100.0 100.0

```

```

1
*CONSTRAINED_EXTRA_NODES_SET
$HMNAME GROUPS 16load center
$HWCOLOR GROUPS 16 4
6 4
*SET_NODE_LIST
$HMSET
$HMNAME SETS 4local system
4 0.0 0.0 0.0 0.0
69812 165761 165762
*RIGIDWALL_PLANAR_FORCES_ID
$HMNAME GROUPS 15Ground
$HWCOLOR GROUPS 15 5
15
1
721.0049364.2432E-05-994.50025721.0049363.2308E-04-993.50025 1.0

```

```

$-----1-----2-----3-----4-----5-----6-----7-----8
$
$-----1-----2-----3-----4-----5-----6-----7-----8

```

```

*DEFINE_CURVE
$HMNAME CURVES 1LoadCurve_1
$HWCOLOR CURVES 1 3
$HMCURVE 2 2 LoadCurve1
1 0 0.02 1.0 0.0 0.0 0
0.0 0.0
0.2632 0.005
0.5263 0.015

```

	0.7895			0.035			
	1.0526			0.055			
	1.3158			0.09			
	1.5789			0.133			
	1.8421			0.195			
	2.1053			0.275			
	2.3684			0.37			
	2.6316			0.475			
	2.8947			0.59			
	3.1579			0.7			
	3.4211			0.81			
	3.6842			0.905			
	3.9474			0.96			
	4.2105			0.985			
	4.4737			0.995			
	4.7368			0.999			
	5.0			1.0			
	100.0			1.0			
*DEFINE_CURVE							
\$HMNAME	CURVES		2	LoadCurve_2			
\$HWCOLOR	CURVES		2	4			
\$HMCURVE		3	3	LoadCurve2			
		2	0	1.0	15000.0	0.0	0.0
			0.0		1.0		
			2.0		1.0		
*DEFINE_CURVE							
\$HMNAME	CURVES		3	LoadCurve_3			
\$HWCOLOR	CURVES		3	3			
\$HMCURVE		1	1	LoadCurve3			
		3	0	1.0	1.0	0.0	0.0
			0.0		35.0		
			0.35		35.0		
			0.36		39.0		
			10.0		39.0		
*DEFINE_CURVE							
\$HMNAME	CURVES		4	curve1			
\$HWCOLOR	CURVES		4	3			
\$HMCURVE		1	2	curve1			
		4	0	1.0	1.0		
			0.0		0.0		
			0.06		24.0		
			0.07		26.0		
			0.08		27.3		
			0.09		28.2		
			0.1		28.85		
			0.12		29.75		
			0.14		30.3		
			0.15		30.5		
			2.0		400.0		
*DEFINE_CURVE							
\$HMNAME	CURVES		5	curve2			
\$HWCOLOR	CURVES		5	3			
\$HMCURVE		1	3	curve2			
		5	0	0.01	1.0		
			0.0		0.0		
			0.2632		0.005		
			0.5263		0.015		
			0.7895		0.035		
			1.0526		0.055		
			1.3158		0.09		
			1.5789		0.133		
			1.8421		0.195		
			2.1053		0.275		
			2.3684		0.37		
			2.6316		0.475		
			2.8947		0.59		
			3.1579		0.7		
			3.4211		0.81		
			3.6842		0.905		
			3.9474		0.96		
			4.2105		0.985		

```

4.4737          0.995
4.7368          0.999
5.0             1.0
200.0           1.0
*DEFINE_CURVE
$HMNAME CURVES      6LoadCurve_6
$HWCOLOR CURVES      6      3
$HMCURVE 1      1 LoadCurve6
6      0      0.6      1.0      0.0      0.0      0
0.0      0.0
0.05632      0.005
0.08263      0.015
0.10895      0.035
0.13526      0.055
0.16158      0.09
0.18789      0.133
0.21421      0.195
0.24053      0.275
0.26684      0.37
0.29316      0.475
0.31947      0.59
0.34579      0.7
0.37211      0.81
0.39842      0.905
0.42474      0.96
0.45105      0.985
0.47737      0.995
0.50368      0.999
0.5      1.0
2.0      1.0

```



## E.6 Partial Input File Used for Two-piece wheel Traveling and Steering Simulation

```

*TITLE
Tire 18.00-33 - Rim 33-13.00/2.5- 2 piece rim-5mph
$-----1-----2-----3-----4-----5-----6-----7-----8
$                               CONTROL CARDS                               $
$-----1-----2-----3-----4-----5-----6-----7-----8
*CONTROL_TERMINATION
$$  ENDTIM      ENDCYC      DTMIN      ENDENG      ENDMAS
    1.65
*CONTROL_TIMESTEP
$$  DTINIT      TSSFAC      ISDO      TSLIMIT      DT2MS      LCTM      ERODE      MSIST
    0.0          0.67                -2.000E-06
*CONTROL_HOURLASS
$$  IHQ         QH
    6
*CONTROL_SOLID
$$  ESORT      FMATRX      NIPTETS      SWLOCL
    1           1
$$  PM1        PM2        PM3        PM4        PM5        PM6        PM7        PM8        PM9        PM10
*CONTROL_BULK_VISCOSITY
$$  Q1         Q2         IBQ
    1.5         0.06        -2
*CONTROL_CONTACT
$$  SLSFAC     RWPNAL     ISLCHK     SHLTHK     PENOPT     THKCHG     ORIEN     ENMASS
    1
$$  USRSTR     USRFRC     NSBCS     INTERM     XPENE     SSTHK     ECDT     TIEDPRJ
    1
*CONTROL_ENERGY
$$  HGEN      RWEN      SLNTEN     RYLEN
    2          2          2
*CONTROL_ACCURACY
$$  OSU       INN       PIDOSU
    1          2
*DAMPING_GLOBAL
$$  LCID      VALDMP     STX        STR        STZ        SRX        SRY        SRZ
    3
$-----1-----2-----3-----4-----5-----6-----7-----8
$                               MATERIAL CARDS                               $
$-----1-----2-----3-----4-----5-----6-----7-----8
*MAT_ELASTIC
$HMNAME MATS      1Elastic steel
    17.8000E-09   210000.0   0.28
*MAT_ELASTIC
$HMNAME MATS      2Tire-Chafer-300
    27.1900E-10   300.0      0.33
*MAT_ELASTIC
$HMNAME MATS      3Tire-bead-1000
    37.1900E-10   1000.0     0.33
*MAT_ELASTIC
$HMNAME MATS      4Tire-Apex-100
    47.1900E-10   100.0      0.33
*MAT_ELASTIC
$HMNAME MATS      5Tire-Liner-210
    57.1900E-10   210.0      0.33
*MAT_ELASTIC
$HMNAME MATS      6Tire-Sidewall-10
    67.1900E-10   10.0       0.33
*MAT_ELASTIC
$HMNAME MATS      7Tire-Shoulder-9
    77.1900E-10   9.0        0.33
*MAT_ELASTIC
$HMNAME MATS      8Tire-Sidetread-15
    87.1900E-10   15.0       0.33
*MAT_ELASTIC
$HMNAME MATS      9Tire-undertread-4
    97.1900E-10   4.0        0.33

```

```

*MAT_ELASTIC
$HMNAME MATS      10Tire-tread-40
    107.1900E-10    40.0    0.33
*MAT_ELASTIC
$HMNAME MATS      11Elastic steel.1
    117.8000E-09   210000.0    0.28
*MAT_ELASTIC
$HMNAME MATS      12Tire-Chafer-300.2
    127.1900E-10    300.0    0.33
*MAT_ELASTIC
$HMNAME MATS      13Tire-bead-1000.3
    137.1900E-10   1000.0    0.33
*MAT_ELASTIC
$HMNAME MATS      14Tire-Apex-100.4
    147.1900E-10    100.0    0.33
*MAT_ELASTIC
$HMNAME MATS      15Tire-Liner-210.5
    157.1900E-10   210.0    0.33
*MAT_ELASTIC
$HMNAME MATS      16Tire-Sidewall-10.6
    167.1900E-10    10.0    0.33
*MAT_ELASTIC
$HMNAME MATS      17Tire-Shoulder-9.7
    177.1900E-10     9.0    0.33
*MAT_ELASTIC
$HMNAME MATS      18Tire-Sidetread-15.8
    187.1900E-10    15.0    0.33
*MAT_ELASTIC
$HMNAME MATS      19Tire-undertread-4.9
    197.1900E-10     4.0    0.33
*MAT_ELASTIC
$HMNAME MATS      20Tire-tread-40.10
    207.1900E-10    40.0    0.33
*MAT_ELASTIC
$HMNAME MATS      30Elastic steel.2
    307.8000E-09   210000.0    0.28
*MAT_ELASTIC
$HMNAME MATS      31Tire-Chafer-300.3
    317.1900E-10    300.0    0.33
*MAT_ELASTIC
$HMNAME MATS      32Tire-bead-1000.4
    327.1900E-10   1000.0    0.33
*MAT_ELASTIC
$HMNAME MATS      33Tire-Apex-100.5
    337.1900E-10    100.0    0.33
*MAT_ELASTIC
$HMNAME MATS      34Tire-Liner-210.6
    347.1900E-10   210.0    0.33
*MAT_ELASTIC
$HMNAME MATS      35Tire-Sidewall-10.7
    357.1900E-10    10.0    0.33
*MAT_ELASTIC
$HMNAME MATS      36Tire-Shoulder-9.8
    367.1900E-10     9.0    0.33
*MAT_ELASTIC
$HMNAME MATS      37Tire-Sidetread-15.9
    377.1900E-10    15.0    0.33
*MAT_ELASTIC
$HMNAME MATS      38Tire-undertread-4.10
    387.1900E-10     4.0    0.33
*MAT_ELASTIC
$HMNAME MATS      39Tire-tread-40.11
    397.1900E-10    40.0    0.33
*MAT_ELASTIC
$HMNAME MATS      40Elastic steel.1.12
    407.8000E-09   210000.0    0.28
*MAT_ELASTIC
$HMNAME MATS      41Tire-Chafer-300.2.13
    417.1900E-10    300.0    0.33
*MAT_ELASTIC
$HMNAME MATS      42Tire-bead-1000.3.14

```

```

427.1900E-10 1000.0 0.33
*MAT_ELASTIC
$HMNAME MATS 43Tire-Apex-100.4.15
437.1900E-10 100.0 0.33
*MAT_ELASTIC
$HMNAME MATS 44Tire-Liner-210.5.16
447.1900E-10 210.0 0.33
*MAT_ELASTIC
$HMNAME MATS 45Tire-Sidewall-10.6.17
457.1900E-10 10.0 0.33
*MAT_ELASTIC
$HMNAME MATS 46Tire-Shoulder-9.7.18
467.1900E-10 9.0 0.33
*MAT_ELASTIC
$HMNAME MATS 47Tire-Sidetread-15.8.19
477.1900E-10 15.0 0.33
*MAT_ELASTIC
$HMNAME MATS 48Tire-undertread-4.9.20
487.1900E-10 4.0 0.33
*MAT_ELASTIC
$HMNAME MATS 49Tire-tread-40.10.21
497.1900E-10 40.0 0.33
*MAT_RIGID
$HMNAME MATS 21Rigid Rim base mounting ring
217.8000E-09 210000.0 0.28
0.0
0
*MAT_RIGID
$HMNAME MATS 22Rigid Rim base mounting ring.11
227.8000E-09 210000.0 0.28
0.0
0
*MAT_RIGID
$HMNAME MATS 23Rigid AXle
237.8000E-09 210000.0 0.28
-1.0 1 100100
0
*MAT_RIGID
$HMNAME MATS 50Rigid Rim base mounting ring.22
507.8000E-09 210000.0 0.28
0.0
0
*MAT_RIGID
$HMNAME MATS 51Rigid Rim base mounting ring.11.23
517.8000E-09 210000.0 0.28
0.0
0
*MAT_RIGID
$HMNAME MATS 52Rigid AXle.24
527.8000E-09 210000.0 0.28
-1.0 1 100100
0
*MAT_CABLE_DISCRETE_BEAM
$HMNAME MATS 24Tire-beam-20000
247.8000E-09 20000.0 50.0 0
*MAT_CABLE_DISCRETE_BEAM
$HMNAME MATS 25Bead-beam
257.8000E-09 2000000.0 50.0 0
*MAT_CABLE_DISCRETE_BEAM
$HMNAME MATS 26Chafer-beam
267.8000E-09 1000000.0 50.0 0
*MAT_CABLE_DISCRETE_BEAM
$HMNAME MATS 27Tire-beam-20000.12
277.8000E-09 20000.0 50.0 0
*MAT_CABLE_DISCRETE_BEAM
$HMNAME MATS 28Bead-beam.13
287.8000E-09 2000000.0 50.0 0
*MAT_CABLE_DISCRETE_BEAM
$HMNAME MATS 29Chafer-beam.14
297.8000E-09 1000000.0 50.0 0
*MAT_CABLE_DISCRETE_BEAM

```

```

$HMNAME MATS      53Tire-beam-20000.25
537.8000E-09 20000.0          50.0          0
*MAT_CABLE_DISCRETE_BEAM
$HMNAME MATS      54Bead-beam.26
547.8000E-09 2000000.0        50.0          0
*MAT_CABLE_DISCRETE_BEAM
$HMNAME MATS      55Chafer-beam.27
557.8000E-09 1000000.0        50.0          0
*MAT_CABLE_DISCRETE_BEAM
$HMNAME MATS      56Tire-beam-20000.12.28
567.8000E-09 20000.0          50.0          0
*MAT_CABLE_DISCRETE_BEAM
$HMNAME MATS      57Bead-beam.13.29
577.8000E-09 2000000.0        50.0          0
*MAT_CABLE_DISCRETE_BEAM
$HMNAME MATS      58Chafer-beam.14.30
587.8000E-09 1000000.0        50.0          0
$-----1-----2-----3-----4-----5-----6-----7-----8
$              SECTION CARDS              $
$-----1-----2-----3-----4-----5-----6-----7-----8
*SECTION_BEAM
$HMNAME PROPS      1Bolt beam
1 2 0.0 1.0
506.707 0.0243 0.0243 0.00405
$HMNAME PROPS      2Discrete cable Beam
2 6 1.0 2.0 1.0 0.0
100.0 7.8 3.14 0.0 0.0 1.0 0.0
$HMNAME PROPS      3Bolt beam.1
3 2 0.0 1.0
506.707 0.0243 0.0243 0.00405
$HMNAME PROPS      4Discrete cable Beam.2
4 6 1.0 2.0 1.0 0.0
100.0 7.8 3.14 0.0 0.0 1.0 0.0
$HMNAME PROPS      10Bolt beam.2
10 2 0.0 1.0
506.707 0.0243 0.0243 0.00405
$HMNAME PROPS      11Discrete cable Beam.3
11 6 1.0 2.0 1.0 0.0
100.0 7.8 3.14 0.0 0.0 1.0 0.0
$HMNAME PROPS      12Bolt beam.1.4
12 2 0.0 1.0
506.707 0.0243 0.0243 0.00405
$HMNAME PROPS      13Discrete cable Beam.2.5
13 6 1.0 2.0 1.0 0.0
100.0 7.8 3.14 0.0 0.0 1.0 0.0
*SECTION_SHELL
$HMNAME PROPS      5Shell-0.01mm
5 0 0.832 3 0.0
0.01 0.01 0.01 0.01
*SECTION_SHELL
$HMNAME PROPS      6Shell-0.01mm.3
6 0 0.832 3 0.0
0.01 0.01 0.01 0.01
*SECTION_SHELL
$HMNAME PROPS      14Shell-0.01mm.6
14 0 0.832 3 0.0
0.01 0.01 0.01 0.01
*SECTION_SHELL
$HMNAME PROPS      15Shell-0.01mm.3.7
15 0 0.832 3 0.0
0.01 0.01 0.01 0.01
*SECTION_SOLID
$HMNAME PROPS      7Solid
7 1
$HMNAME PROPS      8Solid.4
8 1
$HMNAME PROPS      9Solid.1
9 1
$HMNAME PROPS      16Solid.8
16 1
$HMNAME PROPS      17Solid.4.9
17 1

```

```

17      1
$HMNAME PROPS      18Solid.1.10
18      1
*HOURGLASS
$HMNAME PROPS      10Solid Hourglass control
10      4      0.1
$HMNAME PROPS      11Solid Hourglass control.5
11      4      0.1
$HMNAME PROPS      12Solid Hourglass control.11
12      4      0.1
$HMNAME PROPS      13Solid Hourglass control.5.12
13      4      0.1
$HMNAME PROPS      19Tire hourglass
19      5      1.0
$-----1-----2-----3-----4-----5-----6-----7-----8
$              CONTACT CARDS              $
$-----1-----2-----3-----4-----5-----6-----7-----8
*CONTACT_SURFACE_TO_SURFACE_ID
$HMNAME GROUPS      1Rim1 End-Rim2 End
$HWCOLOR GROUPS      1      29
1Rim1 End-Rim2 End
2      1      0      0      1      1
0.35      0.25      1.0      300.0      200.0
1.0      1.0
0

1      1
*CONTACT_SURFACE_TO_SURFACE_ID
$HMNAME GROUPS      2Rim1-Rim2
$HWCOLOR GROUPS      2      29
2Rim1-Rim2
4      3      0      0      1      1
0.35      0.25      1.0      300.0      200.0
1.0      1.0
0

1      1
*CONTACT_SURFACE_TO_SURFACE_ID
$HMNAME GROUPS      3Front rim-Bead
$HWCOLOR GROUPS      3      29
3Front rim-Bead
5      9      0      0      1      1
0.95      0.9      1.0      5.0      20.0

1      1
*CONTACT_SURFACE_TO_SURFACE_ID
$HMNAME GROUPS      4Back rim - Rear Bead
$HWCOLOR GROUPS      4      29
4Back rim - Rear Bead
7      10      0      0      1      1
0.95      0.9      1.0      5.0      20.0

1      1
*CONTACT_SURFACE_TO_SURFACE_ID
$HMNAME GROUPS      5Front rim - Chafer
$HWCOLOR GROUPS      5      29
5Front Rim - Chafer
6      11      0      0      1      1
0.95      0.9      1.0      5.0      20.0
10.0      10.0
0

1      1
*CONTACT_SURFACE_TO_SURFACE_ID
$HMNAME GROUPS      6Back Rim - Chafer
$HWCOLOR GROUPS      6      29
6Back Rim - Chafer

```

8	12	0	0			1	1
0.95	0.9	1.0	5.0	20.0			
10.0	10.0						
0							
1	1						
*CONTACT_SURFACE_TO_SURFACE_ID							
\$HMNAME	GROUPS	18	Back Rim - Chafer.6				
\$HWCOLOR	GROUPS	18	29				
18Back Rim - Chafer							
21	25	0	0			1	1
0.95	0.9	1.0	5.0	20.0			
10.0	10.0						
0							
1	1						
*CONTACT_SURFACE_TO_SURFACE_ID							
\$HMNAME	GROUPS	17	Front rim - Chafer.5				
\$HWCOLOR	GROUPS	17	29				
17Front Rim - Chafer							
19	24	0	0			1	1
0.95	0.9	1.0	5.0	20.0			
10.0	10.0						
0							
1	1						
*CONTACT_SURFACE_TO_SURFACE_ID							
\$HMNAME	GROUPS	16	Back rim - Rear Bead.4				
\$HWCOLOR	GROUPS	16	29				
16Back rim - Rear Bead							
20	23	0	0			1	1
0.95	0.9	1.0	5.0	20.0			
10.0	10.0						
0							
1	1						
*CONTACT_SURFACE_TO_SURFACE_ID							
\$HMNAME	GROUPS	15	Front rim-Bead.3				
\$HWCOLOR	GROUPS	15	29				
15Front rim-Bead							
18	22	0	0			1	1
0.95	0.9	1.0	5.0	20.0			
10.0	10.0						
0							
1	1						
*CONTACT_SURFACE_TO_SURFACE_ID							
\$HMNAME	GROUPS	14	Rim1-Rim2.2				
\$HWCOLOR	GROUPS	14	29				
14Rim1-Rim2							
17	16	0	0			1	1
0.35	0.25	1.0	300.0	200.0			
1.0	1.0						
0							
1	1						
*CONTACT_SURFACE_TO_SURFACE_ID							
\$HMNAME	GROUPS	13	Rim1 End-Rim2 End.1				
\$HWCOLOR	GROUPS	13	29				
13Rim1 End-Rim2 End							
15	14	0	0			1	1
0.35	0.25	1.0	300.0	200.0			
1.0	1.0						
0							
1	1						
*CONTACT_AUTOMATIC_GENERAL_ID							
\$HMNAME	GROUPS	19	Beam contacts.7				
\$HWCOLOR	GROUPS	19	29				
19Beam contacts							
89		2				1	1

```

0
1 1
*CONTACT_AUTOMATIC_GENERAL_ID
$HMNAME GROUPS 7Beam contacts
$HWCOLOR GROUPS 7 29
7Beam contacts
43 2 1 1

0
1 1
*CONSTRAINED_EXTRA_NODES_SET
$HMNAME GROUPS 22Back Joint
$HWCOLOR GROUPS 22 29
31 45
*SET_NODE_LIST
$HMSET
$HMNAME SETS 45Back joint
45 0.0 0.0 0.0 0.0
534877 534880
*CONSTRAINED_EXTRA_NODES_SET
$HMNAME GROUPS 21Front Joint
$HWCOLOR GROUPS 21 29
8 44
*SET_NODE_LIST
$HMSET
$HMNAME SETS 44Front joint
44 0.0 0.0 0.0 0.0
534876 534882
*CONSTRAINED_EXTRA_NODES_SET
$HMNAME GROUPS 23Axle
$HWCOLOR GROUPS 23 29
21 46
*SET_NODE_LIST
$HMSET
$HMNAME SETS 46Axle joint
46 0.0 0.0 0.0 0.0
534878 534879 534881 534883
*RIGIDWALL_PLANAR_ID
$HMNAME GROUPS 8Ground
$HWCOLOR GROUPS 8 3
8
41
81.994-4.243E-05-927.02024 81.994-4.243E-05-926.02024 0.65
*RIGIDWALL_PLANAR_ID
$HMNAME GROUPS 20Ground.9
$HWCOLOR GROUPS 20 3
20
87
81.994-4.243E-05-927.02024 81.994-4.243E-05-926.02024 0.65
*CONSTRAINED_NODAL_RIGID_BODY
$HMNAME COMPS 24Mounting disc-1.1
$HWCOLOR COMPS 24 54
47 0 0 0
*SET_NODE_LIST
$HMSET
$HMNAME SETS 47rigid719909nodeset.1
47 0.0 0.0 0.0 0.0
861810 612593 612594 612595 612596 612597 612598 612599
$-----1-----2-----3-----4-----5-----6-----7-----8
$ LOAD AND BOUNDARY CARDS $
$-----1-----2-----3-----4-----5-----6-----7-----8
*LOAD_BODY_Z
$HMNAME LOADCOLS 7LoadBody_7
$HWCOLOR LOADCOLS 7 3
2 9810.0
*BOUNDARY_PRESCRIBED_MOTION_RIGID_LOCAL

```

```

$HMNAME LOADCOLS      1Constrained x movement-local
$HWCOLOR LOADCOLS    1      20
      21      1      2      15      0.0      0
*BOUNDARY_PRESCRIBED_MOTION_RIGID
$HMNAME LOADCOLS      2Moving 5mile/hour
$HWCOLOR LOADCOLS    2      3
      21      2      0      15      2235.0      0      0.55
*BOUNDARY_PRESCRIBED_MOTION_RIGID
$HMNAME LOADCOLS      3Turn 90 degree/second
$HWCOLOR LOADCOLS    3      20
      21      7      0      30      3.142      0      0.9
*LOAD_SEGMENT_SET
$HMNAME LOADCOLS      4Tire-pressure-145PSI-10Bar-1.0MPa
$HWCOLOR LOADCOLS    4      5
      13      1      1.0
$HMNAME LOADCOLS      5Tire-pressure-145PSI-10Bar-1.0MPa.1
$HWCOLOR LOADCOLS    5      5
      26      16      1.0
*SET_SEGMENT
$HMNAME CSURFS      1Rim-1-end
$HWCOLOR CSURFS    1      6
      1
      2179      1754      180632      180632
*LOAD_NODE_POINT
$HMNAME LOADCOLS      6Force 527778N
$HWCOLOR LOADCOLS    6      8
      532871      3      14      -527778.0      0
$-----1-----2-----3-----4-----5-----6-----7-----8
$                                     DEFINE CURVE CARDS                                     $
$-----1-----2-----3-----4-----5-----6-----7-----8
*DEFINE_CURVE
$HMNAME CURVES      1Pressure load
$HWCOLOR CURVES    1      3
$HMCURVE      1      2 curve1
      1      0      1.0      1.0
      0.0      0.0
      0.1      1.0
      3.0      1.0
*DEFINE_CURVE
$HMNAME CURVES      2Gravity
$HWCOLOR CURVES    2      4
$HMCURVE      1      3 curve1
      2      0      1.0      1.0
      0.0      0.0
      0.05      1.0
      3.0      1.0
*DEFINE_CURVE
$HMNAME CURVES      3Global damping-39-71
$HWCOLOR CURVES    3      5
$HMCURVE      1      1 curve1
      3      0      1.0      1.0
      0.0      39.0
      0.2      39.0
      0.201      71.0
      3.0      71.0
*DEFINE_CURVE
$HMNAME CURVES      4Force curve
$HWCOLOR CURVES    4      6
$HMCURVE      1      2 curve1
      4      0      1.0      1.0
      0.0      0.0
      0.2      0.0
      0.3      1.0
      3.0      1.0
*DEFINE_CURVE
$HMNAME CURVES      5Rotation + Turn
$HWCOLOR CURVES    5      7
$HMCURVE      1      3 curve1
      5      0      1.0      1.0
      0.0      0.0
      0.2      1.0

```



```

3.0                                1.0
*DEFINE_CURVE
$HMNAME CURVES                    6Pressure load.1
$HWCOLOR CURVES                    6      3
$HMCURVE 1 2 curve1
6      0      1.0      1.0
0.0      0.0
0.1      1.0
3.0      1.0

*DEFINE_CURVE
$HMNAME CURVES                    7Gravity.2
$HWCOLOR CURVES                    7      4
$HMCURVE 1 3 curve1
7      0      1.0      1.0
0.0      0.0
0.05      1.0
3.0      1.0

*DEFINE_CURVE
$HMNAME CURVES                    8Global damping-39-71.3
$HWCOLOR CURVES                    8      5
$HMCURVE 1 1 curve1
8      0      1.0      1.0
0.0      39.0
0.2      39.0
0.201      71.0
3.0      71.0

*DEFINE_CURVE
$HMNAME CURVES                    9Force curve.4
$HWCOLOR CURVES                    9      6
$HMCURVE 1 2 curve1
9      0      1.0      1.0
0.0      0.0
0.2      0.0
0.3      1.0
3.0      1.0

*DEFINE_CURVE
$HMNAME CURVES                   10Rotation + Turn.5
$HWCOLOR CURVES                   10      7
$HMCURVE 1 3 curve1
10     0      1.0      1.0
0.0      0.0
0.2      1.0
3.0      1.0

*DEFINE_CURVE
$HMNAME CURVES                   11Pressure load.2
$HWCOLOR CURVES                   11      3
$HMCURVE 1 2 curve1
11     0      1.0      1.0
0.0      0.0
0.1      1.0
3.0      1.0

*DEFINE_CURVE
$HMNAME CURVES                   12Gravity.3
$HWCOLOR CURVES                   12      4
$HMCURVE 1 3 curve1
12     0      1.0      1.0
0.0      0.0
0.05      1.0
3.0      1.0

*DEFINE_CURVE
$HMNAME CURVES                   13Global damping-39-71.4
$HWCOLOR CURVES                   13      5
$HMCURVE 1 1 curve1
13     0      1.0      1.0
0.0      39.0
0.2      39.0
0.201      71.0
3.0      71.0

*DEFINE_CURVE
$HMNAME CURVES                   14Force curve.5
$HWCOLOR CURVES                   14      6

```

```

$HMCURVE      1      2 curve1
              14      0      1.0      1.0
                    0.0      0.0
                    0.25     0.0
                    0.35     1.0
                    3.0      1.0

*DEFINE_CURVE
$HMNAME CURVES      15Rotation + Turn.6
$HWCOLOR CURVES      15      7
$HMCURVE      1      3 curve1
              15      0      1.0      1.0
                    0.0      0.0
                    0.2      1.0
                    3.0      1.0

*DEFINE_CURVE
$HMNAME CURVES      16Pressure load.3
$HWCOLOR CURVES      16      3
$HMCURVE      1      2 curve1
              16      0      1.0      1.0
                    0.0      0.0
                    0.1      1.0
                    3.0      1.0

*DEFINE_CURVE
$HMNAME CURVES      17Gravity.4
$HWCOLOR CURVES      17      4
$HMCURVE      1      3 curve1
              17      0      1.0      1.0
                    0.0      0.0
                    0.05     1.0
                    3.0      1.0

*DEFINE_CURVE
$HMNAME CURVES      18Global damping-39-71.5
$HWCOLOR CURVES      18      5
$HMCURVE      1      1 curve1
              18      0      1.0      1.0
                    0.0      39.0
                    0.2      39.0
                    0.201    71.0
                    3.0      71.0

*DEFINE_CURVE
$HMNAME CURVES      19Force curve.6
$HWCOLOR CURVES      19      6
$HMCURVE      1      2 curve1
              19      0      1.0      1.0
                    0.0      0.0
                    0.2      0.0
                    0.3      1.0
                    3.0      1.0

*DEFINE_CURVE
$HMNAME CURVES      20Rotation + Turn.7
$HWCOLOR CURVES      20      7
$HMCURVE      1      3 curve1
              20      0      1.0      1.0
                    0.0      0.0
                    0.2      1.0
                    3.0      1.0

*DEFINE_CURVE
$HMNAME CURVES      21Pressure load.1.8
$HWCOLOR CURVES      21      3
$HMCURVE      1      2 curve1
              21      0      1.0      1.0
                    0.0      0.0
                    0.1      1.0
                    3.0      1.0

*DEFINE_CURVE
$HMNAME CURVES      22Gravity.2.9
$HWCOLOR CURVES      22      4
$HMCURVE      1      3 curve1
              22      0      1.0      1.0
                    0.0      0.0
                    0.05     1.0

```

```

3.0          1.0
*DEFINE_CURVE
$HMNAME CURVES      23Global damping-39-71.3.10
$HWCOLOR CURVES    23      5
$HMCURVE  1      1 curve1
23          0      1.0      1.0
          0.0      39.0
          0.2      39.0
          0.201    71.0
          3.0      71.0

*DEFINE_CURVE
$HMNAME CURVES      24Force curve.4.11
$HWCOLOR CURVES    24      6
$HMCURVE  1      2 curve1
24          0      1.0      1.0
          0.0      0.0
          0.2      0.0
          0.3      1.0
          3.0      1.0

*DEFINE_CURVE
$HMNAME CURVES      25Rotation + Turn.5.12
$HWCOLOR CURVES    25      7
$HMCURVE  1      3 curve1
25          0      1.0      1.0
          0.0      0.0
          0.2      1.0
          3.0      1.0

*DEFINE_CURVE
$HMNAME CURVES      26Pressure load.2.13
$HWCOLOR CURVES    26      3
$HMCURVE  1      2 curve1
26          0      1.0      1.0
          0.0      0.0
          0.1      1.0
          3.0      1.0

*DEFINE_CURVE
$HMNAME CURVES      27Gravity.3.14
$HWCOLOR CURVES    27      4
$HMCURVE  1      3 curve1
27          0      1.0      1.0
          0.0      0.0
          0.05     1.0
          3.0      1.0

*DEFINE_CURVE
$HMNAME CURVES      28Global damping-39-71.4.15
$HWCOLOR CURVES    28      5
$HMCURVE  1      1 curve1
28          0      1.0      1.0
          0.0      39.0
          0.2      39.0
          0.201    71.0
          3.0      71.0

*DEFINE_CURVE
$HMNAME CURVES      29Force curve.5.16
$HWCOLOR CURVES    29      6
$HMCURVE  1      2 curve1
29          0      1.0      1.0
          0.0      0.0
          0.25     0.0
          0.35     1.0
          3.0      1.0

*DEFINE_CURVE
$HMNAME CURVES      30Rotation + Turn.6.17
$HWCOLOR CURVES    30      7
$HMCURVE  1      3 curve1
30          0      1.0      1.0
          0.0      0.0
          0.2      1.0
          0.5      1.0
          0.6      0.0
          3.0      0.0

```

## Appendix F: Copyright Permissions

### Copyright permission for reference [5]

On Mon, Sep 30, 2013 at 11:58 AM, Brent Tarini <[brenttarini@nsiw.com](mailto:brenttarini@nsiw.com)> wrote:  
Hi Weldon, not an issue for you to use the pictures below in your dissertation.

Take care Weldon

Thanks,  
Brent

Sent from my BlackBerry

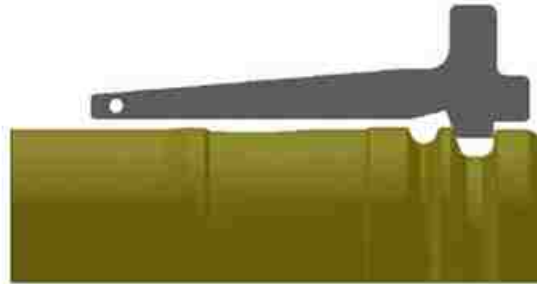
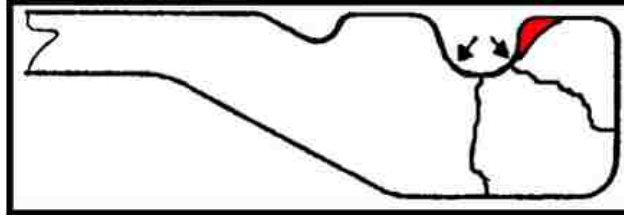
---

**From:** Weldon Li [<mailto:weldonli@gmail.com>]  
**Sent:** Monday, September 30, 2013 09:41 AM  
**To:** Brent Tarini  
**Subject:** permission requested for using the pictures

Hello, Brent,

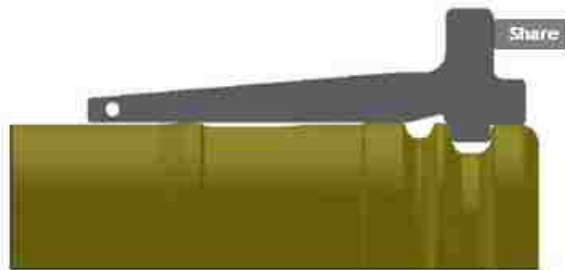
I am completing a doctoral dissertation at the University of Windsor entitled "Mechanical Analysis of Heavy-duty Mining Vehicle Wheels to Enhance Safety." I would like your permission to include in my dissertation the following pictures in your presentation at the TAC meeting at Sault Ste Marie in June 2010:





**GO**

DETAIL A  
SCALE 1 : 2



**NO-GO**

DETAIL B  
SCALE 1 : 2



**GO**

DETAIL E  
SCALE 1 : 3



**NO-GO**

DETAIL F  
SCALE 1 : 3

My dissertation will be deposited to the University of Windsor Leddy library.

[or]

My dissertation will be deposited to the University of Windsor's online theses and dissertations repository (<http://winspace.uwindsor.ca>) and will be available in full-text on the internet for reference, study and / or copy.

I will also be granting Library and Archives Canada and ProQuest/UMI a non-exclusive license to reproduce, loan, distribute, or sell single copies of my thesis by any means and in any form or format. These rights will in no way restrict republication of the material in any other form by you or by others authorized by you.

Please confirm in writing or by email that these arrangements meet with your approval.

Thank you very much for your attention to this matter.

—

Best Regards

Weldon Li

## Copyright permission for reference [7]

On Tue, Jan 21, 2014 at 6:01 AM, Limited\_agreements <[Limited\\_agreements@cat.com](mailto:Limited_agreements@cat.com)> wrote:  
Hi Zhanbiao,

I had an internal discussion regarding your concern and we have come to a conclusion that the term period only applies to the period in which you are allowed to print new copies of the dissertation. Existing copies do not need to be destroyed after the expiration date. In the event you want to re-print or re-produce new copies of the dissertation prior to the expiration date, you will need to apply again for the renewal agreement.

I hope this helps.

Best regards,  
Uttara

-----Zhanbiao Li <[li12c@uwindsor.ca](mailto:li12c@uwindsor.ca)> wrote: -----

To: Limited\_agreements <[Limited\\_agreements@cat.com](mailto:Limited_agreements@cat.com)>  
From: Zhanbiao Li <[li12c@uwindsor.ca](mailto:li12c@uwindsor.ca)>  
Date: 01/13/2014 06:00PM  
Subject: Re: Zhanbiao Li\_Limited Copyright Approval Agreement\_1.9.2014

Hello Uttara,

I am very appreciative of your help.

My concern is that the 'time period' is not suitable for me since one copy of my dissertation will be stored in the library of University of Windsor for many years (at least over 50 years), some copies will be kept by other related agents and myself. Based on the requirement in the limited agreement, I have to destroy my dissertation after December 24, 2016. It is impossible for me to destroy them. I am wondering if the "time period" can be removed from the limited agreements.

Thanks

Zhanbiao Li

On Mon, Jan 13, 2014 at 1:50 AM, Limited\_agreements <[Limited\\_agreements@cat.com](mailto:Limited_agreements@cat.com)> wrote:

Hi Zhanbiao,

Please find attached the fully executed copy of the Limited Copyright Agreement in relation to the article which you intend to use in your doctoral dissertation at the University of Windsor.

Best Regards,  
Uttara



**Limited\_agreements**

Jan 22 (1 day ago) ☆



to me ▾

Hi Zhanbiao,

As stated earlier by me, the time period stated on the agreement is only a time period provided for printing new copies of the dissertation; i.e. in the three year term granted to you, you may go ahead and print copies of the dissertation. However, there is no time limit for destruction of existing copies upon expiry of the term provided in the agreement. Hence, we need not make any revisions to the agreement provided to you.

Let me know in case of any further concern.

Best regards,  
Uttara

**LIMITED COPYRIGHT APPROVAL**

Grantor: Caterpillar Inc.	Requestor: Zhanbiao Li
Address: 100 NE Adams	Contact: Zhanbiao Li
Phone: (309) 675-4867	Address: 1743 Mayrand Crescent
Fax: (309) 675-1711	Tecumseh, Ontario N8N 4R4
	Canada
	Phone: 011 1 519 253 3000
	E-mail: <a href="mailto:li12c@uwindsor.ca">li12c@uwindsor.ca</a>

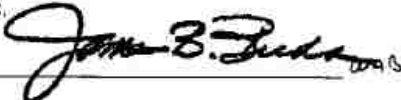
Definitions

1. "Consent" means: Grantor's written approval of Requestor's Work(s) in response to Requestor's Submission
2. "Licensed Right(s)" means: Copyright in the Licensed Work(s)
3. "Licensed Work(s)" means: The work(s) referenced or set out in Exhibit A
4. "Requestor's Work(s)" means: The work(s) referenced or set out in Exhibit B, which works incorporate or are based on the Licensed Work(s)
5. "Recipient(s)" means: Visitors of online thesis and dissertations repository of University of Windsor at <http://winspace.uwindsor.ca>
6. "Purpose" means: Illustration of the difference between the OTR wheels and normal wheels in the doctoral dissertation entitled "Mechanical Analysis of Heavy-duty Mining Vehicle Wheels to Enhance Safety," at University of Windsor.
7. "Submission" means: Transmittal of one (1) copy of Requestor's Work(s) to Grantor
8. "Time Period" means: December 25, 2013 to December 24, 2016

Grantor grants Requestor a non-exclusive, personal, and nontransferable right and license to make and, subject to receiving Consent, distribute Requestor's Work(s) to Recipient(s) for the Purpose during the Time Period. Requestor will mark each Requestor's Work(s) as follows:

"Reprinted Courtesy of Caterpillar Inc."

Requestor will only distribute copies of the Requestor's Work(s) for which Consent has been granted as provided hereinabove. Requestor will cease use of the Requestor's Work and the Licensed Work upon expiration of the Time Period and will certify, upon Grantor's request, that such use has ceased and that Requestor has destroyed any media or files containing the Licensed Work. No other right or license is granted hereunder by way of implication, estoppel or otherwise.

Caterpillar Inc.  
Signature:   
Title: Executive Vice President  
Name: James B. Buda  
Date: December 19, 2013

1102009-1



Copyright permission for reference [9]

RE: Permission requested to use the picture.



Reference x

Brown, Rodney M - MSHA [Brown.Rodney@dol.gov](mailto:Brown.Rodney@dol.gov) Sep 30  
to Zhanbiao

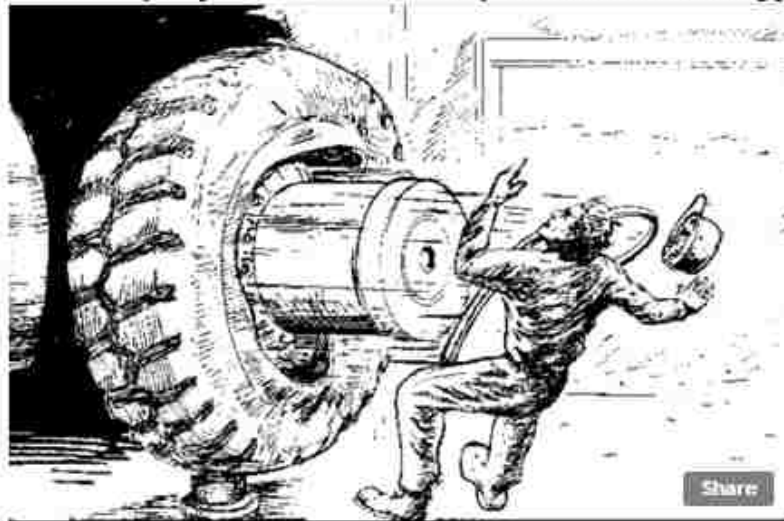
Thank you for your question. You may use the subject photograph.

**From:** Zhanbiao Li [<mailto:li12c@uwindsor.ca>]  
**Sent:** Monday, September 30, 2013 12:12 PM  
**To:** Ask MSHA  
**Subject:** Permission requested to use the picture.

September 27, 2013  
Mine Safety and Health Administration  
U.S. Department of Labor

To Whom It May Concern:

I am completing a doctoral dissertation at the University of Windsor entitled "Mechanical Analysis of Heavy-duty Mining Vehicle Wheels to Enhance Safety." I would like your permission to include in my dissertation the following picture:



This picture is located on page 36 in the PDF file titled "Tire and Rim Safety Awareness Program", revised 1996. This file can be accessed in the following link: <http://www.msha.gov/S&HINFO/IG60.PDF>

My dissertation will be deposited to the University of Windsor Leddy library.  
[or]

My dissertation will be deposited to the University of Windsor's online theses and dissertations repository (<http://winspace.uwindsor.ca>) and will be available in full-text on the internet for reference, study and / or copy.

I will also be granting Library and Archives Canada and ProQuest/UMI a non-exclusive license to reproduce, loan, distribute, or sell single copies of my thesis by any means and in any form or format. These rights will in no way restrict republication of the material in any other form by you or by others authorized by you.

Please confirm in writing or by email that these arrangements meet with your approval.

Thank you very much for your attention to this matter.

Sincerely,

Zhanbiao Li

## Copyright permission for reference [10]

On Tue, Nov 5, 2013 at 7:34 AM, Sherman, Carla D. (CDC/NIOSH/EID) <[cgs4@cdc.gov](mailto:cds4@cdc.gov)> wrote:  
Thank you for your request for information. Your recent inquiry to CDC-INFO has been copied to the National Institute for Occupational Safety and Health (NIOSH) in Cincinnati, Ohio. NIOSH, an institute within the CDC, is responsible for conducting research and making recommendations for the prevention of work-related injury and illnesses.

Publications and databases of the United States Federal Government are within the public domain, and therefore, are not generally copyrighted. However, it would be appreciated if you would cite the source for any NIOSH material that you use. Also, on occasion, our documents may contain copyrighted material. In those instances, you must obtain permission from the original source to reproduce that information.

If you need additional help, please feel free to contact me.

Carla D. Sherman  
Technical Information Specialist  
National Institute for Occupational Safety and Health  
4676 Columbia Parkway  
Cincinnati, OH 45226  
[513-533-8532](tel:513-533-8532)  
[csherman@cdc.gov](mailto:csherman@cdc.gov)

**From:** CDC-INFO Response (CDC)  
**Sent:** Wednesday, October 02, 2013 12:41 PM  
**To:** NIOSH Cincinnati EID Technical Information (CDC)  
**Subject:** RESPONSE REQUIRED: Topic: Copyright, Priority: Medium, Mode: Email [ref:\_00DU0YCBU\_500U08t]x:ref ]

Please let us know immediately if your group will provide the answer to the inquiry below or if the inquiry should be referred elsewhere (i.e., to a state or local health department, another CDC program, or other federal agency). Specific guidance on a referral and contact information would be appreciated.

This inquiry is being escalated because CDC-INFO is unable to provide information.

Programs are asked to reply within 3 business days of receipt of this escalation. If there is a delay, please let us know when to expect the answer so we can share that information with the inquirer.

Questions about this inquiry can be directed to the CDC-INFO Correspondence Team by replying to this e-mail. Please reference the inquiry number below and include the e-mail thread line in your response. The thread line is the e-mail chain including this e-mail and the original e-mail request. To include the thread line, reply to this message without deleting the historical e-mail chain.

---

Thank you.

EM

The privacy of the inquirer should be protected in any transmission or storage of this e-mail.

---

Original Email

---

From : null

To : [cdcinfo@cdc.gov](mailto:cdcinfo@cdc.gov)

Date : 2013-10-02 09:28:06

Subject : CDC-INFO: Inquiry



Subject: Permission required using pictures in Fatality reports Other:  
[othersubject] From: General Public Email Address: [weldonli@gmail.com](mailto:weldonli@gmail.com)  
Your Question: Oct 2, 2013 To Whom It May Concern: I am completing a  
doctoral dissertation at the University of Windsor entitled "Mechanical  
Analysis of Heavy-duty Mining Vehicle Wheels to Enhance Safety." I would  
like your permission to include in my dissertation the following  
pictures: Figure 4 and Figure 5 in the link:  
<http://www.cdc.gov/niosh/face/stateface/ma/07ma058.html>. Figure 1 in the  
link: <http://www.cdc.gov/niosh/face/stateface/ak/03ak006.html>, to show  
the two-piece rim structure My dissertation will be deposited to the  
University of Windsor Leddy Library. [or] My dissertation will be  
deposited to the University of Windsor's online theses and  
dissertations repository (<http://winspace.uwindsor.ca>) and will be  
available in full-text on the internet for reference, study and / or  
copy. I will also be granting Library and Archives Canada and  
ProQuest/UMI a non-exclusive license to reproduce, loan, distribute, or  
sell single copies of my thesis by any means and in any form or format.  
These rights will in no way restrict republication of the material in any  
other form by you or by others authorized by you. Please confirm in  
writing or by email that these arrangements meet with your approval.  
Thank you very much for your attention to this matter. Sincerely,  
Zhanbiao Li Optional Information Contact: [name], [title],  
[companyorganization]

Best Regards

Weldon Li



Fiore, Michael (DPH)

Oct 18 (1 day ago) ☆



to me -

Hi Zhanbiao,

Yes you have permission to use Figure 4 in MA FACE report 07MA058 in your dissertation.

Figure 5 was accessed from the OSHA web site ([www.osha.gov/Publications/wheel/wheel-chart-booklet.pdf](http://www.osha.gov/Publications/wheel/wheel-chart-booklet.pdf)).

Can you send me a link to or an electronic copy of your dissertation when it is final, as I would like to read it.

Good luck,

Michael Fiore

---

Michael A. Fiore, MS  
Massachusetts FACE Project  
Massachusetts Department of Public Health  
Occupational Health Surveillance Program  
250 Washington Street, 6th Floor  
Boston, Massachusetts 02108  
Tel: [617-624-5627](tel:617-624-5627) Fax: [617-624-5676](tel:617-624-5676)  
Web site: [www.mass.gov/dph/ohsp](http://www.mass.gov/dph/ohsp)  
DPH Blog: <http://publichealth.blog.state.ma.us/>

**From:** Zhanbiao Li [<mailto:li2c@uwindsor.ca>]

**Sent:** Friday, October 18, 2013 10:40 AM

**To:** Fiore, Michael (DPH)

**Subject:** copyright permission requested

Hello Michael,

Christina Spring from Public Affairs Officer & Team Lead | CDC-NIOSH forwarded me your contact information.

I am completing a doctoral dissertation at the University of Windsor entitled "Mechanical Analysis of Heavy-duty Mining Vehicle Wheels to Enhance Safety." I would like your permission to include in my dissertation the following figures:

Figure 4 and Figure 5 in the fatality report "Mechanic Dies while Changing a Tire Mounted on a Multi-piece Split Rim Wheel", which can be find in the link: <http://www.cdc.gov/niosh/face/stateface/ma/07ma058.html>.

I'd like to include these pictures in my dissertation to show the rusted rim, and how to take care of multi-piece rims.

They will be referred in the reference list at the end of the dissertation as:

[12] Fatality Assessment and Control Evaluation (FACE) Program, U.S. Department of Health and Human Services(2007). Mechanic Dies while Changing a Tire Mounted on a Multi-piece Split Rim Wheel,Massachusetts Case Report: 07-MA-058. <<http://www.cdc.gov/niosh/face/stateface/ma/07ma058.html>> accessed on June 5, 2013.

My dissertation will be deposited to the University of Windsor Leddy library.

Please confirm in writing or by email that these arrangements meet with your approval.

Thank you very much for your attention to this matter.

Sincerely,

Zhanbiao Li

**Copyright permission for reference [11]**

On Mon, Sep 30, 2013 at 2:23 PM, Rick Banting <[RickBanting@workplacesafetynorth.ca](mailto:RickBanting@workplacesafetynorth.ca)> wrote:

Hi Weldon,

No Problem to use the Multi -Piece Rim figure. You can complement Workplace Safety North in foot note if possible.

Rick

**Richard Banting**  
Electrical - Mechanical Specialist  
**WORKPLACE SAFETY NORTH**  
T [705 474 7233](tel:7054747233) x246 | [1 888 730 7821](tel:18887307821)  
M [705 493 0028](tel:7054930028)  
F [705 472 5800](tel:7054725800)  
[rickbanting@workplacesafetynorth.ca](mailto:rickbanting@workplacesafetynorth.ca)

Find out more by visiting us at: [www.workplacesafetynorth.ca](http://www.workplacesafetynorth.ca)

---

**From:** Cindy Hunter  
**Sent:** September-30-13 2:17 PM  
**To:** Rick Banting  
**Subject:** RE: permission requested for using the figure

Hi Rick

I am comfortable with permitting it.  
We typically request the illustration (or whatever) be attributed to (in this case) the Mine and Aggregates Safety and Health Association, now Workplace Safety North.

Cindy

---

**From:** Rick Banting  
**Sent:** September-30-13 2:14 PM  
**To:** Cindy Hunter  
**Cc:** Dwayne Plamondon  
**Subject:** FW: permission requested for using the figure

Hi Cindy,

One of the graduate students at the U. of Windsor has asked to use a sketch taken from one episode of MASHA's Safety Meeting Topic series, Multi-piece Rims, Controlling The Hazard. May he use it as per request below.

Rick

**From:** Weldon Li [<mailto:weldonli@gmail.com>]  
**Sent:** September-30-13 1:07 PM  
**To:** Rick Banting  
**Subject:** permission requested for using the figure



Hello, Rick,

I am completing a doctoral dissertation at the University of Windsor entitled "Mechanical Analysis of Heavy-duty Mining Vehicle Wheels to Enhance Safety." I would like your permission to include in my dissertation the following figure:



The document can be accessed in the following link: <http://www.workplacesafetynorth.ca/sites/default/files/resources/Multi-Piece%20Rims%20Presentation.pdf>

My dissertation will be deposited to the University of Windsor Leddy library.  
[or]

My dissertation will be deposited to the University of Windsor's online theses and dissertations repository (<http://winspace.uwindsor.ca>) and will be available in full-text on the internet for reference, study and / or copy.

I will also be granting Library and Archives Canada and ProQuest/UMI a non-exclusive license to reproduce, loan, distribute, or sell single copies of my thesis by any means and in any form or format. These rights will in no way restrict republication of the material in any other form by you or by others authorized by you.

Please confirm in writing or by email that these arrangements meet with your approval.

Thank you very much for your attention to this matter.

Sincerely,

Best Regards

Weldon Li



Copyright permission for reference [16]

RE: permission requested using a figure in the website



Reference x

Satch Reed <satchreed@comcast.net>  
to li12c

Sep 30



Hi:

You have permission to use the rim dimension diagram as you choose.

Regards  
Satch Reed  
Publisher  
[www.secondchancegarage.com](http://www.secondchancegarage.com)

-----Original Message-----

From: [li12c@uwindsor.ca](mailto:li12c@uwindsor.ca) [mailto:[li12c@uwindsor.ca](mailto:li12c@uwindsor.ca)]  
Sent: Monday, September 30, 2013 1:51 PM  
To: [satchreed@comcast.net](mailto:satchreed@comcast.net)  
Subject: permission requested using a figure in the website

Email Message: From Second Chance Garage September 30, 2013

To Whom It May Concern:

I am completing a doctoral dissertation at the University of Windsor entitled "Mechanical Analysis of Heavy-duty Mining Vehicle Wheels to Enhance Safety." I would like your permission to include in my dissertation the rim dimension figure in the following link: <http://www.secondchancegarage.com/public/265.cfm>.

My dissertation will be deposited to the University of Windsor Leddy library.  
[or]

My dissertation will be deposited to the University of Windsor's online theses and dissertations repository (<http://winspace.uwindsor.ca>) and will be available in full-text on the internet for reference, study and / or copy.

I will also be granting Library and Archives Canada and ProQuest/UMI a non-exclusive license to reproduce, loan, distribute, or sell single copies of my thesis by any means and in any form or format. These rights will in no way restrict republication of the material in any other form by you or by others authorized by you.

Please confirm in writing or by email that these arrangements meet with your approval.

Thank you very much for your attention to this matter.

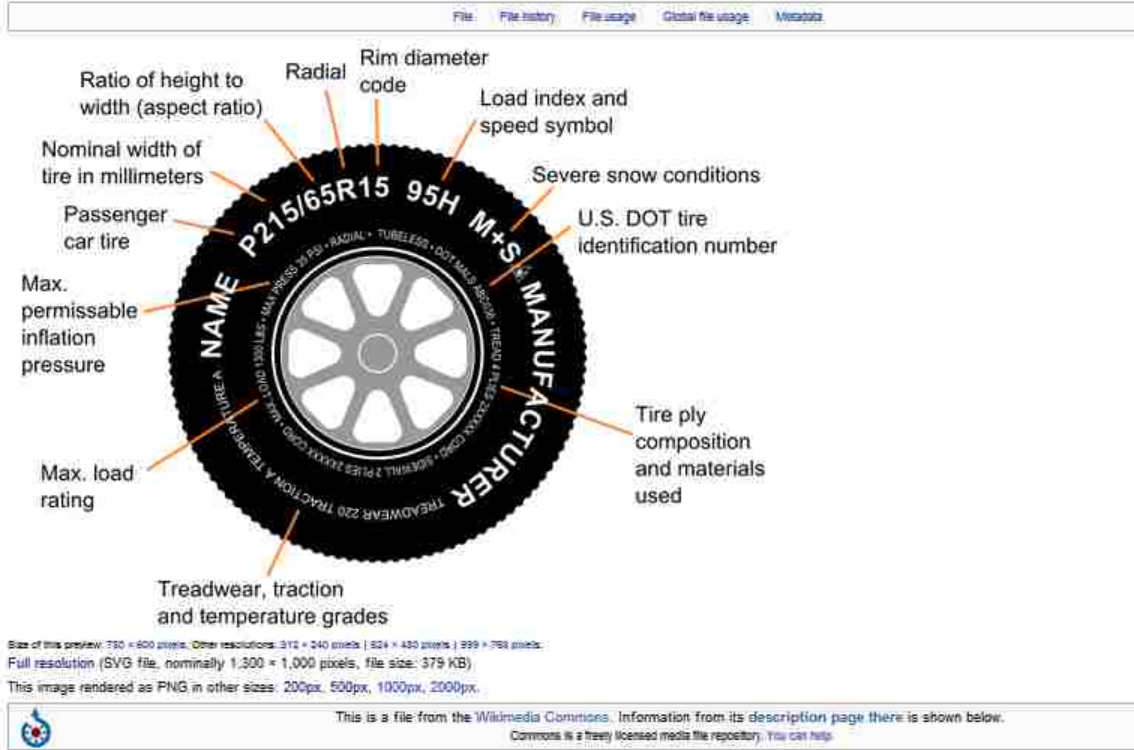
Sincerely,

Zhanbiao Li

## Copyright permission for reference [17]

File:Tire code - en.svg

From Wikipedia, the free encyclopedia



### Summary [\[edit\]](#)

<b>Description:</b>	English: tire identification diagram showing various labeling features. English terms.
<b>Date:</b>	
<b>Source:</b>	Own work
<b>Author:</b>	Flanker

### Licensing: [\[edit\]](#)

I, the copyright holder of this work, hereby publish it under the following license:

This file is licensed under the [Creative Commons Attribution 3.0 Unported](#) license.

You are free:

- to share – to copy, distribute and transmit the work
- to remix – to adapt the work

Under the following conditions:

- attribution – You must attribute the work in the manner specified by the author or licensor (but not in any way that suggests that they endorse you or your use of the work).

## Copyright permission for reference [18]

On Fri, Oct 18, 2013 at 1:54 AM, 岩澤亨 <[iwasawa@topy.co.jp](mailto:iwasawa@topy.co.jp)> wrote:

Dear Mr zhanbiao li

Thank you for your mail.  
Sorry for this late reply.

This morning, the use of the figures was admitted by technical Administration Dept. of our company.

However, there is one request.

When your disseration is completed, please contact me by an email. Thank you.

I pray for the success of your disseration.

Sincerely yours,

Tohru Iwasawa

\*\*\*\*\*  
岩澤 亨  
トピー工業株式会社 総務部  
〒141-8634  
東京都品川区大崎1-2-2  
アートヴィレッジ大崎セントラルタワー  
TEL:03-3493-0777  
FAX:03-3493-0200  
[E-mail:iwasawa@topy.co.jp](mailto:iwasawa@topy.co.jp)

2013/10/17 Zhanbiao Li <[li12c@uwindsor.ca](mailto:li12c@uwindsor.ca)>

Hello Mr. Tohru Iwasawa,

I have replied your email one week back and have not receive your response yet.

I am completing a doctoral dissertation at the University of Windsor entitled "Mechanical Analysis of Heavy-duty Mining Vehicle Wheels to Enhance Safety." This research is supported by Workplace Safety Insurance Board and other industry partners in Ontario, Canada. I would like your permission to include in my dissertation the following figures in "Multi-piece Rims for Industrial and Construction Vehicles - RIM INSTRUCTION MANUAL":

The two figures in page 7 and the top figure in page 8. The purpose to use these three figures is to illustrate the structures of three-piece rim and five-piece rim.

The figure in page 23 to show correct and wrong installation of the lock ring.

The figure on the left side of page 27 to illustrate the sprung lock ring and the good lock ring.

The reference document can be accessed via: <http://www.topy.co.jp/english/dept/wheel/pdf/71424250-e.pdf>.

My dissertation will be deposited to the University of Windsor Leddy library.

[or]

My dissertation will be deposited to the University of Windsor's online theses and dissertations repository (<http://winspace.uwindsor.ca>) and will be available in full-text on the internet for reference, study and / or copy.

I will also be granting Library and Archives Canada and ProQuest/UMI a non-exclusive license to reproduce, loan, distribute, or sell single copies of my thesis by any means and in any form or format. These rights will in no way restrict republication of the material in any other form by you or by others authorized by you.

Please confirm in writing or by email that these arrangements meet with your approval.

Thank you very much for your attention to this matter and I look forward to getting your permission.

Sincerely,

On Wed, Oct 2, 2013 at 4:53 AM, 岩澤亨 <[t-iwasawa@topy.co.jp](mailto:t-iwasawa@topy.co.jp)> wrote:

Dear Mr zhanbiao li

Thank you for your mail.

Sorry for this late reply.

My name is Tohru Iwasawa and I am in charge of General Affairs Dept. at Topy Industries, Limited.

Before we can give you any permission, there are two questions we would like you to tell us:

- ①What is the point of argument of the dissertation?
- ②For what explanation do you want to use the figures for?

Please let me know.

Sincerely yours,

Tohru Iwasawa




\*\*\*\*\*  
岩澤 亨  
トピー工業株式会社 総務部  
〒141-8634  
東京都品川区大崎1-2-2  
アートヴィレッジ大崎セントラルタワー  
TEL:03-3493-0777  
FAX:03-3493-0200  
[E-mail:t-iwasawa@topy.co.jp](mailto:t-iwasawa@topy.co.jp)

—  
Best Regards

Weldon Li



## Copyright permission for reference [19]

 **Spring, Christina M. (CDC/NIOSH/OD)** Oct 17 (2 days ago)  

to me -

Hi Zhanbiao,


I've heard back from the program staff. The Alaska FACE program, who led the publication of this piece, no longer exists. So for your needs, if the photo provides a citation than we ask if you could please include it in your paper. If there is no citation, then you don't need to add it, but we do ask that you acknowledge the Alaska FACE program and the NIOSH FACE program

Let me know if there's anything else we can do to help.

Thanks,  
Christy

**From:** Zhanbiao Li [mailto:[li12c@uwindsor.ca](mailto:li12c@uwindsor.ca)]  
**Sent:** Thursday, October 17, 2013 1:08 PM

**To:** Spring, Christina M. (CDC/NIOSH/OD)  
**Subject:** Re: copyright permission requested



Hello Christy,

Thanks for your update.

Zhanbiao Li

On Thu, Oct 17, 2013 at 1:03 PM, Spring, Christina M. (CDC/NIOSH/OD) <[dsa9@cdc.gov](mailto:dsa9@cdc.gov)> wrote:  
Hi Zhanbiao,

I wanted to let you know that I did receive your email and I am reaching out to our program staff to get an answer on the permission to use the figures. I hope to have a response for you soon.

Thanks,  
Christy

Christine Spring, M.A.  
Public Affairs Officer & Team Lead | CDC-NIOSH  
395 E Street, S.W. | Suite 9200 | Washington, DC 20201  
p. [202-245-0633](tel:202-245-0633) | f. [202-245-0648](tel:202-245-0648)  
[dsa9@cdc.gov](mailto:dsa9@cdc.gov)  
I telework on Wednesdays, available at [202-246-4695](tel:202-246-4695)

**From:** Zhanbiao Li [mailto:[li2c@uwindsor.ca](mailto:li2c@uwindsor.ca)]  
**Sent:** Thursday, October 17, 2013 11:09 AM  
**To:** Spring, Christina M. (CDC/NIOSH/OD)  
**Subject:** copyright permission requested

Hello Christina,

I am completing a doctoral dissertation at the University of Windsor entitled "Mechanical Analysis of Heavy-duty Mining Vehicle Wheels to Enhance Safety." I would like your permission to include in my dissertation the following figures:

Figure 4 and Figure 5 in the fatality report "Mechanic Dies while Changing a Tire Mounted on a Multi-piece Split Rim Wheel", which can be find in the link: <http://www.cdc.gov/niosh/face/stateface/ma/07ma058.html>

Figure 1 in the fatality report "Worker Struck By Multi-piece Rim during Wheel Installation", which can be find in the link: <http://www.cdc.gov/niosh/FACE/stateface/ak/03ak006.html>

I'd like to include these pictures in my dissertation to show the structures of two-piece rim, the rusted rim, and how to take care of multi-piece rims.

They will be referred in the reference list at the end of the dissertation as:

[12] Fatality Assessment and Control Evaluation (FACE) Program, U.S. [Department of Health and Human Services](#)(2007). Mechanic Dies while Changing a Tire Mounted on a Multi-piece Split Rim Wheel,Massachusetts Case Report: 07-MA-058. <<http://www.cdc.gov/niosh/face/stateface/ma/07ma058.html>> accessed on June 5, 2013.

[21] Fatality Assessment and Control Evaluation (FACE) Program, U.S. [Department of Health and Human Services](#)(2003). Worker Struck By Multi-piece Rim during Wheel Installation,Alaska Case Report: 03AK006, <<http://www.cdc.gov/niosh/FACE/stateface/ak/03ak006.html>> accessed June 7, 2013.

My dissertation will be deposited to the University of Windsor Leddy library.



Please confirm in writing or by email that these arrangements meet with your approval.

Thank you very much for your attention to this matter.




Sincerely,


Zhanbiao Li

Copyright permission for reference [20] [30]

Re:Ask An Expert (Request #3140455) Reference x  

---

 **Workplace Health and Safety** [whs@gov.ab.ca](mailto:whs@gov.ab.ca) via [uwindsor.ca](http://uwindsor.ca) Oct 1   

to li12c 

Hello,

Thank you for inquiring through Occupational Health and Safety's "Ask the Expert" function.

The information is available to the public for general use, if you include the material in your paper please be sure to site your source.

If you require further assistance or wish to discuss your situation with a Safety Advisor, please contact our Occupational Health and Safety Contact Centre at [1-866-415-8690](tel:1-866-415-8690).

Sincerely,  
Alberta Occupational Health and Safety  
[1-866-415-8690](tel:1-866-415-8690)  
[www.worksafely.org](http://www.worksafely.org)



Copyright permission for reference [21] [22]

Copyright permission requested

inbox x



**Weldon Li** <weldonli@gmail.com>  
to Mark

10/25/13



Hello Mark,

The two-piece rim manuscript is being reviewed by Dr. Altenhof now. We will submit it for publication soon.

Here I want to get a copyright permission from you for using figures in WSIB's documents.

I am completing a doctoral dissertation at the University of Windsor entitled "Mechanical Analysis of Heavy-duty Mining Vehicle Wheels to Enhance Safety."

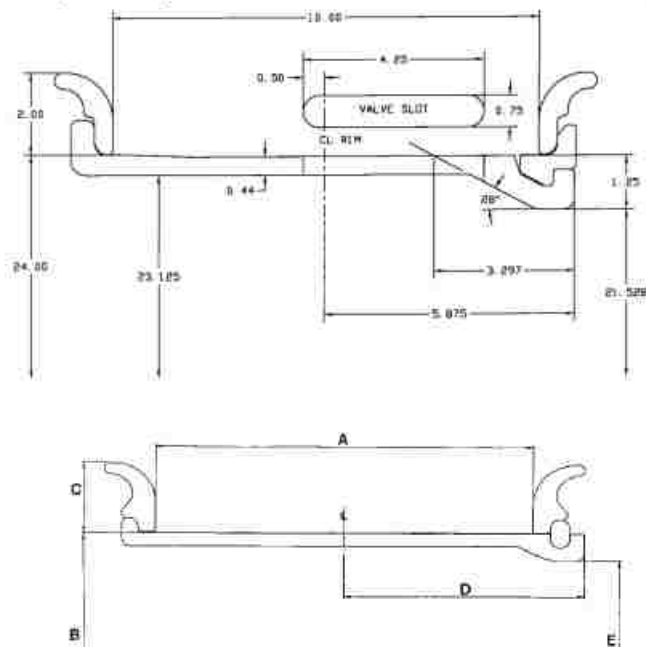
I would like your permission to include in my dissertation the following figures:

The 7-piece rim



link: <http://www.nsiw.com/UploadedFiles/File/qc7%20quick%20change%20wheel%20broc.pdf>

The 4-piece rim figures:



On page 18 and 25 of "North Shore Industry Wheel - Earthmover and Construction Products Catalog".

I want to use the figures to show the structures of multi-piece rims.

My dissertation will be deposited to the University of Windsor Leddy library.

[or]

My dissertation will be deposited to the University of Windsor's online theses and dissertations repository (<http://winspace.uwindsor.ca>) and will be available in full-text on the internet for reference, study and / or copy.

Please confirm in writing or by email that these arrangements meet with your approval.

Thank you very much for your attention to this matter.

Sincerely,

Weldon Li

**Mark Thomas** <markthomas@nsiw.com>

10/25/13



to me ▾

[I don't see a problem with this, please procede](#)

Best Regards,

Mark Thomas

**NORTH SHORE WHEEL**

Office:  [\(705\)942-8484 Ext 28](tel:(705)942-8484) | Cell:  [\(705\)542-4604](tel:(705)542-4604)

Copyright permission for reference [25]

On Tue, Oct 1, 2013 at 10:05 AM, <[jude.decastro@goodvear.com](mailto:jude.decastro@goodvear.com)> wrote:

Weldon it is OK to use

Good luck

Let me know when you are completely finished

Thanks

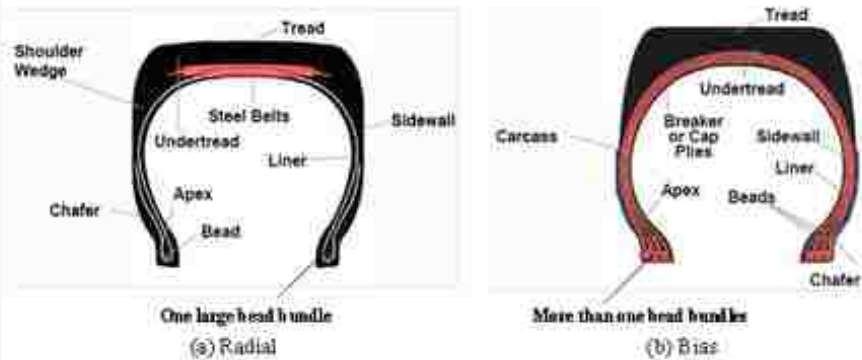
Sent from BlackBerry

---

**From:** Weldon LI [[weldonli@gmail.com](mailto:weldonli@gmail.com)]  
**Sent:** 09/30/2013 08:06 PM AST  
**To:** Jude Decastro  
**Subject:** permission requested using figures

Hello, Jude,

I am completing a doctoral dissertation at the University of Windsor entitled "Mechanical Analysis of Heavy-duty Mining Vehicle Wheels to Enhance Safety." I would like your permission to include in my dissertation the following pictures in your presentation titled "ABC's of OTR".



My dissertation will be deposited to the University of Windsor's online theses and dissertations repository (<http://winspace.uwindsor.ca>) and will be available in full-text on the internet for reference, study and / or copy.

I will also be granting Library and Archives Canada and ProQuest/UMI a non-exclusive license to reproduce, loan, distribute, or sell single copies of my thesis by any means and in any form or format. These rights will in no way restrict republication of the material in any other form by you or by others authorized by you.

Please confirm in writing or by email that these arrangements meet with your approval.

Thank you very much for your attention to this matter.

Sincerely,

Best Regards

Weldon LJ

**Copyright permission for reference [26] [28]**

On Wed, Oct 16, 2013 at 7:58 PM, <[jude.decastro@goodyear.com](mailto:jude.decastro@goodyear.com)> wrote:

Weldon both of these publication's are for public view via the internet so I see no problem with you using them

Go ahead

Good luck

Thanks

Goodyear Canada Inc.  
Jude deCastro  
Regional and Corporate Account Manager Off Road Tires  
211 Edenwood Crescent  
Orangeville, Ontario, Canada  
L9W 4M8  
Phone [519-938-5506](tel:519-938-5506)  
Fax [519-938-5507](tel:519-938-5507)  
Mobile [705-690-4156](tel:705-690-4156)

JLTTGWD

\*Contains Confidential and/or Proprietary Information. May not be copied or disseminated without the express written consent of The Goodyear Tire & Rubber Company.\*

From: Weldon Li <[weldonli@gmail.com](mailto:weldonli@gmail.com)>  
To: [jude.decastro@goodyear.com](mailto:jude.decastro@goodyear.com)  
Date: 10/16/2013 01:18 PM  
Subject: Copyright permission requested

Hello Jude,

I have sent an email to Goodyear OTR two weeks back to ask for copyright permission for my Ph. D. dissertation and did not get any response yet. Could you give me the permission to use the following pictures in Goodyear's documents?

Figure 2.1 on page 10 in "Radial Truck Tire and Retread Service Manual" ([http://www.goodyear.ca/truck/pdf/radialretrserv/Retread\\_All\\_V.pdf](http://www.goodyear.ca/truck/pdf/radialretrserv/Retread_All_V.pdf)) to illustrate the difference between a radial tire and a bias tire.

The figure on page 15 in "Off-the-Road Tire Engineering Data" (<http://www.goodyearotr.com/cfm/web/otr/info/pdf/otrdatabook.pdf>) to show tire deformation dimensions.

My dissertation "Mechanical Analysis of Heavy-duty Mining Vehicle Wheels to Enhance Safety" will be deposited to the University of Windsor Leddy library.

[or]

My dissertation will be deposited to the University of Windsor's online theses and dissertations repository (<http://winspace.uwindsor.ca>) and will be available in full-text on the internet for reference, study and / or copy.

Thank you very much for your attention to this matter.

Sincerely,

Weldon Li



## Copyright permission for reference [32]



Thorne, Gordon  
to me ▾

Oct 3



Best of luck, Zhanbiao Li, with the completion of your doctoral dissertation!

Gordon

---

**From:** Weldon Li [mailto:[weldonli@gmail.com](mailto:weldonli@gmail.com)]

**Sent:** Thursday, October 03, 2013 8:49 AM

...

**To:** Thorne, Gordon

**Subject:** Re: Other corporate information

Hello Mr. Gordon Thorne,

Thanks for your correction.

I will do as you requested.

Zhanbiao Li

On Thu, Oct 3, 2013 at 11:44 AM, Thorne, Gordon <[Gordon.Thorne@worksafebc.com](mailto:Gordon.Thorne@worksafebc.com)> wrote:

Hello Zhanbiao,

Please adjust your citation as follows, to correspond with WorkSafeBC's requirements:

[34] *WorkSafeBC, Workers' Compensation Board of BC (2005). Welding on assembled wheel results in explosion, Incident Investigation Report, 2005.*

Note the deletion of the Incident number. WorkSafeBC policy requires that all Investigation reference numbers be deleted in such usages.

Thank you,  
Gordon Thorne

---

**From:** Weldon Li [mailto:[weldonli@gmail.com](mailto:weldonli@gmail.com)]

**Sent:** Wednesday, October 02, 2013 4:42 PM

**To:** Thorne, Gordon

**Subject:** Re: Other corporate information

Hello Mr. Gordon Thorne,

The caption used for the figure is "*Figure 2.16 The exploded tire involved in the incident [34].*" with reference number 34. At the end of the dissertation, this reference will appear at the reference list such as:

[34] *WorkSafety BC, Workers' Compensation Board of BC (2005). Welding on assembled wheel results in explosion, Incident Investigation Report, NI # 2005108320019, 2005.*  
<<http://www2.worksafebc.com/PDFs/investigations/IIR2005108320019.pdf>> accessed on June 15, 2013.

In the text, A few incidents were explained to explain why multi-piece rims have hazards and my research is to redesign the multi-piece rims to make them safer.

The reference format is standard and consistent in my dissertation.

Please indicate if this kind of reference is acceptable for you.

Thanks.

Zhanbiao Li  
PLp

On Wed, Oct 2, 2013 at 3:52 PM, Thorne, Gordon <[Gordon.Thorne@worksafebc.com](mailto:Gordon.Thorne@worksafebc.com)> wrote:

Hello Zhanbiao.

Thank you for your email.

WorkSafeBC grants you permission to use the WorkSafeBC image specified for the sole purpose described in your email.

Please accompany a copy of the image with the following credit line: "© WorkSafeBC. Used with permission."

Please indicate if you intend to provide any caption or text related specifically to this image.

I look forward to hearing back from you at your convenience.

Thank you.

Gordon Thorne  
Manager, Product and Program Development  
WorkSafeBC



-----Original Message-----  
Received: 10/2/2013 10:55:01 AM

WCB Feedback Submission Contents

Name: Zhanbiao Li  
Phone: [519 9791156](tel:5199791156)  
E-mail: [li12c@uwindsor.ca](mailto:li12c@uwindsor.ca)  
Account Number:  
Subject: Other corporate information  
Message:

To Whom It May Concern:

I am completing a doctoral dissertation at the University of Windsor entitled "Mechanical Analysis of Heavy-duty Mining Vehicle Wheels to Enhance Safety." I would like your permission to include in my dissertation the exploded tire figure on page 1 in "Incident Investigation Report - Welding on assembled wheel results in explosion" to illustrate the incident. The document may be accessed via: <http://www2.worksafefbc.com/PDFs/investigations/IIR2005108320019.pdf>

My dissertation will be deposited to the University of Windsor Leddy library.

[or]

My dissertation will be deposited to the University of Windsor's online theses and dissertations repository (<http://winspace.uwindsor.ca>) and will be available in full-text on the internet for reference, study and / or copy.

I will also be granting Library and Archives Canada and ProQuest/UMI a non-exclusive license to reproduce, loan, distribute, or sell single copies of my thesis by any means and in any form or format. These rights will in no way restrict republication of the material in any other form by you or by others authorized by you.

Please confirm in writing or by email that these arrangements meet with your approval.

Thank you very much for your attention to this matter.

Sincerely,

Zhanbiao Li

Follow us on Twitter, YouTube, or one of our many social networks:

[http://www.worksafebc.com/news\\_room/SocialNetworks/default.asp](http://www.worksafebc.com/news_room/SocialNetworks/default.asp)

#### CONFIDENTIALITY DISCLAIMER

The information contained in this transmission may contain privileged and confidential information of WorkSafeBC - the Workers' Compensation Board. It is intended for review only by the person(s) named above. Dissemination, distribution or duplication of this communication is strictly prohibited by all recipients unless expressly authorized otherwise. If you are not the intended recipient, please contact the sender by reply email and destroy all copies of the original message. Thank you.

## Copyright permission for reference [33]



## Copyright permission for reference [81]



**Terri Kelly** <terri@sae.org>  
to me ▾

Jan 16 (7 days ago) ☆



Dear Zhanbiao,

Thank you for your correspondence requesting permission to reprint figures 1 and 2 from SAE document J328 Feb2005 in your PhD thesis for the University of Windsor entitled "Mechanical Analysis of Heavy-duty Mining Vehicle Wheels to Enhance Safety."

Permission is hereby granted, and subject to the following conditions:

- Permission is for this one-time use only. New requests are required for further use or distribution of the SAE material.
- The following credit statement must appear directly below the figures: "Reprinted with permission from SAE J328 Feb 2005 © 2005 SAE International. Further use or distribution is not permitted without permission from SAE."
  - The figures must also be locked images within your thesis/document so that further copy/paste feature is not allowed.

As for the reference you noted below, you can include this wording in the reference section of your thesis. However, this is not the link you should include in this reference. The correct link that must be included is [http://standards.sae.org/J328\\_200502/](http://standards.sae.org/J328_200502/). This link takes the reader to the SAE website where they can purchase a copy of the full standard from SAE.

If you are not able to meet these terms and conditions, then we suggest that you remove the images from your thesis and include a normative reference to the figures and the SAE standard in your thesis.

Again, thank you for contacting SAE. Please feel free to contact me if you need further assistance.

Best regards,

---

**Terri Kelly**  
Intellectual Property Rights Administrator

**SAE INTERNATIONAL**  
400 Commonwealth Drive  
Warrendale, PA 15096

o [+1 724 772 4095](tel:+17247724095)

f [+1 724-776-9765](tel:+17247769765)

e [terri@sae.org](mailto:terri@sae.org)

[www.sae.org](http://www.sae.org)

**From:** Zhanbiao Li [mailto:[l12c@uwindsor.ca](mailto:l12c@uwindsor.ca)]

**Sent:** Monday, November 11, 2013 8:46 AM

**To:** copyright

**Subject:** copyright permission requested

\*\*\*

To Whom It May Concern:

I am completing a doctoral dissertation at the University of Windsor entitled "Mechanical Analysis of Heavy-duty Mining Vehicle Wheels to Enhance Safety." I would like your permission to include in my dissertation the following figures. The figures are in the article "SURFACE VEHICLE RECOMMENDED PRACTICE - Wheels - Passenger Car and Light Truck Performance Requirements and Test Procedures- SAE J328", Rev. FEB2005, Copyright 2005, which can be retrieved via the link <http://fsyulie.vicp.net:107/index/images/userfiles/media/SAE%20J328-2005.pdf>

Figure 1-Dynamic cornering fatigue (typical set-up)

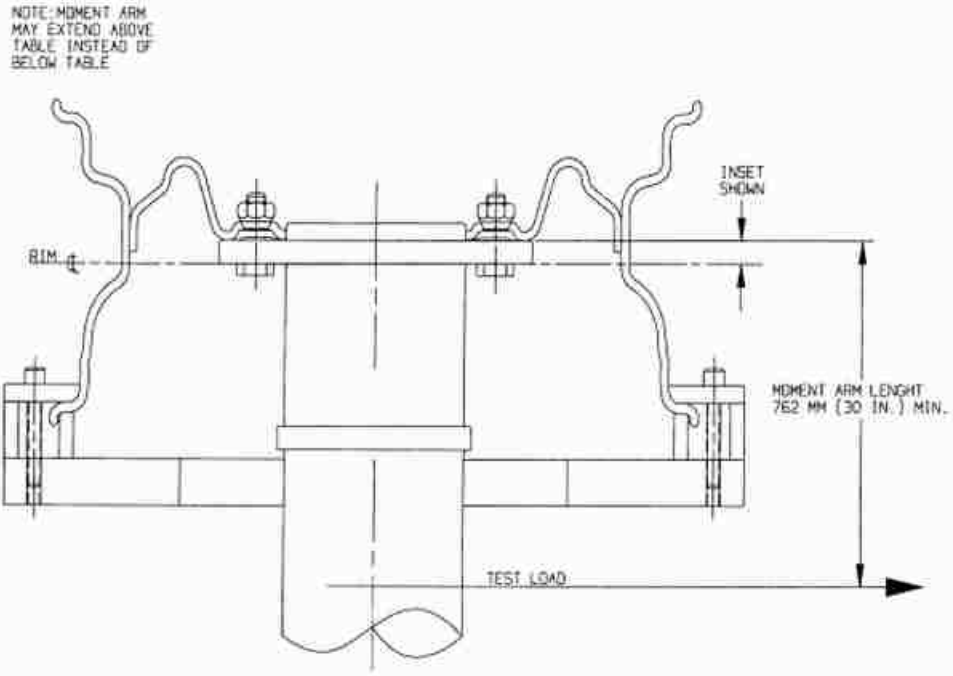


FIGURE 1—DYNAMIC CORNERING FATIGUE (TYPICAL SET-UP)

Figure 2—Radial fatigue (typical set-up)

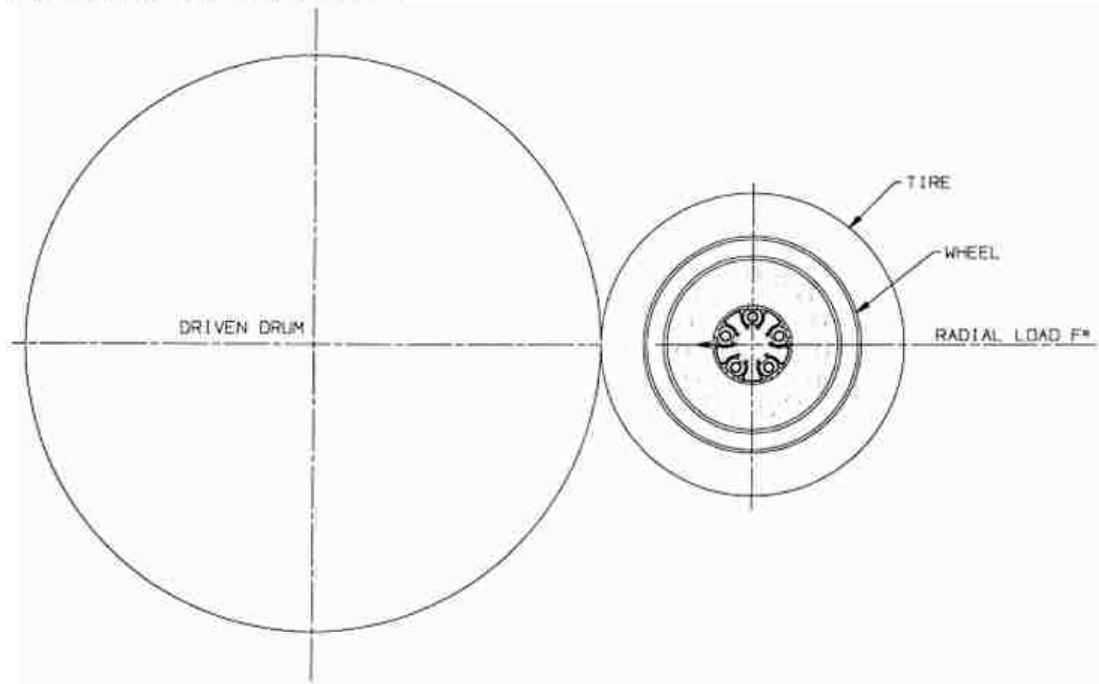


FIGURE 2—RADIAL FATIGUE (TYPICAL SET-UP)

I'd like to include the figures in my dissertation to show the fatigue test methods for wheels.

The figures will be referred in the reference list at the end of the dissertation as:

[83] SAE (Society of Automotive Engineers) International (2005). SURFACE VEHICLE RECOMMENDED PRACTICE - Wheels - Passenger Car and Light Truck Performance Requirements and Test Procedures- SAE J328, Rev. Feb. 2005, 400 Commonwealth Drive, Warrendale, PA <<http://fsyujie.vicp.net:107/index/images/userfiles/media/SAE%20J328-2005.pdf>> accessed on July 11, 2013.

My Dissertation is expected to be finished in April 2014 and will be produced 6 hard copies: one for my adviser, one for Graduate Studies at the University of Windsor, one for University library, one for myself, and two for industry partners.

My dissertation will be deposited to the University of Windsor's online theses and dissertations repository (<http://winspace.uwindsor.ca>) and will be available in full-text on the internet for reference and study.

Please confirm in writing or by email that these arrangements meet with your approval.

Thank you very much for your attention to this matter.

Sincerely,

Zhanbiao LI



## Copyright permission for reference [105]

permission requested using figures in nCode  
document



Reference x

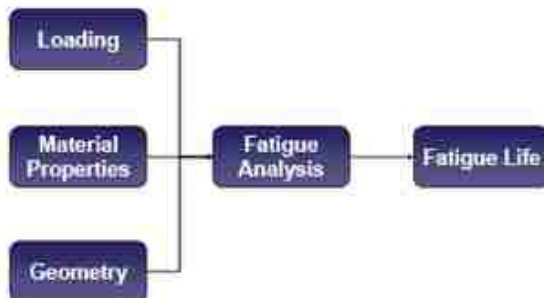
Weldon Li <weldonli@gmail.com>  
to Kurt

10/2/13



Hello Munson,

I am completing a doctoral dissertation at the University of Windsor entitled "Mechanical Analysis of Heavy-duty Mining Vehicle Wheels to Enhance Safety." I would like your permission to include in my dissertation the following two figures (on page 12 and 44) in the material "Practical Fatigue Theory".



I am using these two figures to show Miner's rule and the five-box structure of nCode DesignLife. You may find the file I am using in the attachment.

My dissertation will be deposited to the University of Windsor Leddy library.

[or]

My dissertation will be deposited to the University of Windsor's online theses and dissertations repository (<http://winspace.uwindsor.ca>) and will be available in full-text on the internet for reference, study and / or copy.

I will also be granting Library and Archives Canada and ProQuest/UMI a non-exclusive license to reproduce, loan, distribute, or sell single copies of my thesis by any means and in any form or format. These rights will in no way restrict republication of the material in any other form by you or by others authorized by you.

Please confirm in writing or by email that these arrangements meet with your approval.

Thank you very much for your attention to this matter.

Sincerely,

Zhanbiao Li

Best Regards

Weldon Li



## Copyright permission for reference [128]

Picture  Inbox x



**david.malmstrom@kaimarglobal.com**

to me >

Dear Zhanbiao,

Please go ahead and use the picture.

Best regards,

**David Malmström**  
Marketing Coordinator  
Kalmar Forklift trucks

Cargotec Sweden AB  
Torggatan 3  
340 10 Lidhult, SWEDEN  
Phone: [+46\(0\)372 378248](tel:+46(0)372378248)  
[david.malmstrom@kaimarglobal.com](mailto:david.malmstrom@kaimarglobal.com)  
[www.kaimarglobal.com](http://www.kaimarglobal.com)

First Name	Zhanbiao
Last Name	Li
Subject	<a href="#">Contact request</a>
Magazine	<a href="#">(Select)</a>
Language	<a href="#">(Select)</a>
Amount	
Message	To Whom It May Concern:

I am completing a doctoral dissertation at the University of Windsor entitled "Mechanical Analysis of Heavy-duty Mining Vehicle Wheels to the figure on the title page of "Kalmar Technical Information Container Handler ContChamp 42-45 tonnes". I want to use the figure to illustrate document may be accessed via: <http://www.kalmarind.nl/source.php/38881/Products%20Tech%20doc%20DRF%20Toplift.pdf>.

My dissertation will be deposited to the University of Windsor Leddy library.

[or]

My dissertation will be deposited to the University of Windsor's online theses and dissertations repository (<http://winspace.uwindsor.ca>) copy.

Please confirm in writing or by email that these arrangements meet with your approval.  
Thank you very much for your attention to this matter.

If you can not meet my request, please inform me the right person I shall contact.

Sincerely,

Zhanbiao Li

University of Windsor

401 Sunset Ave.

N9B 3P4

Windsor

Ontario

Canada

[ll12c@uwindsor.ca](mailto:ll12c@uwindsor.ca)

By Email

Company overview

<http://www.carqotec.com/en-global/about-us/company-overview/Pages/default.aspx>



**Title:** A threaded-connection locking mechanism integrated into a multi-piece mining wheel for enhanced structural performance and safety

**Author:** Zhanbiao Li, Sante DiCecco, Aleksander Tonkovich, William Altenhof, Richard Banting, Henry Hu

**Publication:** Journal of Terramechanics

**Publisher:** Elsevier

**Date:** August 2013

Copyright © 2013, Elsevier

Logged in as:

Zhanbiao Li

LOGOUT

### Order Completed

Thank you very much for your order.

This is a License Agreement between Zhanbiao Li ("You") and Elsevier ("Elsevier"). The license consists of your order details, the terms and conditions provided by Elsevier, and the [payment terms and conditions](#).

[Get the printable license.](#)

License Number	3253021028301
License date	Oct 20, 2013
Licensed content publisher	Elsevier
Licensed content publication	Journal of Terramechanics
Licensed content title	A threaded-connection locking mechanism integrated into a multi-piece mining wheel for enhanced structural performance and safety
Licensed content author	Zhanbiao Li, Sante DiCecco, Aleksander Tonkovich, William Altenhof, Richard Banting, Henry Hu
Licensed content date	August 2013
Licensed content volume number	50
Licensed content issue number	4
Number of pages	20
Type of Use	reuse in a thesis/dissertation
Portion	full article
Format	electronic
Are you the author of this Elsevier article?	Yes
Will you be translating?	No
Order reference number	
Title of your thesis/dissertation	Mechanical Analyses of multi-piece mining wheels to enhance safety
Expected completion date	Dec 2013
Estimated size (number of pages)	300
Elsevier VAT number	GB 494 6272 12
Permissions price	0.00 USD
VAT/Local Sales Tax	0.00 USD / 0.00 GBP
Total	0.00 USD

ORDER MORE...

CLOSE WINDOW



**Title:** Experimental observations of tyre deformation characteristics on heavy mining vehicles under static and quasi-static loading

**Author:** Aleksander Tonkovich, Zhanbiao Li, Sante DiCecco, William Altenhof, Richard Banting, Henry Hu

**Publication:** Journal of Terramechanics  
**Publisher:** Elsevier  
**Date:** June–August 2012  
 Copyright © 2012, Elsevier

Logged in as:  
Zhanbiao Li  
Account #: 3000709465

LOGOUT

### Order Completed

Thank you very much for your order.

This is a License Agreement between Zhanbiao Li ("You") and Elsevier ("Elsevier"). The license consists of your order details, the terms and conditions provided by Elsevier, and the [payment terms and conditions](#).

[Get the printable license.](#)

License Number	3253031039117
License date	Oct 20, 2013
Licensed content publisher	Elsevier
Licensed content publication	Journal of Terramechanics
Licensed content title	Experimental observations of tyre deformation characteristics on heavy mining vehicles under static and quasi-static loading
Licensed content author	Aleksander Tonkovich, Zhanbiao Li, Sante DiCecco, William Altenhof, Richard Banting, Henry Hu
Licensed content date	June–August 2012
Licensed content volume number	49
Licensed content issue number	3–4
Number of pages	17
Type of Use	reuse in a thesis/dissertation
Portion	full article
Format	electronic
Are you the author of this Elsevier article?	Yes
Will you be translating?	No
Order reference number	
Title of your thesis/dissertation	Mechanical Analyses of multi-piece mining wheels to enhance safety
Expected completion date	Dec 2013
Estimated size (number of pages)	300
Elsevier VAT number	GB 494 6272 12
Permissions price	0.00 USD
VAT/Local Sales Tax	0.00 USD / 0.00 GBP
Total	0.00 USD

ORDER MORE...

CLOSE WINDOW



**Title:** Stress and fatigue life analyses of a five-piece rim and the proposed optimization with a two-piece rim

**Author:** Zhanbiao Li, Sante DiCecco, William Altenhof, Mark Thomas, Richard Banting, Henry Hu

**Publication:** Journal of Terramechanics

**Publisher:** Elsevier

**Date:** April 2014

Copyright © 2014, Elsevier

Logged in as:  
Zhanbiao Li  
Account #:  
3000709465

LOGOUT

### Order Completed

Thank you very much for your order.

This is a License Agreement between Zhanbiao Li ("You") and Elsevier ("Elsevier"). The license consists of your order details, the terms and conditions provided by Elsevier, and the [payment terms and conditions](#).

[Get the printable license.](#)

License Number	3381491392995
License date	May 03, 2014
Licensed content publisher	Elsevier
Licensed content publication	Journal of Terramechanics
Licensed content title	Stress and fatigue life analyses of a five-piece rim and the proposed optimization with a two-piece rim
Licensed content author	Zhanbiao Li, Sante DiCecco, William Altenhof, Mark Thomas, Richard Banting, Henry Hu
Licensed content date	April 2014
Licensed content volume number	52

Number of pages	15
Type of Use	reuse in a thesis/dissertation
Portion	full article
Format	electronic
Are you the author of this Elsevier article?	Yes
Will you be translating?	No
Title of your thesis/dissertation	Mechanical Analysis of Heavy Mining Vehicle Wheel Assemblies to Enhance Safety
Expected completion date	Aug 2014
Estimated size (number of pages)	300
Elsevier VAT number	GB 494 6272 12
Permissions price	0.00 USD
VAT/Local Sales Tax	0.00 USD / 0.00 GBP
Total	0.00 USD

ORDER MORE...

CLOSE WINDOW

## VITA AUCTORIS

NAME: Zhanbiao Li

PLACE OF BIRTH: Honghu, China

YEAR OF BIRTH: 1966

EDUCATION: University of Windsor, Ph. D. in mechanical engineering, Windsor, ON, 2014

University of Windsor, M. A. Sc. in mechanical engineering, Windsor, ON, 2003

Huazhong University of Science & Technology, B. Sc. in mechanical engineering, Wuhan, China, 1987